UNIVERSIDAD AUTÓNOMA DE MADRID

FACULTAD DE CIENCIAS

Instituto Universitario de Ciencia de Materiales Nicolás Cabrera

Conformational Dynamics and Assembly of the Ribosomal Stalk Proteins:
A multi-photon fluorescence micro-spectroscopy study in living cells

A thesis submitted for the degree of:
Doctor in Biophysics

Sebastian Raja

Supervisors

Dra. M. Pilar Lillo Villalobos
Dra. Carolina García Rodríguez

Madrid, 2013

The work Included in this thesis report has been done in the Physical Chemistry Institute “Rocasolano” (CSIC) under the guidance and direction of Dra. M. Pilar Lillo Villalobos and the co-direction of Dra. Carolina García Rodríguez. It has been supported by Grants CTQ 2009-12412 and CTQ 2010-16457 from Spanish Ministry of Science and Innovation and a Predoctoral fellowship from CSIC, JAE PRE 2008-105-2.

INSTITUTO DE QUÍMICA FÍSICA ROCASOLANO
CSIC
Department of Biological Physical Chemistry

UNIVERSIDAD AUTÓNOMA DE MADRID
FACULTAD DE CIENCIAS
INSTITUTO UNIVERSITARIO DE CIENCIA DE MATERIALES
NICOLÁS CABRERA

Madrid, 2013

DEVOTED TO MY BELOVED

FATHER LORD JESUS CHRIST AND MOTHER VIRGIN MARY

Acknowledgements

Completing my PhD degree is probably one of the most challenging and an unforgettable experience in my life so far. The list of the people I want to thank will not fit to a single Acknowledgement section. I have tried to consolidate in this section the reminiscence from my journey to this stage of my career. Here, I deeply acknowledge and convey my sincere thanks to those people who were both for being significant and important to my life.

First and foremost, I would like to express my deep and sincere gratitude to my primary supervisor, Dr. M. Pilar Lillo for giving me the opportunity to pursue research in her laboratory. I arrived to Spain in September 2008. Since then my supervisor Pilar has been constantly encouraging me, supporting me and putting all the resources I needed at my disposal. I would like to gratefully acknowledge her enthusiastic supervision during this work. She provided the vision; valuable suggestions and direction necessary for me to proceed through my PhD. She is very energetic and she always managed to put enormous effort for any scientific discussion. Apart from our day-to-day project discussions, I have encountered many instances where she made me to grow up as a person – more specifically as a logical thinker. She molded me with appropriate attitude in science; her guidance will make me as a proper scientist in future. But this thesis would not have been possible without the help, guidance and patience of my secondary supervisor, Dr. Carolina García. She did not only teach me many things in the lab but also she gave me the inspiration to always improve. Her good advice and deep knowledge, has been invaluable on both an academic and a personal level. Both of them remain my best role model for a scientist, mentor and teacher. I want to be more thankful to both of them, till the end of my life.

I consider myself very fortune to work with distinguished Molecular biologist Prof. Dr. Juan Pedro García Ballesta, from Centro de Biología Molecular Severo Ochoa, CSIC-UAM, Madrid. I am so pleased to thank him for introducing me to ribosome world. This thesis belongs to his biological queries. I

can’t even think of the fulfillment of this thesis without his contribution.

I am so grateful and obliged to acknowledge my well-wisher, teacher and a prominent spectroscopist Prof. Dr. A. Ulises Acuña. I am delighted to work with such a great scientist and respectful human, his generous support and encouragement helps me to finish this PhD thesis. I am very blessed and thankful for the incredible love from his family members especially from his wife Mrs. Pilar, she make my life colorful in special occasions.

I would like to pay my sincere regard to my friend Mr. Miguel Ángel Sacristán, the cool and bright dude in the lab. I learnt a lot from him while doing experiments and data analysis, along with unlimited fun. He helped me to absorb microscope handling and anisotropy measurements.

I am so grateful to thank Mr. José Antonio Serna. His contribution is innumerable with microscope development. He made our life so comfortable in crucial time; I enjoyed working with him.

I pleased to thank Dr. José Miguel Mancheño Gómez for providing pure EGFP protein. I have very nice time with him in the institute.

I would like to thank IQFR library members Mrs Esperanza Iglesias Fernandez, Ms. Adoracion Urrea Salazar, Mr. Angel González González and Mr. Jorge Pariente Moronta, who supported me lot to provide articles and books and they are so lovable in all the occasions in the institute.

My wife Annie, a lively personality, has always been able to bring me smile anytime. I am thanking for your patience, comprehension and the unconditional support you have always demonstrated to me during difficult timings and you make my life meaningful with our loveable son Mr. Aaron Miguel. He brought joy and peace to my life. I owe a great deal of gratitude to my in-laws Mr. Santhanam and Mrs. Flora Santhanam, for their constant source of love encouragement and support throughout the long road of my life.

My parents, the reason for my existence and whose contribution cannot be put into words, they always given unconditional love and support, without them which I would not believe in myself enough to be who I am. I would take this opportunity to thank my parents Mr. Jayaraj and Mrs. Therasal Jayaraj for the

constant support and encouragement in everything I have done. They always allowed me to choose my career. My grandparents, with whom I partly grew up in my childhood, are esteemed monuments of inspiration in my life. They are very proud of me not only because of my achievement but my constant effort to be better myself.

I so grateful to thank my mentor Prof Dr. M. Jeyabal, who expanded my horizon about my life at my young age, would be the happiest person seeing me with PhD degree. I would take this opportunity to thank my promoter Mr. Santhanasami for his prayer and support throughout my life. I want to sincerely thank Fr. Xavier and Fr .Emilio for their constant support and prayers during these years.

I felt myself to be the luckiest to have friends like Sesha, Rozario, Larens, Vasanth, Bose, Madhan and Charles, for bringing me love and fun that could not have been brought to me by any other means. I feel privileged for having such a lovely friends in my life.

I gratefully thank all IQFR institute members for a generous support and encouragement for the wonderful completion of my thesis.

I am so grateful to acknowledge CSIC for providing me the pre-doctoral fellowship for past four years. I want to thank Madrid community for providing me the safe life for the past five years, I himself really proud to live with Spaniards and I am so thankful for their incredible love.

Thank you

Sebastian Raja

List of Abbreviations and Symbols

τ	Fluorescence lifetime
λ	Wavelength
3D	Three dimensional
80S	80 Svedberg
A	Acceptor
a.u	Arbitrary unit
AF	Autofluorescence
ATP	Adenosine-5'-triphosphate
BS	Back scattered
CP	Central protuberance
cryo-EM	Cryo-electron Microscopy
CTD	Carboxy Terminal Domain
D	Donor
DNA	Deoxyribonucleic acid
DsRed	*Discosoma sp*. red fluorescent protein
E	FRET Efficiency
E. coli	*Escherichia coli*
EF2	Eukariotyc Elongation Factor 2
EF-G	Prokariotyc Elongation Factor G
EGFP	Enhanced Green Fluorescent Protein
em	Emission
ErB	Erythrosine B
exc	Excitation
FAD	Flavin adenine dinucleotide
FCS	Fluorescence Correlation Spectroscopy
FLIM	Fluorescence Lifetime Imaging Microscopy
FMN	Flavin mononucleotide
FP	Fluorescent Protein
FRET	Förster Resonance Energy Transfer

FWHM	Full wave half maximum
G	Instrumentation factor
GAL	Galactose
GAR	GTPase associated region
GFP	Green Fluorescent Protein
GLU	Glucose
GPI-Aps	Glycosyl-phosphatidylinositol anchored protein
GTP	Guanosine triphosphate
IR	Infrared light
IRF	Instrument response function
L25	Ribosomal protein 25
LB	Lysogeny broth
LSL	Lectin LSLa from the mushroom *Laetiporus sulphureus*
MHz	Mega Hertz
mm	Millimeter
MOU	Main Optical Unit
mRNA	messenger RNA
Mrt4	mRNA turnover protein 4
NA	Numerical aperture
NADH	Nicotinamide adenine dinucleotide
Nop7	Nucleolus protein 7
NTD	Amino Terminal Domain
OD_{600}	Optical density at 600nm
OPE (1P)	One photon excitation
ORF	Open reading frame
P0	P0 stalk protein
P1α	P1-alpha stalk protein
P2β	P2-beta stalk protein
PCR	Polymerase chain reaction
pI	Isoelectric point
PMT	Photomultiplier tube

PSF	Point spread function
Q_D	Quantum yield of Donor
$r_{(t)}$	Time-resolved Anisotropy
r_0	Time zero anisotropy
R_0	Förster distance
RNA	Ribonucleic acid
ROI	Region of Interest
rRNA	ribosomal RNA
S. cerevisiae	*Saccharomyces cerevisie*
S_0	Ground singlet state
S_1	Lowest electronically singlet excited state
SAXS	Small-angle X-ray scattering
SB	Stalk base
SC	Synthetic medium
SPAD	Single photon avalanche diode
SRL	Sarcin-ricin loop
St	Stalk
TAP	Tandem affinity purification
TCSPC	Time-correlated single-photon counting
Ti:Sapphire	Titanium-sapphire laser
TIRF	Total internal reflection
TPE	Two photon excitation
tRNA	transfer RNA
WT	Wild type yeast strain (BJ5458)
XRD	X-ray diffraction
YEP	Yeast Extract Peptone
YNB	Yeast Nitrogen base medium
ME	Micro-spectrometer

Index

1 INTRODUCTION

1.1 Motivation and overview……..... **1**

1.2 Organization of the thesis……..…….. **3**

2 GOALS……... **5**

3 BACKGROUND

3.1 Yeast as a eukaryotic model system…… **7**

3.2 The ribosome stalk……..... **8**

3.2.1 Eukaryotic ribosome……. **8**

3.2.2 Structure and function of the ribosome stalk……. **11**

S. cerevisiae ribosome stalk…… **13**

Elongation Factor 2 (EF2) and sordarin……..... **15**

3.2.3 P0 nuclear pre-ribosomal assembly…… **17**

Protein Mrt4…… **19**

Protein Nop7……... **19**

3.3 Time-resolved fluorescence spectroscopy through a microscope.... **20**

3.3.1 Two-photon microscopy *vs.* confocal microscopy……. **20**

Confocal Microscopy……. **20**

Two-photon Microscopy……..... **21**

Lateral and axial resolution: excitation and detection volume…….. **23**

3.3.2 Fluorescence lifetime imaging microscopy (FLIM)……... **26**

Time correlated single-photon counting……..... **28**

Fast FLIM *vs.* FLIM…… **28**

Phasor-FLIM approach.…….. **29**

The phasor transformation (time-domain)……. **30**

Phasor rules……. **31**

3.3.3 Förster resonance energy transfer (FRET)…… **33**

3.3.4 FLIM-FRET…….. **35**

3.3.5 Fluorescence anisotropy with sub-µm spatial resolution…….. **37**

Conformational dynamics, interactions and fluorescence depolarization……. 37

Overview of the different applications of fluorescence anisotropy in the microscope……..... 38

3.4 Fluorescent proteins as dynamic cell probes in fluorescence micro-spectroscopy studies……..... 48

3.4.1 Discover of the Green Fluorescent Protein (GFP)……. 48

3.4.2 The fluorescent protein color palette…….. 49

3.4.3 Two-photon excitation of fluorescent proteins…….. 52

4 MATERIALS AND METHODS

4.1 Reagents……..... 53

4.2 Control fluorophores…… 53

4.3 Purified control proteins…….. 54

4.4 Fusion green fluorescent protein for ribosome stalk dynamics study……. 54

4.4.1 *S. cerevisiae* strains and growth conditions……..... 54

Growth conditions …….. 55

4.4.2 Preparation of subcellular fractions……... 56

Yeast cellular extracts……. 56

Yeast pure ribosomes…….. 56

4.4.3 Inhibition of protein synthesis with sordarin……. 56

4.5 Fusion EGFP and mCherry proteins for P0 nuclear assembly FRET study……. 57

Growth conditions……... 58

4.6 Immobilizing yeast cells for micro-spectroscopy studies…….. 58

4.7 Data acquisition and analysis…….. 59

4.7.1 Time-resolved total fluorescence and fluorescence anisotropy cuvette measurements……..... 59

4.7.2 Time-resolved anisotropy and fluorescence lifetime imaging (FLIM) in live cells using OPE and TPE photon microscopy…… 60

4.7.3 Single point and ROI time-resolved fluorescence data analysis: Iterative reconvolution…….. 62

Total fluorescence and anisotropy decays from cuvette measurements……. 62

Total fluorescence and anisotropy decays from ROIs and single point OPE and TPE microscope measurements……. 62

4.7.4 FRET-ROI measurements for P0 nuclear assembly study in living cells…… 64

4.7.5 FLIM-FRET phasor approach for P0 nuclear assembly study in living cells……... 64

How phasor approach works……... 64

Measuring FRET efficiency in the presence of donor-only proteins 65

5 RESULTS AND DISCUSSION

5.1 Two-photon and One-photon time-resolved micro-spectrometer setup…… 69

5.1.1 Instrumental setup……..... 70

One-photon excitation (OPE)……. 70

Two-photon excitation (TPE)……. 70

Olympus IX71 inverted microscope……... 70

Emission channel…… 71

5.1.2 Detected volume element…….. 71

5.1.3 Time-Tagged-Time-Resolved TTTR acquisition mode……. 73

5.1.4 Picosecond-nanosecond time-resolved fluorescence decays….. 74

Time domain TCSPC window…… 74

Instrument response function IRF determination……... 75

5.1.5 G factor estimation……... 77

5.1.6 Axelrod correction for high numerical aperture objective effect…… 80

5.1.7 Total fluorescence intensity determination for high NA objective systems……..... 81

5.1.8 Rotational diffusion and time-resolved fluorescence anisotropy of protein solutions in the micro-spectrometer……..... 83

Purified EGFP and LSL_t-tagged EGFP in buffer: OPE Cuvette determinations…… 84

Purified EGFP and LSL_t-tagged EGFP in buffer: OPE Micro-spectrometer determinations…….... 87

Purified EGFP and LSL_t-tagged EGFP in buffer: TPE Micro-spectrometer determinations……... 89

5.1.9 OPE and TPE time-resolved anisotropy measurements in living cells……..... 91

5.1.10 Corrected time-resolved anisotropy decays for high NA objective effects…….. 93

5.1.11 Summary…….. 95

5.2 Rotational dynamics of yeast ribosomal stalk proteins in living cells……... 97

5.2.1 Motivation…….. 97

5.2.2 Expression of fusion proteins in *S. cervsisiae* yeast cells…….... 98

5.2.3 Dynamics of free yEGFP, free P2β-yEGFP, and purified yEGFP-tagged ribosomes in buffer: OPE cuvette study…… 101

5.2.4 Dynamics of free yEGFP and L25-EGFP bound to the ribosome in the cytoplasm of S. cerevisiae live cells……... 104

5.2.5 Dynamics of ribosome stalk proteins in S. cerevisiae live cells. Effect of sordarin……... 108

TPE study of the rotational mobility of P0. Effect of sordarin..... 109

OPE study of the rotational mobility of P0. Effect of sordarin… 112

TPE study of the rotational mobility of P1α. Effect of sordarin... 115

TPE study of the rotational mobility of P2β. Effect of sordarin... 117

5.2.6 Global view of the effect of sordarin on the conformational dynamics of the ribosomal stalk proteins…… 119

5.3 Detection of the ribosomal protein P0 in nuclear pre ribosomal complexes……. 123

5.3.1 Motivation…….. 123

5.3.2 Intracellular mobility of the nucleus in live yeast cells…….. 124

5.3.3 Auto fluorescence of WT strain cells in fixed and live conditions……..... **125**

5.3.4 Rotational mobility of Nop7-EGFP and Mrt4-yEGFP proteins in the nucleus of live cells…….. **126**

5.3.5 Interaction profile of P0-yEGFP with Nop7-mCherry and Mrt4-mCherry proteins in live yeast cells……... **127**

5.3.6 Interaction profile of Nop7-EGFP with P0-mCherry and Mrt4-mCherry proteins in live yeast cells……... **132**

5.3.7 FRET-phasor measurements support the existence of P0-Nop7 interactions pre-ribosomal complexes located in the nuclear periphery……. **136**

6 CONCLUSIONS……... **141**

REFERENCES……. **147**

Index of Tables

3. BACKGROUND

3.3. Time-resolved fluorescence spectroscopy through a microscope

Table 3.1. Overview of living cell studies using fluorescence anisotropy methodologies in the microscope……..... **42**

Table 3.2. Overview of biological applications of fluorescence anisotropy micro-spectroscopy techniques in live cells …….. **45**

4. MATERIALS AND METHODS

4.4. Fusion green fluorescent proteins for ribosome stalk dynamics study

Table 4.1. *S.cerevisiae* strains expressing yEGFP-tagged ribosomal stalk proteins……..… **55**

4.5. Fusion EGFP and mCherry proteins for P0 nuclear assembly FRET study

Table 4.2. *S.cerevisiae* strains used for FRET measurements…… **57**

5. RESULTS AND DISCUSSION

5.1. Two-photon and One-photon time-resolved micro spectrometer setup

Table 5.1. Time-resolved fluorescence total intensity and anisotropy decay parameters of all the control proteins, as a function of the environment of EGFP and instrumental setup …….. **86**

Table 5.2. High NA effects on TPE lifetime and fluorescence anisotropy parameters ……..... **95**

5.2. Rotational dynamics of yeast ribosomal stalk proteins in living cells

Table 5.3. Representative intensity and TPE-FLIM images of yEGFP tagged ribosomal proteins in live yeast cells……. **100**

Table 5.4. Fluorescence lifetimes and anisotropy decay parameters of stalk proteins in solution ……..... **102**

Table 5.5. TPE fluorescence lifetimes and anisotropy decay parameters for free yEGFP, L25-EGFP, P0-yEGFP, P1α-yEGFP and P2β-yEGFP expressed in the cytoplasm of living *S. cerevisiae* cells. Effect of Sordarin…….. **107**

Table 5.6. OPE fluorescence lifetimes and anisotropy decay parameters for free yEGFP and P0-yEGFP in the cytoplasm of living *S. cerevisiae* cells. Effect of Sordarin …… **115**

5.3. Detection of the ribosomal protein P0 in nuclear pre ribosomal complexes

Table 5.7. Fluorescence lifetimes parameters of live and fixed WT cells….. **126**

Table 5.8. FRET-ROI analyses: Fluorescence lifetime parameters determined for P0-yEGFP (donor only), P0-yEGFP +Mrt4-mCherry (donor-acceptor), and P0-yEGFP+Nop7-mCherry (donor-acceptor) **131**

Table 5.9. FRET-ROI analyses: Fluorescence lifetime parameters determined for Nop7-EGFP (donor only), Nop7-EGFP+Mrt4-mCherry (donor-acceptor) and Nop7-EGFP+P0-mCherry (donor-acceptor)... **134**

Index of Figures

1. INTRODUCTION

1.1. Motivation and overview

Figure 1.1. A small sectional view of yeast cytoplasm …… **1**

3. BACKGROUND

3.1. Yeast as a eukaryotic model system

Figure 3.1. Structome of *S.cerevisiae* in the G1 phase…….. **7**

3.2. The ribosome stalk

Figure 3.2. Cryo-electron microscopy map of 80S ribosome from *S. cerevisiae*…….. **10**

Figure 3.3. Schematic representation of the eukaryotic ribosomal stalk…... **13**

Figure 3.4. Interaction between P0 CTD and EF2…… **15**

Figure 3.5. Interaction of sordarin with EF2 in the ribosome……... **16**

3.3. Time-resolved fluorescence spectroscopy through a microscope

Figure 3.6. Principle of Two-photon absorption process…….. **22**

Figure 3.7. Effect of scattering in confocal microscopy and TPE microscopy……..... **23**

Figure 3.8. Point spread function representation……... **24**

Figure 3.9. Total intensity image of a *S. cerevisiae* yeast cell expressing Nop7-EGFP in the nucleus and P0-mCherry in the cytoplasm…… **25**

Figure 3.10. Time-correlated single-photon counting TCSPC…….. **28**

Figure 3.11. Graphical representation of phasors in the phasor plot…… **31**

Figure 3.12. Lifetime representation using phasors…….. **32**

Figure 3.13. FRET process scheme……... **33**

Figure 3.14. Dependence of the FRET efficiency (*E*) on Donor-Acceptor distance (*r*)…… **34**

Figure 3.15. Interactions between the anti-tumoral Irvalec and the plasma cell membrane of A549 cells…… **36**

Figure 3.16. Fluorescence decay components in a sample containing interactting (FRET, τ_{fret}) and non-interacting (Donor only, τ_0) species **37**

3.4. Fluorescent proteins as dynamic cell probes in fluorescence microspectroscopy studies

Figure 3.17. 3-D structure of EGFP protein…….…. **50**

Figure 3.18. OPE and TPE absorption spectra of EGFP……... **52**

4. MATERIALS AND METHODS

4.6. Immobilizing yeast cells for micro-spectroscopy studies

Figure 4.1. Schematic representation of live yeast cell preparations for micro-spectroscopy determinations……. **59**

4.7 Data acquisition and analysis

Figure 4.2. Phasor approach. Example I……... **65**

Figure 4.3. Phasor approach. Example II…….. **65**

Figure 4.4. Representation of a FRET trajectory in the phasor plot..... **66**

Figure 4.5. Positioning cursors for FRET efficiency calculation in the phasor plot. ……..... **66**

Figure 4.6. FRET trajectory in the phasor plot…….. **67**

5. RESULTS AND DISCUSSION

5.1. Two-photon and One-photon time-resolved micro-spectrometer setup

Figure 5.1. Optical layout of OPE and TPE time-resolved micro-spectrometer……..…….. **69**

Figure 5.2. Characterization of the effective detection volume element…... **72**

Figure 5.3. Comparison of OPE and TPE parallel $I_{HH}(t)$ and perpendicular $I_{HV}(t)$ polarized fluorescence components…… **74**

Figure 5.4. Effect of the instrumental response function, IRF, on the re-convolution analysis of time-resolved fluorescence decays……... **76**

Figure 5.5. Determination of the instrumental factor $G(x,y,z,t)$ from vertical and horizontal polarized excitation and a collinear setup… **79**

Figure 5.6. Total fluorescence intensity measurements……..... **82**

Figure 5.7. Purified *E. coli* EGFP spectra……. **83**

Figure 5.8. OPE Cuvette measurements: Fluorescence anisotropy decays of EGFP and LSL_t-EGFP in TRIS HCl buffer……..… **85**

Figure 5.9. OPE micro-spectrometer solution measurements: Fluorescence anisotropy decays of EGFP and LSL_t-EGFP in TRIS HCl buffer… **88**

Figure 5.10. TPE micro-spectrometer solution measurements: Fluorescence anisotropy decays of EGFP and LSL_t-EGFP in TRIS HCl buffer……..... **90**

Figure 5.11. OPE and TPE micro-spectrometer single point live cell measurements: Fluorescence anisotropy decays of yEGFP expressed in the cytoplasm of *S. cerevisiae* yeast cells……..... **92**

Figure 5.12. TPE micro-spectrometer single point live cell measurements: fluorescence anisotropy decays of P0-yEGFP expressed in the cytoplasm of *S. cerevisiae* yeast cells…….. **94**

5.2. Rotational dynamics of yeast ribosomal stalk proteins in living cells

Figure 5.13. Lifetime image (FLIM) of a live *S. cerevisiae* yeast cell from P0 strain…… **99**

Figure5.14. Representative OPE time-resolved fluorescence anisotropy measurements of purified yEGFP and stalk proteins tagged with yEGFP from purified ribosomes in buffer (cuvette studies)…… **103**

Figure 5.15. Scheme of the ribosome 60S subunit showing L25 and P0 proteins……..... **105**

Figure 5.16. Representative experiments of single-point TPE fluorescence time-resolved anisotropy of free yEGFP and L25-EGFP expressed in the cytoplasm of live cells…… **106**

Figure 5.17. Representative experiments of single-point TPE fluorescence time-resolved anisotropy of cells expressing P0-yEGFP untreated and treated with sordarin…….…….. **110**

Figure 5.18. Representative experiments of single-point OPE fluorescence time-resolved anisotropy of cells expressing P0-yEGFP with (black) and without sordarin (red)……..... **114**

Figure 5.19. Representative experiments of single-point TPE fluorescence time-resolved anisotropy of cells expressing P1α-yEGFP with (black) and without sordarin (red)…… **116**

Figure 5.20. Representative experiments of single-point TPE fluorescence time-resolved anisotropy of cells expressing P2β-yEGFP with (black) and without sordarin (red)…… **118**

Figure 5.21. Statistical comparison of OPE and TPE rotational correlation times of ribosome stalk proteins. Effect of sordarin treatment…… **121**

5.3. Detection of the ribosomal protein P0 in nuclear pre-ribosomal complexes

Figure 5.22. Three consecutive TPE fluorescence intensity images of a cell from Nop7-EGFP strain……..... **125**

Figure 5.23. TPE autofluorescence intensity images from WT strain..... **125**

Figure 5.24. Representative TPE time-resolved anisotropy decays of cells expressing Mrt4-yEGFP (A, red) and Nop7-EGFP (B, black) proteins in the nucleus ……. **127**

Figure 5.25. Expression profile and FRET-ROI analyses of P0-yEGFP strain (donor only), P0-yEGFP+Mrt4-mCherry (donor-acceptor) and P0-yEGFP+Nop7-mCherry (donor-acceptor) strains…… **130**

Figure 5.26. Expression profile and FRET-ROI analyses of Nop7-EGFP strain (donor only), Nop7-EGFP+Mrt4-mCherry and Nop7-EGFP+P0-mCherry strains (donor-acceptor)……... **133**

Figure 5.27. Rigorous error analysis of lifetime from low and high FRET samples.……...……. **135**

Figure. 5.28. Representative FRET-FLIM analysis using the phasor plot approach for the different pairs……. **137**

Figure 5.29. FRET calculator tool for the phasor approach…….. **138**

ABSTRACT

Fluorescence polarization micro-spectroscopy is a powerful tool which allows, among other applications, to quantify changes in the conformational dynamics of flexible proteins and to characterize biomolecular interactions in specific cellular locations.

In this thesis we present the instrumental setup of a fluorescence micro-spectrometer, with TPE and OPE excitation and polarization detection, together with two applications of time-resolved fluorescence anisotropy and FLIM-FRET micro-spectroscopy techniques in living *S. cerevisae* ribosome stalk studies.The two ribosomal stalk studies presented here share the same protein, P0, but expressed at very different concentrations (~33μM *vs* ~nM-mM), bound to different particles (ribosome and pre-ribosome particles), and located in different cellular regions (cytoplasm and nucleus) of *S. cerevisae* yeast cells, making it an interesting biological system to show the capabilities and limitations of the micro-spectroscopy polarization techniques in living yeast cell studies.

First we focused on the optimization of data acquisition and data analysis to test the quality of the spectroscopic parameters determined through a microscope with a high numerical aperture objective, and all the necessary optics to measure fluorescence anisotropies. We calibrated the instrument with fluorophores and fluorescent proteins in buffer and expressed in the cytoplasm of *S. cerevisiae.* Our results reveal a cytoplasmic apparent microviscosity about two times larger than aqueous solutions viscosity (~2 cP), in agreement with previous determinations in the cytoplasm of mammalian cells.

The carboxy-terminal domains (CTD) of the stalk proteins P0, P1α, and P2β kept its flexible character in the cytoplasm of *S. cerevisiae* cells, although their apparent mobility was slowed down comparing with results from purified ribosomes in buffer.

Our results may confirm the *in vitro* biochemical data from cellular extracts about the existence of a cytoplasmic pool of acidic proteins P1α, and P2β, together with the proteins in the ribosome stalk. The apparent faster mobility observed for these proteins may be explained in two ways: *i)* the experimental rotational correlation times correspond to the average mobility of the two

populations, free and ribosome bound P1α, and P2β proteins, and *ii)* there is a single population of P1α, and P2β showing higher CTD flexibility, comparing with P0 CTD, when are bound to the ribosomal stalk.

In P0-yEGFP samples treated with sordarin, a selective inhibitor of protein synthesis, two populations can be discriminated in terms of yEGFP mobility. An important group of cells seems to be not affected by the treatment with sordarin, while some of them may present a slowdown in their CTD rotational mobility. These results may suggest that sordarin could reduce P0 CTD mobility, and therefore, P0 stalk protein would be involved in the mechanism of action of sordarin. However we didn't detect the presence of the immobile CTD population from the rotational correlation time histogram for the stalk proteins, P1α and P2β, when were treated with sordarin. Therefore, sordarin seems to have no effect on the flexibility of the CTD region of P1α and P2β stalk proteins.

Our results show positive FRET for the donor-acceptor pair Nop7-EGFP/ P0-mCherry. We have found a distribution of FRET efficiencies from zero FRET to 30% FRET. The expression of Nop7 in the nucleus (donor FRET) is much higher than the expression of P0 (acceptor FRET in this study), and there are a high percentage of donor only complexes (containing Nop7 molecules only). Then, the uncertainty in FRET efficiency estimations using ROI-FRET approach from the whole nucleus makes it difficult to conclude about the presence of P0 protein in pre-ribosomal nuclear proteins.

The FLIM-FRET phasor approach provides the necessary spatial resolution and demonstrates that in the nuclear periphery there are pre-ribosomal particles containing P0 and Nop7 close enough (R < 10nm) to undergo FRET, confirming previous reported *in vitro* data from cell extracts and negative cross N&B data determined for the same samples in a complementary study .

Despite of the limitations of the lifetime (~2-2.6 ns) and the different levels of expression of the fluorescent proteins in these biological systems, our TPE and OPE anisotropy approach was able to detect changes in the flexibility of proteins bound to a nanometric size structure, like the ribosome, and to identify protein-protein interactions in the nucleus of living cells.

La micro-espectroscopia de polarización de fluorescencia es una herramienta eficaz que permite, entre otras aplicaciones, cuantificar cambios conformacionales en proteínas flexibles, y caracterizar interacciones biomoleculares en localizaciones celulares específicas.

En esta tesis se presenta la puesta a punto de un micro-espectrómetro de fluorescencia, con excitación de un fotón (OPE) y dos fotones (TPE), y detección de fluorescencia polarizada, junto con dos aplicaciones de los métodos de micro-espectroscopía de fluorescencia, anisotropía de fluorescencia con resolución temporal, y de adquisición de imágenes de vidas y de transferencia de energía resonante (FLIM-FRET), en estudios del tallo ribosómico en levaduras *S. cerevisiae* vivas.

Los estudios realizados sobre el tallo ribosómico comparten la misma proteína, P0, aunque con niveles de expresión muy diferentes (33μM *vs* ~ nM-mM), formando parte de distintos complejos (ribosomas y partículas pre-ribosómicas), y localizada en diferentes regiones celulares (citoplasma y núcleo) de levaduras *S. cerevisiae*. Los componentes del tallo ribosómico han resultado ser un sistema biológico muy interesante para mostrar las capacidades y limitaciones de las técnicas de polarización micro-espectroscopia en estudios de células de levadura viva.

En primer lugar nos hemos centrado en la optimización de los protocolos de adquisición y análisis de datos, para comprobar la calidad de los parámetros espectroscópicos determinados a través de un microscopio con un objetivo de alta apertura numérica, y un sistema de excitación/detección con toda la óptica necesaria para medir anisotropías de fluorescencia.

El micro-espectrómetro de fluorescencia se ha calibrado con fluoróforos control y proteínas fluorescentes en tampón y expresadas en el citoplasma de levaduras *S. cerevisiae* vivas. La micro-viscosidad aparente del citoplasma de las levaduras es aproximadamente el doble de la viscosidad de disoluciones acuosas (~ 2 cP), resultado que está de acuerdo con determinaciones anteriores de la micro-viscosidad en el citoplasma de células de mamíferos.

Los dominios carboxi-terminal (CTD) de las proteínas tallo ribosómico P0,

P1α y P2β conservan en el citoplasma de *S. cerevisiae* su carácter flexible, aunque su movilidad aparente se reduce en comparación con los resultados obtenidos para muestras de ribosomas purificados en tampón.

Nuestros resultados estarían de acuerdo con los datos bioquímicos, obtenidos en un estudio *in vitro* a partir de extractos celulares, que proponen la existencia de una población de proteínas ácidas P1α, y P2β, que se encuentran libres en el citoplasma. Aunque la aparente mayor movilidad detectada en estas proteínas puede interpretarse de dos formas: *i)* los tiempos de correlación rotacional experimentales corresponden a la movilidad media de las dos poblaciones, P1α y P2β, libres y unidas al ribosoma, y *ii)* una única población de P1α y P2β, que presentan una mayor movilidad en sus dominios CTD, en comparación con P0, cuando se encuentran unidas al tallo ribosómico.

En las muestras de P0-yEGFP tratadas con el inhibidor selectivo de la síntesis de proteínas, sordarina, se han detectado dos poblaciones de proteínas P0-yEGFP en términos de la movilidad de yEGFP. Un grupo importante de células parece no afectarse por el tratamiento con sordarina, mientras que una pequeña fracción puede presentar una disminución en la movilidad rotacional de sus CTD. Estos resultados sugieren que el compuesto sordarina podría reducir la movilidad del dominio CTD de P0, y por lo tanto, la proteína P0 estaría involucrada en el mecanismo de acción de sordarina.

No se han detectado cambios en el histograma de tiempos de correlación rotacional de las proteínas P1α y P2β, al tratar las células con sordarina. Por lo que parece que la sordarina no afecta a la movilidad de la región CTD de estas proteínas del tallo ribosómico.

Nuestros resultados muestran una distribución de eficiencias FRET (0-30%) para la pareja donador-aceptor Nop7-EGFP / P0-mCherry en el núcleo de levaduras *S. cerevisiae*. La expresión de Nop7 en el núcleo (donador FRET) es mucho más alta que la expresión de P0 (aceptor de FRET en este estudio), por lo que las eficiencias FRET determinadas presentan un alto porcentaje de complejos con 0% FRET (contienen solo moléculas de Nop7, donadores). De aquí que la gran incertidumbre en las estimaciones de eficiencia FRET, usando la

aproximación ROI-FRET para secciones completas del núcleo, hace que sea difícil concluir sobre la presencia de proteína P0 en las particulas pre-ribosómicas nucleares.

La aproximación FLIM-FRET-fasores proporciona la resolución espacial necesaria en este estudio y muestra una población de partículas pre-ribosómicas en la periferia nuclear que contienen las proteínas P0 y Nop7, lo suficientemente cerca (R <10 nm) para que pueda existir FRET, confirmando los resultados *in vitro* obtenidos en estudios anteriores a partir de extractos celulares y los datos de correlación cruzada N & B, determinados para las mismas muestras en un estudio complementario.

A pesar de las limitaciones del tiempo de vida media de las proteínas fluorescentes utilizadas en este trabajo (~ 2-2,6 ns), y los diferentes niveles de expresión de las proteínas objeto de estudio, las metodologías desarrolladas para el OPE y TPE micro-espectrómetro puesto a punto en este trabajo, nos han permitido cuantificar cambios en la flexibilidad de proteínas que forman parte de complejos de tamaño nanométrico, como el ribosoma, y la identificación y localización de interacciones proteína-proteína en el núcleo de levaduras vivas.

1 INTRODUCTION

1.1 Motivation and overview

Earth is covered with innumerable structured dynamic bio-molecular systems, varying from bacteria to human beings. Understanding the diversity and specialization of these individual systems, and in particular, the ways in which individual cells process information and respond to perturbations, is the goal of many ongoing studies in different fields of science, such as molecular biology, biochemistry and biophysics.

The most abundant constituent of a living cell is water. It accounts for about 70% of a cell's weight. Components of the cell interior are the nucleus, which occupies about 10%, the cell wall with a mass equal to 10–25% of the total dry mass, and the endoplasmic reticulum and vacuole that are the largest organelles. The interior of cells in all living organisms, without exception, has a common feature: the high total concentration of macromolecules they contain, which occupy a considerable fraction (20–30 %) of the total volume (Figure 1.1).

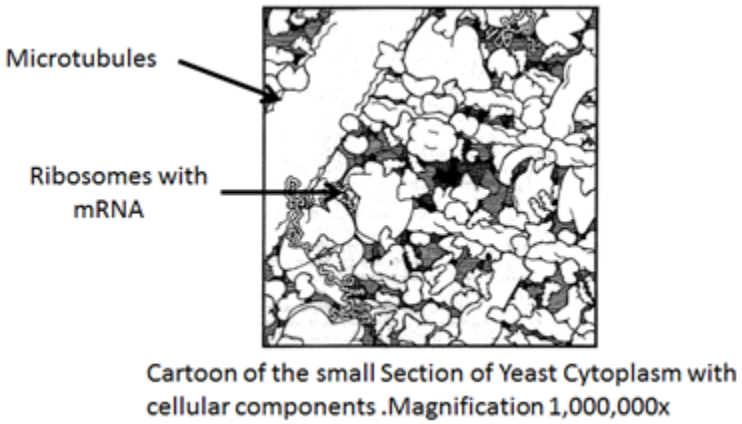

Figure 1.1. A small sectional view of yeast cytoplasm. Sketch shows the small section of *S. cerevisiae (*yeast) cytoplasm, with components such as soluble proteins, ribosomes with mRNA, microtubules, actin filaments and intermediate filaments. (*Image adapted from D.S Goodsell 1993)*

The cytosol is made up of protein filaments that make up the cytoskeleton, as well as soluble proteins and high-molecular-weight protein factories such as ribosomes, and water. The inner granular and fluid portion of the cytoplasm is referred to as endoplasm. Some major organelles that are suspended in the

cytosol are mitochondria, endoplasmic reticulum, Golgi apparatus, vacuoles and lysosomes. The protein synthesis known as translation occurs in the cytoplasm where the ribosomes are located.

In general, the motions and the interactions of biological molecules inside the cell will be dominated by the surrounding water molecules and the crowding effects of the neighbor unrelated macromolecules and network of fibers (Luby-Phelps 2000). The "solvent" cannot be considered as a continuum, and the Stokes-Einstein-Debye hydrodynamic model cannot describe the diffusive behavior of proteins in these media. For simplicity, it was introduced the concept of apparent microviscosity in the Brownian diffusion equations, to take in account the crowding effect in cell processes governed by diffusion (Zorrilla *et al.* 2004b, 2007).

In the last two decades confocal fluorescence microscopy methodologies have evolved to become essential to study the chemistry and physics of the cell (some relevant recent applications: Ziomkiewicz *et al.* 2013; van Wijk *et al*. 2012; Elliot *et al*. 2012, Kremers *et al*. 2011, Roberti *et al*. 2011). These technical advances have opened the door to micro-spectroscopy, *i.e.* the possibility of photophysical and spectroscopic studies through the microscope with high spatial resolution, which can extend to even single molecules. Fluorescence micro-spectroscopic methodologies allow to examine quantitatively dynamic processes in living cells, giving an accurate picture of the cell interior based on the characterization of molecular mobility and interactions.

Fluorescence is sensitive, specific and non-invasive, and the spectroscopic properties of fluorescent probes inform us about their molecular environment. The development and use of fluorescence proteins, tagged to the protein to study, has facilitated the study of biological systems in specific subcellular locations of a single live cell.

In this thesis we extend the cuvette-based fluorescence spectroscopic approaches to the two-photon and confocal fluorescence microscope, adding spatial resolution. One of the main difficulties of the extension of the studies to the microscope is to preserve the spectroscopic signal purity and to set the

conditions to collect enough photons from a fL volume element of a cell without to damage it.

The spectroscopic signals recorded through a fluorescence micro-spectrometer include: *a)* steady-state fluorescence intensity; *b)* fluorescence intensity fluctuations; *c)* time-resolved fluorescence decays, and *d)* time-resolved fluorescence anisotropy decays, with high temporal (ps-μs) and spatial (nm-sub μm) resolution, and acceptable spectral resolution (using filters, usually). The state-of-the-art of time-correlated single photon counting methodologies associated to the microscope deals with excited state lifetimes, rotational correlation times and donor-acceptor distances determined in a pixel of sub-μm dimensions, in living cells. In the case of FRET the spatial resolution is extended to 1-10 nm.

The excitation is an important issue in fluorescence micro-spectroscopy methodologies. Two-photon excitation has many advantages, but it is not always the best choice for living cell studies in the fluorescence microscope. It is very important to calibrate each micro-spectrometer and to adapt the fluorescence methodology to the specific biological system in study. Advantages and disadvantages will be discussed in this thesis.

The aim of this thesis is to unravel the heterogeneity of intracellular protein organization and dynamics using yeast *S. cerevisiae* cells as a eukaryotic model system and state-of-the-art fluorescence micro-spectroscopy techniques.

1.2 Organization of the thesis

Chapter 1. General Introduction.

Chapter 2. Goals, presents the specific goals of this thesis.

Chapter 3. Background, presents relevant information about the biological systems studied in this work, together with the bases of the fluorescence micro-spectroscopy tools developed in this work.

Chapter 4. Materials and Methods, describes all the experimental details for the yeast cell preparations, together with the methodological approaches for fluorescence parameters determinations, in the calibrated cuvette system and in the fluorescence micro-spectrometer.

Chapter 5. Results and Discussion section is divided in three parts:

a) *Section 5.1*. Setup of the time-resolved fluorescence micro-spectrometer for time-resolved fluorescence anisotropy and FLIM-FRET studies. This part of the work represents the core of the thesis. Especial care was taken in the characterization and optimization of the instrument, designing and performing multiple controls, to clarify the information we can get when we apply these methodologies to living yeast cell studies.

b) *Section 5.2*. Application 1: Characterization of the flexibility of the ribosome stalk components in the cytoplasm, using single-point time resolved anisotropy methodologies.

c) *Section 5.3*. Application 2: Study of the assembly of the stalk protein P0, in the nucleus of *S. cerevisiae* cells, using ROI-FRET and FLIM-FRET phasor approaches.

Chapter 6. Conclusions

All the fluorescence protein constructions for *S. cerevisiae* yeast cells used in this work were developed in the laboratory of Dr. Juan Pedro García Ballesta (CBM, CSIC-UAM, Madrid). The strains were grown and characterized in our laboratory for fluorescence micro-spectroscopy measurements (Department of Biological Physical Chemistry. IQFR, CSIC, Madrid). The control proteins EGFP and LSL_t-EGFP were produced in the laboratory of Dr. José Miguel Mancheño (Department of Crystallography and Structural Biology. IQFR, CSIC, Madrid).

2 GOALS

The general goal of this thesis is to develop a set of versatile tools, based on two-photon (TPE) and confocal one-photon (OPE) laser excitation time-resolved fluorescence polarization microscopy, to study the dynamics and interactions of biomolecules in living yeast cells.

The specific goals are:

1. Instrumental micro-spectrometer setup. Incorporation and validation of the polarized excitation (OPE and TPE), and the polarized detection, using a high numerical aperture objective:
   - Determination of fluorescence lifetimes and rotational correlation times of control fluorophores and proteins in buffer, and expressed in the cytoplasm of living yeast cells, with high spatial (nm-sub μm) and temporal (ps-ns) resolution.
   - Optimization of the instrumental response function (IRF) for the deconvolution of the fluorescence polarization decays.
   - Characterization of the optical aberrations effects on the determined fluorescence and anisotropy parameters.
   - Analysis of the advantages and disadvantages of OPE and TPE. Design of specific protocols for their efficient use in time-resolved fluorescence polarization studies in living cells.
2. Development of theoretical models and experimental approaches based on the combination of measurements of intensity and linearly polarized fluorescence, to quantitatively characterize conformational changes and interactions of biomolecules in specific subcellular locations.
3. Characterization of the dynamics of highly flexible proteins in the cytoplasm. Quantification of the rotational dynamics of the major ribosome stalk proteins, P0, P1α, P2β, using the instrumental setup and the experimental approaches developed in this work. Effects of the selective inhibitor of protein synthesis sordarin on the stalk flexibility.
4. Investigation of the potential formation of complexes of pre-ribosomal particles in the nucleus containing the stalk protein P0 or Mrt4 near Nop7 molecules ($R<10$ nm), using FRET-FLIM approaches in living yeast cells.

3 BACKGROUND

3.1 Yeast as a eukaryotic model system

Saccharomyces cerevisiae ("budding" yeast) have been widely used in genetics and cell biology. It is a single cell organism that shares the complex internal cell structure of plants and animals. The cell cycle in yeast is very similar to the cell cycle in humans and it is regulated by homologous proteins. Yeast is the first eukaryotic organism completely sequenced. The genome is composed of about 12,156,677 base pairs and 6,275 genes, compactly organized on 16 chromosomes (Sherman 2002). Yeast have 23% of human genes similarity.

S. cerevisiae cells have a short generation time (~90 min). Cell culture and the maintenance of multiple strains is low cost (Clementi *et al.* 2010). They can be easily transformed, allowing for the addition of new genes or deletion through homologous recombination. They are non-pathogenic and can be handled with little precautions.

Using freeze-substitution and serial ultrathin-sectioning electron microscopy, Yamaguchi *et al.* (2011) have reported the 3D architecture ("structome") of strain S288c (Figure 3.1). The size of *S. cerevisiae* G1 phase cell was ~3.9 μm in length and ~3.2 μm in diameter, with a total cell volume of ~17.1 μm^3. The cell wall was 120 ± 14 nm thick and constituted 17% of the cell volume.

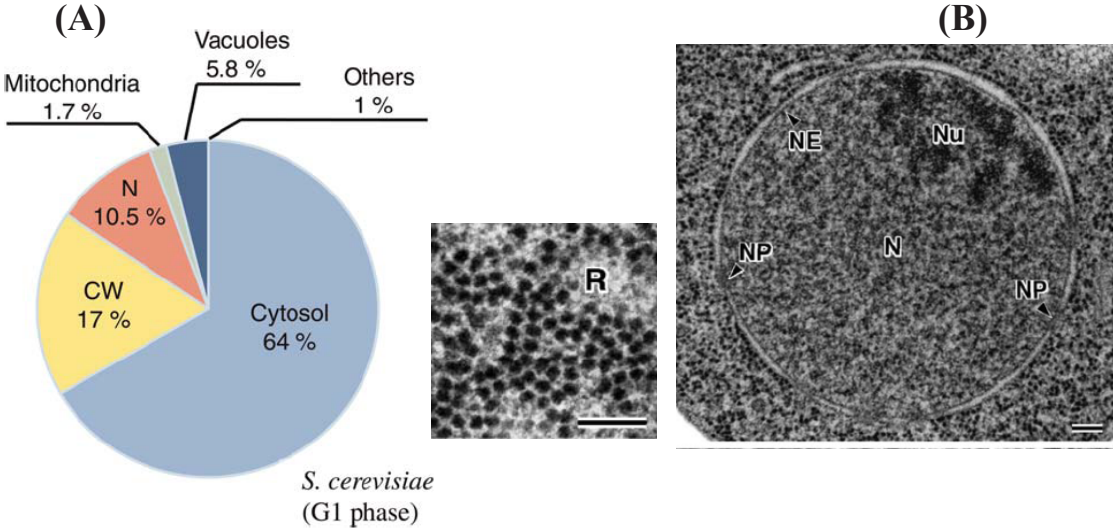

Figure 3.1. Structome of *S. cerevisiae* in the G1 phase (A) Average proportions of the cytosol, cell wall (CW), nucleus (N), mitochondria, vacuoles and other cell components volumes. **(B)** High magnification images of the *nucleus* (N), nuclear envelope (NE), nuclear pore (NP), nucleolus (nu) and ribosomes (R). Bar = 100 nm. (*Image adapted from Yamaguchi et al. 2011*).

The nucleus was enclosed by a double-layered nuclear envelope with ~1.6 μm in diameter and ~1.8 μm^3 in volume, occupying 10.5% of the cell volume. Ribosomes appeared as electron dense particles of ~20 nm in diameter size. They were dispersed randomly throughout the cytoplasm. Many were found attached to the ER as well as the outer nuclear envelope. The total number of ribosome particles in *S. cerevisiae* cells ranged from 183000 to 272000. However, the number per unit volume of cytosol was relatively constant at ~20000/μm^3 (~33μM).

3.2 The ribosome stalk

3.2.1 Eukaryotic ribosome

Protein translation is the process in which the genetic information encoded in mRNA is used to synthesize proteins. Translation takes place on the ribosome: mRNA carries genetic information as a ribonucleotide sequence from chromosomes to ribosome, and ribosomes translate this code to a specific sequence of amino acids that are linked together into a polypeptide chain through multiple biochemical reactions.

During the long history of evolution, protein synthesis has been essential and highly conserved, involving mRNA, soluble factors, ribosomes and other components, which interact and regulate the process. Given its importance, complexity and cost of energy for cells, this mechanism is highly regulated.

Ribosomes are a central part of the cell machinery used to produce proteins: they maintain the correct reading frame and ensure accuracy (about 1 mistakes every 10.000 amino acids). The ribosome is a complex catalytic machine composed of ribosomic RNA (rRNA) and ribosomal proteins, with a ratio between rRNA and proteins of 60/40. It is assembled in the nucleus and irreversibly passes into the cytoplasm.

The ribosome is one of the major components of the cell. The number of ribosomes per cell can vary: a yeast cell can produce 2.000 ribosomes per minute (approximately 200.000 ribosomes per cell, Warner *et al.* 1999), while a mammalian cell can contain millions of ribosomes.

Ribosomes consist of two subunits that bind in the cytoplasm and work as a single translating mRNA into proteins. Ribosomes of prokaryotes and eukaryotes are quite similar, but differ on its sedimentation coefficient: eukaryotic ribosome is 80S (40S and 60S subunits), while prokaryotic ribosome is 70S (30S and 50S subunits).

In eukaryotes, the large 60S subunit contains 25S, 5.8S, 5S rRNA and 46 proteins. It catalyzes the peptide bond formation and contains the poly peptide exit tunnel. Similarly, the small 40S subunit is formed by only one rRNA (18S) and 33 proteins (Frank *et al*. 1995; Frank and Agrawal 2000; Melnikov *et al*. 2012). Several important functions, possibly including peptidyl transfer, have been associated with rRNAs (Spahn *et al*. 2001 and more). Most of the molecular interactions in the ribosome are protein-rRNA interactions, with few protein-protein interactions, which contribute to the stability of the macromolecular complex. The major function of the ribosome is protein translation. Each subunit has three binding sites for rRNA:

- A (aminoacyl) site: accepts the incoming aminoacylated tRNA.
- P (peptidyl) site: holds the tRNA with the nascent peptide chain.
- E (exit) site: holds the deaclyated tRNA before it leaves the ribosome.

Both subunits are involved in the translocation process, in which tRNAs and mRNAs move accurately through the ribosome, one codon each time. The translocation step is catalyzed by elongation factor G (EF-G) in prokaryotes and by elongation factor 2 (EF2) in eukaryotes.

Ribosomes are also important for medical reasons. They are the target of many important antibiotics that inhibit, specifically bacterial protein synthesis using the structural and functional differences between bacterial and eukaryotic ribosomes to interfere preferentially with bacterial ribosomes, like tetracycline, streptomycin, rifamycin, etc. (Santos *et al*. 2002). Moreover, some ribosomal proteins have been reported to be involved in some autoimmune actions (Soto *et al*. 1993). Due to its significance, the 2009 Nobel Prize was awarded to V. Ramakrishnan, T.A. Steitz and A.E. Yonath for their studies on the structure and function of the ribosome (Nobleprize.org).

The components and morphology of the ribosomes are very well conserved from prokaryotes and eukaryotes. *S. cerevisiae* has been established as a model for studying the structure and function of the eukaryotic ribosome because of its easy genetic manipulation, allowing to introducing mutations in ribosomal proteins to carry out functional studies.

The Figure 3.2 shows a cryo-electron microscopy (cryo-EM) map of the *S. cerevisiae* 80S ribosome complex with EF2, with 11.7-Å-resolution (Spahn *et al.* 2004).

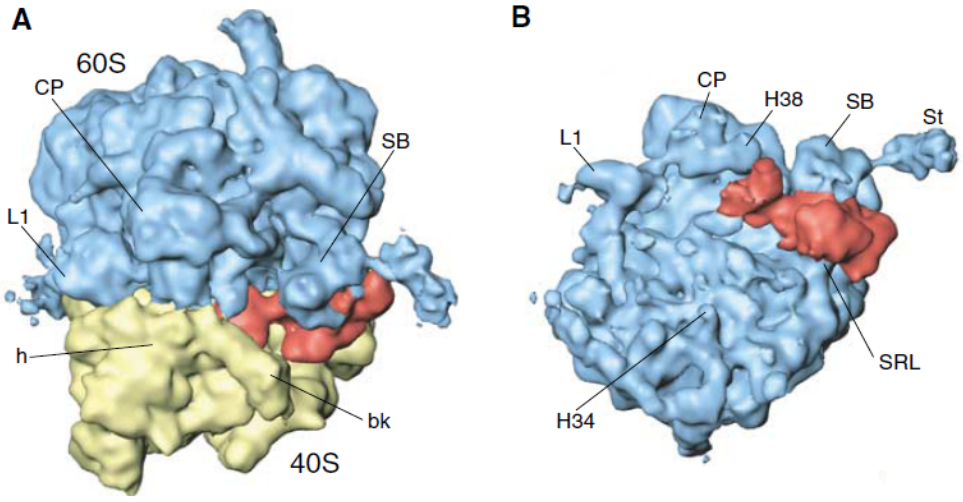

Figure 3.2. Cryo-electron microscopy map of 80S ribosome from *S. cerevisiae*. (A) 80S ribosome complex with EF2: 40S subunit (yellow), 60S subunit (blue) and EF2 (red). **(B)** 60S subunit alone. Landmarks for the 40S subunit: bk, beak; h, head. Landmarks for the 60S subunit: CP, central protuberance; L1, L1 protuberance; SB, stalk base; St, stalk; H34, helix 34; H38, helix 38; SRL, sarcin–ricin loop. (*Image adapted from Spahn et al. 2004*)

Figure 3.2-B illustrates various significant parts of the 60S subunit:

- Sarcin-ricin loop (SRL): the sarcin-ricin loop of 25S rRNA is a factor-binding site that is essential for GTP catalyzed steps in translation (Lancaster *et al.* 2008).
- Central protuberance (CP): contains the major part of 5S rRNA.
- L1: mobile element which interacts with tRNA during translocation. The mobility of L1 helps the release of tRNA from the ribosome (Trabuco *et al*. 2010).

- St: Stalk region.

Recently, Ben-Shem *et al*. (2011) has reported the crystal structure of the 80S ribosome from *S.cerevisiae* at 3.0-Å resolution. This atomic model reveals the architecture of eukaryote-specific elements and their interaction with the universally conserved core, and describes all eukaryote-specific bridges between the two ribosomal subunits. This notable information will be very useful for the design and detailed examination of experiments that explore the eukaryotic translation machine and the evolutionary forces that shaped it.

3.2.2 Structure and function of the ribosome stalk

One of the most interesting structural and functional features of 60S subunit is the ribosome stalk (**St** *in* Figure 3.2 B), a flexible lateral protuberance, highly conserved in all organisms. It is the only structure of the ribosome with more than one copy of the same component, and whose activity is based only on protein-protein interactions (Ban *et al.* 2000).

The stalk plays an important role in protein synthesis, stabilizing the transient binding of elongation and termination factors to the ribosome (Gonzalo & Reboud 2003, Lalioti *et al.* 2002). The binding site of EF2 is very near to the stalk region: the stalk base and the stalk are the EF2 contact elements on the 60S subunit. The presence of sordarin (selective inhibitor of protein synthesis in fungal organisms), prevents the dissociation of EF2 from the ribosome and allows direct visualization of this contact by cryo-EM (Spahn *et al.* 2004).

Ribosome stalk promotes the recognition and recruitment of translation factors to the ribosome, positioning them in the neighborhood of the ribosomal factor binding site. The functional interactions with the factors are performed by the flexible part of the stalk: restriction of this motion inactivates the ribosome (Oleinikov et al. 1993), indicating that the mobility is crucial for the activity of the stalk. Then, this flexible domain can “catch” translation factors and “deliver” to the ribosomal factor binding site, thus efficiently restricting factor diffusion and leading to rapid recruitment (Diaconu *et al.* 2005).

The stalk stimulates GTP hydrolysis by the ribosome bound factors through stabilization of their active GTPase conformation. GTPase activation can be

achieved by either promoting conformational rearrangements within the G domains of the factors that correctly position their own catalytic groups in the active site or donating additional catalytic groups in transacting factors (Diaconu *et al.* 2005; Huang *et al.* 2010).

The stalk is the only ribosomal domain entirely composed of proteins. It has a pentameric structure, with a central protein carrying four small acidic proteins. The bacterial ribosomal stalk has two or three dimers of the acidic 12-kDa proteins L7/L12, which interact through their N-terminal domains (NTD) with the protein L10 (23-kDa). This protein complex is bound to the highly conserved 23S rRNA. The globular L7/L12 C-terminal domain (CTD) is exposed to the cytoplasm and it is bound to the rest of the molecule through a flexible hinge region, involved in the interaction with elongation factors. This CTD is highly mobile.

Evolution has notably increased the complexity of the ribosomal stalk .The eukaryotic stalk is formed by two families of proteins, P1 and P2, which bind as P1/P2 heterodimers to protein P0 (Remacha et al. 1992, Tchorzewski 2002). The resulting P0/$(P1/P2)_2$ pentamer is anchored by the NTD of P0 to the highly conserved 25S rRNA GTPase associated region (GAR) (Lee *et al.* 2012). The eukaryotic protein L10 counterpart, P0, is larger because of its extended CTD (34 kDa), which shows significant sequence similarity with the corresponding L7/L12-like proteins, which have evolved into two families of acidic proteins, P1 and P2 (12 KDa). While L7/L12 dimers are essential for prokaryotes, P1/P2 eukaryotic proteins are not essential, because its function can be done by P0 (due to the homology between P1, P2 and the CTD of P0).

P0 is phosphorylated at the same position as P1 and P2 (the last serine residue close to the carboxylic end). Although the phosphorylation is not essential for the interaction of the P proteins and cell viability, it affects ribosome activity and may regulate the patterns of protein expression (Rodriguez-Gabriel *et al.* 1998). The stalk P0 protein is the minimal stalk structure necessary for ribosome function (Remacha *et al.* 1995b; Santos and Ballesta 1995). Gene disruption methods have indicated that this protein is essential for ribosome

activity and cell viability. All attempts to knock out the P0 gene in haploid and diploid strains have failed (Santos & Ballesta 1994).

These protein families have a variable number of members depending on the organism (Ballesta & Remacha 1996). Figure 3.3 shows a model for the eukaryotic ribosome stalk, in which we can distinguish four different regions: rRNA binding domain, P1/P2 binding domain, hinge region and CTD.

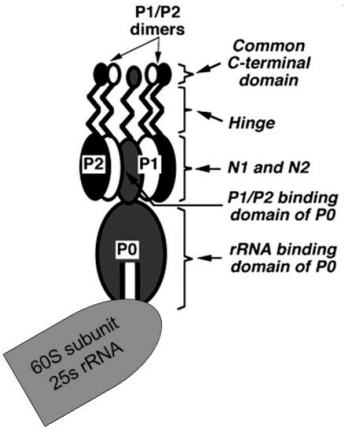

Figure 3.3. Schematic representation of the eukaryotic ribosomal stalk. The P0 NTD is bound to 25S rRNA of the 60S subunit. P0 anchored two dimers of acidic proteins, P1/P2. The CTD of the P-proteins is exposed and the hinge region is extended. (*Image adapted from Gonzalo & Rebound 2003*).

In spite of the wealth of ribosomal structures determined by crystallography or cryo-EM, studies of the whole stalk remain poorly established, because its mobility has hindered its resolution in the available ribosome structures. An insight into the CTD structure has been obtained by NMR (Bocharov *et al.* 2004) and small-angle X-ray scattering (SAXS). Recently, Grela and cols. (Grela *et al.* 2012) have reported a low-resolution model of the structure of the yeast ribosomal stalk in solution, determined by SAXS. The model shows a pentameric stalk complex composed of five proteins, P0–(P1–P2)2, with an elongated shape maximum length of 13 nm, and three distinct lobes, which may correspond to the individual P1–P2 heterodimers anchored to the CTD of the P0 protein.

S. cerevisiae ribosome stalk

The ribosomal stalk of *S. cerevisiae* is composed of one protein P0 and four proteins, P1α, P1β, P2α and P2β, forming two heterodimers, P1α-P2β and P1β-P2α. The stalk acidic proteins share functional and structural homology in all organisms studied. They have a highly acid character (pI 3.5-4.5), similar size

(about 12 KDa) and a central, very flexible, alanine-rich region called hinge, connecting the NTD and CTD domains. Deletion of all acidic proteins has no lethal effect on cells (Santos and Ballesta 1994, Remacha *et al*. 1995b).

The P0 protein binds directly to the 25S rRNA GAR region through its NTD, forming the base of the ribosomal stalk. The CTD of P0 anchors the acidic proteins to the stalk (Gudkov *et al*. 1980; Krokowski *et al*. 2006) and plays a significant role in the interaction with elongation factors. It is extremely similar to the CTD of the acidic proteins: the last amino acids are identical in P0 and in the four acidic proteins, with a consensus sequence DMGFGLFD that is found in virtually in all P proteins (P0, P1 and P2). This peptide is essential for the function of these proteins. Studies of expression of P0 chimeras where the last 120 amino acids were replaced by the different acidic proteins revealed that these proteins were as functional as the P0 wild type, indicating that the ribosome requires one CTD for normal function, independently that this belongs to P0 or the acidic proteins (Guarinos *et al.* 2001).

The ribosome stalk is a very stable entity, in which the cooperative interactions between P1/P2 dimers contribute to this high stability. In *S. cerevisiae*, when the P1α-P2β dimer is absent, a significant decrease of the stability is observed, showing that this dimer may constitute an important consolidation factor. The P1α-P2β heterodimer is the key element in stalk formation, while P1β-P2α has been implicated in the regulation of stalk function (Krokowski *et al*. 2005).

The excess of ribosomal proteins that fail to assemble into ribosomes are identified and targeted for rapid degradation. However, acidic proteins are an exception, since a cytoplasmic pool of acidic stalk proteins has been reported in both bacteria and eukaryotes (Tsurugi *et al.* 1985). There is no cytoplasmic pool of free P0 protein.

In *S.cerevisiae*, the amount of each individual acidic protein free in the cytoplasm is different. P2β was found to be the most abundant acidic protein in the cytoplasm, about 60% of the total in the cell, however only about 20% of P2α and 3% of P1β are detected free in a ribosomal fraction obtained from a cellular

extract (Ballesta &Remacha 1996).

Taking together that eukaryotic protein synthesis can be done in the absence of acidic stalk proteins and the presence of these proteins free in the cytoplasm, exist the possibility that the acidic stalk proteins should be part of the soluble translation factors, with capability to bind to the ribosome to increase protein synthesis efficiency. In this way, the analysis of the stalk composition during different cellular growth phases shows that the concentration of acidic proteins vary with metabolic activity, with less amount of acidic proteins bound to the ribosome in the stationary phase (Saenz-Robles *et al*. 1990). This suggest that can exist different populations of ribosomes (respect to protein stalk composition), all capable to synthesize proteins, but with different translation efficiencies.

Elongation Factor 2 (EF2) and sordarin

EF2 (eukaryotic elongation factor 2), the counterpart to prokaryotic EF-G, occupies an essential role in protein synthesis: EF2 catalyzes the translocation of the two tRNAs and the mRNA after peptidyl transfer on the 80 S ribosome.

Figure 3.4 shows a clear interaction between P0 and EF2: the CTD of P0 contacts with a long α-helix residing domain I of EF2 (Taylor *et al*. 2009).

Sordarin and its derivatives are antifungal compounds of potential clinical interest: they are selective inhibitors of protein synthesis in fungal organisms. In sensitive cells, sordarin blocks the release of EF2 during the translocation step and it acts to stopping protein synthesis.

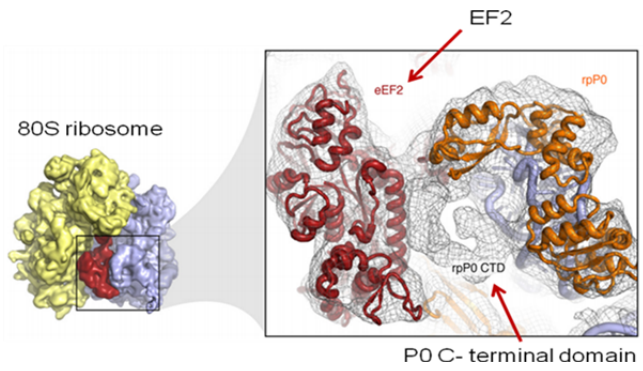

Figure 3.4. Interaction between P0 CTD and EF2.P0 NTD was modeled into the density of cryo-EM map, on the basis of the ortho-logous X-ray structure of L10 from T. maritime (*Diaconu et al. 2005*). Density for P0 CTD is clearly visible and indicative of a clear interaction between P0 CTD and a long α-helix residing domain I of EF2 (*from Taylor et al. 2009*).

Figure 3.5 shows the binding of sordarin to the III domain of EF2 and the binding site of EF2 in the 60S subunit, near to the stalk region.

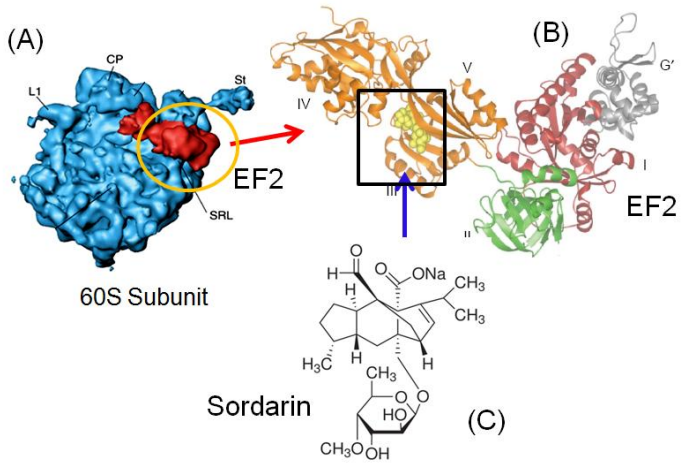

Figure 3.5. Interaction of sordarin with EF2 in the ribosome. (A) Cryo EM map of *S. cerevisiae* 60S subunit complex with EF2 (red). St, stalk (*from Spahn et al. 2004*). **(B)** Domains I, II, III, IV, and V of EF2, with sordarin (yellow) bound to domain III (*from Andersen et al. 2003*). **(C)** Chemical structure of sordarin (*from Dominguez et al. 1998*).

In addition to its therapeutic potential, sordarin is a useful tool for the analysis of the elongation cycle during protein translation. Two proteins have been described as targets of sordarin and its derivatives, EF2 and the stalk ribosomal protein P0: mutants highly resistant to sordarin have been isolated only from strains with mutations in EF2 and P0 (Gomez-Lorenzo & García-Bustos 1998, Andersen et al. 2003). In any case, as sordarin directly binds to EF2, this factor seems to be the primary target of the drug. However, since the ribosome strongly increases the affinity for the drug, the EF2-ribosome complex must be considered as the functional target, where mutations in P0 protein must induce resistance through allosteric effects. Then, the sordarin binding site seems to be quite susceptible to long-distance conformational changes.

In this work we have studied the effect of sordarin on the conformational dynamics of P0 CTD. As we have shown before (Figure 3.4), the P0 CTD interacts with EF2. However, this region is well conserved in all eukaryotes, and therefore, it is unlikely that this domain could be the target of a selective inhibitor of protein synthesis in fungal organisms. There must be other stalk-EF2 interactions contributing to the specificity of sordarin activity.

In this way, Santos (Santos *et al.* 2004) found that residues of P0 in positions 119, 124, and 126 have an important role in determining resistance to sordarin, using a series of protein chimeras containing complementary regions of the human and yeast P0 proteins expressed in yeast. Moreover, since sordarin blocks the eukaryotic EF2 function, the P0 region affecting sordarin susceptibility must correspond to EF2-interacting domains of the ribosomal stalk protein, which affects the drug-binding site in the elongation factor.

The participation of additional stalk proteins and pathways in this process cannot be ruled out. As an example, the remaining components of the ribosome stalk have been shown to be somehow involved in the sordarin mode of action, since in spontaneous mutants sordarin resistance is diminished by deletion of P1α and P2β (Gomez-Lorenzo & García-Bustos 1998).

All these results are compatible with a direct participation of the ribosomal stalk components in sordarin binding to the ribosome, and thus P0 must induce resistance through allosteric effects. In this sense, it must be taken into account that the affinity of EF2 for sordarin increases dramatically upon binding to the ribosome, implying important changes in the drug-binding site, which can be at least partially induced by interaction with protein P0. However, it is difficult to analysed if these interaction sites are involved in the action of sordarin, due to the lack of the three dimensional structure of P0. Still now, the ribosome stalk structure has not been solved in any eukaryotic organism, due to its high flexibility, that itself might play an important role in sordarin action.

3.2.3 P0 nuclear pre-ribosomal assembly

Ribosome synthesis and assembly plays a key role in the overall cellular metabolism (Warner *et al.* 1999) and is tightly coupled to cell growth rate (Dez & Tollervey 2004). However, given the complexity of the process, and in spite of its relevance, our present understanding of ribosome assembly is still very incomplete (Kressler *et al.* 2010).

In this thesis we have focussed on the assembly of the ribosomal stalk. This structural domain is a highly mobile lateral protuberance of the large ribosomal subunit, which is essential for the binding and activation of soluble factors during

translation (Gonzalo & Reboud 2003). The eukaryotic stalk is formed by two families of proteins, P1 and P2. In *S. cerevisiae* two proteins of each family form heterodimers P1α/P1β and P2α/P2β, which bind to protein P0 (Remacha *et al.* 1992; Tchorzewski *et al.* 2000). The resulting P0/$(P1/P2)_2$ pentamer is anchored by the NTD of P0 to the highly conserved 25S rRNA GTPase associated region (GAR) (Lee *et al.* 2012).

The ribosome bound P1/P2 proteins exchange with free proteins present in a cytoplasmic pool (Zinker & Warner 1976, Tsurugi & Ogata 1985, Scharf & Nover 1987, Remacha *et al.* 1995b) during protein synthesis supporting the existence of a cyclic stalk assembly and disassembly process during translation. This process is central to the proposed translation regulation mechanism based on eukaryotic stalk heterogeneity (Ballesta & Remacha 1996), and led us to focus our attention on the stalk assembly pathway.

The assembly of protein P0 has been studied by several groups (Kemmler *et al*. 2009, Rodríguez-Mateos *et al*. 2009b, Lo *et al.* 2009). These studies have convincingly shown that the ribosome assembly factor Mrt4, which shows a close sequence similarity to the P0 NTD (Rodríguez-Mateos *et al*. 2009a), binds to the 25S rRNA GAR at some intermediate nuclear stage of the 60S subunit assembly pathway and is replaced by P0 with the help of protein Yhv1 (Kemmler *et al.* 2009, Lo *et al.* 2009). Most data indicate that this replacement takes place in the cytoplasm after nuclear export of the pre-60S particles (Lo *et al.* 2010). Nevertheless, an important biochemical report indicates that protein P0 is together with nuclear pre-ribosomal complexes purified using different TAP-tagged assembly factors such as Nop7 (Rodríguez-Mateos *et al*. 2009b).

The presence of P0 in nuclear complexes conflicts with the above-mentioned cytoplasmic assembly model, and suggests that either there are alternative routes for stalk assembly or that protein P0 performs different functions at distinct times and places in the ribosome assembly process (Francisco-Velilla *et al*. 2013a).

Any of these alternatives implies changes in the present view of the ribosome assembly pathway. Most structural information on the assembly mechanism has been obtained from *in vitro* experiments focused on the characterization of pre-

ribosomal particles from different stages of the process (Kressler *et al*. 2010). The use of fluorescence microscopy *in vivo*, as pioneered for ribosome assembly research by Hurt *et al.* (1999), has allowed for the determination of the cellular location of Fluorescent protein (FP)-tagged components.

Further progress in characterizing the ribosome assembly process requires spatio-temporal resolution in live cells of the relevant bio-molecular interactions, and in particular that of P0 incorporation.

Protein Mrt4

Mrt4 protein is distributed in the nucleolus, nucleoplasm and co-localize with pre-ribosome particles. This protein is made of 236 aa residues and has a molecular weight of about 27 kDa, and it is an essential component of the ribosome assembly machinery that shares notable sequence homology to P0 ribosomal stalk protein.

Mrt4 cannot bind simultaneously to ribosome in the presence of P0. The N-terminal domain of Mrt4 resembles the rRNA binding domain found in bacterial and eukaryotic L10 and P0 proteins, and the C-terminus resembles that found in the P proteins. The N-terminal domain of the Mrt4 could functionally replace the 26S rRNA binding domain of P0 (Lo *et al,* 2009, Rodríguez-Mateos *et al.* 2009a, Michalec *et al.* 2010).

Protein Nop7

The protein Nop7 is a nucleolar protein. It is made up of 605 aa and has a molecular weight of 70 kDa. This protein is necessary for the biogenesis of 60S ribosomal subunit.

This protein is potentially important for the function of ribosome biogenesis (Miles *et al.* 2005). Biochemical evidences reveals that Nop7 is required for the steps involved in the synthesis of 60S ribosomal subunits (Tang *et al.* 2008). Moreover, the metabolic depletion of Nop7 shows the deficiency of 60S ribosomal subunit and accumulation of halfmer polyribosomes in cells (Adams *et al.* 2002 and Oeffinger *et al.* 2002).

3.3 Time-resolved fluorescence spectroscopy through a microscope

In the last two decades, the techniques of confocal fluorescence microscopy have evolved to become essential to study the chemistry and physics of the cell (Nature Milestones, 2009; Pawley 2006, Diaspro & Sheppard 2007). These technical advances have opened the door to fluorescence micro-spectroscopy studies, *i.e.* the possibility of quantitative photophysical and spectroscopic studies through a microscope with high spatial resolution (sub-μm), which can be extended to even single molecules. Micro-spectroscopy techniques are optimal to study complex physical-chemical processes in live cells and tissues. They are minimally invasive. Instead of fixing and physically sectioning a sample, it is possible to obtain a 3-D dataset from a live specimen, through optical sectioning.

The fluorescence emission can be characterized not only by its intensity and position, but also by its fluorescence lifetime, polarization and wavelength. The fluorescence parameters recorded through an optical microscope with pulsed one-photon (OPE) or two photon (TPE) excitation and time-correlated single-photon counting (TCSPC) detection include: *i)* steady-state fluorescence intensity (single point, intensity fluctuations in real time, and total intensity image acquisition); *ii)* steady-state fluorescence anisotropy (single point and anisotropy image acquisition); *iii)* picosecond time-resolved total fluorescence intensity decays (single point and region of interest, ROI–image acquisition), and *iv)* picosecond time-resolved fluorescence anisotropy (single point and ROI–image acquisition) with an acceptable spectral resolution (using filters, usually) (Kudryavtsev *et al.* 2007). In a fluorescence micro-spectrometer, the XYZ spatial coordinates are stored for each point measurement, with a detected volume element size of ~1 μm^3.

3.3.1 Two-photon microscopy *vs.* confocal microscopy

Confocal Microscopy

Today, the most common optical sectioning technique is confocal microscopy, where fluorescence is created throughout the illuminated sample, and a confocal pinhole is placed in front of the detector, so that only in-focus

fluorescence is recorded. In confocal imaging, the illumination light has to be focused diffraction-limited into the sample. The microscope objective illuminates the sample with a double-inverted cone of light. The excitation photons can be absorbed anywhere in this cone sample, and photobleaching of fluorophores may occur in all the illuminated area, including the focal volume and the out-of-focus region. The pinhole acts as spatial filter for the Z-dimension and thus creates optical sections. Variations in the pinhole size ensure the changes in the optical section thickness; these can be optimized for the chosen objective and wavelength of light.

Lasers are the appropriate light source for confocal microscopes, as only they provide complete collimation at sufficient luminance. Typical lasers are diode lasers and solid-state lasers with a wide range of working wavelengths. Diode head lasers are compact, cheaper and user friendly, but work at single wavelengths, reducing the number of fluorophores that can be excited by each laser, and complicating the instrumental setup when different lasers have to be combined. In a conventional one-photon excitation (OPE) confocal microscope, a fluorescent molecule absorbs a single photon of the right energy; it is excited and subsequently relaxes by emitting another photon. The excitation wavelength is typically in the range of 400-650 nm.

The first application of a microscopic setup that allowed to measure intensities in thicker samples without disturbance from other focal planes was published in 1951 (Naora 1951).

Two-photon Microscopy

A more recently developed optical sectioning method is two-photon excitation (TPE) microscopy. It depends on the simultaneous absorption of two photons (each of which contains half the energy, typically red or infrared, needed to produce the excited state; Figure 3.6). Excitation photons must be so crowded in order to have a significant probability to find two photons at the same place, at the same time, where the fluorescent molecule is. In a TPE microscope, the photons are crowded in both time and space (Piston 2005).

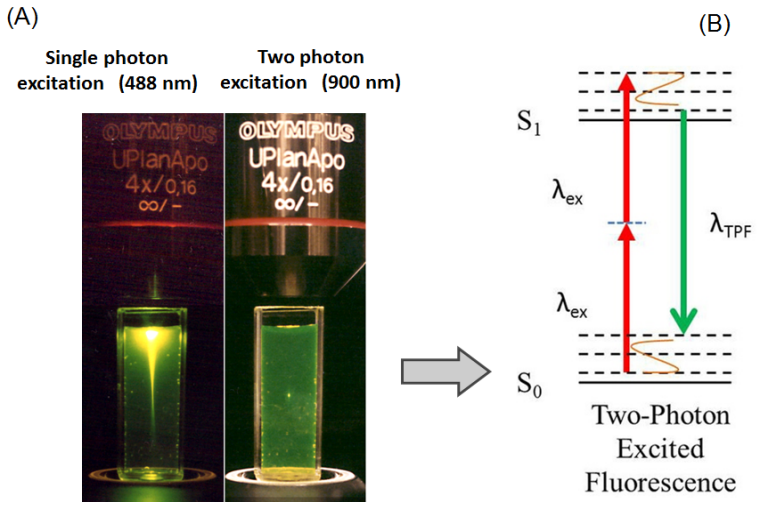

Figure 3.6. Principle of Two-photon absorption process (A) Comparative OPE and TPE process show the excitation volume for both excitations. **(B)** Jablonski diagram indicating the absorption of two photons (red arrow) to excite the fluorescent molecule to an excited state (S_1) from (S_0), and the visible fluorescence emitted during relaxation (green arrow) (*Images adapted from Zipfel et al. 2003 and Larson et al. 2011*).

TPE requires the use short (~100fs) pulsed lasers, focused through the microscope objective lens. Photons are not absorbed by out-of-focus fluorescent molecules. The only place where TPE occurs is the focal or detected volume. This optical sectioning capability of two photon excitation is optimal for deep living tissue and thick scattered samples imaging (as deep as 1mm). It is less sensitive to scattering than OPE, producing higher resolution and contrast images. It is true that red and infrared photons used in TPE are less scattered by the sample than blue or green photons, but the real explanation for the higher resolution and contrast of TPE lies in the path followed by excitation and emission photons (Figure 3.7; Piston 2005). In OPE confocal microscopy scattered excitation photons can excite fluorophores anywhere in the sample, reducing the contrast of the image. The emitted photons can also be scattered, and they will not pass through the confocal pinhole, lowering the detected fluorescence signal, and decreasing the confocal image contrast. In the case of TPE, scattered excitation photons (near infra-red) will not excite the fluorophores, and scattered emission photons will be collected because there is not pinhole needed in this set-up.

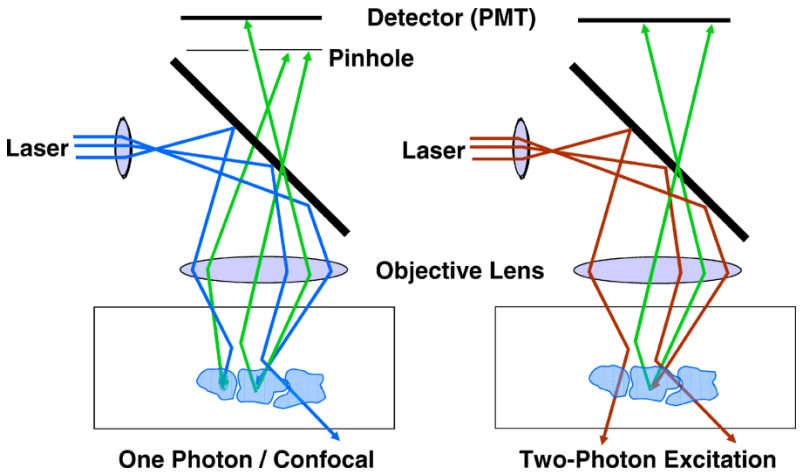

Figure 3.7. Effect of scattering in confocal microscopy and TPE microscopy. Confocal microscopy **(left)**: blue excitation light reaches the focus, and green fluorescence from the focus is collected and passes through a pinhole. Scattered emission photons do not pass through the pinhole (the total fluorescence signal is reduced), while any scattering of the excitation beam can cause fluorescence, which adds background noise to the image. TPE microscopy **(right)**: no pinhole is needed. The scattered fluorescence photons will be collected (the total fluorescence signal is increased). Furthermore, the scattering of red excitation photons does not cause background (*Image from Piston 2005*)

TPE is not optimal for highly pigmented cells and tissues that absorb near-infrared light. TPE works well for longer observation times for live cell studies, reducing the effects of photo-bleaching and photo-toxicity in the whole cell, although we can't forget the additional problems associated with TPE because of the extreme crowding of photons needed. With this highly focused radiation, it is possible to activate other nonlinear processes, which can lead to increased photobleaching and thermal damage, possibly negating the advantages of TPE in thinner samples containing a low number of fluorophores. In these cases, OPE works well, offering better spatial resolution. At the end, to choose between TPE and OPE would depend on the type of sample to study and the photophysics and concentration of fluorophores in the sample.

Lateral and axial resolution: excitation and detection volume

Lateral resolution is the resolution in the plane of the focus. Abbe demonstrated how the diffraction of light by the specimen and the objective lens determined image resolution. The image, in the focal plane, of an infinitely small luminous object point is a circular Airy diffraction image, named point spread

function (PSF; Figure 3.8), with a central bright disk and several secondary lobes. The radius of the central disk is $r_x \sim \lambda/(2 \cdot NA)$, where the numerical aperture $NA = n \cdot \sin\alpha$, n is the refractive index of the object medium, and α is the objective semi-angular aperture (Pawley 2006). The image of two equally bright spots separated by a distance d can be resolved if $d \geq r_x$ (assuming no significant aberrations; Rayleigh criterion).

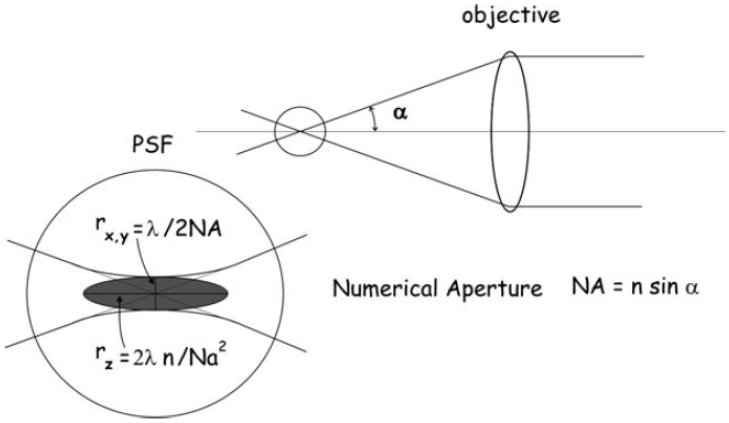

Figure 3.8. Point spread function representation. It describes the image of a point source (*from Quercioli 2011*)

The radius of the PSF in the axial direction for an aberration-free system is $r_z = (2 \cdot \lambda \cdot n)/NA^2$. Similar to the lateral resolution limit, we can use r_z as a measure of the limit of axial resolution of the microscope optics. Then, the shape of the PSF is a sort of ellipsoid, whose major axis is oriented along the optical axis (Z axis). Spectroscopy applications in the microscope can be performed either on a specific volume (at XYZ position on the sample plane; single point measurements), or scanning the sample. An important issue in the design and the use of a TPE or OPE confocal setup for spectroscopy is the full characterization of the size and shape of the effective excitation volume. The fluorescence signal detected through an optical setup can be expressed as the product of the fluorophore concentration in the object plane, the excitation laser profile function and the detection efficiency (Rigler *et al*. 1993).

The effective excitation laser profile in a OPE confocal setup has been the object of several theoretical and experimental works and it is assumed to have a Gaussian shape, both in the object plane and in the optical path direction. This approximation is sufficiently accurate only for a limited range of pinhole diameters (Rigler *et al*. 1993). The size and shape of the effective detection

volume depends on the wavelength λ, the numerical aperture *NA* of the objective and how much of the Gaussian shaped laser beam fits into the back aperture of the objective. In OPE the pinhole diameter defines mainly the effective detection volume along the optical axis. There is only a small dependence of the XY dimensions of the detection volume on the diameter of the pinhole.

TPE efficiency depends on the square of the laser power density, so that the fluorescence intensity from the secondary lobes of the Airy disk is disminished relative to the central spot. Because of this effect, a Gaussian-Lorentzian function is adequate to describe the fluorescence distribution in the detection volume element of a TPE microscope.

The estimate of the radial waist of the detection volume, in OPE and TPE setups, is usually obtained by measuring the fluorescence correlation function of a known dye. These measurements are only weakly sensitive to the actual axial dimension of the volume element, which can be better estimated by imaging calibrated fluorescence labelled microspheres (~100 nm diameter). The effective detection volume, characteristic of TPE, is about 0.2 fL, limited by the wavelength of the light used and by the numerical aperture of the objective.

Yeast *S.cerevisae* cell, used in this work as a eukaryotic model system, have diameters of 4-6 µm. In a typical 2PE setup, the size of the nucleus (~1-3 µm) would be smaller or of the same order of the Z-dimension of the detection volume (Figure 3.9). To do nuclear studies it would be convenient to optimize the Z position in the cell, looking for the maximum fluorescence intensity from a Z stack of images, and furthermore, to evaluate the contribution of fluorophores outside the nucleus or the cellular organelle of interest to the detected fluorescence signal.

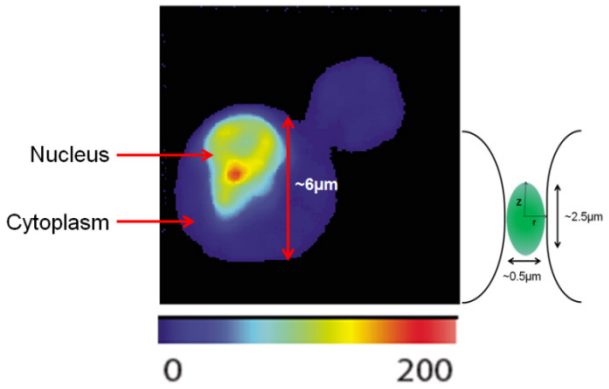

Figure 3.9. Total intensity image of a *S. cerevisiae* yeast cell expressing Nop7-EGFP in the nucleus and P0-mCherry in the cytoplasm.
λ_{exc} = 850nm; λ_{em} = 520/35nm.
It is shown for comparison the approximated size of the TPE volume element of the 2PE micro-spectrometer used in this work

3.3.2 Fluorescence lifetime imaging microscopy (FLIM)

Fluorescence imaging is one of the most powerful techniques for monitoring biomolecules within the context of living systems with high spatial and temporal resolution. However, fluorescence intensity depends either on the fluorophore environment and on the local probe concentration and both contributions cannot be easily discriminated.

Fluorescence lifetime (τ) represents the average time fluorophores remain in the excited state after excitation. For fluorophores showing a single lifetime, fluorescence intensity, *i(t)*, decays mono-exponentially:

$$i(t) = i_0 \cdot \mathrm{e}^{-t/\tau} \qquad [3.1]$$

In the case of biological samples, most of the fluorophores show a distribution of decay times or a sum of discrete exponentials:

$$i(t) = i_0 \cdot \sum_i a_i \cdot e^{-t/\tau_i} \qquad [3.2]$$

In the multi-exponential case, we can use two types of average lifetimes (Valeur 2002) to represent the lifetime, the amplitude average lifetime, $<\tau>_1$ and the intensity average lifetime, $<\tau>_2$:

$$<\tau>_1 = \sum_i a_i \cdot \tau_i \Big/ \sum_i a_i \qquad [3.3]$$

$$<\tau>_2 = \sum_i a_i \cdot \tau_i^2 \Big/ \sum_i a_i \cdot \tau_i \qquad [3.4]$$

where a_i are the pre-exponential factors, which represent the fractional contribution (molar fraction) of the species with lifetime τ_i.

The experimental fluorescence decay is the convolution of the fluorescence decay, *i(t)*, with the instrumental function IRF (O'Connor & Phillips 1984):

$$I(t) = i(t) \otimes IRF \qquad [3.5]$$

The IRF is characteristic for each time-resolved micro-spectrometer setup. It represents the pulse shape the instrument records for a sample with infinitely short fluorescence lifetime.

Fluorescence lifetime-resolved imaging uses the fact that the fluorescence lifetime of a fluorophore depends on its molecular environment but not on its concentration. Molecular effects in a sample can therefore be investigated

independently of the variable and usually unknown concentration of the fluorophore (Lakowicz 2006, Berezin & Achilefu 2010 and Roberts *et al*. 2011). Due to advances in instrumentation in the last few decades, it has become possible to couple measurements of average fluorescence lifetimes with the most common modes of fluorescence microscopy, resulting in fluorescence lifetime imaging microscopy, FLIM.

A FLIM image is composed of pixel-by-pixel average fluorescence lifetimes, rather than photon counts: the local environment determines the fluorescent lifetime, which is then used to calculate an image that is independent of probe concentration. FLIM allows image contrast to be based on the average lifetimes of the fluorophores in each region of the cell, which can be presented on a colour scale. Furthermore, separating the fluorescence signal into its elementary lifetime components provides a practical way to increase image contrast and quantitatively distinguish the spatial distribution of multiple fluorophores with different average lifetimes (Levitt *et al.* 2009 and Borst & Visser 2010).

The most frequent FLIM applications are:

- Local environment sensing: fluorescence lifetime can change depending on the fluorophore environment (which means polarity, pH, temperature, ion concentration, etc.) and is therefore used as a parameter for biological sensors. The advantage over intensity-based measurements is that no special ratiometric fluorophores are needed.
- Detection of molecular interactions by Förster resonance energy transfer (FRET): this is the most frequent FLIM application. FLIM-FRET measures the decrease of the fluorescence lifetime of a donor on interaction with an acceptor. The fluorescence lifetime serves as a sensor parameter for intra- and intermolecular interactions, allowing for distance measurements in the nanometer range. These interactions can be determined *in vitro* as well as *in vivo* by fusing the molecules of interest to appropriate fluorescent proteins.
- Autofluorescence measurements: the decay parameters of endogenous fluorophores inform us about the metabolic state of cells or tissues.

By resolving changes in the binding, conformation, and composition of

biologically relevant compounds FLIM delivers information not accessible by steady-state fluorescence techniques.

Time correlated single-photon counting

Fluorescence lifetime measurements in the time domain are usually realized by using the time-correlated single photon counting (TCSPC) technique. It allows the reconstruction of the fluorophore emission decay profile from single photon excitation/emission events collected over many cycles using pulsed laser excitation (O'Connor & Phillips 1984). The time difference between the excitation pulse and the detected photon (start-stop time in Figure 3.10) is measured by using fast electronics. Then, the histogram representing the fluorescence decay curve is built from multiple excitation/emission cycles, localizing each emission photon in the corresponding time bin (Figure 3.10).

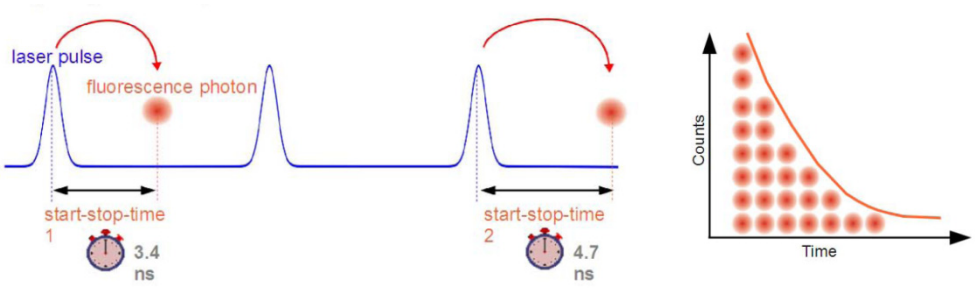

Figure 3.10. Time-correlated single-photon counting TCSPC. Start-stop timing in TCSPC and fluorescence lifetime histogram representing the fluorescence decay of the fluorophore in the time-domain acquisition mode (*from Wahl et al. 2009*)

In order to preserve single-photon statistics, the average count at the detector should be lower than 1.5% of the excitation rate.

Fast FLIM *vs*. FLIM

Fast FLIM calculation uses the average of all the start-stop TCSPC times corresponding to all the detected photons in each pixel as an approximation for the intensity average lifetime, $<\tau>_2$. Since no fitting is involved, this kind of calculation is very fast, but the average lifetime values are just approximated, especially if the pixel decays have low number of photons and a high

background. This approach provides no information beyond the average lifetime, *i.e.* it does not allow to discriminate between changes in the molar fraction (a_i) or the lifetimes (τ_i) of the fluorophores associated to each pixel.

FLIM technique collects the fluorescence intensity decay profile of each pixel of the image and fits the pixel fluorescence decay, using one or more exponential functions in order to match the different molecular species and their relative fractions with the correspondent lifetimes and amplitudes. This implies some technical challenges concerning data acquisition and also data analysis and interpretation:

- FLIM images are originated by the lifetime contribution of the different molecular species existing in the sample, each one of them having multiple lifetime components (Wouters *et al.* 2001 and Peter *et al.* 2004).
- Acquisition time per pixel is limited, especially when working with living cells, resulting in a small amount of photons per pixel, usually not enough to distinguish species with multiple exponential fitting.
- Resolving the decay at each pixel requires fitting a function; this is a complex computational task that requires experience in data fitting, and it can´t be done in an automatic way.
- Moreover, it would be necessary to include the IRF convolution in the lifetime analysis in the case the lifetime is of the same order of the full width at half maximum (FWHM) of the instrument IRF.

Phasor-FLIM approach

The phasor approach (Digman *et al.* 2008a) is an innovative tool which differs completely from the usual multi-exponential fitting of lifetime decay. It allows a straightforward interpretation of fluorescence signal in living tissues without the calculation of fluorescence lifetimes. The analysis is instantaneous since is not based on calculations or nonlinear fitting: the phasor approach has the potential to simplify the way data are analysed in FLIM.

The phasor method for lifetime analysis takes a different approach (Jameson *et al.* 1984, Gratton *et al.* 1984, Clayton *et al.* 2004, Hanley & Clayton 2005, Redford *et al.* 2005 and Caiolfa *et al.* 2007). Digman *et al*. (2008a) generalize the

phasor analysis to include time-domain data and introduced the helpful concept of trajectories in the phasor space.

In the phasor approach, the decay at each pixel (*i,j*) of a FLIM image is transformed into a coordinate pair corresponding to the phase and modulus of a vector, which is called a phasor. The ensemble of the phasor for all pixels of the image provides a two dimensional histogram called the phasor plot. Each pixel of the image gives a point in the phasor plot (its location is unique, irrespective of the number of exponentials needed for the description of the fluorescence intensity decay), and *vice versa*, each point of the phasor plot can be associated to a pixel of the image. Since every molecular species has a specific phasor, we can identify molecules by their position in the phasor plot.

The phasor approach gives many simplifications and advantages to FLIM technique:

- The decay of each pixel is represented in a graphical global view and the algorithm used is fit-free and it does not require a priori knowledge on the system.
- Every chemical species has its own "fingerprint" and so complex systems can be interpreted straigthforward: this method provides high selectivity in identifying fluorescence components that cannot be separated by a multi-exponential fitting or by analysing the average fluorescence lifetime.
- All this can be done through a fast analysis.

The phasor approach can be applied to every technique that acquires fluorescence lifetime images, such as TCSPC and frequency domain methods.

The phasor transformation (time-domain)

The phasor concept comes from the frequency domain. A phasor, being a quantity analogous to a vector, is described by a module M and a phase ϕ. The x and y coordinates of the phasor in the phasor plot are respectively:

$$g = M \cdot \cos\phi \qquad s = M \cdot \sin\phi \qquad [3.6]$$

Figure 3.11 shows two phasors represented in the phasor plot. The semicircle is called the "universal circle":

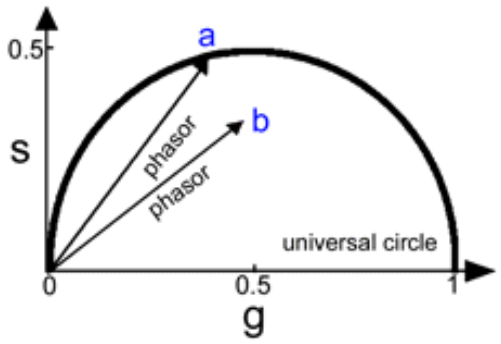

Figure 3.11. Graphical representation of phasors in the phasor plot. The phasor is identified by its module *M* and its phase ϕ. *g* is the *x*-coordinate and *s* is the *y*-coordinate of the phasor in the phasor plot (*from Caiolfa et al. 2007*)

Estimations of the average lifetime in terms of the phase and modulation can be performed in each pixel by eq. 3.7 and 3.8:

$$\tau_\phi = \frac{1}{\omega}\tan\phi \qquad [3.7]$$

$$\tau_M = \frac{1}{\omega}\sqrt{\left(\frac{1}{M^2}-1\right)} \qquad [3.8]$$

where ω is the angular frequency ($\omega = 2\pi f$), and f is the repetition rate of the laser (Hz). For samples having a single lifetime, $\tau_\phi = \tau_M$, however for samples showing multiple lifetimes, the apparent phase and modulation lifetimes are different ($\tau_\phi < \tau_M$).

In the time-domain acquisition method, the *s* and *g* coordinates of the phasor associated to each pixel (*i,j*) are calculated from the Fourier transform of the corresponding decay curve $I_{i,j}(t)$ (Eq. 3.9 and 3.10):

$$g_{i,j}(\omega) = \frac{\int_0^\infty I_{i,j}(t)\cdot\cos(\omega\cdot t)\cdot dt}{\int_0^\infty I_{i,j}(t)\cdot dt} \qquad [3.9]$$

$$s_{i,j}(\omega) = \frac{\int_0^\infty I_{i,j}(t)\cdot\sin(\omega\cdot t)\cdot dt}{\int_0^\infty I_{i,j}(t)\cdot dt} \qquad [3.10]$$

where the indexes *i* and *j* identify the position of a pixel in the FLIM image.

Phasor rules

- Phasors from single exponential total fluorescence decays lie on the universal circle.

- Phasors from multi-exponential total fluorescence decays will lie inside the universal circle, and are a linear combination of the individual lifetimes. Figure 3.12 shows the analysis of a sample with two molecular species with lifetimes t_1

and t_2. All possible weighting of the two species in this sample will be on the straight line joining the locations of the phasors corresponding to the two single lifetimes. The ratio of the linear combination determines the fraction of the components *1* and *2* (fractional intensity, f_1 and f_2) in pixel (i,j), and identifies the exact location of the experimental phasor.

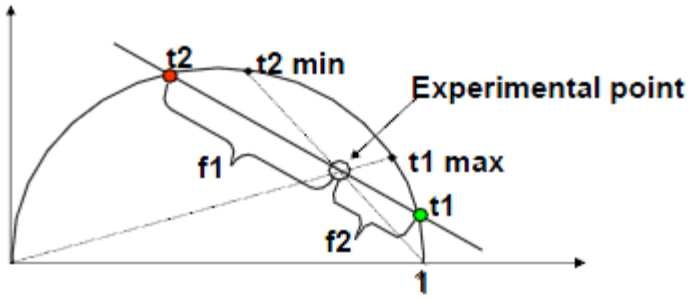

Figure 3.12. Lifetime representation using phasors. Mixtures of components with lifetimes t_1 and t_2 must be on the line between t_1 and t_2 in proportion to their fractional intensity contribution (*from Digman et al. 2012)*

In the case of many molecular species, all the possible combinations are contained in a polygon where the vertices are coincident with the phasor locations of the individual pure molecular species.

- For interacting species, such as a FRET pair, in which the presence of the acceptor reduces the lifetime of the donor, the resulting phasor cannot lie in the line joining the phasor of the two non-interacting species. FRET phasor describes a curved trajectory: the realizations of all possible phasors that are quenched with different FRET efficiencies describe a curved trajectory in the phasor plot, as we will see later.

- Every molecular species has a specific location in the phasor plot. This identification between species and phasors can be considered a "phasor fingerprint": we can identify molecules by their position in the phasor plot.

- However, a location in the phasor plot does not correspond biunivocally to one species. Different species may have the same phasor location, even if they have a different lifetime distribution. This coincidence happens only for one specific frequency (one harmonic). Multi-harmonics analysis separates molecules with two different lifetime distributions and it identifies them univocally

- The resolution of phasors depends on the counts in each pixel: for high spatial resolution, 100 photons in each pixel of the image are enough.

- The phasors corresponding to cellular autofluorescence are spread over a larger area due to the low intensity per pixel and to pixel heterogeneity.

3.3.3 Förster resonance energy transfer (FRET)

Förster-type Resonance Energy-Transfer (FRET) has become a valuable standard tool in cell biology to localize molecular interactions. FRET, is a nonradiative process in which an excited donor fluorophore transfers energy to an acceptor chromophore in the ground state, through long-range dipole-dipole interactions. It falls in the category of non-radiative relaxation pathways because no fluorescence emission is associated with the energy loss for the donor molecule.

The rate of energy transfer depends upon the extent of spectral overlap of the emission spectrum of the donor with the absorption spectrum of the acceptor (Figure 3.13), the quantum yield of the donor, the relative orientation of the donor and acceptor transition dipoles, and the distance between the donor and acceptor molecules (Förster 1965, Stryer 1978, Clegg 1996 and Lakowicz 2006). The distance dependence of FRET allows measurement of distances between donors and acceptors.

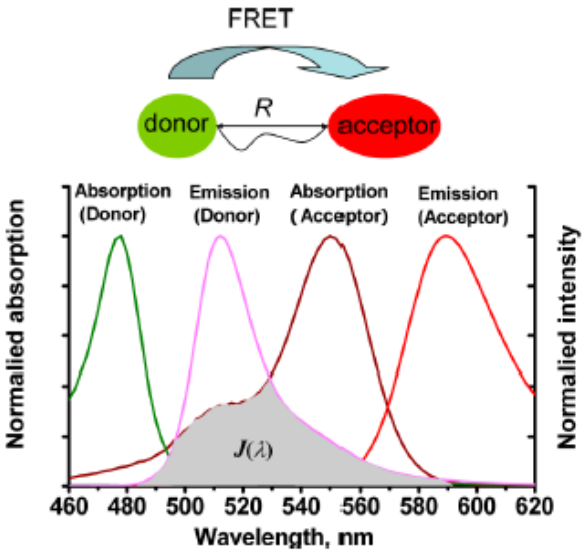

Figure 3.13. FRET process scheme. This figure shows the absorption and emission spectra for both donor and acceptor molecules of a FRET pair. Efficient FRET requires significant overlap between the donor emission and acceptor excitation spectra. (*from Yuan et al. 2013*)

FRET does not require the acceptor chromophore to be fluorescent. In most applications, however, both donor and acceptor are fluorescent, and the occurrence of energy transfer manifests itself through quenching of donor

fluorescence and a reduction of the donor fluorescence lifetime, accompanied also by an increase in acceptor fluorescence emission.

The distance at which FRET efficiency is 50% is called the Förster distance, R_0, which is typically in the range of 10 to 70 Å. The rate of FRET, $k_T(r)$ is given by:

$$k_T(r) = \frac{1}{\tau_D}\left(\frac{R_0}{r}\right)^6 \qquad [3.11]$$

where τ_D is the lifetime of the donor in the absence of acceptor, and r is the donor-to-acceptor (D-A) distance. The rate of FRET depends strongly on D-A distance. Consequently, FRET measurements can be utilized as an effective "molecular ruler" for determining distances between biomolecules labelled with appropriate donor and acceptor fluorophores.

The value of R_0 (Å) may be calculated from the following expression:

$$R_0 = 0.211 \cdot \left(\kappa^2 \cdot n^{-4} \cdot Q_D \cdot J(\lambda)\right)^{1/6} \qquad [3.12]$$

where the orientation factor, κ^2, is a function of the relative orientation of donor and acceptor transition dipoles; $J(\lambda)$ is the overlap integral of the donor emission and acceptor absorption spectra (wavelength expressed in nm); n represents the refractive index of the medium, and Q_D is the quantum yield of the donor.

The FRET efficiency, E, is the fraction of photons absorbed by the donor which are transferred to the acceptor, and is related to the donor-acceptor separation distance, r, by equation 3.13:

$$E = \frac{R_0^6}{R_0^6 + r^6} \qquad [3.13]$$

This equation shows that the transfer efficiency is strongly dependent on distance when the D–A distance is near R_0 (Figure 3.14):

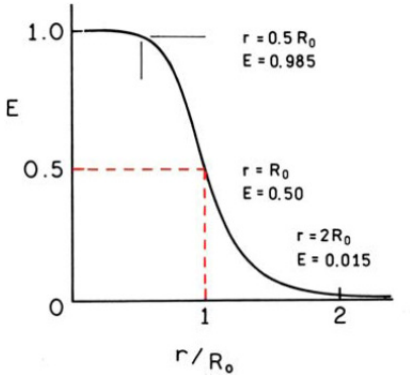

Figure 3.14. Dependence of the FRET efficiency (*E*) on Donor-Acceptor distance (*r*). The efficiency quickly increases to 1 as the D–A distance decreases below R_0 (Förster distance) (*from Lakowicz 2006*)

3.3.4 FLIM-FRET

Fluorescence lifetime imaging, FLIM, offers a solution for quantitative analysis of molecular interactions by FRET, measuring the fluorescence lifetime of a donor in the absence (τ_D) and presence (τ_{DA}) of an acceptor (Bastiaens & Squire 1999, Tramier *et al*. 2002, Jares-Erijman & Jovin 2006, Yasuda *et al*. 2006, Goedhart *et al*. 2007, Padilla-Parra *et al.* 2008 and Molina-Guijarro *et al*. 2011).

FRET efficiency is typically measured using the ratio of steady-state fluorescence intensity of the donor, in the absence (F_D) and presence (F_{DA}) of acceptor:

$$E = 1 - \frac{F_{DA}}{F_D} \qquad [3.14]$$

Quantification by intensity-based FRET is difficult since it bears the uncertainty of artifacts due to differences in excitation power, photobleaching or spectral crosstalk as well as the unknown concentrations of both molecules in living cells.

From FLIM-FRET methodologies, the FRET efficiency *E* can then be easily calculated from the lifetime ratio of the donor-acceptor and the donor-only samples, τ_{DA} and τ_D, which are independent of the concentration of donor and acceptor proteins and photobleaching:

$$E = 1 - \frac{\tau_{DA}}{\tau_D} \qquad [3.15]$$

Fluorescence resonance energy transfer (FRET) detected by fluorescence lifetime imaging microscopy (FLIM), FLIM-FRET, is the most frequent FLIM application. In a FLIM-FRET image, it is possible to spatially differenciate FRET regions from the decrease in the fluorescence lifetime of the donor (in donor channel) and the increase in acceptor emission intensity (in acceptor channel), if the acceptor is a fluorophore (example in Figure 3.15).

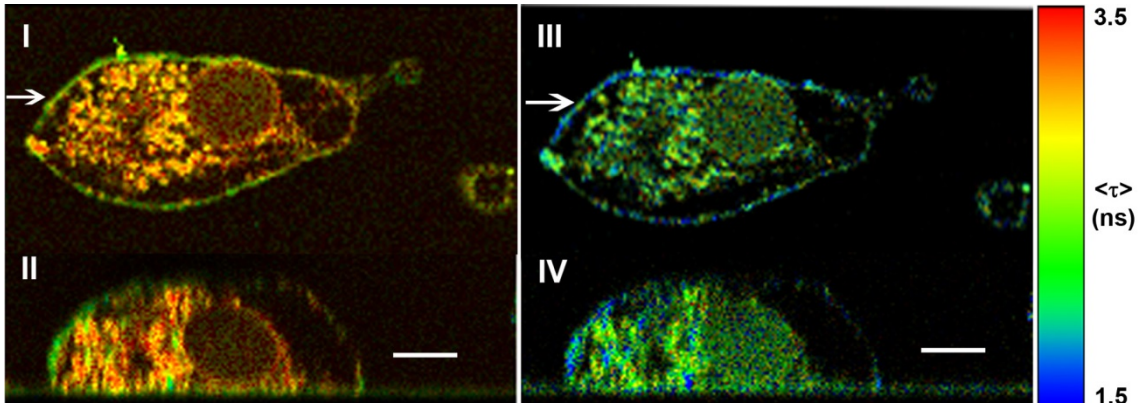

Figure 3.15. Interactions between the anti-tumoral Irvalec and the plasma cell membrane of A549 cells. It was demonstrated by using FLIM-FRET that, at cytotoxic concentrations, Irvalec molecules are forming some kind of assemblies all throughout the plasma membrane where the individual molecules of the drug are close enough to each another (< 50 Å) as to suggest that the compound self-organizes in the plasma membrane, forming supramolecular structures that could trigger the disruption of membrane integrity.
Donor: Irvalec-Oregon Green488 (Irv-OG488); Acceptor: Irvalec-Alexa 555 (Irv-A555)
A549 cell exposed to a mix of 0.6 μM Irv-OG488, 1.8 μM Irv-A555 and 2.4 μM Irvalec
I (XY section) and II (YZ section): donor channel FLIM image
III (XY section) and IV (YZ section): acceptor channel FLIM image. Scale bar: 10 mm
(*from Molina-Guijarro et al. 2011)*

FRET–FLIM can be a very useful tool to ascertain protein-protein, protein-ligand, protein-lipid and protein-DNA interactions in single living cells. FRET-FLIM is currently employed not only in biophysics or chemistry but also in bio-medicine, thanks to new advancements in technology and also new developments in data treatment.

The probably most significant advantage of FLIM-FRET is that FLIM can distinguish between interacting and non-interacting protein fractions, because both, the fraction of interacting proteins and the distance between the proteins, influence FRET efficiency (Calleja *et al.* 2003, Becker *et al.* 2004, Yasuda *et al.* 2006, Padilla-Parra *et al.* 2009 and Becker 2012). FLIM solves the problem by multi-exponential decay analysis, able to discriminate the fluorescence lifetimes and amplitudes of the decay components present in the heterogeneous cellular environment.

Figure 3.16 shows an example of the composition of a donor decay function

approximated by a double-exponential model, with a slow lifetime component from the noninteracting (unquenched) and a fast component from the interacting (quenched) donor molecules:

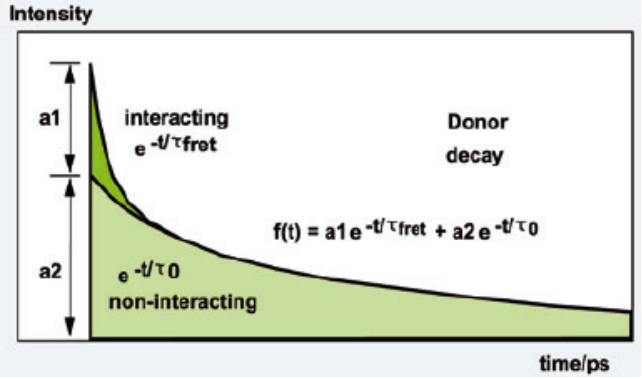

Figure 3.16. Fluorescence decay components in a sample containing interacting (FRET, τ_{fret}) and non-interacting (Donor only, τ_0) species (*from Becker 2012*)

The double-exponential decay analysis delivers the lifetimes, $\tau_0 = \tau_D$ and $\tau_{fret} = \tau_{DA}$, and the amplitudes, a_1 and a_2, of the two decay components. From these parameters can be derived the true FRET efficiency for the interacting proteins (Eq. 3.14), the ratio of the distance and the Förster radius (r/R_0, Eq 3.13), and the ratio of the relative numbers of interacting and non-interacting donor molecules.

3.3.5 Fluorescence anisotropy with sub-µm spatial resolution

Conformational dynamics, interactions and fluorescence depolarization

Live cell fluorescence micro-spectroscopy methodologies provide a potent way to characterize the structure, 3D-organization and dynamics of proteins and protein complexes, with high spatial and temporal resolution. Specifically, analysis of time-resolved fluorescence depolarization measurements provides very accurate characterization of the angular reorientation movements of fluorophores in the ps-ns time region (Valeur 2002). Depending on the type of coupling between the fluorophore and the rest of the molecular structure, this analysis allows to quantify a variety of dynamic phenomena, such as the hydrodynamic properties of the structure (rotational diffusion; Acuña *et al.* 1987), segmental flexibility and conformational changes (Lillo *et al.* 1997; Zorrilla *et al.* 2004a), interactions with other molecules (Diederix *et al.* 2008), oligomers stoichiometry (Zorrilla *et al*. 2004b), and lipid order and fluidity of cell membranes (Guizy *et al*. 2008).

Performing excitation and detection of polarized light in living cells through an inverted microscope requires taking into account several factors which add complexity to the fluorescence determinations and data analysis, such as: *a)* the distribution of fluorophores transition moments may not be isotropic in the detected volume (< 1fL); *b)* the directions of the excitation and detection beams are collinear; *c)* the detected fluorescence polarization intensities are highly dependent on the optical characteristics of the microscope setup; *d)* depolarization associated to the scattering of the emitted photons; *e)* heterogeneity of fluorescent labelling of intracellular structures which carries heterogeneity of the photophysical properties of the fluorophores in different subcellular locations, etc.

Overview of the different applications of fluorescence anisotropy in the microscope

Fluorescence depolarization technique has long been used for *in vitro* and living cells cuvette studies. In the last twenty years, several groups used the confocal or the TPE arrangement to limit a spatial area of sampling, and added all the optics/electronics to measure time-resolved anisotropy decays in specific subcellular locations of individual living cells, with high spatial resolution (sub-μm). In Tables 3.1 and 3.2 we show the most relevant applications in living cells. Currently, measurements of linear polarized fluorescence intensity are included in the specifications of commercial OPE and TPE microscopes, thus the use of these methodologies has increased significantly in recent years.

Axelrhod (1979, 1989) established the principles for fluorescence polarization measurements with a microscope. He introduced the theory and he proposed practical suggestions for running steady-state polarization experiments on the surface or interior of very small sub-volumes of cells. His first application was the determination of the orientation of the membrane fluorescence probe DiI-C_{18} in the membrane of erythrocyte ghosts. The work of Verkman group was pioneering introducing time-resolved polarization measurements by adapting a flash lamp and a gated photomultiplier to an epi-fluorescence microscope, with applications in the determination of cytoplasmic viscosity in MDCK and

Swiss3T3 fibroblast cells, and the membrane fluidity of tubule cells from rabbit kidney (Dix and Verkman, 1990; Fushimi *et al.* 1990).

Entwistle and Noble (1992a, 1992b) used confocal fluorescence polarization microscopy to find the concentration of fluorophore at which the response to incident light becomes nonlinear in intensity.

Wu *et al.* (1996) used steady-state fluorescence anisotropy imaging to monitor membrane changes in human astrocytoma cells induced by ATP depletion. They were looking at the effects of the antioxidants gossypol and tirilazad on cell membranes undergoing stress from iodoacetic acid-induced ATP depletion. In the same way Piston group determined the orientation of eosin-5-maleimide on the erythrocyte anion channel protein band 3 in erythrocyte ghosts by measuring confocal fluorescence steady-state anisotropy (Blackman *et al.* 1996). They found evidence for three rotational species that could account for several uniaxial rotational diffusion times.

Coppey group published two OPE time-resolved anisotropy studies of the torsional dynamics of DNA (Traimer *et al.* 2000) and the monomer-dimer distribution of GFP tagged proteins (homo-FRET study; Gautier *et al.* 2001) in living cells (single point measurements with high spatial resolution). They introduced the convolution with the instrumental function IRF into the analysis and measured the effect of the numerical aperture of the objective, *NA*, on the time zero anisotropy (r_0).

Diaspro and Chirico groups (Diaspro et *al.* 2001 and Olivini *et al.* 2001) modified a confocal laser scanning head for TPE microscopy to run time-resolved fluorescence polarization studies in living cells, in the frequency domain acquisition mode.

Jovin group (Clayton *et al.* 2002) published a nice experimental and theoretical work about the measurement of time-resolved anisotropy in the frequency domain mode in a confocal microscope, and the application in EGFP-expressing bacteria. The rotational mobility of EGFP and Dsred fluorescence proteins were measured in cytoplasm and in solution using one and two photon microscopes (Hess *et al.* 2003).

Homo-FRET anisotropy methods coupled with hetero-FRET FLIM and theoretical modeling showed the presence of nanometer-sized clusters of glycosyl-phosphatidylinositol-anchored proteins (GPI-Aps) at the plasma membrane of cells (Sharma *et al.* 2004). The same group (Goswami *et al.* 2008) published an extensive analysis of the surface distribution and dynamic remodeling of GPI-AP nanoclusters in the unperturbed cell.

Guerritsen group (Bader *et al.* 2007 and 2009) determined the protein cluster size of fluorescently tagged GPI-AP in living cells, by using homo-FRET measurements and a time-gated photon counting confocal anisotropy imaging system. They showed 3D clustering of GFP-labelled GPI-AP in the plasma membrane of NIH 3T3 fibroblasts, with the size of the clusters being evaluated using photobleaching methods.

The fluorescence polarization elucidated the structure of individual components of nuclear pore complex (NPC) in live cells. This technique allowed the researchers to distinguish between ordered and disordered domains associated with the NPC components. Moreover this study also provided a comprehensive theoretical and experimental framework for anisotropy imaging experiments to be applied to study many other intracellular protein complexes (Kampmann *et al.* 2011; Mattheyses *et al.* 2010).

Suhling group combined time-resolved fluorescence anisotropy imaging, TRFAIM, and total internal reflection imaging, TIRF-FLIM to measure intracellular viscosities using molecular rotors and homo dimerization measurement in plasma membrane and cytoplasm (Suhling *et al.* 2004; Levitt *et al.* 2011a and 2011b).

Vogel group developed a fluorescence polarization and fluctuation analysis single molecule method (FPFA) and determined the number of subunits present on calcium–calmodulin dependent protein kinase-II (CaMKIIa) holoenzyme in live cells (Nguyen *et al*. 2012).

In this work we make use of all the previous advancements in time-resolved fluorescence polarization micro-spectroscopy methods, to setup a TPE micro-spectrometer for time-resolved fluorescence anisotropy measurements in the

time-domain mode, including the convolution effect of the instrumental response function, IRF. We are interested in conformational dynamic changes of the C-terminal domain region of yeast ribosomal stalk proteins associated with tetracyclic antibiotics interactions. The rotational mobility of these proteins in the cytoplasm of *S. cerevisiae* yeast cells (~50ns) is in the limit of the resolution of time-resolved anisotropy methods for the fluorescent protein EGFP (τ = 2.6 ns) as fluorescence probe. We have explored the advantages and disadvantages of using TPE and OPE, and the effect of the background, time acquisition, time shift of parallel and perpendicular polarized decays and global analysis including IRF convolution to the final rotational correlation times values.

Table 3.1. Overview of living cell studies using fluorescence anisotropy methodologies in the microscope

Application **Biological System** **Type of cells**	**Subcellular compartment**	**Fluorophore**	**Excitation**	**Anisotropy measurement**	**IRF Convo-lution**	**Axelrod correc-tion**	**Comments**	**Ref.**
Intracellular Viscosity **MDCK, 3T3 cells**	Cytoplasm	BCECF & Indo-1	OPE	SS, TR-TCSPC Image	Yes	Yes	Microscope *vs.* cuvette study	Dix & Verkman 1990
Torsional Dynamics **DNA** **S2 cells**	Nucleus	Hoechst 33342 EtBr	OPE	TR-TCSPC Point	Yes	Yes		Traimer *et al.* 2000
Monomer- Dimer distribution **TK_{27} &TK_{366}** **Herpes Virus,** **Cos7 cells**	Cytoplasm, Nucleus	GFP	OPE	TR-TCSPC Point	Yes	Yes	homoFRET study	Gautier *et al.* 2001
Rotational Mobility **EGFP** **Bacteria**	Cytoplasm	EGFP	OPE	TR-Freq Domain Image	Yes	Yes		Clayton *et al.* 2002
Rotational Mobility **LynB** **RBL-2H3 cells**	Plasma Membrane, Cytoplasm	EGFP, DsRed	OPE TPE	TR-TCSPC Point	Yes	Yes		Hess *et al.* 2003
Intracellular Viscosity **B-cell cells**	Cytoplasm	CFSE	OPE	TR Image	Yes	No	Multi-well plates study	Suhling *et al.* 2004

Table 3.1 (cont.). Overview of living cell studies using fluorescence anisotropy methodologies in the microscope

Application **Biological System** **Type of cells**	**Subcellular compartment**	**Fluorophore**	**Excitation**	**Anisotropy measurement**	**IRF Convo-lution**	**Axelrod correc-tion**	**Comments**	**Ref.**
Protein Cluster Size **GPI** **NIHT3 cells**	Golgi, Membrane	GFP	TPE	SS, TR Image	Yes	Yes	Time-gated anisotropy photobleaching Homo-FRET	Bader *et al.* 2007 & 2009
Structure & Conformation **CaMKII** **HeLa cells**	Cytoplasm	Venus	TPE	SS, TR Image	Yes	No	FRET	Thaler *et al.* 2009
Protein Oligomerization **5-HT$_{1A}$** **CHO cells**	Membrane	EYFP	TPE	SS, TR Point	Yes	No		Paila *et al.* 2011
Intracellular Viscosity **HEK cells**	Cytoplasm	CCVJ, DCVJ	OPE	SS, TR Image	Yes	Yes		Levitt *et al.* 2011a
Protein Homodimerization **APP** **HEK293 cells**	Cytoplasm	EGFP	OPE	SS, TR Image	Yes	Yes	trFAIM TIRFLIM	Devauges *et al.* 2012
Protein organization **CaMKII** **HEK293 cells**	Cytoplasm	Cerulean, Venus	TPE	SS Point	No	No	FCS, homo-FRET Brightness	Nguyen *et al.* 2012

Table 3.1 (cont.). Overview of living cell studies using fluorescence anisotropy methodologies in the microscope

Application **Biological System** **Type of cells**	**Subcellular compartment**	**Fluorophore**	**Excitation**	**Anisotropy measurement**	**IRF Convo-lution**	**Axelrod correc-tion**	**Comments**	**Ref.**
orientation & order **NPC** **Yeast**	Nucleus, membrane	EGFP	OPE	SS Image	No	Yes		Mattheyses *et al*. 2010 Kampmann *et al.* 2011
Nano clusters on cell surfaces. GPI **CHO cells**	Cytoplasm, membrane	PLF, PLA PLB	TPE	SS, TR Image	Yes	No	Anisotropy photobleaching Homo-FRET	Goswami *et al.* 2008
Chromatin Compaction **H2B** **HELA cells**	Nucleus	EGFP	Arc Lamp	SS Image	No	No		Hameed *et al* 2012
Protein Polymerization. Actin **HEK293 cells**	Cytoplasm	GFP, CFP YFP	TPE	SS Image	Yes	Yes	Hetero- and Homo-FRET	Vishwasrao *et al.* 2012

Cells: MDCK: Madin Darby Canine Kidney; 3T3: Fibroblast; RBL-2H3: rat basophilic leukemia; CHO: Chinese hamster ovary; S2: Schneider 2; HEK293: Human Embryonic Kidney 293.

Proteins: APP: Amyloid precursor protein; NPC: Nuclear pore complex; H2B: a member of the histone complex; GPI: Glycosylphosphatidylinositol anchor protein; LynB: lck/yes-related novel protein B; CaMKII: Ca2+/calmodulin-dependent protein kinases II; 5-HT_{1A}: Serotonin1A receptor; TK_{27}&TK_{366} : herpes simplex virus thymidine kinase

Fluorophores and Methodologies: BCECF: -2,7biscarboxyethyl-5(and6)carboxy Fluorecein; CFSE: Carboxy fluorescein succinimidyl ester; Indo-1: Indo-1-Calcium Indicator; Hoechst 33342 and EtBr (Ethidium bromide): DNA Intercalators; PLF: Nα-pteroyl- Nε -(4'Fluoresceinthiocarbamoyl)-L-lysine; PLA: Nα-pteroyl-Nε-Alexa546-L-lysine; PLB: Nα-pteroyl-Nε-bodipy-L-lysine; CCVJ: 9-(2-carboxy-2-cyanovinyl)julolidine; DCVJ: 9-(2,2-dicyanovinyl)julolidine; GFP, CFP, YFP: Green,Cyan,Yellow Fluorescent Proteins; SS: Steady-state; TR: Picosecond time-resolved; TCSPC: Time-correlated single-photon counting; FRET: Förster-type resonance energy-transfer; trFAIM: Time-resolved fluorescence anisotropy Image; TIRFLIM: Total internal reflection Fluorescence lifetime Imaging microscopy. FCS: Fluorescence correlation spectroscopy; OPE: One photon Excitation; TPE: Two photon Excitation; IRF:Instrument response function.

Table 3.2. Overview of biological applications of fluorescence anisotropy micro-spectroscopy techniques in live cells

Application	Comments	References
Protein Oligomerization	Homo and hetero dimerization of β1 and β2 adrenergic receptor using BRET	Mercier *et al.* 2002
	Ligand regulated oligomerization studies on β2-adrenoceptors using FRET and Anisotropy	Fung *et al.* 2009
	Degree of oligomerization state of Band 3 and GPI linked membrane proteins using homoFRET	Yeow & Clayton 2007
	Dimerization and organization of CaMKII domains, *in vivo*, in the context of the holo-enzyme using Anisotropy, Fluorescence Fluctuations and FRET methodologies	Nguyen *et al*. 2012
	Clustering of GPI anchoring proteins using FRET	Kenworthy & Edidin 1998
	Clustering in GPI anchor protein domains at the cell surface detected by homo-FRET	Varma & Mayor 1998
	Size and lipid dependent organization of GPI anchored proteins in live cells using homo- and hetero-FRET	Sharma *et al*. 2004
	Determination of cluster sizes of GFP labelled lipid markers using homo-FRET	Bader *et al.* 2007
	Protein interaction measurements between BACE and LDL receptor protein, using FRET-FLIM on lipid rafts at the cell surface	Von Armin *et al.* 2005
	Distribution and functional characterization of neurokinin-1 receptor in the plasma membrane	Meyer *et al*. 2006
	Measuring cell surface cortical actin activity and it regulates on spatial organization of nanoclusters of GPI anchored proteins as shown by homo FRET	Goswami *et al.* 2008

Table 3.2 (cont.). Overview of biological applications of fluorescence anisotropy micro-spectroscopy techniques in live cells		
Application	**Comments**	**References**
Protein Oligomerization (cont)	Real-time measurements of FRET and fluorescence anisotropy in CaMKII N or C terminal subunits tagged with Venus expressed in both HeLa and hippocampal neuronal cells. It is proposed that CaMKII holoenzyme is inhibited as dimeric units, and they monomerize upon activation.	Thaler *et al.* 2009
	Measuring homo-dimerization of amyloid precursor protein in plasma membrane using homo FRET	Devauges *et al.* 2012
Rotational mobility of fluorophores	Monitorization of changes in nuclear morphology	Rao *et al.* 2007
	Determination of changes in membrane fluidity	Li *et al*. 2007
	Monitorization of changes in DNA digestion by nucleases using fluorescence anisotropy imaging	Cao *et al*. 2006
	Characterization of the mobility of DNA intercalator	Traimer *et al.* 2000
	Rotational mobility of EGFP and DsRed in the cytoplasm , a comparative study on OPE and TPE microscope	Hess *et al.* 2003 & Clayton *et al.* 2002
	Rotational diffusion of Thymidine kinase protein and estimation of the oligomerization state in the cytoplasm and nucleus	Gautier *et al*. 2001
	Measuring fluorescence anisotropy of molecular rotors CCVJ, DCVJ, BODIPY-C_{12}	Levitt *et al.* 2011a

Table 3.2 (cont.). Overview of biological applications of fluorescence anisotropy micro-spectroscopy techniques in live cells		
Rotational mobility of fluorophores (cont)	Mapping viscosity	Levitt *et al*. 2009 & Kuimova *et al*. 2009

Proteins: BACE: β-site of amyloid precursor protein cleaving enzyme; **LDL:** Low-Density Lipoprotein Receptor related protein; **GPI:** Glycosylphosphatidylinositol anchor protein; **CaMKII:** Ca2+/calmodulin-dependent protein kinases II.

Fluorophores: CCVJ: 9-(2-carboxy-2-cyanovinyl)julolidine; **DCVJ:** 9-(2,2-dicyanovinyl)julolidine; **BODYPY-C_{12}:** boron-dipyrromethene-C_{12}; **EGFP, DsRed**: Green, Red Fluorescent Proteins

Methodologies: **FRET:** Förster-type resonance energy-transfer; **BRET:** Bio luminescence resonance energy transfer; **OPE**: One photon Excitation**; TPE**: Two photon Excitation; **FLIM:** Fluorescence lifetime Imaging microscopy

3.4 Fluorescent proteins as dynamic cell probes in fluorescence micro-spectroscopy studies

Fluorescent proteins (FPs) are genetic tools for cellular and subcellular imaging *in vitro* and *in vivo*. The discovery and development of FPs from jellyfish and other marine organisms has drastically transformed cell research in recent years, providing life scientists a minimally invasive tool for studying protein dynamics and function in live cells and tissues.

Fluorescent proteins are members of a structurally homologous class of proteins that share the unique property of being self-sufficient to form a visible wavelength chromophore from a sequence of 3 amino acids within their own polypeptide sequence. These probes are unique when compared with synthetic fluorophores since they are genetically encoded and can be expressed and retained within the living cell: it is common practice to introduce a gene (or a gene chimera) encoding an engineered fluorescent protein into living cells and subsequently visualize the location and dynamics of the gene product using fluorescence microscopy.

Many different colors of fluorescent proteins have now been produced in the laboratory or found in nature: with multiple colors, many processes can be visualized simultaneously in cells. When coupled with the recent advances in live-cell imaging that have occurred over the past decade, the FPs have truly ushered in a new era for research related to cell biology, medicine, and physiology.

3.4.1 Discover of the Green Fluorescent Protein (GFP)

GFP was first purified from the bioluminescent jellyfish *Aequorea victoria* by Dr. Osamu Shimomura at 1970s (Morise *et al.* 1974). Prasher obtained a single full-length clone (*gfp*10) that encoded the complete *Aequorea* GFP sequence in 1992 (Prasher *et al.* 1992). Using the clone isolated by Prasher, Chalfie successfully expressed GFP in both bacteria and the sensory neurons of *Caenorhabditis elegans* nematode worms, demonstrating for the first time that chromophore formation (and fluorescence) required no additional factors that

were specific to the jellyfish (Chalfie *et al.* 1994). In 1996, the crystal structure for GFP was solved, revealing that the cyclic tri-peptide chromophore (Ser65, Tyr66, and Gly67) was buried in the center of a nearly perfect cylinder formed by a tightly interwoven eleven-stranded "β-barrel" structure (Ormö *et al* 1996).

As the protein folds, the tri-peptide sequence is positioned at the core of the β-barrel, driving the cyclization and dehydration reactions necessary to form the mature chromophore, and revealing that the entire protein sequence is required to generate a functional chromophore. The cylindrical geometry of GFP is conserved in all the FPs yet discovered, and appears to be ideally suited to the primary function of protecting the chromophore.

The β-barrel structure has dimensions of approximately 24 Å × 42 Å, and the tight packing of amino acid residues imparts a high level of stability to the protein. A lack of clefts and gaps for access of small ligands, combined with the fact that the chromophore is located near the exact center of the protein (~ 60º to the long axis of the barrel), partially explains the extraordinary photostability and high quantum yields that are observed. Fortunately, both the amino and carboxy termini are exposed on the surface of the barrel, and therefore are available to be employed as linkers to fusion proteins without significantly affecting the structural integrity of the fluorophore (Tsien 1998, review).

3.4.2 The fluorescent protein color palette

Mutations that alter the residues immediately adjacent to the GFP chromophore generally have a significant impact on the spectral properties of the protein. Surprisingly, however, several amino acid substitutions in regions of the polypeptide far removed from the chromophore were also found to profoundly affect the spectral characteristics of the protein. These protein engineering approaches have generated many different spectral variants from the *Aequorea* GFP (Day *et al.* 2009).

The native green fluorescent protein fluorophore exists in two states. A protonated form, the predominant state, has an excitation maximum at 395 nm, and a less prevalent, unprotonated form that absorbs at approximately 475 nm. In solution, excitation at 395 nm gives emission peaking at 508 nm, whereas

excitation at 475 nm gives a maximum at 503 nm. The fact that the emission maximum depends on the excitation wavelength indicates that the population includes at least two chemically distinct species, which do not fully equilibrate within the lifetime of the excited state (Heim *et al.* 1994).

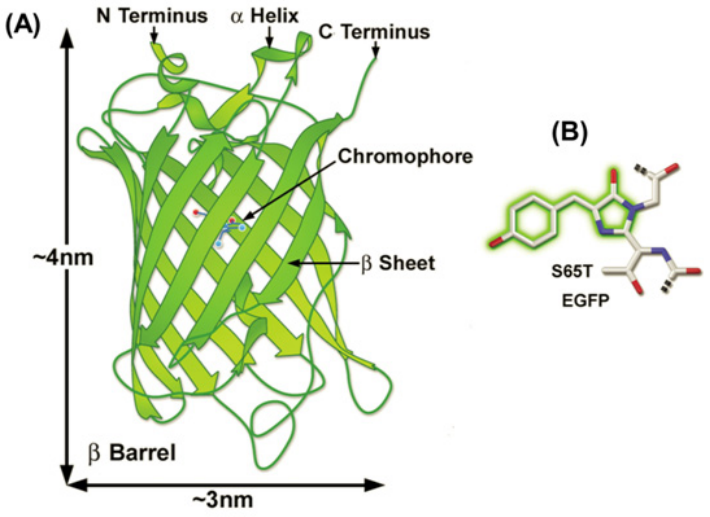

Figure 3.17. 3-D structure of EGFP protein. (A) β-Barrel structure and dimensions of EGFP with the chromophore at the centre. **(B)** Mature EGFP chromophore (S65T) (*adapted from Rizzo et al. 2009*).

The most commonly used mutation is a replacement of Ser65 by Thr, or S65T. In S65T, the wild-type 395-nm excitation peak is suppressed, and the 470-475 nm peak is enhanced five-six-fold in amplitude and shifted to 489–490 nm (Heim *et al*. 1995, Delagrave *et al*. 1995, Cheng *et al*. 1996). This mutation is featured in the most popular variant of green fluorescent protein, termed enhanced GFP (EGFP) (Figure 3.17). The enhanced green fluorescent protein, EGFP, has an excitation maximum at 484 nm with absorbance extinction coefficient of 56.000 $M^{-1}cm^{-1}$ and an emission maximum at 507-509 nm, with a quantum yield of 0.60 (Tsien 1998, Drobizhev *et al.* 2011).

Excited state dynamics and photo physical properties of GFP and its mutants were well characterized by Ward (Perozzo *et al.* 1988) and Prendergast (Nageswara Rao *et al*. 1980) and other groups (Chattoraj *et al*. 1996; Lossau *et al*. 1996; Patterson *et al*. 1997; Kummer *et al*. 1998; Striker *et al*. 1999), including an extensive study of pH-dependent photophysics (Haupts *et al*., 1998).

Maturation of the wild-type fluorophore is quite efficient at 28 ºC, but increasing the temperature to 37 ºC substantially reduces overall maturation and results in decreased fluorescence. In order to adapt FPs for use in mammalian

systems, a basic modification was undertaken and is now found in the most popular varieties of FPs derived from *Aequorea Victoria*. Mutation of the phenylalanine residue at position 64 (Phe64) to leucine results in improved maturation of fluorescence at 37ºC, which is at least equivalent to that observed at 28 ºC (Tsien 1998).

Mutagenesis efforts in the original *Aequorea victoria* jellyfish GFP have resulted in new FPs that range in color from blue (EBFP, ECFP, etc.) to yellow (EYFP, Citrine, Venus, etc.), and are some of the most widely used *in vivo* reporter molecules in biological research. Longer wavelength fluorescent proteins, emitting in the orange and red spectral regions have been developed from the marine anemone, *Discosoma striata*, and reef corals belonging to the class *Anthozoa*.

Red-emitting fluorescent proteins (RFPs) were first described in the late 1990s. The first of the commercially available RFPs, called DsRed, was cloned from the mushroom anemone *Discosoma striata*. When it is expressed in mammalian cells, DsRed is an obligate tetramer that requires nearly 20 h to fully mature (Baird *et al.* 2000). In addition, there is a tendency for DsRed to form oligomers, and this can lead to the aberrant behavior of the proteins that are fused to DsRed.

A few of the problems with DsRed fluorescent proteins have been overcome through mutagenesis. In 2004, a report of Shaner described a series of red-shifted proteins obtained by mutating DsRed (Shaner *et al.* 2004). These proteins, termed mCherry, mRaspberry, mPlum, and mTomato exhibited emission maxima as high as 649 nm.

mCherry is one of the most promising monomeric proteins derived from DsRed. It offers fast maturation, large absorption cross-section and high photostability. It was already reported as a good FRET acceptor for EGFP (Tramier *et al.* 2006). mCherry has an excitation maximum at 587 nm, emission maximum at 610 nm, molar extinction coefficient of 72.000 $M^{-1}cm^{-1}$ and a quantum yield of 0.22.

3.4.3 Two-photon excitation of fluorescent proteins

FPs are suitable for TPE microscopy, technique that has the advantages of reduced out-of-focus photobleaching, less autofluorescence, deeper tissue penetration and intrinsically high three-dimensional resolution. Drobizhev *et al*. have presented a systematic characterization of the TPE properties of 48 fluorescent proteins, combining published and new data (Drobizhev *et al.* 2011).

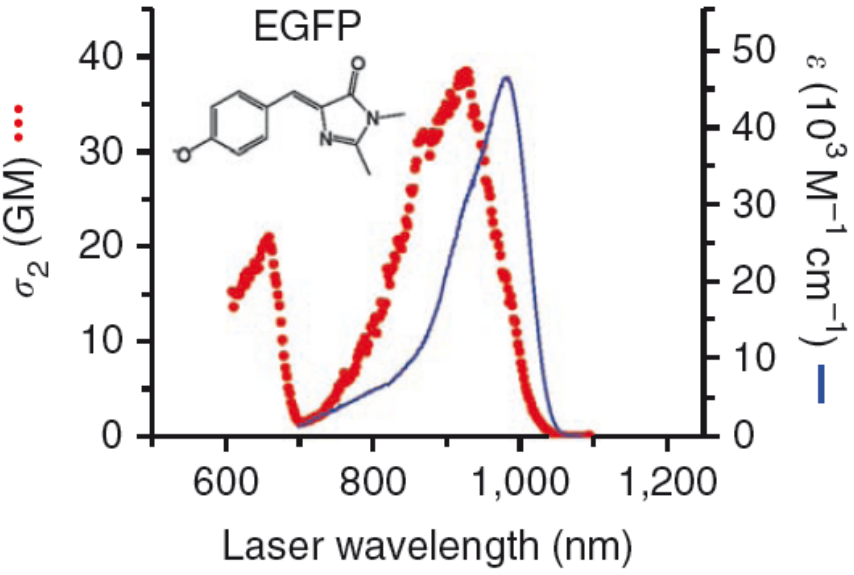

Figure 3.18. OPE and TPE absorption spectra of EGFP. Two-photon absorption spectra (σ_2) are presented versus laser wavelength, used for excitation. Two-photon absorption cross-section, σ_2, (measured in Goeppert-Mayer units, 1 GM = 10^{-50} cm^4 s) characterizes the probability of the simultaneous absorption of two photons whose energies add up to match the molecular transition energy. For the purpose of comparison, in one-photon absorption spectra (ε) the actual excitation wavelength is multiplied by a factor of two *(from Drobizhev et al. 2011).*

Figure 3.18 represents the one- and two-photon absorption spectra of EGFP. Two-photon absorption spectrum was collected in a broader range (550–1400 nm). The power dependence of the fluorescence signal was quadratic for all data presented, assuring that the spectra represent pure two-photon absorption. EGFP has a two-photon maximum excitation peak at 927 nm, with a two-photon cross-section σ = 39 GM (Drobizhev *et al.* 2011), which decreases to 23 ± 1 GM at 850 nm, with an excitation efficiency ~65% (Herz *et al.* 2010). Photobleaching is ~2 times higher for 850nm comparing with 920nm excitation (Herz *et al.* 2010).

4 MATERIALS AND METHODS

4.1 Reagents

Inorganic salts, acids, bases and organic reagents were provided by Merck, Panreac, Sigma-Aldrich and Fluka. Culture medium components were from Conda-Pronadisa.

Other reagents used: β-mercaptoethanol and glucose (Merck); uridine (Alfa-Aesar); aminoacids, protease inhibitor cocktail (aprotinine, leupeptine, bebstatine, pepstatine, antipain), PMSF and agarose low melting point (Sigma); and sordarin sodium salt from Sigma-Aldrich.

Glass beads were from Thomas Scientific and microscope cover glasses 1.5# (24x32 mm and 20x20 mm) were from Marienfeld (Germany).

4.2 Control fluorophores

A solution 48 nM of Fluorescein in 0.1M NaOH (τ = 3.96 ns) was used to test the instrument alignment, the detected OPE and TPE volume element, and the G factor for fluorescence anisotropy determinations. λ_{exc}= 482nm (OPE) or 780 nm (TPE); λ_{em} = FF01-520/35 (Semrock, Germany) .

A solution 4μM Erythrosine B in deionized water, quenched by 5.4 M KI (τ = 9 ps), was used to determine the instrumental response function, IRF. λ_{exc}= 482nm (OPE) or 780 nm (TPE); λ_{em} = FF01-562/40 (Semrock, Germany) .

Calibration of the detection volume element in OPE and TPE setups: TetraSpeck fluorescent microspheres (100 nm; T7279, Life Technologies, CA), labelled with a mixture of four different dyes showing for separate excitation/emission peaks: 350/440 nm (blue); 505/515 nm (green); 575/585 nm (orange), and 655/685 nm (dark red). Beads stock suspensions were sonicated and diluted in MilliQ water. Sets of 5 μl of the diluted suspension were applied to the surface of a clean coverslip, and spread with the pipet tip. We waited the droplet to dry, we covered with another coverslip, and we sealed the "sandwich coverslip" with nail polish.

Control solutions were prepared fresh every day from stocks samples, and measured before to start cell experiments.

4.3 Purified control proteins

Escherichia coli-expressed and affinity-purified (~98% pure) Enhanced Green Fluorescence protein (EGFP), and the β-trefoil lectin domain of the pore forming toxin LSL_a from the mushroom *Laetiporus sulphureus* LSL_{150} EGFP tagged, (LSLt-EGFP; López-Gallego *et al.* 2012) were a gift from Dr. Mancheño laboratory (IQFR-CSIC).

Protein solutions 500 μM in Tris HCl buffer at pH 8 were used to calibrate the OPE and TPE time-resolved micro-spectrometer used in this work.

4.4 Fusion green fluorescent protein for ribosome stalk dynamics study

This study was realized in collaboration with Dr. Juan Pedro Garcia Ballesta (Centro de Biologia Molecular Severo Ochoa, CSIC-UAM), who provided us the *S. cerevisiae* strains used in this work. We have used yeast cells expressing ribosome stalk proteins tagged with the fluorescent protein GFP. These constructions were carried out with a synthetic GFP gene with optimal codons for translation in yeast cells, as well as two chromophore mutations for increase GFP f1uorescence (Cormack *et al.* 1997). This yeast enhanced GFP, yEGFP3 (yEGFP in this work), was evaluated as an efficient reporter of gene expression in *S. cerevisiae* as well as *C. albicans* (Cormack *et al*. 1997).

Although there were other genes encoding EGFP with better spectroscopic characteristics, we have selected yEGFP for P0, P1α and P2β EGFP constructions because it was used previously to study the structure and composition of the ribosome stalk of *S. cerevisiae* with two-photon spectroscopy techniques, such us fluorescence correlation spectroscopy (FCS) and scanning FCS (García-Marcos *et al.* 2008).

4.4.1 *S. cerevisiae* strains and growth conditions

All *S. cerevisiae* strains were derived from the proteinase deficient strain BJ5458 (Martínez *et al.* 1999), which had a reduced autofluorescence. The fundamental clone characteristics were described in García-Marcos *et al.* (2008).

Table 4.1 describes the *S. cerevisiae* strains uses in this study. P0, P1α, P2β

strains expressed the main ribosome stalk proteins, object of this study, with yEGFP bound to the CTD.

Table 4.1. *S. cerevisiae* strains expressing yEGFP-tagged ribosomal stalk proteins

Strain	Native protein missing	Expressed EGFP tagged protein	Nutritional requirements
WT	-------	-------	Trp, Lys, Leu, Ura
P0	P0	P0-yEGFP	Trp, Lys, Ura
P1α	P1α	P1α-yEGFP	Lys, Leu, Ura
P2β	P2β	P2β-yEGFP	Trp, Lys, Leu
L25	L25	L25-EGFP	Trp, Lys, Leu, Ura
EGFP	-------	yEGFP	Trp, Lys, Leu

Other strains used as controls in this work were:

- L25 strain expressed the 60S subunit ribosomal protein L25 with EGFP bound to the CTD without linker, as a control of hindered motion.
- EGFP strain expressed yEGFP fluorescent protein free in the cytoplasm of the cells, as a control of free motion.
- WT strain is the wild-type strain, without yEGFP, as a control of autofluorescence.

Growth conditions

Cells were grown in sterile conditions in minimal YNB medium (0.67% yeast nitrogen base), supplemented with the essential aminoacids indicated in nutritional requirements (50 μg/ml). L25 strain was grown in rich YEP medium (2% bactopeptone, 1% yeast extracts). Both media were supplemented with 2% glucose (YEPD, YNBD). Cells were grown at 30ºC with orbital shaking (200 rpm) until exponential phase (OD_{600} ~0.4-0.8). For fluorescence experiments, cells were pelleted and resuspended in freshly YNBD containing the nutritional

requirements of the strains, in order to reduce the background of the fluorescence measurements.

4.4.2 Preparation of subcellular fractions

Yeast cellular extracts

Yeast cells were grown as previously described. Cells in exponential phase were collected by centrifugation at 5000 rpm for 10 min at 4°C. The pellet was washed with mQ H_2O and buffer 1: 10 mM Tris-HCl, pH 7.4, 20 mM $MgCl_2$, and 5 mM β-mercaptoethanol. Finally, the cell pellet was resuspended in buffer 1 containing a protease inhibitor cocktail (aprotinine, leupeptine, bebstatine, pepstatine, antipain and PMSF, 10 µg/ml of each one). One volume of glass beads was added to break the cells by serious shaking for 40 sec. in a Savant Fast prep FP120 (Bio101) at 4°C. The supernatant fraction (cellular extract) was collected by centrifugation at 13,000 rpm for 20 min. in a Beckman high speed centrifuge.

Yeast pure ribosomes

Free ribosomes were separated from the cellular extract by centrifugation at 4°C in a TL100.2 rotor for 90 min. at 90.000 rpm. The pellet (crude ribosomes) was resuspended in buffer 2 (20 mM Tris-HCl, pH 7.4, 500 mM NH_4Ac, 100 mM $MgCl_2$, 5 mM β-mercaptoethanol) and then centrifuged through a discontinuous sucrose gradient (20% - 40% sucrose in buffer 2) at 90.000 rpm for 2 hours at 4°C in a rotor of TL1002. The final pellet (pure ribosomes) was washed and resuspended in buffer 1. Ribosome concentration was quantified from the absorbance at 260 nm, assuming that 14 OD_{260} units correspond to a ribosome concentration of 1 mg/ml.

4.4.3 Inhibition of protein synthesis with sordarin.

Yeast cells were grown as previously described. Cells in exponential phase were pelleted and resuspended in freshly YNBD containing 30 µg/ml of sordarin (stock solution 1mg/ml in water). Cells were incubated 30 min. at 30ºC before measurements.

4.5 Fusion EGFP and mCherry proteins for P0 nuclear assembly FRET study

The study on pre-ribosomal stalk protein assembly was done in collaboration with the group of Dr. Juan Pedro Garcia Ballesta (CBM. CSIC-UAM). All the strains used in this work were developed from his laboratory: the fundamental clone characteristics were described in Francisco-Velilla *et al.* 2013b.

As in the case of the rotational dynamics of ribosomal stalk proteins study, the *S. cerevisiae* strains used for the experiments were derived from the proteinase deficient strain BJ5458 (Martínez *et al.* 1999), which had a reduced autofluorescence. Table 4.2 shows the *S. cerevisiae* strains used in this application.

Table 4.2. *S. cerevisiae* strains used for FRET measurements

Strain	Native protein missing	Expressed fusion proteins	Nutritional requirements
P0-yEGFP	P0	P0-yEGFP	Trp, Lys, Ura
P0-yEGFP+ Nop7mCherry	P0, Nop7	P0-yEGFP + Nop7-mCherry	Trp, Lys
P0-yEGFP+ Mrt4-mCherry	P0, Mrt4	P0-yEGFP + Mrt4-mCherry	Trp, Lys
Mrt4-yEGFP	Mrt4	Mrt4-yEGFP	Trp, Lys, Leu, Ura
Nop7-EGFP	Nop7	Nop7-EGFP	Trp, Lys, Leu, Ura
Nop7-EGFP+ P0mCherry	Nop7, P0	Nop7-EGFP + P0-mCherry	Trp, Lys, Leu, Ura
Nop7-EGFP+ Mrt4-mCherry	Nop7, Mrt4	Nop7-EGFP + Mrt4-mCherry	Trp, Lys, Leu, Ura
Nop7-EGFP+ P2β-mCherry	Nop7, P2β	Nop7-EGFP + P2β-mCherry	Trp, Lys, Leu, Ura
WT	-------	-------	Trp, Lys, Leu, Ura

Growth conditions

Cells were grown in sterile conditions in YEP medium (2% bactopeptone, 1% yeast extracts) or in minimal YNB medium (0.67% yeast nitrogen base) supplemented with 50 µg/ml of the essential aminoacids indicated in nutritional requirements (Table 4.2). Both media were supplemented with 2% glucose (YEPD, YNBD). Cells were grown at 30ºC with orbital shaking (200 rpm) until exponential phase (OD_{600} ~0.4-0.8). For fluorescence experiments, cells were pelleted and resuspended in freshly YNBD containing the nutritional requirements of the strains, in order to reduce the background of the fluorescence measurements.

4.6 Immobilizing yeast cells for micro-spectroscopy studies

The cellular immobilization procedure is essential to avoid cell displacements during spectroscopic measurements in the microscope.

First we change cell rich media to minimal media with 2% glucose, to minimize the fluorescence background: 500µl of yeast cells (pre-exponential phase OD_{600} ~ 0.4–0.8) were collected and centrifuged at 5000 rpm for 10 minutes at room temperature. Pellets were collected and re-suspended in 100µl of the corresponding fresh minimal media (YNBD containing the nutritional requirements of the strains).

We have immobilized the *S. cerevisiae* cells by pressing a small volume of cells between two coverslips. The first trial was to mix 10 µl of cells in minimal media with 10 µl of melted 2% low gelling temperature agarose (Sigma Type VII) in the same medium, and deposited in a microscope slide and pressed with a cover slip. To prevent media from evaporation, cover borders were sealed with nail polish to get a "cover slip sandwich", without air gaps.

This type of preparation was used for long time measurements. For short time experiments, during ~1 hour after sandwich preparation, we prepared the cover slip sandwiches mixing 10 µl of cells with 10 µl of fresh minimal media, just before each experiment (Figure 4.1).

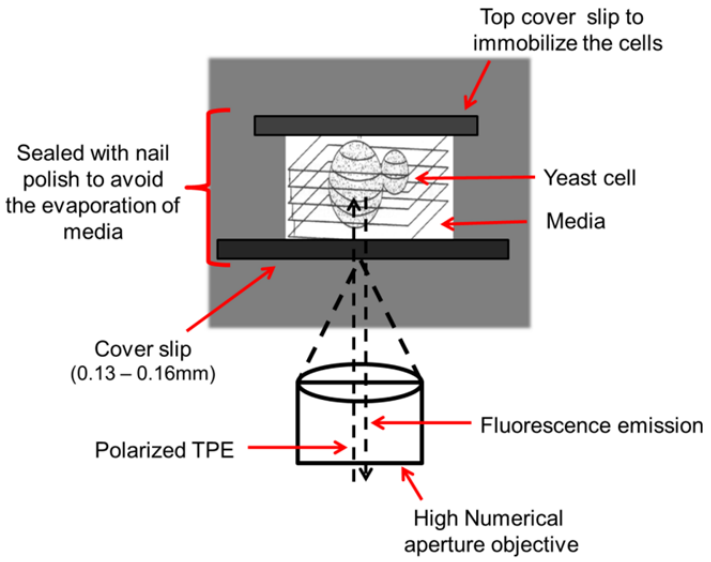

Figure 4.1. Schematic representation of live yeast cell preparations for micro-spectroscopy determinations. The sandwich cover slip helps reducing cellular displacements during measurements, keeping cells wet and alive in the corresponding culture media.
Polarized TPE light pass through the high numerical aperture objective (60x w, 1.2NA).
Collinear optical condition: the excitation and emission photons have the same path.
Z scan allows extracting different optical sectioned images of the sample.

Special care must be taken while pressing the slides to avoid spill over of cells due to pressure; we have used tissue paper to wet the media. While mixing with pipette, vigorous mixing may lead to air bubble formation in the slide, hence, gentle mixing is advisable.

4.7 Data acquisition and analysis

The data acquisition methodology will differ between various measurements. This chapter describes in detail live cell anisotropy and FRET measurements strategies using the OPE cuvette system, and the OPE and TPE time-resolved polarization microscope optimized in this work.

4.7.1 Time-resolved total fluorescence and fluorescence anisotropy cuvette measurements

Time-resolved fluorescence intensity and fluorescence anisotropy measurements were performed by the time-correlated single-photon counting (TCSPC) technique using the laser spectrometer with picosecond diode laser

excitation described previously (Lillo *et al*. 2002).

Fluorophore solutions were excited by means of vertically polarized light pulses from Pico Quant 482 nm picosecond diode laser beam at 5 MHz, with a time resolution of 6.1ps/channel. The fluorescence collected in the horizontal plane, at 90° to the excitation beam, was focused on a monochromator (f = 100 mm, 8 nm bandwidth) through a cutoff filter to minimize the scattering of the fluorescence signal, a Polaroid HNP'B film polarizer, and finally detected with a R1564U-06 microchannel plate (Hamamatsu). The system was optimized for fluorescence ultra-microcuvettes 105.251-QS 3x3 mm, 45 µl (Hellma, Germany).

The decay of the total fluorescence intensity, $I(t) = I_m(t)$, was recorded with the emission polarizer set at the magic angle (m = 54.7°) relative to the vertically polarized excitation beam. The two components of the fluorescence, polarized parallel $I_{VV}(t) = I_{par}(t)$ and perpendicular $I_{VH}(t) = I_{per}(t)$ to the plane of polarization of the excitation beam, were recorded sequentially by alternating the orientation of the emission polarizer every 5 min. The instrument response function (IRF) was acquired at the excitation wavelength using a colloidal silica suspension (LUDOX on mQ H_2O). An adequate blank was measured from each sample.

4.7.2 Time-resolved anisotropy and fluorescence lifetime imaging (FLIM) in live cells using OPE and TPE photon microscopy

Time-resolved fluorescence intensity and fluorescence anisotropy measurements were carried out in live yeast cells expressing P0, P1α, P2β, L25, Mrt4 and Nop7 proteins tagged with the fluorescent proteins yEGFP, EGFP and mCherry in cytoplasm and nucleus of live yeast cells by the TCSPC technique, using a modified Microtime 200 system (PicoQuant, Germany) (see Results). We have implemented both, one photon and two photon excitation options:

Setup for OPE: Horizontal polarized excitation from a 482 nm picosecond diode laser beam set up at 5 MHz (PicoQuant, Germany).

Setup for TPE: Horizontal polarized excitation in the Y-axial direction, from a femtosecond-pulsed Mai-Tai laser (750-850 nm) at 80.6 MHz, propagates along the Z axis and then is condensed to a diffraction-limited spot by the objective lens. The excitation power (0.5–1 mW) at the sample was adjusted

using a variable optical attenuator LS-107AT (Lasing, SA Spain) to achieve rates of counting less than 10^6 photons/s.

The coordinate system XYZ was defined with respect to the microscope, where Z is the optical axis and XY is the imaging plane. The emission path of the time-resolved micro-spectrometer was common for OPE and TPE: band pass filters FF01-520/35 (Semrock, Germany) located in front of each detector. Measurements were performed at room temperature (T = 22ºC).

Fluorescence lifetime image XY scans (FLIM-XY) of FPs-tagged proteins expressed in yeast cells were recorded at different Z values, to optimize the optimal Z for each yeast cell study. Fast FLIM X-Y scans were recorded with an acquisition time per pixel of 1.2ms, with an apparent resolution of 0.05µm/pixel. The overall acquisition time was of 60–180s, depending on the image size.

From FLIM images of entire cells, single XY locations corresponding to different regions in the cytoplasm or the nucleus, were randomly selected for the acquisition of single-point total fluorescence intensity $I_{total}(t)$. For anisotropy determinations, the two components of the fluorescence, polarized parallel, $I_{HH}(t) \approx I_{par}(t)$, and perpendicular $I_{HV}(t) \approx I_{per}(t)$ to the plane of polarization of the excitation beam were acquired simultaneously (30s total time per decay curve) using a broad band (450–700 nm) polarizing beam splitter cube (Ealing optics) and two band pass filters FF01-520/35 (Semrock, Germany) in front of each detector.

Acquisitions times greater than 30 seconds per point lead to photobleaching of the fluorophore EGFP in the detected volume. We have collected data from 10 to 20 cells for each cover slip preparation, and no more than two points per cell, with a maximum observation time of 1 hour per preparation.

For the samples used in this work, the number of photons per pixel we were able to accumulate in the FLIM and polarized images was very low, which resulted in very noisy decays for single pixels. We have combined single point time resolved measurements with fluorescence decays from N pixels corresponding to a region of interest (ROI) in specific subcellular locations of single cells expressing the FPs-tagged proteins, like the cytoplasm or the nucleus.

TCSPC total fluorescence intensity histograms (0.004ns/channel) were built summing fluorescence photons from specific ROIs using SymphoTime software (PicoQuant, Germany).

4.7.3 Single point and ROI time-resolved fluorescence data analysis: Iterative reconvolution

Total fluorescence and anisotropy decays from cuvette measurements

The fluorescence lifetimes were determined from the total intensity decay at the magic angle, $I_m(t)$ by iterative reconvolution analysis, using non-linear least-squares global methods. For multi-exponential total intensity decays, the amplitude-weighted lifetime $<\tau>_1$ was calculated as $\sum a_i \cdot \tau_i$, in which a_i represent the normalized amplitudes.

The fluorescence anisotropy decay, $r(t)$, was determined by simultaneous analysis of the $I_{VV}(t)$ and $I_{VH}(t)$ emission intensity components, assuming a mono exponential function with a correlation time ϕ, corresponding to the global protein motion.

We have used the Global analysis program from Globals Unlimited (from the Laboratory for Fluorescence Dynamics, LFD. Irvine, CA) (Beechem *et al*. 1991, Beechem 1992).

Total fluorescence and anisotropy decays from ROIs and single point OPE and TPE microscope measurements

Total fluorescence decays were fitted to multiexponential functions by iterative reconvolution analysis with a single IRF (OPE) or periodical IRF (TPE), using non-linear least squares global methods from Globals Unlimited (LFD. Irvine, CA) (Beechem *et al*. 1991, Beechem 1992) general purpose program.

Fluorescence anisotropy decays, $r(t)$, were determined by simultaneously analysis of the parallel $I_{HH}(t)$ and perpendicular $I_{HV}(t)$ polarized components using the same routines. The first approximation analysis consisted of finding the $r(t)$ parameters, time zero anisotropy, $r(0)$, and rotational correlation time, ϕ, that best fit the two experimental polarized decay functions $I_{HH}(t)$ and $I_{HV}(t)$

$$i_{par}(t) = \frac{i_{total}(t)}{3} \cdot [1 - r(t)] \quad [4.1]$$

$$i_{per}(t) = \frac{i_{total}(t)}{3} [1 + 2 \cdot r(t)] \quad [4.2]$$

$$i_{total}(t) = \sum a_i \cdot e^{-t/\tau_i} \quad [4.3]$$

$$r(t) = r(0) \cdot e^{-t/\phi} \quad [4.4]$$

$$I_{HH}(t) \approx i_{par}(t) \otimes IRF + blank \quad [4.5]$$

$$G \cdot I_{HV}(t) \approx i_{per}(t) \otimes IRF + blank \quad [4.6]$$

In cell studies, to minimize the number of fitting parameters, we fixed the lifetimes determined independently from $I_{total}(t)$. G factor was determined every day from the global analysis of $I_{HH}(t)$ and $I_{HV}(t)$ from a 48 nM fluorescein solution. G values were in the range of 1 to 1.18 for our microscope conditions.

The IRF and the blank were an important issue in TPE experiments, especially for samples showing long lifetimes and/or rotational correlation times. The time window in TPE was fixed to 12.2 ns (laser frequency 82 MHz), therefore we only measured the first part of the decay, which also contains photons from the previous pulse. The autofluorescence was very low in the experimental conditions used in this work, so we estimated the background (blank) from the calculated dark counts of the detectors for 30 s time acquisition.

A limitation of this approach is that our detectors doesn't present exactly the same dark count level and Globals program assumes the same blank value for $I_{HH}(t)$ and $I_{HV}(t)$ functions.

For OPE, we were able to extend the time window up to 200 ns (laser frequency 5 MHz), and the exact background was estimated from the experimental $I_{HH}(t)$ and $I_{HV}(t)$ functions. Then, the blank value was subtracted manually and also, the proper weight for $I_{HH}(t)$ and $I_{HV}(t)$ background corrected curves was introduced in Globals program. This method provides more precise rotational correlation time values for specific subcellular regions, taking properly in account the contribution of the background in the fluorescence anisotropy decay.

4.7.4 FRET-ROI measurements for P0 nuclear assembly study in living cells

Multi-photon fluorescence-lifetime imaging (2P-FLIM) and FRET measurements were carried out in live yeast cells expressing P0, Mrt4 and Nop7 proteins tagged with EGFP (donor) and mCherry (acceptor).

For each sample, fluorescence images in the donor and acceptor regions were acquired simultaneously with two single-photon avalanche diodes through a dichroic beam splitter FF560-Di01 and two band pass filters FF01-520/35 and FF01 685/40 nm (Semrock, Germany).

Although the cells were immobilized in the coverslip sandwich, one limitation in our measurements was the natural motion of the nucleus during image acquisition. To minimize this effect, we acquired four consecutive images for each cells, at the optimal Z position, with a time interval of 0.8-1 min between images, and we discarded the very blurred or low counts images.

Total fluorescence intensity decays, *I(t)*, of EGFP- and m-Cherry tagged protein complexes were built from the photons from ROIs corresponding to the whole nucleus of single cells, and analysed to a multi-exponential function, as described in 4.7.3 section. Decays with less than 30,000 total counts were not included in the FRET-ROI analysis.

Lifetime values were presented as mean of N cell nucleus ± 1 standard deviation. Differences between donor-only and donor-acceptor values were assessed by independent two-sample t-test. Origin 8.5 software was used.

4.7.5 FLIM-FRET phasor approach for P0 nuclear assembly study in living cells

FLIM-FRET phasor data was processed using the SimFCS software developed at the Laboratory of Fluorescence Dynamics (Univ. California, Irvine)

How phasor approach works

Figures 4.2 and 4.3 are presented as examples for the use of the phasor approach. Figure 4.2 (left) shows the fluorescence intensity image of a yeast cell expressing the nuclear protein Nop7 tagged with EGFP. The color code indicates

very low counts in the cytoplasm (Dark blue color), corresponding to cell autofluorescence and high number of counts in a region inside the nucleus, probably corresponding to the nucleolus (Red color). Each pixel in the image has associated one point in the phasor plot (right).

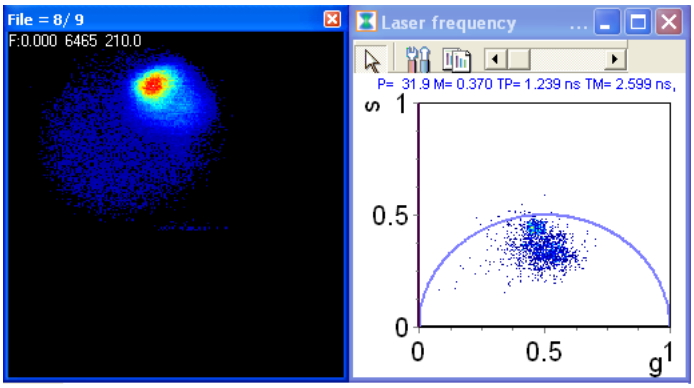

Figure 4.2. Phasor approach. Example I. Left: fluorescence intensity image of a *S. cerevisiae* yeast cell expressing the nuclear protein Nop7 tagged with EGFP. Right: phasor plot associated to this image.

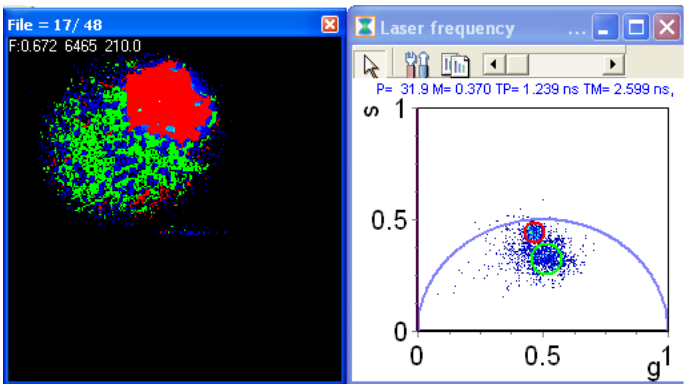

Figure 4.3. Phasor approach. Example II. Left: fluorescence intensity image of the cell shown in Figure 4.2 showing in red and green the pixels of the image with phasors located inside the red and green cursors in the phasor plot. Right: Two phasor clusters selected in phasor plot from Figure 4.2 with cursors red and green.

In Figure 4.3 we have inserted manually two cursors of different size and color to highlight different phasor clusters corresponding to different cell regions in the intensity image (right): *i)* red cursor for the nucleus labelled with Nop7-EGFP, and *ii)* green cursor for the cytoplasm auto-fluorescence. Each pixel in the intensity image now is colored according to the cursor color where the phasor is included in the phasor plot (left).

Measuring FRET efficiency in the presence of donor-only proteins

If the total intensity of the donor-only protein is mono-exponential (τ_D), and all the donor molecules are interacting with acceptor proteins with a constant donor-acceptor distance, r, the position of the phasor for the donor-acceptor sample, with lifetime τ_{DA}, moves to the right along the universal circle, depending on the FRET efficiency:

$$\tau_{DA} = \tau_D \cdot (1 - E) \qquad [4.7]$$

If the donor-only protein has a multi-exponential decay, the realizations of all possible phasors that are quenched with different efficiencies describe a curved trajectory in the phasor plot that ends in the autofluorescence phasor cluster. Then, the experimental position of the phasor of a given pixel along the trajectory determines the amount of quenching and therefore the FRET efficiency (Figure 4.4).

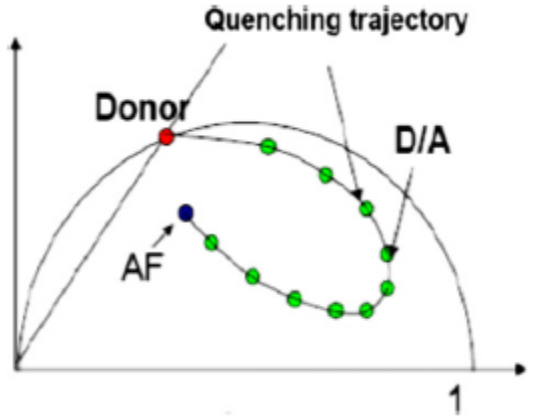

Figure 4.4. Representation of a FRET trajectory in the phasor plot. As the donor is quenched via FRET, the trajectory of the donor-acceptor phasor moves towards the autofluorescence phasor, describing a curved trajectory in the phasor plot. **AF:** Autofluorescence phasor **D/A**: donor-acceptor phasor.

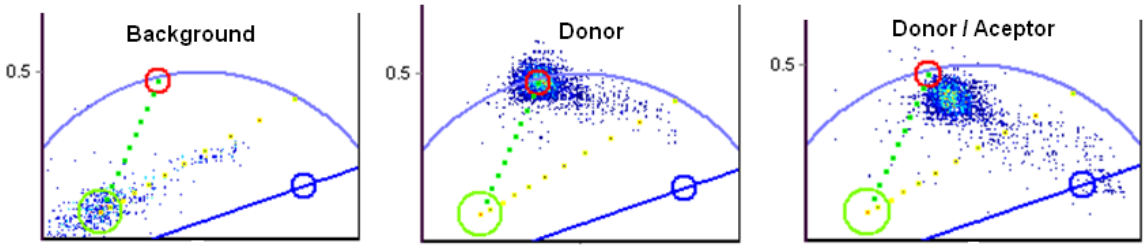

Figure 4.5. Positioning cursors for FRET efficiency calculation in the phasor plot. Left: phasors corresponding to an autofluorescence image (green cursor). Center: phasors corresponding to a donor-only image (red cursor). Right: phasors obtained from a donor-acceptor image, indicating the presence of FRET

Most of the cases present two populations: an interacting fraction, corresponding to donor molecules quenched by FRET and a non-interacting fraction in which the donor lifetime remains unchanged (unquenched donor). For proper FRET efficiency calculation in the phasor approach, it would be necessary to know: *i)* the position of the donor-only or donor unquenched phasor, determined from an independent preparation in which the acceptor is absent (Figure 4.5, center, red cursor), and *ii)* the background or autofluorescence

phasor, determined from an unlabelled preparation or from a cell unlabelled region in the donor only sample (Figure 4.5, left, green cursor). The green dotted line represents 0% FRET efficiency, and all phasor points in this line are representative of a decrease in donor lifetime due to background contribution. Phasor points in the right side of this line are indicative of FRET. The yellow dotted line marks 50% FRET efficiency.

The contributions of the background and the donor unquenched were evaluated independently, and introduced in the FRET calculator of SimFCS program which uses the rule of the linear combination with the background phasor and the donor unquenched (Figure 4.6).

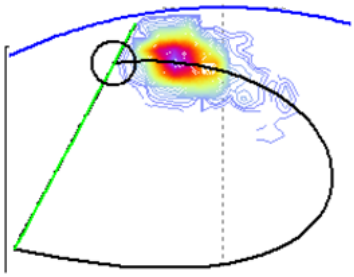

Figure 4.6. FRET trajectory in the phasor plot. Green line represents 0% FRET efficiency. Black line represents FRET trajectory crossing through donor/acceptor phasor points.

The operator moves the cursor along the curved trajectory to the point where there is a cluster of phasors in the donor/acceptor image, and estimates the FRET efficiency. Using the reciprocal property of the cursor, the pixels in the image corresponding to a given FRET efficiency are highlighted.

5 RESULTS AND DISCUSSION

5.1 Two-photon and One-photon time-resolved micro-spectrometer setup

The laser fluorescence micro-spectrometer (ME) used in this work is essentially a set of instruments clustered around an inverted fluorescence microscope IX71 (Olympus, Japan), using mono- (OPE) or multi-photon (TPE) excitation. The core of the instrument is the MicroTime 200 system from PicoQuant (Germany). It contains the complete confocal optics and electronics for recording virtually all aspects of the fluorescence dynamics of microscopic samples or femtoliter volumes.

Data acquisition and data analysis methodologies, using OPE and TPE with horizontal and vertical polarized excitation were developed in our laboratory, and optimized to measure steady-state and time-resolved fluorescence polarization decays in living cells, with high spatial resolution.

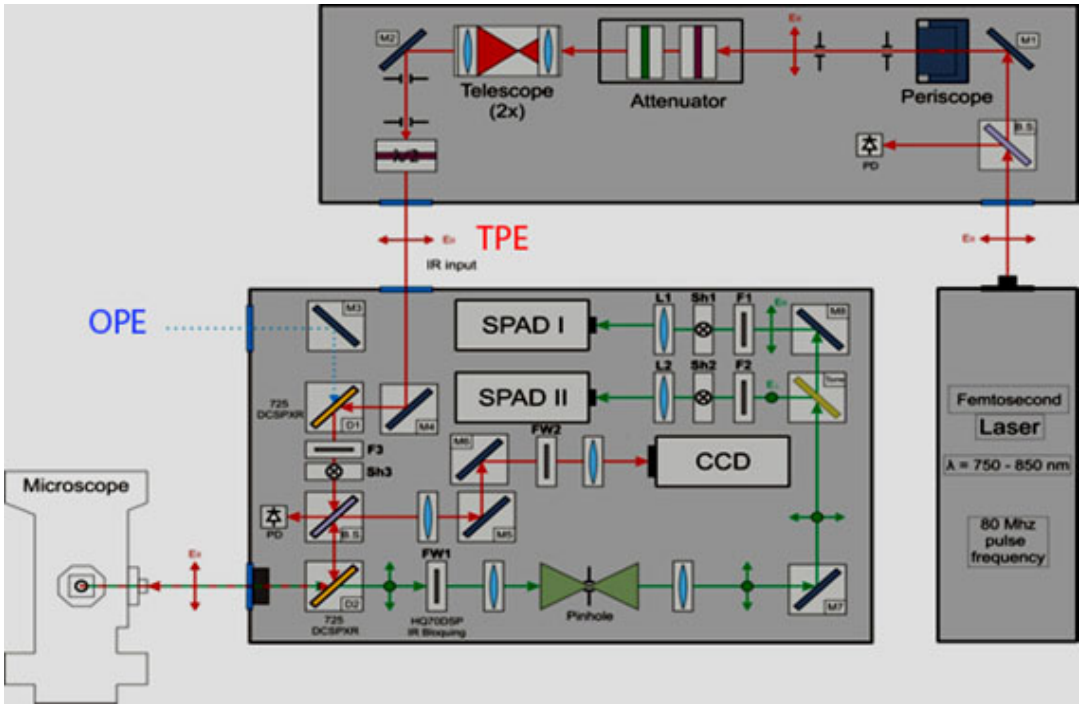

Figure 5.1. Optical layout of OPE and TPE time-resolved micro-spectrometer.
This setup contains four basic blocks:

1. Excitation
   - One-photon excitation (OPE) from laser coupling unit (LCU), connected to the Main Optical Unit (MOU) through a single mode fibre cable
   - Two-photon excitation (TPE) from fs Ti:Za MaiTai laser
2. Main Optical Unit (MOU) box contains filters, beam splitters and two SPAD detectors.
3. IX71 Olympus inverted microscope.
4. Data acquisition and control electronics (not shown)

The basic architecture of the microscope system is shown in Figure 5.1. It is composed of four main parts: *i)* OPE and TPE excitation channels, *ii)* Olympus IX71 inverted microscope, *iii)* the main optical unit (MOU), containing major optical excitation an emission elements, with two Single Photon Avalanche Diode (SPAD) detectors, and *iv)* data acquisition and control electronics. The short description of equipment parameters are described below.

5.1.1 Instrumental setup

One-photon excitation (OPE)

LDH-P-C-405B and LDH-P-C-485 picosecond laser diode heads working at 405 and 482 nm respectively, with 50-100 ps (FWHM) pulses, and a variable repetition rate up to 40 MHz. They are integrated in the laser combining unit (LCU, PicoQuant), and connected to the MicroTime 200 system through a single mode fibre cable, polarization maintaining (cut off < 375 nm). One photon excitation is always horizontal polarized (Y direction in the X-Y microscope plane). The excitation power is adjusted using with the PDL 828- Sepia II Diode laser driver unit (PicoQuant), to achieve rates of counting less than 10^6 photons/s.

Two-photon excitation (TPE)

Mode locked femtosecond-pulsed Ti:Sapphire laser (MaiTai, Spectra Physics). It provides ~100 fs horizontal polarized pulses (750-850 nm; 80.6 MHz) entering directly to the MicroTime 200 system, through the free space port. The excitation power (0.5–1 mW) at the sample is adjusted using a variable optical attenuator LS-107AT (Lasing, SA Spain).

With this setup, wavelength excitation changes, from OPE to TPE are relatively simple, because they share the same excitation and emission path inside the Main Optical Unit (MOU). We just need to change laser clean-up and dichroic filters, using pre-aligned exchangeable dichroic mounts.

Olympus IX71 inverted microscope

The objective used in this work was the UPL SAPO 60x Planapochromat, NA 1.2, water immersion, with variable collar correction for 0.15-0.2 mm glass

coverslips and working distance 280 μm. Transmission optimized for 400-900nm.

Images can be scanned in X/Y as well as in X/Z or Y/Z direction using two optical piezo units:

- The manual XY stage of the microscope has adapted a P-733 piezo-nanopositioning stage (Physik Instrumente PI GmbH, Germany), with scanning ranges to 100 x 100 μm in XY and resolution 1 nm.

- The P-721 PIFOC microscope objective Z-nanopositioner (PI GmbH, Germany) is mounted between the turret and the objective. Range up to 100 μm with 1nm resolution

Emission channel

The fluorescence-emitted photon as well as the back-scattered light was guided back to the Main Optical Unit (MOU) using the right side port of the microscope through a movable 100% mirror used to optically couple the microscope objective to the MOU. Fluorescence photons go through appropriate dichroic and laser clean-up filters, the pinhole (variable 30-150 μm for OPE; for TPE we select a 150 μm pinhole to clean possible scatter contamination). Finally, the fluorescence signal is wavelength or polarization selected using a polarizer beam splitter or dichroic filters before to reach the detectors. There are two detectors mounted in the main optical unit. Each detector channel has its dedicated filter holder and a mechanical shutter. The optical unit contains two single-photon counting avalanche diode modules SPCM-AQR-14 (400–1100 nm, with >70% detection efficiency at 630 nm). Typical FWHM values for the instrumental response functions for these detectors are ~450 ps, and the shape varies with the counting rate and the wavelength.

5.1.2 Detected volume element

We use the estimation of the radial waist of the detection volume from the fluorescence autocorrelation function of a solution of Fluorescein 48 nM, as a control of the alignment of the instrument. These measurements are only weakly sensitive to the actual axial dimension of the volume element.

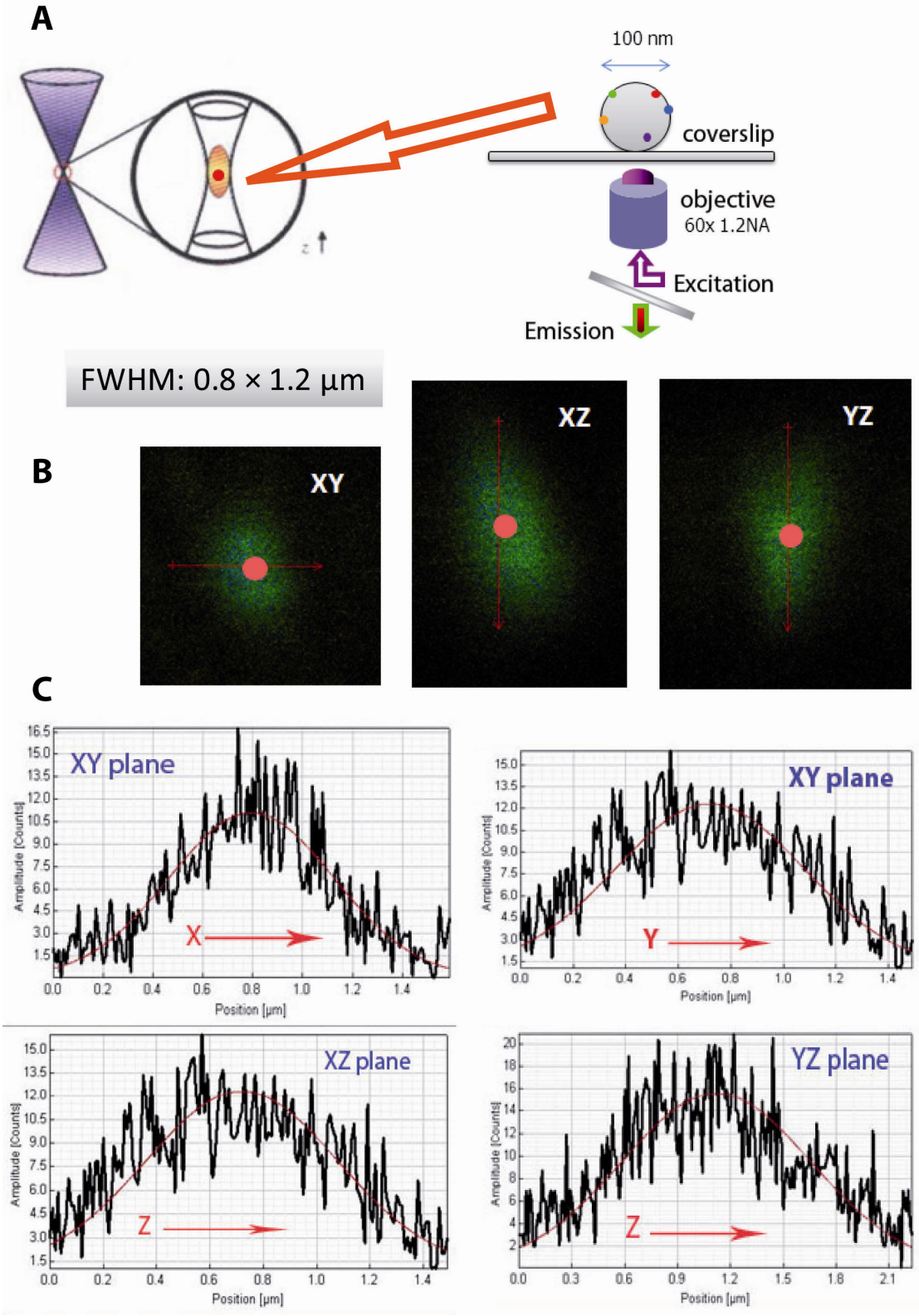

Figure 5.2. Characterization of the effective detection volume element. (A) Cartoon showing, in an approximate way, the relative sizes of the microspheres and the volume element. **(B)** Representative FLIM images corresponding to XY, XZ and YZ sections of a single TetraSpeck fluorescent microsphere. The red dot represents approximately, the real size of the microsphere. **(C)** Intensity distribution of fluorescence detected in X, Y and Z, quantified from the XY, XZ, and YZ TPE sections presented in (B). λ_{exc} = 850 nm, λ_{em} = FF01-685/40 (Semrock, Germany).

,

Then, we have calibrated the detection volume, in OPE and TPE setups, by imaging 100 nm diameter TetraSpeck fluorescent microspheres (Life Technologies, CA), Figure 5.2 shows a representative set of XY, XZ and YZ FLIM images of a single microsphere. These images allowed us to quantitatively characterize the effective detection volume corresponding to each setup. The advantage of these microspheres are: *i)* the size (100 nm) is much smaller than the detection volume, and their images inform very accurately about the size and shape of the effective detection volume element for the different experimental condition; *ii)* the microspheres are labelled with a mixture of four different fluorescence dyes, from blue to dark red spectral regions, covering almost all the spectral excitation/ emission region. The total fluorescence intensity images show nearly Gaussian detection volume elements with dimensions of 0.8×0.8×1.2 μm (FWHM).

5.1.3 Time-Tagged-Time-Resolved TTTR acquisition mode

The instrument contains associated electronics to assign different tags to each detected fluorescence photon in the microscope:

- The emission wavelength and polarization (vertical or horizontal).
- The spatial location (X, Y, Z) of the emitting fluorophore.
- The time increment between the excitation pulse (START) and emission pulse (STOP) from the detector, for TCSPC time-domain time-resolved acquisition, using the TimeHarp 300 card (PicoQuant), with a minimum time resolution of 0.004 ns/channel, and a maximum of 4096 channels.
- The arrival time of the STOP pulse determined from an independent digital clock.

In this way, SymphoTime v5.3.2 acquisition and analysis software (PicoQuant) produces a master file containing all the necessary basic information to virtually apply all algorithms and methods for the analyses of fluorescence dynamics.

For each focal volume element we have reconstructed the integrated intensity corresponding to the steady state signal, the depolarization and decay curves of fluorescence intensity (picosecond-nanoseconds), and the fluctuations in

fluorescence intensity during the acquisition time (seconds).

5.1.4 Picosecond-nanosecond time-resolved fluorescence decays

Time domain TCSPC window

We build the TCSPC histograms for the total fluorescence intensity, *I(t)*, and parallel, $I_{HH}(t)$, and perpendicular, $I_{HV}(t)$, fluorescence polarized functions from the TTTR file, fixing the time-resolution to 0.004 ns/channel (TPE) or 0.004-0.008 ns/channel (OPE) using the SymphoTime software. The calculated decays correspond to: *i)* single point data; *ii)* single pixels; *iii)* pixels from regions of interest ROI of an image, or *iv)* pixels from the whole image.

MaiTai fs laser works at 80.6 MHz, so the maximum time windows in TPE TCSPC experiments will be 12.4 ns, at 0.004 ns/channel. Every 12.4 ns we will have an excitation pulse, and in the case of fluorophores with lifetimes slower than ~2ns, the initial part of the decay is contaminated with fluorescence photons from previous pulse. This results in a large uncertainty in the estimation of the background contribution to the fluorescence decays (see Figure 5.3A, blue arrow).

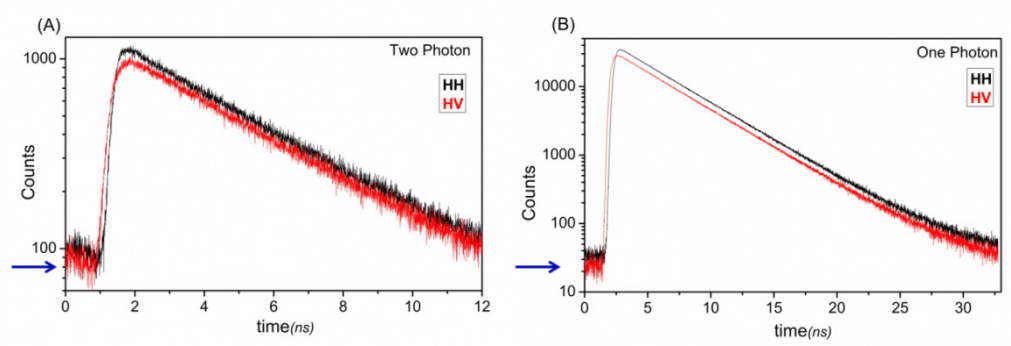

Figure 5.3. Comparison of OPE and TPE parallel $I_{HH}(t)$ and perpendicular $I_{HV}(t)$ polarized fluorescence components. Single point OPE and TPE polarization measurements of a Fluorescein 48 nM solution, τ = 3.98 ns. 60 s total time acquisition. T=22ºC.
(A) TPE, λ_{exc} = 850 nm, λ_{em}= 520/35 nm (FF01-520-35) 0.004 ns/channel. Blue arrow highlights the contamination of the initial part of the decay with fluorescence photons from previous excitation pulse (12 ns earlier).
(B) OPE, λ_{exc} =482 nm, λ_{em}=520/35nm (FF01-520-35) 0.008 ns/channel. Blue arrow highlights the flat behavior of the initial part of the decays, representing the real background counts.

The OPE laser diode heads work at variable frequency up to 40 MHz. For the biological systems studied here, the frequency was set to 5 Mz, which correspond

to a maximum time window of 200 ns, at 0.050 ns/channel, and a minimum time window of 16.4 ns, at 0.004 ns/channel.

In OPE, we can easily estimate the background contribution from the first and last channel region of the decay curves, where the fluorophore decay is finished, and only the uncorrelated counts are accumulated (Figure 5.3 B, blue arrow).

Instrument response function IRF determination

Optimal iterative re-convolution analysis of the fluorescence decays requires determining the IRF function under similar experimental conditions of the experimental decays. The IRF can be estimated from the experimental decay of a sample with infinitely short fluorescence lifetime.

We tried first to use as IRF the temporal profile of the backscattered excitation light, determined from the coverslip scattered light at the focus. But this approach didn't work well for re-convolution analysis, especially for TPE decays. The main reason was that the APD detectors are sensitive to the emission wavelength, λ_{em}. Excitation wavelength were typically much shorter than λ_{em} in OPE, and much longer than λ_{em} in TPE (near-infrared excitation).

In this work we have used a solution of Erythrosine B, EB, quenched with potassium iodide (KI). The lifetime of EB in 5.4 M KI (EB-KI) decreases to 9 ps, with a quantum yield of 0.0035. The relatively high brightness of EB makes this compound attractive to evaluate the IRF of detectors in the wavelength emission region of 540-570 nm (Szabelski *et al*. 2009).

In Figure 5.4 A we present for comparison the re-convolution analysis of a total fluorescence intensity decay of Fluorescein 48 nM assuming a mono-exponential function, using Globals program, with a backscattered IRF (BS, left) and an EB-KI IRF (ER-KI, right), and their respective weighted residuals distributions. The fit using back-scattered IRF failed to satisfactorily resolve the decay. In order to get proper residual distribution in the re-convolution analysis using a BS IRF, it was necessary to introduce an extra short lifetime component with negative pre-exponential in the fitting model (data not shown). In this example, the lifetime of fluorescein was not affected (τ =3.98 ±0.02 ns). But,

decays showing short lifetimes (τ < 1 ns) or multiples lifetimes will not be properly recovered using BS IRFs in the re-convolution analysis.

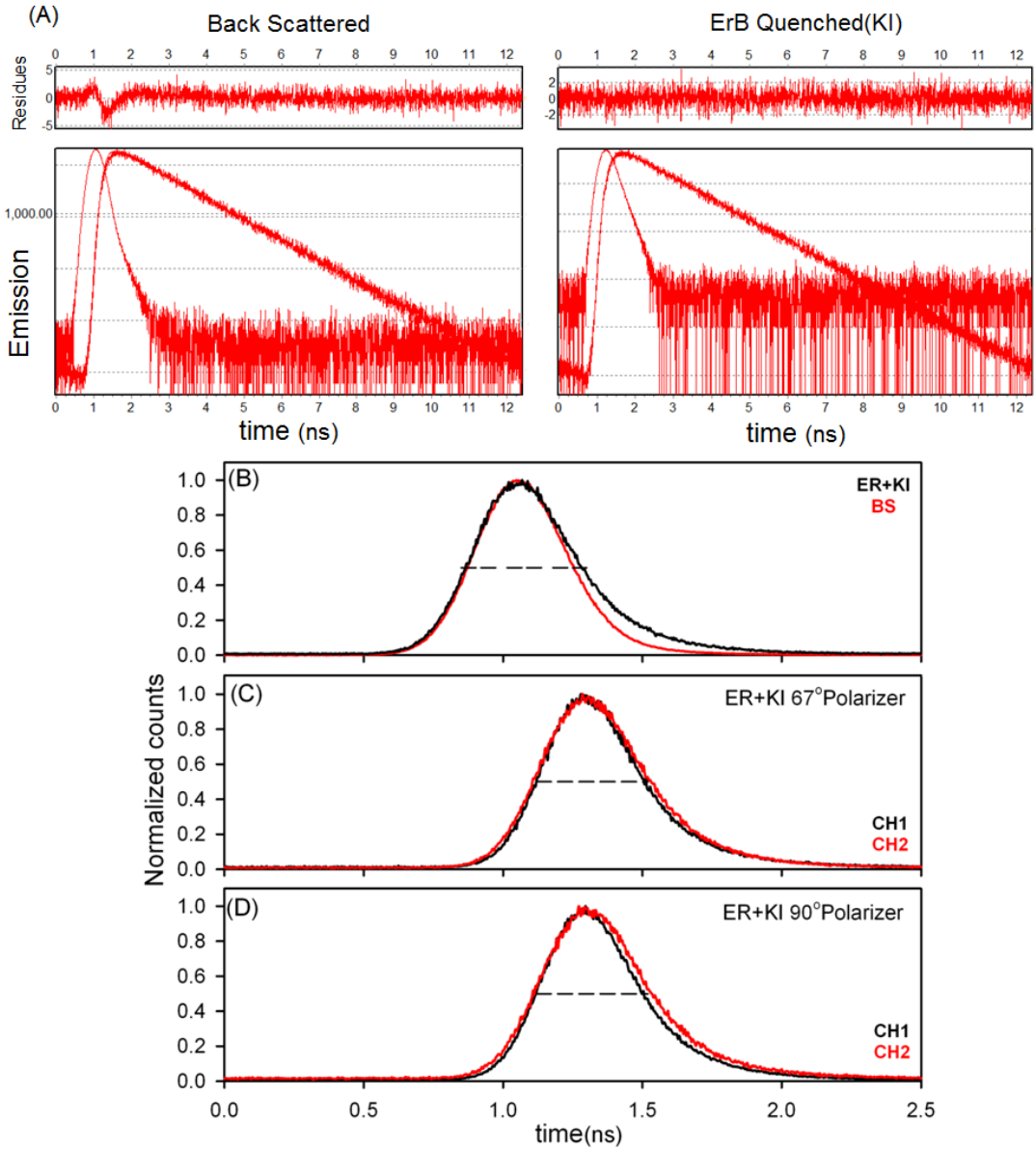

Figure 5.4. Effect of the instrumental response function, IRF, on the re-convolution analysis of time-resolved fluorescence decays. (A) TPE fluorescence intensity decay of 48 nM Fluorescein in 0.1M NaOH analysed using Globals program (LFD. Irvine, CA), and two different IRFs: the BS IRF (left), and the EB-KI IRF (right). Each decay curve is accompanied at the top with the corresponding weighting residuals distribution for the fit. **(B)** Overlap of the BS IRF (red) and the EB-KI IRF (black) functions. **(C-D)** Overlap of the ER-KI IRF determined for the two detectors associated to channel 1 (CH1, black) and channel 2 (CH2, red), using a beam splitter polarizer, for two excitation polarization conditions: half wave plate set at 67º and 90º (horizontal polarized excitation).

BS IRF: λ_{exc} = 780 nm; λ_{em} = 780 nm; **EB-KI IRF**: λ_{exc} = 780 nm; λ_{em} = 560 nm (FF01-562/40)

Fluorescein-NaOH 0.1M: λ_{exc} = 780 nm; λ_{em} = 520 nm (FF01-520/35, Semrock)

Figure 5.4 B shows the differences in shape between BS and EB-KI IRFs for 780 nm TPE excitation. Figure 5.4 C-D show the differences between the ER-KI IRFs determined for the two detectors of the instrument, using a polarizer beam splitter to analyse horizontal and vertical polarized light in channel 1 and 2 respectively. To increase the number of counts detected for ER-KI in channel 2, we have changed the polarization direction of the excitation light from 90º (horizontal) to 67º, by using a half wave plate at the entrance of the MOU unit.

We conclude that the EB-KI IRF is a good option for re-convolution analysis of total intensity and polarized parallel and perpendicular intensity decays acquired with the micro-spectrometer. The decays should be analysed with their corresponding instrumental function, determined for detector 1 or detector 2.

5.1.5 G factor estimation

The G factor takes in account the different transmission efficiencies of the detectors for the two polarized components. In the case of horizontal polarized excitation, the G corrected time-resolved fluorescence anisotropy function is given by:

$$r(t) = \frac{I_{par}(t) - G \cdot I_{per}(t)}{I_{par}(t) + 2 \cdot G \cdot I_{per}(t)} \qquad [5.1]$$

where $I_{par}(t)$ and $I_{per}(t)$ are the parallel and perpendicular polarized components of the fluorescence, with respect the polarization direction of the excitation light.

For horizontal polarized excitation, we acquired simultaneously the parallel, and perpendicular, components by using a beam-splitter polarizer before detector 1 (horizontal component; $I_{HH}(t) \approx I_{par}(t)$) and detector 2 (vertical component; $I_{HV}(t) \approx I_{per}(t)$), and $G = S_H / S_V$, were S_H and S_V represent the sensitivity of the horizontal and vertical detection channels. When the emission wavelength is selected by filters, and the detectors are near equivalent, we would expect G factors values near to 1.

There are different approaches to estimate the *G* factor in the microscope:

- The tail-matching method using a solution of a fast rotating dye (Ghosh *et al*. 2012). Fluorescein molecules in aqueous solutions, tumble rapidly many times (rotational correlation time $\phi \sim 180$ ps at 21ºC) within the fluorophore

lifetime (τ~ 4 ns), and its fluorescence emission will be totally depolarized at times t > 2 ns. Then, the G factor can be estimated from the ratio of the horizontal, $I_{HH}(t)$, and vertically, $I_{HV}(t)$, experimental polarized components at times > 2 ns:

$$G(x,y,z,t) = \frac{S_H}{S_V} = \frac{I_{HH}(t)}{I_{HV}(t)} \quad [5.2]$$

- A better approach for a collinear excitation/emission setup determine the G factor from the horizontal and vertical polarized components, with horizontal and vertically polarized excitation (Blackman *et al.* 1996, Siegel *et al.* 2003):

$$G(x,y,z,t) = \sqrt{\frac{I_{VH}(x,y,z,t)\cdot I_{HH}(x,y,z,t))}{I_{VV}(x,y,z,t)\cdot I_{HV}(x,y,z,t)}} \quad [5.3]$$

were $I_{VV}(t)$ and $I_{VH}(t)$ represent the parallel and perpendicular fluorescence experimental polarized components for vertical polarization excitation.

We have measured the four polarized components $I_{VV}(t)$, $I_{VH}(t)$, $I_{HH}(t)$ and $I_{HV}(t)$ for a solution of Fluorescein 48 nM in 0.1 M NaOH, and determined the $G(x,y,z,t)$ factor using Eq. 5.3. A half-wave plate was used to transform the original horizontal polarization of the laser beam to vertical polarization. Channel 1 and Channel 2 in our instrumental setup present a relative time-shift of ~80-120 ps. If we don't synchronize in time the experimental decays before to calculate the G factor using Eq. 5.2, the $G(x,y,z,t)$ function present at short times values very different than 1, depending of the experimental time-shift (Figure 5.5 A, grey points). The dark count background is also an important issue in the G factor estimation.

We estimated the instrumental time-shift by overlapping the EB-KI curves determined for channel 1 and channel 2, and we time-shifted manually the parallel decay with respect the perpendicular to synchronize both. The $G(x,y,z,t)$ corrected function calculated from the background subtracted and synchronized polarization decays presents a shorter peak at short times (Figure 5.5 A, black points).

We realized that the corrected $G(x,y,z,t)$ function estimated in this way and from tail-matching approach were very sensitive to the time synchronization correction in horizontal and vertically polarized components. Small errors in

the time-shift correction result in big changes in the shape of corrected *G* function at short times.

Iterative re-convolution Globals program (LFD. Irvine, CA) works with a constant *G* factor value, instead a variable *G(x,y,z,t)* function. For times >2 ns, corrected *G(x,y,z,t)* function determined from Eq. 5.3 gives an average *G* factor value of 1.16 for the experiment presented in Figure 5.5 A (red line), while the uncorrected G function gives an average *G* value of 1.2.

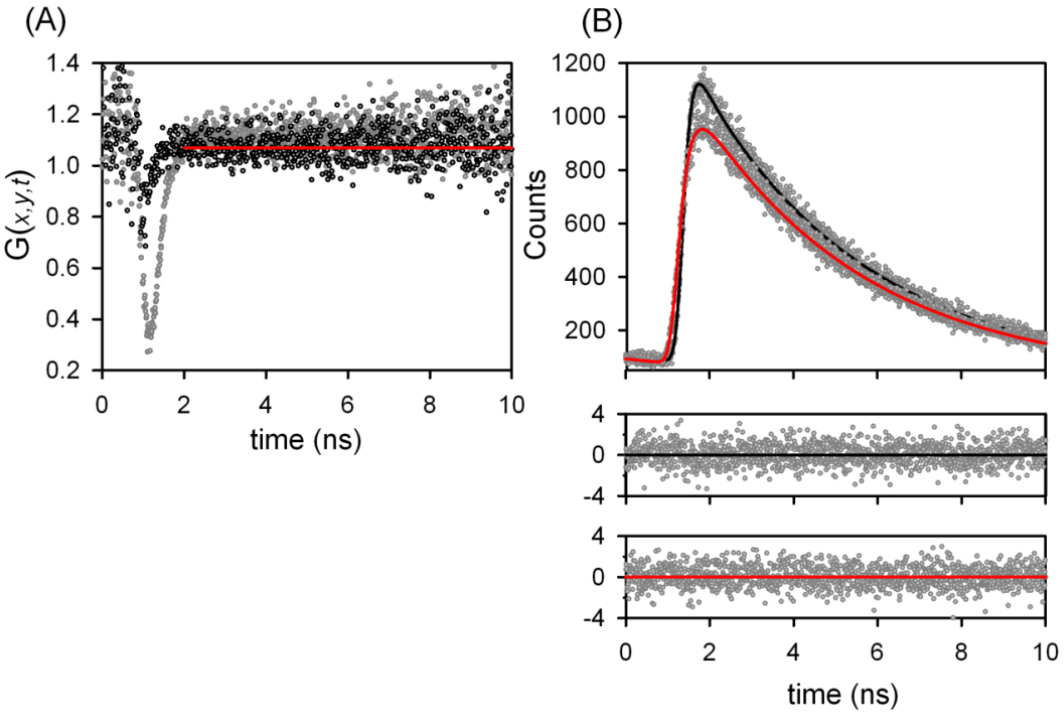

Figure 5.5. Determination of the instrumental factor *G(x,y,z,t)* from vertical and horizontal polarized excitation and a collinear setup. (A) *G(x,y,z,t)* calculated from raw parallel and perpendicular components, using Eq 5.2, shows values very different than 1 (gray dots) at t < 2 ns, and G~1.2 for t>2 ns. Corrected *G(x,y,z,t)*~1.15 for t>2 ns (black dots, and red line) **(B)** Re-convolution analysis of I_{HH} and I_{HV} components of Fluorescein 48 nM-NaOH 0.1 M. G factor from the fit was 1.15
λ_{exc}= 780 nm; λ_{em} = 520 nm (FF01-520-35, Semrock)

- The approach we have used in this work to determine the *G* factor in the specific conditions of the experiment optimizes the time-shift correction with Globals analysis program. Every day we collected the horizontal and vertically polarized decays of a solution of Fluorescein 48 nM-NaOH 0.1M, and we global analysed them using Globals program (Figure 5.5 B). The fitting parameters were: *i)* the lifetime of fluorescein; *ii)* the rotational correlation time of fluorescein; *iii)* the time-shift of parallel and

perpendicular components *iv)* the dark counts, and *v)* the G factor. In the previous example, with this procedure we got a *G* factor value of 1.15, coincident with the estimated average value from Eq. 5.2 using the corrected decays.

5.1.6 Axelrod correction for high numerical aperture objective effect

In our instrumental OPE and TPE microscope setup, the laser beam is horizontally polarized (Y-direction in the XY plane of the sample). The excitation beam and the fluorescence are collinear (Z-direction). When light is collected by a high numerical aperture (NA) lens, the measured polarized components parallel, $I_{HH}(t)$, and perpendicular, $I_{HV}(t)$, will contain a mix of polarizations in the X and Y directions, which results in that $I_{HH}(t)$ and $I_{HV}(t)$ are not equivalent to the theoretical functions, $I_{par}(t)$ and $I_{per}(t)$. Axelrod (1979, 1989) proposed how to correct these functions:

$$I_{HH} = k_3 \cdot I_Y + k_2 \cdot I_X + k_1 \cdot I_Z \quad [5.4]$$

$$G \cdot I_{HV} = k_2 \cdot I_Y + k_3 \cdot I_X + k_1 \cdot I_Z \quad [5.5]$$

The correction factors k_1, k_2, and k_3 are a function of the numerical aperture *NA* of the objective and the refractive index of the sample:

$$k_1 = {}^1\!/_3 \cdot (2 - 3 \cdot \cos\theta_0 + cos^3\,\theta_0) \quad [5.6]$$

$$k_2 = {}^1\!/_{12} \cdot (1 - 3 \cdot \cos\theta_0 + 3 \cdot cos^2\,\theta_0 - cos^3\,\theta_0) \quad [5.7]$$

$$k_3 = {}^1\!/_4 \cdot (5 - 3 \cdot \cos\theta_0 - cos^2\,\theta_0 - cos^3\,\theta_0) \quad [5.8]$$

where θ_0 is the angular aperture of the lens, defined as $NA = n \cdot sin\theta_0$. In our 3D coordinates nomenclature, I_{par} becomes I_Y, with respect to the coordinate plane of the sample, and $I_{per} = I_X = I_Z$. In the limit of zero *NA*, k_3=1.0, and $k_1 = k_2$=0.0.

For our instrument, for a *NA* 1.2 objective, k_1= 0.2622; k_2=0.015, and k_3=0.86, and the experimental parallel, $I_{HH}(t)$, and perpendicular, $I_{HV}(t)$, components are related to the theoretical components $I_{par}(t)$ and $I_{per}(t)$ by Eq. 5.9 and 5.10:

$$I_{HH}(t) = 0.756 \cdot I_{par}(t) + 0.244 \cdot I_{per}(t) \quad [5.9]$$

$$I_{HV}(t) = 0.013 \cdot I_{par}(t) + 0.987 \cdot I_{per}(t) \quad [5.10]$$

Eq. 5.11 and 5.12 give the estimations for the corrected $I_{par}(t)$ and $I_{per}(t)$ decays as a function of the experimental $I_{HH}(t)$ and $I_{HV}(t)$ decays, assuming Axelrhod corrections:

$$I_{par}(t) = 1.3284 \cdot I_{HH}(t) - 0.3284 \cdot I_{HV}(t) \quad [5.11]$$

$$I_{per}(t) = 1.0175 \cdot I_{HV}(t) - 0.0175 \cdot I_{HH}(t) \quad [5.12]$$

These corrections are more accurate when applied to $NA \sim 1.0$. In general, they represent the minimum level of corrections. For $NA \geq 1.3$, additional effects of the steep focusing angle on polarized light transmission become more apparent and will reduce the experimental anisotropy values (Piston and Rizzo, 2008).

Reflection optics and other nonlinear processes may also distort the polarization signals detected with the micro-spectrometer, especially in the TPE mode. Brasselet group (Schön *et al.* 2008) published a detailed study of the effect of reflection optics (primarily the dichroic beamsplitter) and high numerical aperture focusing on two-photon fluorescence polarization responses in model samples.

Next, we describe a set of control experiments we run to verify the *NA* effects and their possible correction in our micro-spectrometer setup.

5.1.7 Total fluorescence intensity determination for high *NA* objective systems

Here we are looking for the better experimental approach for the acquisition of the total fluorescence intensity decay in the micro-spectrometer. As we showed before, the emission light collected with and without polarizers in the emission channel and horizontal polarized excitation may contain a complex mixture of $I_{par}(t)$ and $I_{per}(t)$ decays. Each instrumental setup has to be tested with appropriate control samples to determine the best experimental approach to determine the time-resolved total intensity function.

In Figure 5.6 we have compared the two approaches we have used in this work for the measurement of the total fluorescence intensity: *i)* the direct

intensity measurement, $I_{open}(t)$, and *ii)* the calculated sum from the experimental horizontal and vertically polarized components, previously synchronized and *G* factor corrected, $I_{HH}(t)+2\cdot G\cdot I_{HV}(t)$. Using Axelrhod corrections we can estimate the contribution of the theoretical functions $I_{par}(t)$ and $I_{per}(t)$ to the experimental total intensity decays:

$$I_{open}(t) = I_{HH}(t) + I_{HV}(t) = 0.769 \cdot \left[I_{par}(t) + 1.6 \cdot I_{per}(t)\right] \quad [5.13]$$

$$I_{HH}(t) + 2 \cdot G \cdot I_{HV}(t) = 0.782 \cdot \left[I_{par}(t) + 2.836 \cdot G \cdot I_{per}(t)\right] \quad [5.14]$$

$$I_{total}(t) = I_{par}(t) + 2 \cdot I_{per}(t) \quad [5.16]$$

As we can see from Eq. 5.13 to 5.16, both experimental approaches for the total fluorescence intensity would differ from the theoretical function $I_{total}(t)$. It is important to note that we just include Axelrhod corrections for the effect of the high *NA* of the objective, to obtain Eq. 5.13 and 5.14, and there are other possible optical aberrations not included in these corrections.

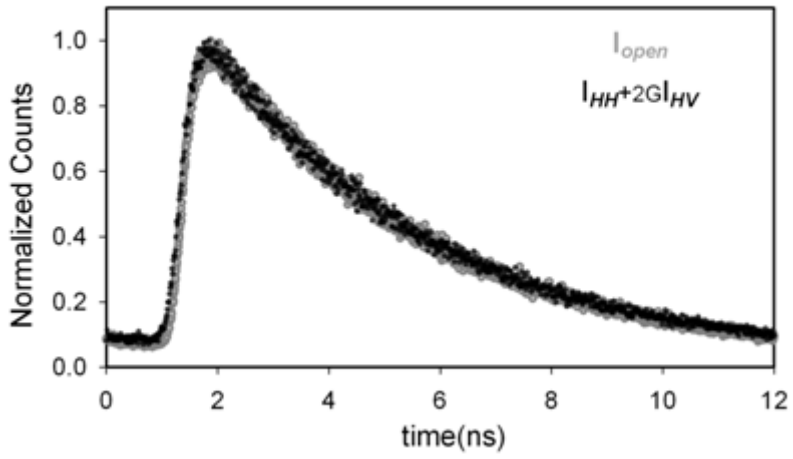

Figure 5.6. Total fluorescence intensity measurements.
Experimental time-resolved fluorescence decay of 48 nm Fluorescein in 0.1 M NaOH, I_{open}, measured without a polarizer in the emission channel, and horizontal polarized excitation.
Calculated $I_{HH}(t)+2\cdot G\cdot I_{HV}(t)$ was built from the polarized intensity components measured using a beam splitter polarizer to separate the horizontal $I_{HH}(t)$ and the vertical $I_{HV}(t)$ components of the emitted light.
λ_{exc}= 780 nm; λ_{em} = 520 nm (FF01-520/35, Semrock). 80.6 MHz. 60X 1.2 NA water objective

For a solution of Fluorescein 48 nM in 0.1 M NaOH the two approaches for the total intensity decay are coincident within experimental error. Besides, the analysis of the two functions provides the correct lifetime value for fluorescein.

Since the measurement of $I_{open}(t)$ is a direct measurement, all the fluorescence lifetimes in this work have been determined from $I_{open}(t)$ functions.

5.1.8 Rotational diffusion and time-resolved fluorescence anisotropy of protein solutions in the micro-spectrometer

We have two independent problems: *i)* to determine the accuracy of the lifetimes and anisotropy parameters determined with the micro-spectrometer, and *ii)* to determine the resolution of the instrument to discriminate species of different size and conformation.

We have tested the capability of the instrumental OPE and TPE time-resolved anisotropy microscope setup to characterize the lifetimes and rotational dynamics of different mutants of GFP, free and bound to control proteins, in different media, to better understand the observed changes when GFPs are bound to the proteins of interest: the components of the ribosome stalk.

The controls used in this study were E. coli-purified free EGFP (see Figure 5.7), and (hemolytic lectin) LSL_t-tagged EGFP in TRIS buffer solution: OPE cuvette, and OPE and TPE micro-spectrometer measurements. The hemolytic lectin LSLa from the mushroom *Laetiporus sulphureus* tagged with EGFP was used as a high molecular weight control for OPE and TPE measurements (López-Gallego *et al.* 2012). The EGFP protein is bound to the N terminal domain of LSL. Molecular weight of LSL_t-EGFP (45 kDa) is near two times the molecular weight of free EGFP (27 kDa).

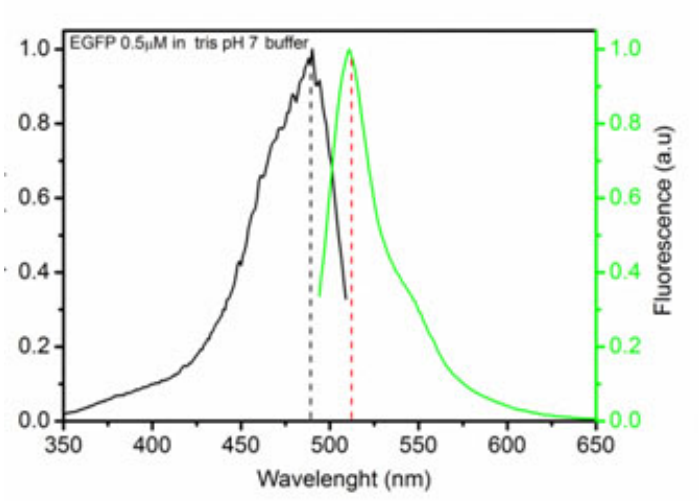

Figure 5.7. Purified *E. coli* EGFP spectra. Normalized corrected excitation (black) and emission spectra (green) of 0.5 μM of *E.coli* purified EGFP in TRIS HCl buffer, pH 7. Black and green dotted lines show excitation and emission maximum at 490 and 510 nm, respectively.
Excitation spectra (λ_{em} = 515nm)
Emission spectra (λ_{ex} = 482 nm)
4 nm slits

Time-resolved micro-spectrometer measurements were complemented with cuvette OPE experiments, using a calibrated laser spectrometer (Lillo et al. 2002).

Purified EGFP and LSL_t-tagged EGFP in buffer: OPE cuvette determinations

Lifetime components and pre-exponential factors of free EGFP and LSL_t-EGFP in TRIS HCl buffer solution at 22ºC are presented in Table 5.1. The main fluorescence lifetime, τ_1=2.86±0.05 ns, has a contribution of 78-80%, and there is a second component, τ_2=1.8±0.4 ns. In general, all the fluorescent proteins have a complex photophysics, including equilibria between different ground and excited states, proton transfer, and photo-conversion processes. These multiple states and the inter-conversion between them would lead to an inherent muti-exponential decay, which depends on the excitation/emission wavelength, pH of the media, aggregation of fluorophores, and interactions of the fluorophore with other proteins.

The rotational correlation times (ϕ) of EGFP and LSL_t-EGFP in TRIS HCl buffer solution were determined and the results are summarized in Table 5.1. In Figure 5.8 we present the calculated time-resolved anisotropy functions from the experimental and fitted parallel, $I_{VV}(t)$, and perpendicular, $I_{VH}(t)$, polarized components:

$$r(t) = \frac{I_{VV}(t) - G \cdot I_{VH}(t)}{I_{VV}(t) + 2 \cdot G \cdot I_{VH}(t)} \qquad [5.17]$$

The global analysis of the parallel and perpendicular polarized components yields single rotational correlation time, ϕ, of 14.5±0.5 ns and 21±1 ns at 22°C, respectively. They reflect the global rotation of the proteins.

The time zero anisotropy was similar in both the proteins, r_0 = 0.39, a value near the OPE theoretical limit (r_0 = 0.4).

The global rotational correlation time is a function of the molecular hydrodynamic volume, V_H, the absolute temperature, T, the Boltzmann constant, k_B, and the solvent viscosity (η) (Stokes-Einstein-Debye relationship). For a globular protein we have (Zorrilla *et al.* 2004b):

$$\phi = \frac{\eta \cdot V_H}{k_B \cdot T} \quad [5.18]$$

$$V_H = \frac{4}{3}\pi \cdot R_H^3 \quad [5.19]$$

where R_H is the hydrodynamic radius of the molecule.

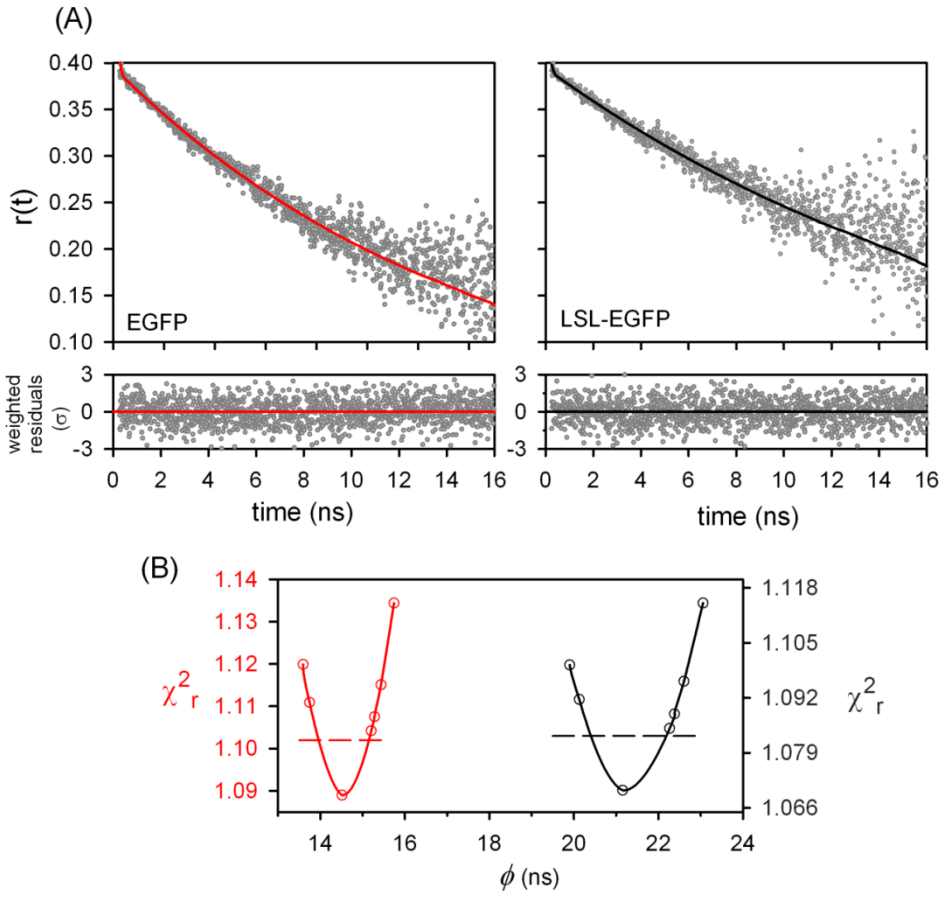

Figure 5.8. OPE Cuvette measurements: Fluorescence anisotropy decays of EGFP and LSL$_t$-EGFP in TRIS HCl buffer. (A) Fluorescence anisotropy decays built from the experimental and fitted polarized components, $I_{VV}(t)$ and $I_{VH}(t)$, for EGFP (left) and LSLt N-terminal tagged EGFP (right). Experimental $r(t)$: grey points. Fitted $r(t)$: red and black continuous line. The corresponding weighted residual distributions are shown below the anisotropy decays. **(B)** Confidence intervals determined from the rigorous error analysis, for the rotational correlation times are shown as solid lines for EGFP (red), and LSL$_t$-EGFP (black). Dashed lines represent the χ^2 value corresponding to the 67% confidence level ($\pm 1\sigma$) measurement.
The intensity and anisotropy fitting parameters are presented in Table 5.1
ϕ (EGFP) =14.5±0.5ns. ϕ (LSL$_t$-EGFP) = 21 ± 1ns.
λ_{exc}= 482 nm; λ_{em}= 515 nm (slits 16 nm). 5 MHz. T=22ºC

The estimated hydrodynamic radius for EGFP and LSL$_t$-EGFP, assuming globular conformations, would be 2.45 nm and 2.78 nm respectively.

From the x-ray structure of GFP (Ormö *et al.* 1996), the shape of fluorescent

proteins, FP, can be approximated as a cylinder of 2.4 nm diameter and 4.2 nm height, with anisotropic rotation, which would result in multi-exponential fluorescence anisotropy decay for EGFP samples.

Table 5.1. Time-resolved fluorescence total intensity and anisotropy decay parameters of all the control proteins, as a function of the environment of EGFP and instrumental setup

Sample	Setup	a_1	τ_1 (ns)	a_2	τ_2 (ns)	$<\tau>_I$	r_0	ϕ (ns)
EGFP/ TRIS buffer	Cuvette	0.80 (±0.1)	2.86 (±0.05)	0.20 (±0.1)	1.8 (±0.4)	2.6 (±0.3)	0.386 (±0.005)	14.5 (±0.5)
	OPE	0.74 (±0.04)	2.86 (2.85-3.0)	0.26 (±0.04)	1.8 (±0.2)	2.6 (±0.1)	0.283 (±0.003)	14.4 (±0.5)
	TPE	-	2.78 (±0.02)	-	-	[2.78] (±0.02)	0.447 (±0.005)	14.7 (±0.6)
yEGFP/ cytoplasm *S. cerevisiae*	OPE n=17	0.64 (±0.02)	2.3 (±0.05)	0.36 (±0.02)	1.0 (±0.1)	1.8 (±0.1)	0.284 (±0.01)	31 (±3)
	TPE n=21	0.44 (±0.02)	2.6 (±0.2)	0.56 (±0.02)	1.2 (±0.2)	1.8 (±0.2)	0.32 (±0.09)	32 (±4)
LSL_t-EGFP/ TRIS buffer	Cuvette	0.78 (±0.1)	2.85 (±0.05)	0.22 (±0.1)	1.8 (±0.4)	2.6 (±0.3)	0.388 (±0.005)	21 (±1)
	OPE	0.74 (±0.04)	2.85 (2.82-3.25)	0.26 (±0.04)	1.7 (±0.2)	2.6 (±0.2)	0.284 (±0.002)	21.6 (±0.80)
	TPE	-	2.77 (±0.02)	-	-	[2.77] (±0.02)	0.434 (±0.005)	21 (±2)

Total fluorescence intensity and horizontal and vertically polarized time-resolved decays were analysed using Globals Program (LFD. Irvine, CA)

Total intensity (pre-exponentials a_i , and fluorescence lifetimes, τ_i), and fluorescence anisotropy parameters (time zero anisotropy, r_0, and rotational correlation time, ϕ)
$<\tau>_I$: amplitude average lifetime (Eq. 3.3)

Numbers in parentheses represent the upper and lower limit of the recovered values (at the 67% confidence level) using rigorous error analysis, as described in Beechem *et al.* (1991).
For yEGFP expressed in the cytoplasm, numbers in parenthesis represent the sample-to-sample error for *n* independent experiments.

Total concentration of EGFP and LSL_t-EGFP, in buffer solution, were 500 nM (20 mM Tris HCl, NaCl 100 mM, pH 8.0)

OPE cuvette: λ_{exc}=482 nm; λ_{em}=515nm (slit 16 nm); 5 MHz. T=22ºC
OPE Micro-spectrometer: λ_{exc}=482 nm; λ_{em}=515 nm (monochromator slit 16 nm). 5 MHz. T=22ºC
TPE Micro-spectrometer: λ_{exc}=850 nm; λ_{em}=FF01-520/35 (Semrock). 80.6 MHz. T=22 ºC

In general, the lifetime of FPs is too short to proper determine their slow rotation component (about the short axis of the cylinder), and the experimental rotational correlation times would correspond to the average of the three theoretical rotational correlation times (Cantor and Schimmel 1980). This may be the reason for the range of published rotational correlation time values for different FPs, in different media (see for example Swaminathan *et al.* 1997, Volkmer *et al.* 2000, Hink *et al.* 2000, Uskova *et al*. 2000, Hess *et al.* 2003). The average rotational correlation time values will depend on the type of FP mutant, the FP microenvironment, the sensitivity of the instrument, and the analysis method.

The lifetimes and rotational correlation times determined in our cuvette calibrated instrument, using Globals program (LFD, Irvine. CA), indicate that: *i)* free EGFP (27 kDa) in TRIS buffer shows a single average rotational correlation time of 14.5±0.5ns; *ii)* EGFP photophysics is not affected when is tagged to LSL_t protein: both samples show the same lifetime pattern. This agrees well with this tag playing no role in the folding of its C-terminal counterpart (López-Gallego *et al*. 2012); *iii)* the average rotational correlation time determined for LSL_t- EGFP (45 kDa) is shorter that predicted for globular rotation of the two fused proteins LSL_t and EGFP. This result is indicative of protein flexibility, since any possible rigid model for LSL_t- EGFP would rotate much slower than the experimental value. The more probable explanation is to assume that LSLt is connected to EGFP by a flexible hinge.

Purified EGFP and LSL_t-tagged EGFP in buffer: OPE Micro-spectrometer determinations

Single point time-resolved total intensity, $I_{open}(t)$, and polarized components, $I_{HH}(t)$ and $I_{HV}(t)$, were acquired during 30 s for free EGFP and LSLt-EGFP in TRIS HCl buffer 500 nM solutions using the OPE micro-spectrometer setup at 22ºC.

Lifetime components, pre-exponential factors and anisotropy parameters are presented in Table 5.1. Fluorescence lifetimes and the amplitude average lifetime, $<\tau>_I$=2.6 ns, determined from $I_{open}(t)$, are essentially the same to the

cuvette lifetime values.

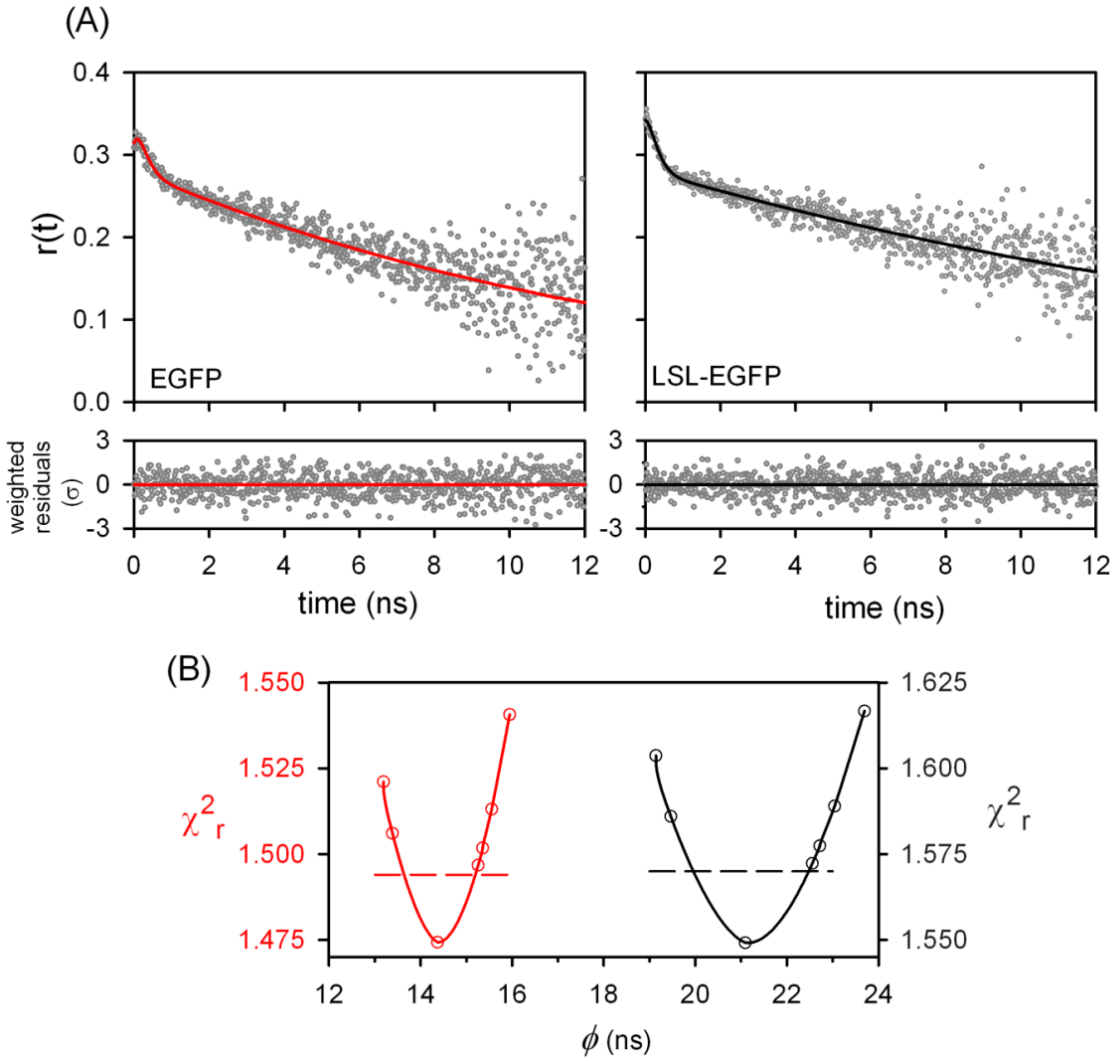

Figure 5.9. OPE micro-spectrometer solution measurements: Fluorescence anisotropy decays of EGFP and LSL$_t$-EGFP in TRIS HCl buffer. (A) Fluorescence anisotropy decays built from the experimental and fitted polarized components, $I_{HH}(t)$ and $I_{HV}(t)$, for EGFP (left) and LSLt N-terminal tagged EGFP (right). Experimental *r(t)*: grey points. Fitted *r(t)*: red and black continuous line. The corresponding weighted residual distributions are shown below the anisotropy decays. **(B)** Confidence intervals determined from the rigorous error analysis, for the rotational correlation times are shown as solid lines for EGFP (red), and LSL$_t$-EGFP (black). Dashed lines represent the χ^2 value corresponding to the 67% confidence level ($\pm 1\sigma$) measurement.
The intensity and anisotropy fitting parameters are presented in Table 5.1
ϕ(EGFP) =14.4 ± 0.5 ns. ϕ(LSL$_t$-EGFP) = 21.6 ± 0.8 ns.
λ_{exc}= 482 nm; λ_{em} = FF01-520/35 nm, 5 MHz. T=22ºC
60X 1.2 NA water immersion objective

Figure 5.9 A presents the time-resolved anisotropy decays corresponding to EGFP (left) and LSLt-EGFP (right), giving best-fit rotational correlation times of 14.4±0.5 ns and 21.6±0.8 ns respectively. The lifetimes and rotational correlation

times totally match with those determined using the calibrated cuvette instrument for the same samples, showing the adequacy of the time-resolved anisotropy methods developed in this work to determine rotational correlation times of biomolecules in solution. Figure 5.9 B presents the χ^2 surface determined from the rigorous error analysis corresponding to EGFP (left) and LSLt-EGFP anisotropy fitting. The uncertainty of rotational correlation times are similar for OPE cuvette and micro-spectrometer measurements.

The time zero anisotropies, r_0, determined from the time resolved anisotropy decays measured with the OPE micro-spectrometer setup (~0.284) are significantly lower than the corresponding cuvette values (~0.388). Decrease in r_0 was predicted and observed by Axelrod (1979, 1989), Tramier *et al.* (2000) and others. This is caused mainly by the high numerical aperture (NA) objective effects.

Purified EGFP and LSL_t-tagged EGFP in buffer: TPE Micro-spectrometer determinations

Single point time-resolved total intensity, $I_{open}(t)$, and polarized components, $I_{HH}(t)$ and $I_{HV}(t)$, were acquired during 30 s for free EGFP and LSLt-EGFP in TRIS HCl buffer 500 nM solutions using the TPE micro-spectrometer setup.

Lifetime components, pre-exponential factors and anisotropy parameters are presented in Table 5.1. TPE $I_{open}(t)$ measurements of EGFP and LSLt-EGFP indicated a single lifetime of 2.78±0.02 ns at 850 nm excitation and 22ºC. Figure 5.10 A presents the time-resolved anisotropy decays corresponding to EGFP (left) and LSLt-EGFP (right), giving best-fit rotational correlation times of 14.7 ± 0.6 ns and 21 ± 2 ns respectively.

The lifetimes and rotational correlation times determined for the two samples with the OPE and TPE micro-spectrometer are essentially equivalent. Figure 5.10 B presents the χ^2 surface determined from the rigorous error analysis corresponding to EGFP and LSLt-EGFP anisotropy fitting, showing the variations in confident limits of rotational correlation time for both proteins, indicated as dashed lines.

The uncertainty of LSLt-EGFP rotational correlation time is significantly

higher in TPE than OPE. This is because the background is less well defined in TPE than OPE for longer rotational correlation times (see section 5.1.9).

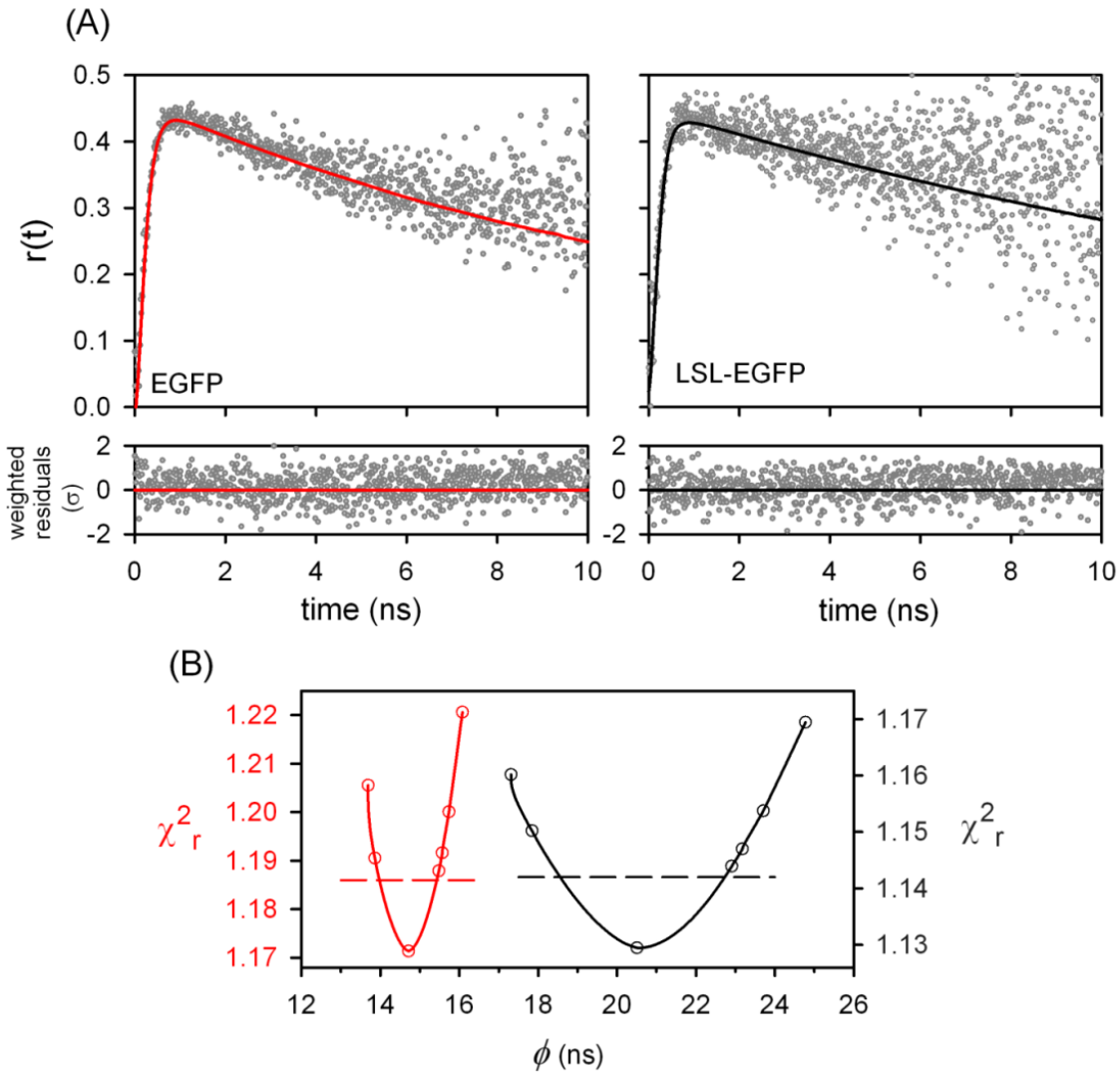

Figure 5.10. TPE micro-spectrometer solution measurements: Fluorescence anisotropy decays of EGFP and LSL$_t$-EGFP in TRIS HCl buffer. (A) Fluorescence anisotropy decays built from the experimental and fitted polarized components, $I_{HH}(t)$ and $I_{HV}(t)$, for EGFP (left) and LSLt N-terminal tagged EGFP (right). Experimental $r(t)$: grey points. Fitted $r(t)$: red and black continuous line. The corresponding weighted residual distributions are shown below the anisotropy decays. **(B)** Confidence intervals determined from the rigorous error analysis, for the rotational correlation times are shown as solid lines for EGFP (red), and LSL$_t$-EGFP (black). Dashed lines represent the χ^2 value corresponding to the 67% confidence level ($\pm 1\sigma$) measurement.
The intensity and anisotropy fitting parameters are presented in Table 5.1
ϕ(EGFP) =14.7 ± 0.6 ns. ϕ(LSL$_t$-EGFP) = 21 ± 2 ns.
λ_{exc}= 850 nm; λ_{em}= FF01-520/35 nm, 80.6 MHz. T=22ºC
60X 1.2 NA water immersion objective

The time zero anisotropy determined from the time resolved anisotropy decays measured with the TPE micro-spectrometer setup (~0.44) are

significantly lower than the maximum TPE theoretical value (0.57).

5.1.9 OPE and TPE time-resolved anisotropy measurements in living cells

Free yEGFP was expressed in *S. cerevisiae* yeast cytoplasm to test the capability of the OPE and TPE micro-spectrometer setup to determine rotational correlation times in *S.cerevisiae* living yeast cells. OPE conditions: excitation wavelength λ_{exc} = 482 nm; 5 MHz. TPE conditions: excitation wavelength λ_{exc} = 850 nm; 80.6 MHz. For all the measurements the 60X *NA* 1.2 water immersion objective was used, and the emission filter was FF01-520/5 (Semrock, Germany).

Resuspended cells in fresh media were immobilized between two microscope cover slips (see Materials and Methods). The appropriate X,Y,Z cytoplasmic location for single point time-resolved data acquisition was selected from Z section-FLIM images of single cells. Acquisition times were 30 s for each polarized component.

It is important to note that the FP construction used here, yEGFP, is a different mutant of the green fluorescent protein, showing a different lifetime distribution comparing with EGFP. We found two fluorescence lifetimes of 2.3-2.6 ns and 1.0-1.2 ns, with apparently different distribution in OPE and TPE experiments (see Table 5.1). The amplitude average lifetime (1.8 ns) is significantly lower than measured for the purified EGFP mutant in solution (2.6 ns for OPE, and 2.78 ns for TPE).

Figure 5.11 A presents the single point time-resolved anisotropy decays for random XYZ locations of EGFP expressed in the cytoplasm of *S. cerevisiae* yeast cells, measured with TPE (2P-yEGFP, left) and OPE (1P-yEGFP, right). Global re-convolution analysis of $I_{HH}(t)$ and $I_{HV}(t)$ polarized components gives rotational correlation times of 32 ± 4 ns and 31 ± 3 ns respectively, about 2-fold slower than EGFP in buffer solution. The experimental rotational correlation times are in the range of previous published values (see for example Swaminathan *et al.* 1997, Volkmer *et al.* 2000, Gautier *et al.* 2001, Hess *et al.* 2003), and reflect the crowded characteristics of the cytoplasm.

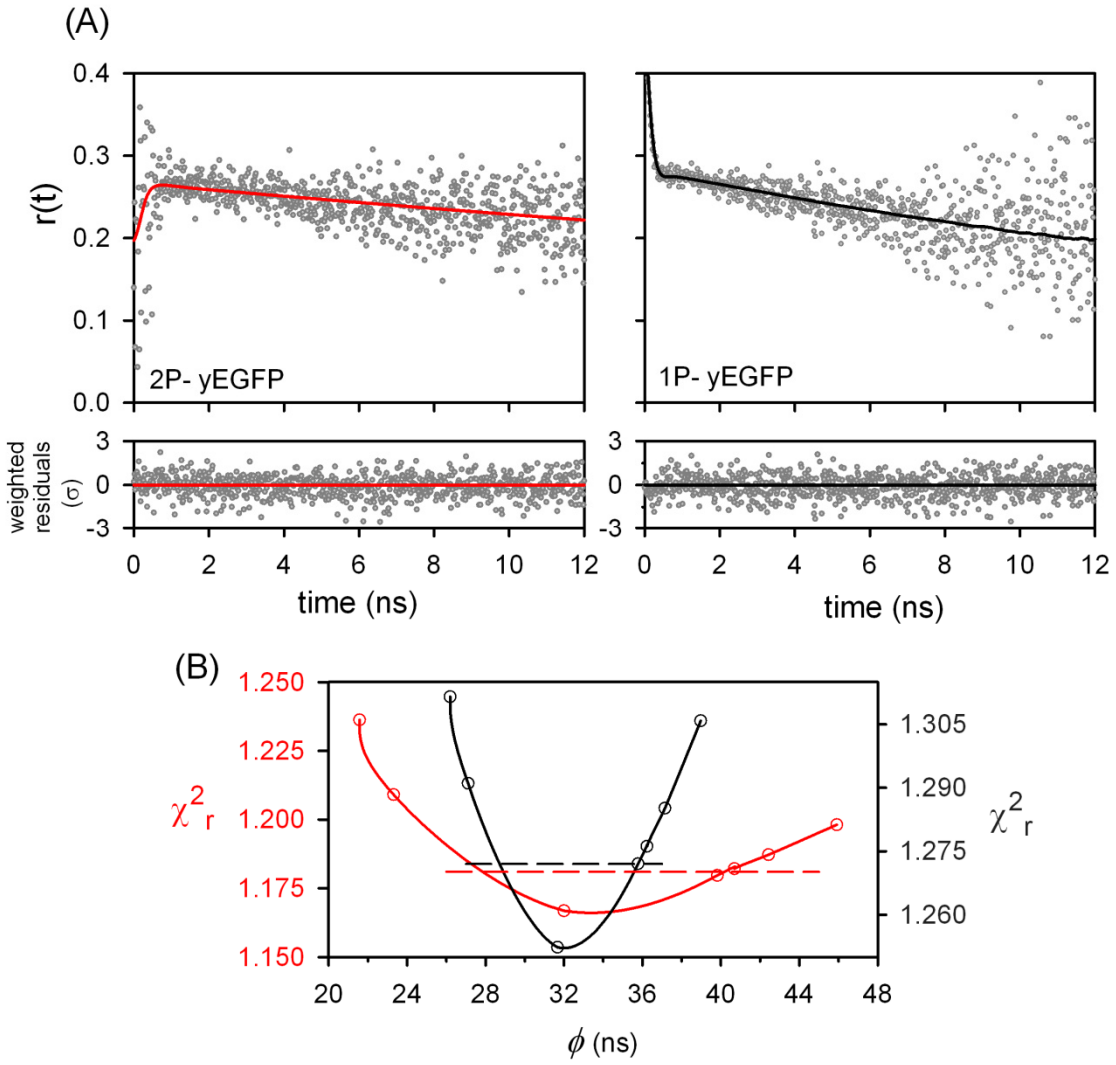

Figure 5.11. OPE and TPE micro-spectrometer single point live cell measurements: Fluorescence anisotropy decays of yEGFP expressed in the cytoplasm of *S. cerevisiae* yeast cells. (A) Fluorescence anisotropy decays built from the experimental and fitted polarized components, $I_{HH}(t)$ and $I_{HV}(t)$, for TPE (2P-yEGFP, left) and OPE (1P-yEGFP, right). Experimental *r(t)*: grey points. Fitted *r(t)*: red and black continuous line. The corresponding weighted residual distributions are shown below the anisotropy decays. **(B)** Confidence intervals determined from the rigorous error analysis, for the rotational correlation times are shown as solid lines for TPE (red), and OPE (black). Dashed lines represent the χ^2 value corresponding to the 67% confidence level ($\pm 1\sigma$) measurement.
The intensity and anisotropy fitting parameters are presented in Table 5.1
ϕ (2P-yEGFP) =32 ± 4 ns. ϕ (1P-yEGFP) = 31 ± 3 ns.
λ_{exc}= 850 nm; λ_{em} = FF01-520/35 nm, 80.6 MHz. T=22ºC
60X 1.2 NA water immersion objective

Figure 5.11 B presents the χ^2 surface determined from the rigorous error analysis corresponding to yEGFP expressed in the cytoplasm OPE and TPE anisotropy fitting, showing the variations in confident limits of rotational correlation time for both experiments, indicated as dashed lines.

The uncertainty of TPE rotational correlation time is significantly much higher in TPE than OPE. This is because the background is less well defined in TPE than OPE for longer rotational correlation times.

These results reveal: *i)* the capability of the TPE and OPE micro-spectrometer to quantify rotational motions of proteins in the cytoplasm of *S. cerevisiae* yeast cells, *ii)* the rotational correlation times of yEGFP reveal a cytoplasmic apparent microviscosity about 2 times larger than that of aqueous solution at room temperature, *iii)* OPE time-resolved anisotropy techniques are more appropriates for the determination of long rotational correlation times.

The time zero anisotropy, r_0, determined for OPE was similar (0.284) to the determined for purified EGFP in buffer solution (0.283). However, the TPE r_0 values were significantly lower (0.32) than determined for the purified EGFP protein in solution (~0.44). Therefore, apparently optical aberrations affecting r_0 are stronger for TPE measurements in living cells, comparing with aqueous dilute solutions.

5.1.10 Corrected time-resolved anisotropy decays for high *NA* objective effects

Figure 5.12 A shows an example of the fluorescence anisotropy decay, *r(t),* built from the experimental polarized components, $I_{HH}(t)$ and $I_{HV}(t,$ (left), and the manually corrected *r(t)* function, built from the $I_{par}(t)$ and $I_{per}(t)$ decays corrected by using Eq. 5.11 and 5.12 (Axelrhod based corrections; right) for P0-yEGFP sample. Anisotropy parameters were determined from global analysis of the two polarized components and red and black solid lines represent the calculated fit functions for the raw and corrected polarized components respectively. The lifetimes, time zero anisotropy and rotational correlation time values are listed in Table 5.2.

For this example, the main effect of using the raw $I_{HH}(t)$ and $I_{HV}(t)$ polarized components instead the corrected $I_{par}(t)$ and $I_{per}(t)$ in the anisotropy analysis was that the determined time-zero anisotropy, r_0 value, decreased from 0.35 to 0.29.

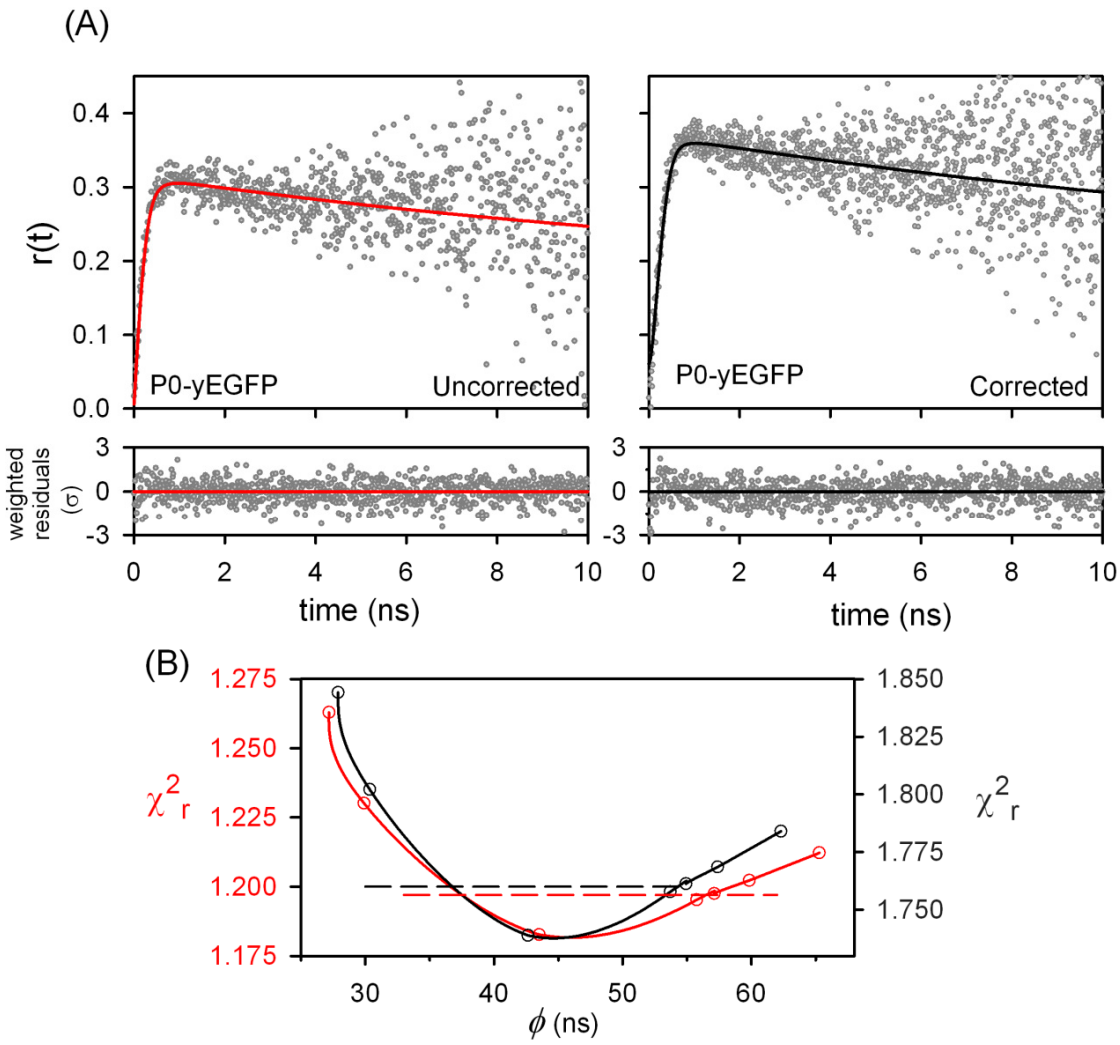

Figure 5.12. TPE micro-spectrometer single point live cell measurements: Fluorescence anisotropy decays of P0-yEGFP expressed in the cytoplasm of *S. cerevisiae* yeast cells. **(A)** Fluorescence anisotropy decays built *i)* from the experimental and fitted polarized components, $I_{HH}(t)$ and $I_{HV}(t)$ (left), and *ii)* from the corrected $I_{par}(t)$ and $I_{per}(t)$ using Axelrhod based corrections (Eq. 5.11 and 5.12; right). Experimental and corrected *r(t)*: grey points. Fitted *r(t)*: red and black continuous line. The corresponding weighted residual distributions are shown below the anisotropy decays. **(B)** Confidence intervals determined from the rigorous error analysis, for the rotational correlation times are shown as solid lines for TPE (red), and OPE (black). Dashed lines represent the χ^2 value corresponding to the 67% confidence level ($\pm 1\sigma$) measurement.
The intensity and anisotropy fitting parameters are presented in Table 5.1

ϕ (P0-yEGFP)$_{uncorrected}$ =44 ± 6 ns. ϕ (P0-yEGFP)$_{corrected}$ = 43 ± 6 ns.
$(r_0)_{uncorrected}$ = 0.29 ± 0.01; $(r_0)_{corrected}$ = 0.35 ± 0.01
λ_{exc}= 850 nm; λ_{em} = FF01-520/35 nm, 80.6 MHz. T=22ºC
60X 1.2 NA water immersion objective

Both analyses show randomly distributed weighted residuals, and similar lifetimes and rotational correlation times. Thus, we can determine rotational

correlation times directly from the experimental time-resolved polarized components. However, in the case of steady-state anisotropy measurements, where we can't separate the time zero anisotropy and rotational correlation time contributions, it would be necessary to work with the corrected polarized components.

Table 5.2. High *NA* effects on TPE lifetime and fluorescence anisotropy parameters

Polarized components	a_1 (±0.02)	τ_1 (ns) (±0.3)	a_2 (±0.02)	τ_2 (ns) (±0.3)	$<\tau>$ (ns) (±0.2)	r_0 (±0.01)	ϕ (ns) (± 6)
$I_{HH}(t)$, $I_{HV}(t)$ (experimental)	0.42	2.7	0.58	1.3	1.9	0.29	44
$I_{par}(t)$, $I_{per}(t)$ (corrected)	0.41	2.7	0.59	1.3	1.9	0.35	43

Global analysis of experimental functions ($I_{HH}(t)$ and $I_{HV}(t)$), and corrected ($I_{par}(t)$ and $I_{per}(t)$) polarized parallel and perpendicular components for the ribosomal stalk protein P0 (P0-yEGFP), expressed in live yeast cytoplasm.

Fluorescence lifetimes and fluorescence anisotropy decays were analysed using Globals software (LFD. Irvine, CA). Numbers in parentheses represent the upper and lower limit of the recovered values (at the 67% confidence level) using rigorous error analysis, as described in Beechem *et al.* (1991).

5.1.11 Summary

- The fitting methodology developed in this work to analyse single-point time-resolved fluorescence $I_{open}(t)$, $I_{HH}(t)$, $I_{HV}(t)$ data from the OPE-TPE micro-spectrometer, at XYZ locations with sub-µm spatial resolution, which includes iterative re-convolution with the instrument response function, IRF (Globals program from LFD, Irvine. CA), allowed us to resolve minor lifetime differences and provided a quantitative comparison for the different GFP variants, and between cellular and solution environments of GFPs, under the same experimental conditions.

- We have determined the rotational correlation times of purified free EGFP, and LSL_t-EGFP in TRIS HCl buffer, from the time-resolved fluorescence anisotropy decays measured using OPE and TPE setups under the micro-spectrometer:

  ϕ (EGFP, OPE)= 14.4±0.5 ns and ϕ (EGFP, TPE) = 14.7±0.6 ns.

  ϕ (LSL_t-EGFP, OPE)= 21.6±0.8 ns and ϕ (LSL_t-EGFP, TPE) = 21±2 ns.

  These results are coincident with the rotational correlation time determined in our calibrated cuvette system, for the same samples: 14.5±0.5 ns and 21±1 ns respectively
- We have determined the rotational correlation time of a different GFP variant (yEGFP) expressed in the cytoplasm of *S. cerevisiae* yeast cells. Single-point time-resolved fluorescence data ($I_{open}(t)$, $I_{HH}(t)$, $I_{HV}(t)$) were measured at specific XYZ cytoplasm locations in living yeast cells. The optimal acquisition time was 30 s per point, using excitation powers lower than 1 mW at the sample. The cytoplasm crowded environment of yEGFP slows its rotational mobility by comparison with EGFP in buffer solution, revealing a cytoplasmic apparent microviscosity about two times larger than aqueous solutions viscosity (~2 cP).
- The uncertainty in long rotational correlation times increased in TPE *vs.* OPE determinations. The main reasons are: shorter time window, the convolution with a periodical IRF and the difficulty estimating the real background contribution on the fluorescence decays. Therefore, OPE time-resolved anisotropy techniques are more appropriates for the determination of long rotational correlation times.
- On the other hand, single-point TPE anisotropy determinations in yeast cells induces less photo-damage than OPE, when different Z- locations need to be studied in the same cell.
- OPE and TPE experimental steady-state anisotropy and time-zero anisotropy (r_0) determinations were underestimated when the 60x NA1.2 water immersion objective was used. Axelrhod based corrections partially solved this problem.

5.2 Rotational dynamics of yeast ribosomal stalk proteins in living cells

5.2.1 Motivation

Protein synthesis is an essential process for cells that takes place in the ribosomes. The ribosome stalk is a flexible lateral protuberance of the 60S subunit, highly implicated in the regulation of protein synthesis. As we have seen in the Introduction, the eukaryotic ribosome stalk has a pentameric structure, with a central protein carrying four small acidic proteins.

Ribosome stalk proteins are present in a similar general organization across all biological kingdoms, even though the primary structures of the P-proteins have extensively evolved. This structural evolution occurred in parallel with the evolution of elongation factors. These arguments propose that the lateral flexible stalk has been combined to a primitive core of the ribosome to improve translation efficiency.

It has been reported that the CTD of stalk proteins is a very flexible domain highly implicated in translation regulation through the modulation of the interactions between soluble translation factors and the ribosome. These results suggest a possible relation between stalk flexibility and modulation of ribosomal function. However, in spite of the wealth of ribosomal structures determined by crystallography or cryo-EM, studies of the whole stalk remain poorly established, because its mobility has hindered its resolution in the available ribosome structures.

Time-resolved fluorescence anisotropy measurements inform about the rotational diffusion of the fluorophores during the lifetime of their excited state. The link between the fluorescence depolarization and the fluorophore rotational motions has resulted in numerous applications of this technique in biochemical research; hence any factor that modifies the rotational mobility of the fluorophore will also alter its anisotropy.

Here we will apply this technique to the characterization of the conformational dynamics of highly flexible proteins in living cells. The objective of this section consists on the study of the rotational dynamics of major ribosome

stalk proteins, P0, P1α, P2β, using time-resolved fluorescence anisotropy methods with high temporal (ps-ns) and spatial (sub μm) resolution in living cells, in order to evaluate if the mobility of the ribosomal stalk plays a role in the regulation of protein synthesis, and if this mobility can be affected by the selective inhibitor of protein synthesis, sordarin.

This study was carried on live *S cerevisiae* yeast cells, as a model of the eukaryotic ribosome, expressing the major ribosome stalk proteins tagged with the fluorescent protein yEGFP.

5.2.2 Expression of fusion proteins in *S. cervsisiae* yeast cells

We used *S. cerevisiae* strains that expressed ribosome stalk proteins tagged with the fluorescent protein yEGFP, all of them derived from the proteinase deficient strain BJ5458 (Martínez *et al.* 1999), which showed reduced autofluorescence:

- P0, P1α, P2β strains expressed the main ribosome stalk proteins, object of this study, with yEGFP attached to their carboxi-terminal domain, CTD.
- L25 strain expressed the 60S subunit ribosomal protein L25 with EGFP attached to the C-terminal without any linker, as a control of hindered motion of EGFP.
- EGFP strain expressed yEGFP fluorescent protein free in the cytoplasm of the cells, as a control for free motion of EGFP.
- WT strain was the wild-type strain, without yEGFP, as a control of autofluorescence.

To analyse the autofluorescence and expression profile of these yEGFP tagged proteins, cells were grown up to exponential phase and immobilized for fluorescence intensity and TPE-FLIM images as described in Materials and Methods. Figure 5.13 shows a typical FLIM image of a yeast cell from P0 strain: the green color corresponds to the average lifetime of yEGFP bound to the stalk protein P0 of the 60S ribosome subunit (schematic representation in the left), with ribosomes homogeneously distributed throughout the cytoplasm, and black color corresponds to the vacuole and the surrounding media (low or no counts).

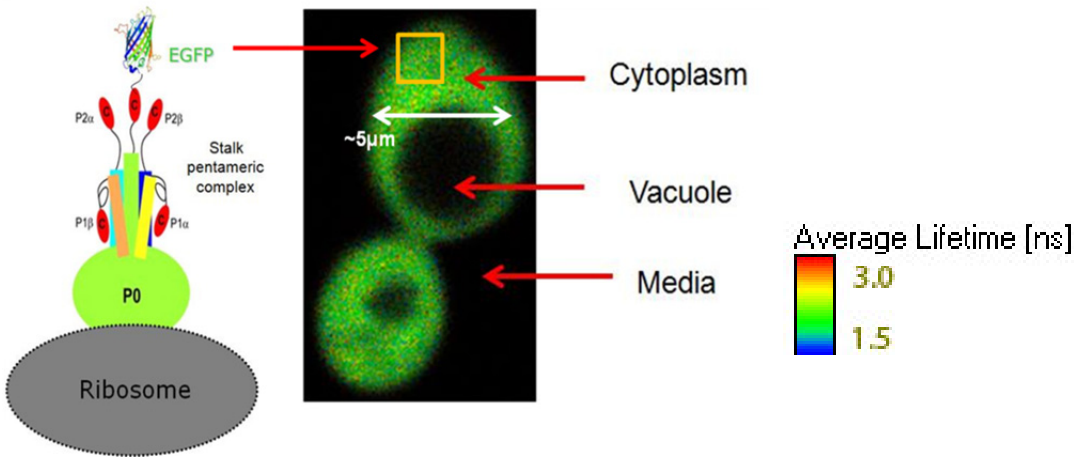

Figure 5.13. Lifetime image (FLIM) of a live *S. cerevisiae* yeast cell from P0 strain. Left: scheme of a ribosome with the stalk protein P0 tagged with yEGFP. Center: FLIM image of a P0 strain cell. Green color correspond to an intensity weighted average lifetime of P0-yEGFP expressed in the cytoplasm $<\tau>_2$ ~2.1 ns (see Table 5.5); black color for the vacuole and media indicates near no counts. Right: color scale for FLIM image: Blue: 1.5 ns, Red: 3.0 ns λ_{exc}=850nm, λ_{em}= FF01-520/35 (Semrock). T=22ºC

Table 5.3 shows representative fluorescence intensity and TPE-FLIM images of the yeast strains used in this Section. All intensity images showed almost homogeneous distribution of yEGFP tagged proteins in the cytoplasm. Likewise, FLIM images showed similar intensity average fluorescence lifetimes, $<\tau>_2$, of yEGFP tagged proteins expressed in the cytoplasm.

WT strain (BJ5458) showed a very low level of autofluorescence (Table 5.3), with 4-6 counts/pixel (1.2 ms/pixel) in the cytoplasm, comparing with the yEGFP fluorescence signals for the other strains of ~350counts/pixel or even up to ~450 counts/pixel in the case of P2β, in the same experimental conditions, giving a good signal to noise ratio for FLIM images

FLIM images showed slightly fluorescence lifetime differences between strains. Color code for FLIM images was set in the range of 1.5-3 ns. No significant differences between strains were found: we can see green color FLIM images for yEGFP tagged stalk proteins and free yEGFP, corresponding to intensity average lifetimes, $<\tau>_2$ ~2.0 ns, and yellow color FLIM images for L25 strain, $<\tau>_2$ ~2.5 ns (labelled with a different variant of EGFP; Table 5.5).

Table 5.3. Representative intensity and TPE-FLIM images of yEGFP tagged ribosomal proteins in live yeast cells

Strain (expressing EGFP tagged proteins)	Fluorescence Intensity Image	FLIM
WT	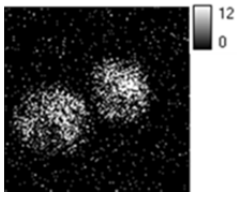	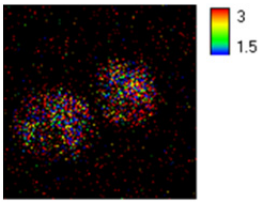
P0 (P0-yEGFP)	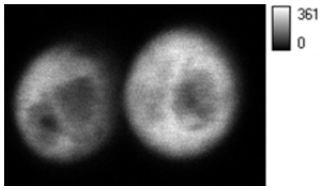	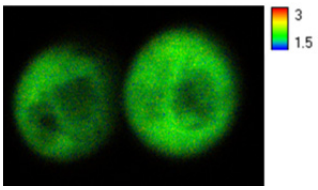
P1α (P1α-yEGFP)	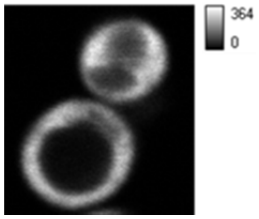	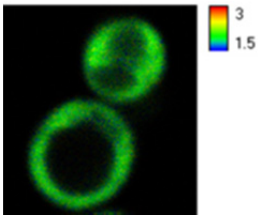
P2β (P2β-yEGFP)	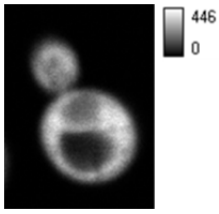	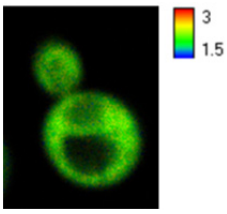
L25 (L25-EGFP)	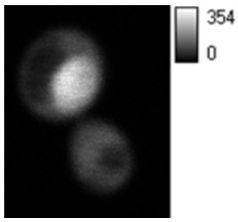	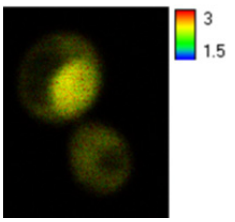
GFP (yEGFP)	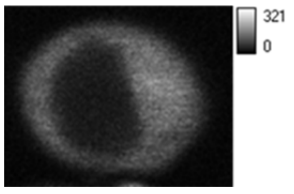	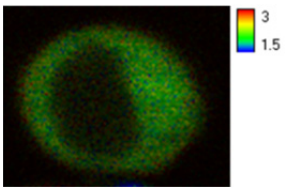

Samples: cells were grown up to exponential phase and immobilized for measurements (see Materials and Methods).
Fluorescence intensity images: code set in the range 0 to the maximum counts per pixel in the image.
FLIM images represents the intensity-weighted average lifetime, $<\tau>_2$ determined for each pixel. Color code set in the range 1.5 to 3 ns.

The observed homogeneous distribution of tagged ribosome proteins suggests that tagged proteins complemented the absence of the native proteins in the transformed strains, with little or no effect on cell growth. Therefore, we assumed the presence of the EGFP tag did not affect the regulation of native ribosome stalk components.

5.2.3 Dynamics of free yEGFP, free P2β-yEGFP, and purified yEGFP-tagged ribosomes in buffer: OPE cuvette study

Once we tested the yeast strains were expressing the fusion proteins without affecting normal cell growth, we measured the rotational dynamics of the purified proteins and ribosomes in buffer 1 (10 mM TRIS-HCl, pH 7.4, 20 mM $MgCl_2$, and 5 mM β-mercaptoethanol), using the calibrated OPE time-resolved laser micro-spectrometer for cuvette measurements (Lillo *et al.* 2002), with λ_{exc}=482 nm at T=30ºC.

We have performed fluorescence intensity and anisotropy measurements in two different samples: purified free proteins yEGFP and P2β-yEGFP (from cellular extracts of yEGFP and P2βstrains), and purified ribosomes from yeast cells expressing P0-yEGFP, P1α-yEGFP and P2β-yEGFP (from cellular extracts of P0, P1α and P2β strains), by ultracentrifugation and posterior purification in a discontinuous sucrose gradient (see Materials and Methods Section).

All the fluorescence total intensity decays were bi-exponential (Table 5.4), with two lifetimes, $\tau_1 \sim 2.2\text{-}2.4$ ns and $\tau_2 \sim 0.9\text{-}1.2$ ns, with amplitude-weighted average lifetimes, $<\tau>_1 \sim 1.6\text{-}2$ ns. The observed differences may be indicative of small changes in the microenvironment of yEGFP in the different constructions.

The fluorophore yEGFP presented similar lifetimes in the purified P2β-yEGFP and free yEGFP proteins in buffer. However P2β-yEGFP bound to the ribosome presented a significant increase in the contribution of lifetime τ_1, while P0-yEGFP showed a decrease. Curiously, these differences were observed together with variations in the time-zero anisotropy, r_0. Purified P2β-yEGFP and free yEGFP proteins in buffer showed the highest value $r_0 \sim 0.384$, near the

fundamental anisotropy value for OPE (theoretical maximum for r_0 value in OPE is 0.40, Lakowicz 2006), indicating a small angle between absorption and emission transition moments in yEGFP. The yEGFP-tagged proteins bound to ribosomes showed slightly lower r_0 values, r_0 = 0.375 for P0-yEGFP (~2% decrease), r_0~0.365 for P1α-yEGFP (~5% decrease), unlike P2β-yEGFP that showed a significant ~16% decrease (r_0 = 0.322). All these results together suggest the existence of slightly differences in the microenvironment of yEGFP in the different samples, probably due to possible interactions of yEGFP with neighboring residues of the CTD of P0, P1α and P2β, when bound to the ribosome. These local interactions may activate photophysical processes in yEGFP, responsible for the changes in the time-zero anisotropy values.

Table 5.4. Fluorescence lifetimes and anisotropy decay parameters of stalk proteins in solution

Sample	a_1 (±0.05)	τ_1 (ns) (±0.1)	a_2 (±0.05)	τ_2 (ns) (±0.1)	$\langle\tau\rangle_1$ (ns) (±0.1)	$\langle\tau\rangle_2$ (ns) (±0.2)	r_0 (±.005)	ϕ (ns) (±1)	ϕ [a] (ns) (±1)
Free yEGFP	0.58	2.3	0.42	1.0	1.8	2.0	0.382	12	15
Free P2β-yEGFP	0.47	2.4	0.53	1.2	1.8	2.0	0.384	12	15
P0-yEGFP ribosome	0.57	2.2	0.43	0.9	1.6	1.9	0.375	21	26
P1α-yEGFP ribosome	0.61	2.2	0.39	0.9	1.7	1.9	0.365	23	28
P2β-yEGFP ribosome	0.69	2.4	0.31	1.0	2.0	2.2	0.322	26	32

Samples: free yEGFP from cellular extracts; purified ribosomes containing P1α-yEGFP and P2β-yEGFP, and purified free P2β-yEGFP from cellular extracts, were resuspended in buffer 1.
λ_{exc}= 482 nm, λ_{em}= 515 nm (slits 8 nm). T= 30ºC. 5 MHz. Cuvette measurements.

Fluorescence lifetimes and fluorescence anisotropy decays were analysed using Globals program (LFD. Irvine, CA). Numbers in parentheses represent the upper and lower limit of the recovered values (at the 67% confidence level) using rigorous error analysis, as described in Beechem *et al.* (1991).

[a] Calculated rotational correlation time values at T=22ºC.

Figure 5.14 shows the time-resolved fluorescence anisotropy decays determined at 30ºC for the purified ribosome samples in buffer, together with a sample of free yEGFP protein in buffer for comparison.

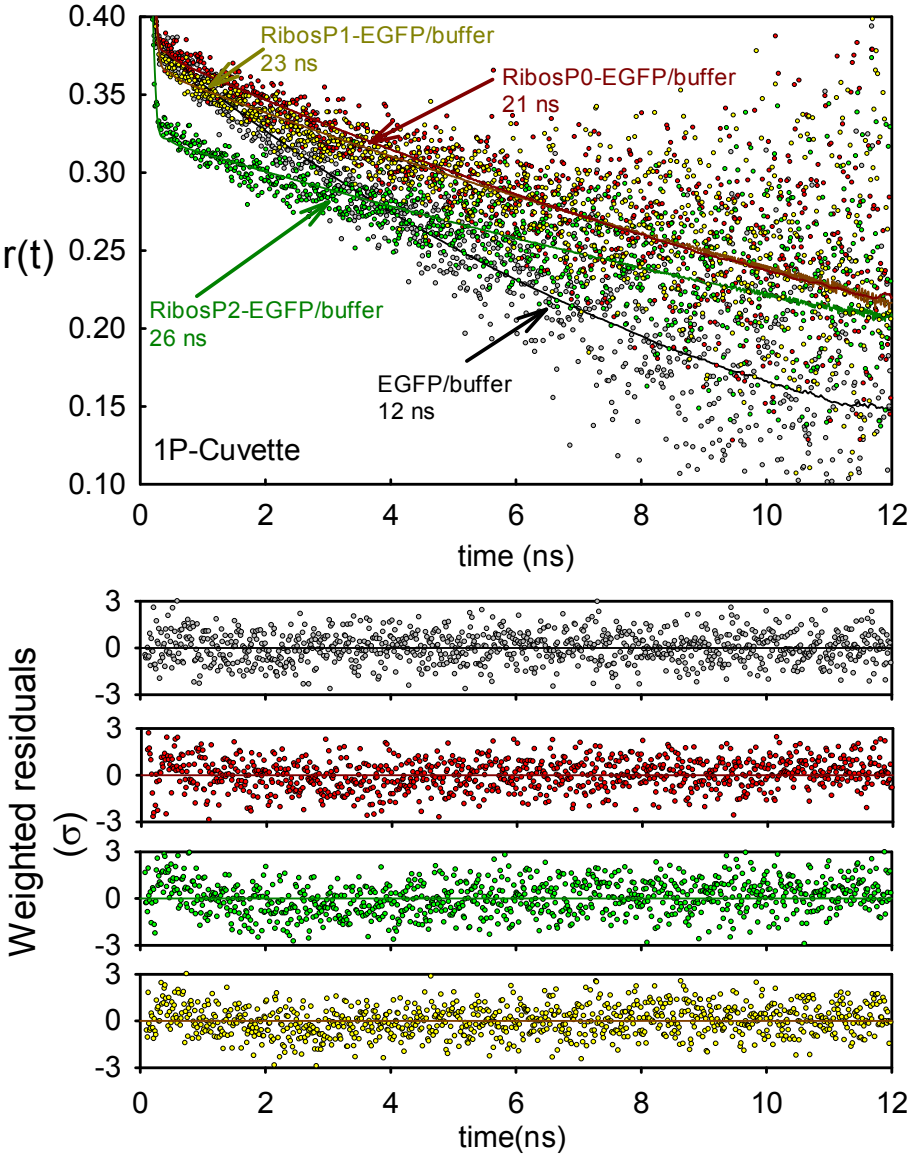

Figure 5.14. Representative OPE time-resolved fluorescence anisotropy measurements of purified yEGFP and stalk proteins tagged with yEGFP from purified ribosomes in buffer (cuvette studies). Purified ribosomes from yeast cells expressing P0-yEGFP (red), P1α-yEGFP (yellow), P2β-yEGFP (green) and purified free yEGFP protein from cellular extracts of EGFP strain (dark grey), resuspended in buffer 1, were measured in the laser cuvette spectrometer.

Solid lines correspond to the fitted data. The randomly distributed weighted residuals are shown below to illustrate the good quality of the fit, with χ^2 values lower than 1.1 for all the experiments.

λ_{exc}= 482 nm, λ_{em} = 515 nm (8 nm slits), 5 MHz. T=30ºC.

We don't observe any difference in the rotational correlation time of free proteins yEGFP (27 kDa) and P2β-yEGFP (39 kDa) having yEGFP attached trough the flexible CTD chain, ϕ = 12 ns. For globular proteins the rotational correlation time is proportional to the molecular mass. Therefore, if the two fused proteins (P2β and yEGFP) were rotating as one rigid unit, it would be expected a rotational correlation time $\phi \geq 17$ ns for P2β-yEGFP, compared to the experimental value of 12 ns. The CTD is very flexible, and our results confirm that yEGFP attached to the CTD of P2β, was freely moving together with the CTD, and it rotation was not affected by the presence of P2β.

When the stalk proteins were bound to the ribosome, the rotational motions of yEGFP were slowed down, with rotational correlation times, $\phi = 21\pm1$ ns for P0-yEGFP, $\phi = 23\pm1$ ns for P1α-yEGFP, and $\phi = 26\pm1$ ns for P2β-yEGFP, around ~1.8-2.2 times slower than yEGFP motions in the unbound proteins. The global rotation of the whole ribosome (~4×10^6 Da) is in the ms range, and time resolved anisotropy techniques only can inform about rotational motions in the ns range, thus these experimental rotational correlational times are informing about the flexibility of the proteins bound to the "immobile" ribosome (60S subunit of the ribosome). Our results revealed that yEGFP rotational motions were affected by the presence of the other P-proteins of the ribosome stalk, suggesting some kind of interaction between the CTD domains of neighbor proteins in the ribosome stalk. The CTD domain of P0 seemed to be more flexible and less affected by the presence of the other stalk proteins. However the mobility and the photophysical properties of yEGFP attached to the CTD of P2β seemed to be more influenced by the presence of the CTD of the other stalk proteins, or by its own CTD.

5.2.4 Dynamics of free yEGFP and L25-EGFP bound to the ribosome in the cytoplasm of *S. cerevisiae* live cells

We have calibrated the TPE micro-spectrometer for rotational motion studies in live yeast cells, analysing the behavior of two control strains expressing free yEGFP, and the EGFP-tagged ribosomal protein, L25.

L25 is a primary 60S subunit protein that binds to 25S rRNA and plays a major role in large subunit assembly and protein translation, helping in the enzymatic processing of nascent polypeptides. The ribosome itself serves as a platform for the spatially and temporally regulated association of enzymes, targeting factors and chaperones that act upon the nascent polypeptides emerging from the exit tunnel. L25, located near the exit channel, is involved in almost all interactions of the ribosome with ribosome associated factors (Kramer *et al.* 2009). L25 strain express the ribosomal protein L25 with EGFP attached to the CTD without any linker. As L25 protein lacks any flexible region in its CTD like stalk proteins, then it can be used as a control sample for EGFP restricted motions. The strain expressing free yEGFP was used in this work as a control sample for totally free motion of yEGFP in the crowded cytoplasm.

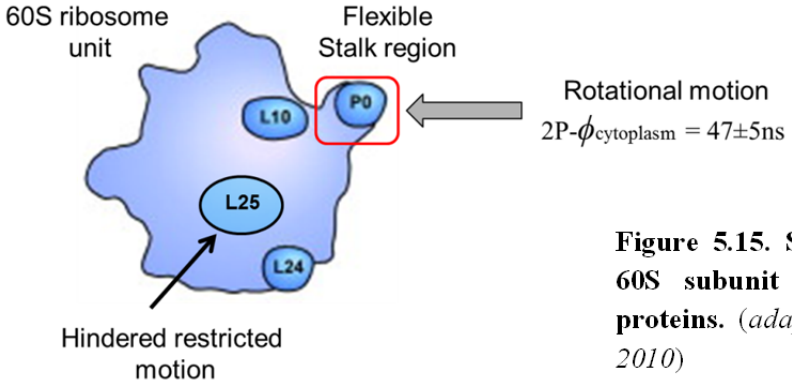

Figure 5.15. Scheme of the ribosome 60S subunit showing L25 and P0 proteins. (*adapted from Kressler et al. 2010*)

Single-point time-resolved fluorescence intensity and anisotropy measurements were carried out in the cytoplasm of live yeast cells expressing L25-EGFP and free yEGFP, using the laser micro-spectrometer with TPE excitation setup, as was described in Materials and Methods.

We performed fluorescence measurements selecting random points in the cytoplasm of the yeast cells, as the expression profile of *S. cerevisiae* strains showed homogeneous distribution of the fusion proteins in the cytoplasm (Table 5.3). In each point, we recorded total fluorescence intensity, $I_{open}(t)$, and parallel, $I_{HH}(t)$, and perpendicular, $I_{HV}(t)$, polarized fluorescence intensity decays for 30 s, to avoid photobleaching of EGFP, and cell damage. The decays were extracted from the TTTR raw data file using SymphoTime software (PicoQuant), and were

analysed with Globals software (LFD, Irvine, CA) as described in Materials and Methods.

Figure 5.16 shows a representative time-resolved anisotropy experiment for these proteins, with fluorescence intensity and anisotropy parameters in figure legend.

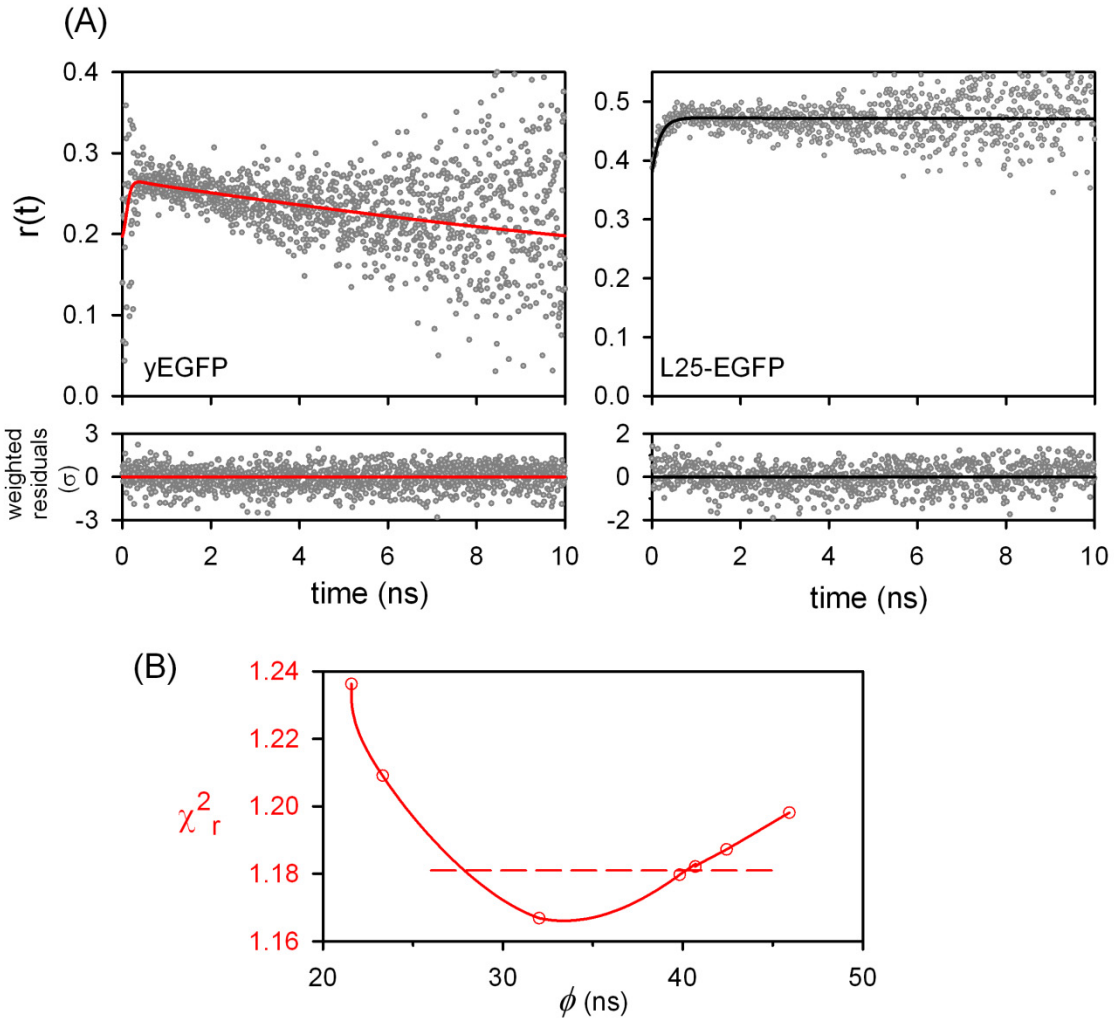

Figure 5.16. Representative experiments of single-point TPE fluorescence time-resolved anisotropy of free yEGFP and L25-EGFP expressed in the cytoplasm of live cells. (A) Fluorescence anisotropy decays built from the experimental and fitted polarized components, $I_{HH}(t)$ and $I_{HV}(t)$, for yEGFP (left) and L25-EGFP (right). The corresponding weighted residual distributions are shown below the anisotropy decays (χ^2 values lower than 1.5 for all the experiments). Experimental *r(t)*: grey points. Fitted *r(t)*: red and black continuous line
yEGFP: a_1=0.45, τ_1=2.6 ns, a_2=0.55, τ_2=1.2 ns, ϕ=32 ns
L25-EGFP: a_1=0.86, τ_1=2.6 ns, a_2=0.14, τ_2=1.1 ns, r_0=r_∞ (no motion).
(B) Confidence interval determined from the rigorous error analysis, for the rotational correlation time is shown as a solid line for yEGFP (red). Dashed line represents the χ^2 value corresponding to the 67% confidence level ($\pm 1\sigma$) measurement.

λ_{exc} = 850 nm, λ_{emiss}= FF01-520/35 (Semrock). 80.6 MHz. T= 22°C.

Table 5.5. TPE fluorescence lifetimes and anisotropy decay parameters for free yEGFP, L25-EGFP, P0-yEGFP, P1α-yEGFP and P2β-yEGFP expressed in the cytoplasm of living *S. cerevisiae* cells. Effect of Sordarin

Sample	a_1 (±0.02)	τ_1 (ns) (±0.2)	a_2 (±0.02)	τ_2 (ns) (±0.2)	$<\tau>_1$ (ns) (±0.2)	$<\tau>_2$ (ns) (±0.3)	r_0	$<\phi>$ (ns)
yEGFP (n=21)	0.44	2.6	0.56	1.2	1.8	2.1	0.32 (±0.09)	32 (±4)
P0-yEGFP (n=68)	0.40	2.7	0.60	1.3	1.8	2.1	0.32 (±0.07)	47 (±6)
P0-yEGFP + Sordarin (n=51)	0.41	2.6	0.59	1.2	1.8	2.0	0.34 (±0.07)	52 (±8)
P1α-yEGFP (n=66)	0.41	2.6	0.59	1.2	1.8	2.0	0.29 (±0.07)	44 (±5)
P1α-yEGFP + Sordarin (n=49)	0.43	2.6	0.57	1.2	1.8	2.1	0.35 (±0.08)	45 (±5)
P2β-yEGFP (n=89)	0.45	2.6	0.55	1.3	1.9	2.1	0.25 (±0.06)	41 (±4)
P2β-yEGFP + Sordarin (n=39)	0.43	2.6	0.57	1.2	1.8	2.1	0.31 (±0.08)	42 (±4)
L25-EGFP (n=7)	0.84	2.6	0.16	1.1	2.4	2.5	0.45 (±0.01)	-----

Samples: inmovilized yeast cells in freshly YNBD medium. .
Sordarin treatment: cells in freshly YNBD medium were preincubated with 30 µg/ml sordarin for 30 min. at 30ºC without washing before measurements.
Fluorescence lifetimes and anisotropy decays were analysed using Globals program (LFD. Irvine, CA). Numbers in parentheses represent the sample-to-sample error (confidence limits at the 67% level, ±1σ). *n* represents the number of independent cell measurements

λ_{exc} = 850 nm, λ_{em}= FF01-520/35 (Semrock). 80.6 MHz. T= 22°C

As was expected, the rotational behavior of free yEGFP and L25-EGFP/ribosome were very different in the cytoplasm: yEGFP showed a single rotational correlation time of 32± 4 ns, reflecting free rotational motion of the

fluorescent protein yEGFP in the crowded environment of the cytoplasm (about 2-fold slower than EGFP in buffer solution, see 5.1.9 Section); while L25-EGFP displayed a residual anisotropy, r_∞, coincident with the time zero anisotropy, r_0, indicative of totally hindered motion when it is bound to the ribosome.

Mean values from yEGFP samples (n=21), and L25-EGFP samples (n= 7) have been summarized in Table 5.5. The contribution of the longest lifetime changes from 44% for yEGFP to 84% for L25-EGFP. This behavior is indicative of the different microenvironment of the EGFP fluorophore in these two samples, besides that L25-EGFP has a different variant of EGFP, which results in an increase in the amplitude-weighted average lifetime, $<\tau>_I$, from =1.8ns to 2.4 ns.

L25-EGFP showed essentially no motion in the time-resolved anisotropy experiment. These results suggested that the ribosomal protein L25 was located in the 60S subunit in a very restricted environment, unlike yEGFP, which is fully exposed and freely rotating in the cytoplasm.

The time-resolved anisotropy decays of these two proteins showed the sensitivity of the instrument to the two most extreme cases of mobility we may found for any EGFP tagged protein expressed in the cytoplasm of living yeast cells, from total free rotation to totally hindered motion.

5.2.5 Dynamics of ribosome stalk proteins in *S. cerevisiae* live cells. Effect of sordarin

In the previous Section we characterized the photophysics and hydrodynamical behavior of the purified free yEGFP and the yEGFP tagged proteins in aqueous solutions. Rotational motions of yEGFP-tagged stalk proteins bound to the purified ribosomes showed rotational correlation times, $\phi \sim$ 26-32 ns in buffer 1 at 22ºC. The flexibility of the CTD domains of these stalk proteins were near the resolution limit for the fluorescence lifetime of the yEGFP variant (see section 5.2.3).

Here we present the time-resolved fluorescence anisotropy study we run for these samples, using the TPE micro-spectroscopy polarization methodologies developed in this work. We expected the rotational motions of these proteins will be slowed down in the cytoplasm of living cells due to macromolecular crowding

effects. Designing the experiment we were aware of the limitations of this study, owing to the short lifetime of EGFP, especially for the yEGFP variant, which showed two fluorescence lifetimes with a high percentage of a short lifetime, resulting in shorter average lifetimes than other EGFP variants.

Based on the results obtained for free yEGFP and hindered L25-EGFP (section 5.2.4), our goal here was just to distinguish between flexible and rigid states of the CTD stalk proteins, depending on the ribosome state, treating cells with Sordarin.

Sordarin and its derivatives are antifungal compounds of potential clinical interest. They are selective inhibitors of protein synthesis in fungal organisms. In sensitive cells, sordarin blocks the release of EF2 during the translocation step, stopping protein synthesis. Previous published work was compatible with a direct participation of the ribosomal stalk components in the binding of sordarin to its target. Moreover, EF2 and the stalk ribosomal protein P0 have been described as targets of sordarin and its derivatives (Santos *et al*. 2004). However, the participation of additional proteins and pathways in this process cannot be ruled out: other components of the ribosome stalk have been shown to be somehow involved in the sordarin mode of action (Gómez-Lorenzo *et al*. 1998).

In summary, the ribosome stalk is a highly flexible domain of the 60S subunit, and its mobility may be related with the recruitment of the soluble factors that regulated protein synthesis. Sordarin is an antifungal compound that blocks the ribosome function through its binding to the soluble factor EF2. Several previous reports were focusing in the role of the stalk in the way of action of sordarin. These data suggested that stalk mobility could be related to the inhibitory action of sordarin. Therefore, we have studied here if the mobility of stalk proteins was affected by sordarin.

TPE study of the rotational mobility of P0. Effect of sordarin.

P0 can be considered as the most important protein in the ribosome stalk. P0 forms the stalk base, its CTD domain serves to anchor the acidic proteins and it is essential for cell viability.

We have characterized the possible changes in the mobility of the CTD

domain of the stalk protein P0, by performing time-resolved fluorescence intensity and anisotropy measurements in the cytoplasm of live yeast cells, expressing P0-yEGFP, in the absence and in the presence of 30 µg/ml of sordarin (30 min. preincubation without washing).

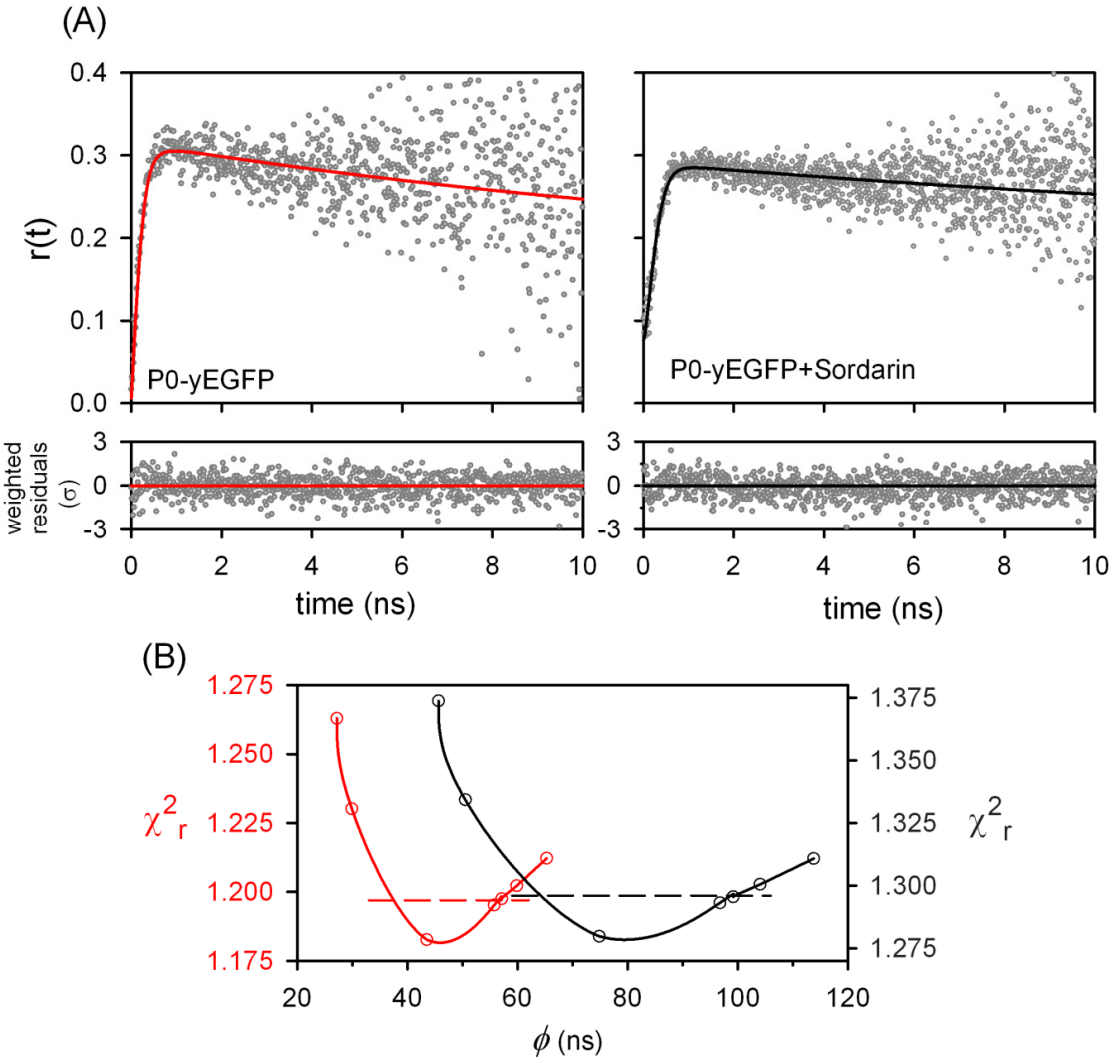

Figure 5.17. Representative experiments of single-point TPE fluorescence time-resolved anisotropy of cells expressing P0-yEGFP untreated and treated with sordarin. (A) Fluorescence anisotropy decays built from the experimental and fitted polarized components, $I_{HH}(t)$ and $I_{HV}(t)$, for untreated (left) and treated with sordarin (right) P0-yEGFP cells. The corresponding weighted residual distributions are shown below the anisotropy decays (χ^2 values lower than 1.5 for all the experiments).

Experimental $r(t)$: grey points. Fitted $r(t)$: red and black continuous line

P0-yEGFP: a_1=0.42, τ_1=2.65 ns, a_2=0.58, τ_2=1.26 ns, ϕ=43 ns

P0-yEGFP sordarin: a_1=0.40, τ_1=2.6 ns, a_2=0.60, τ_2=1.25 ns, ϕ=75 ns.

(B) Confidence intervals determined from the rigorous error analysis, for the rotational correlation times are shown as solid lines for P0-yEGFP (red) and P0-yEGFP sordarin (black). Dashed line represents χ^2 value corresponding to 67% confidence level ($\pm 1\sigma$) measurement.

λ_{exc} = 850 nm, λ_{emiss}= FF01-520/35 (Semrock), 80.6 MHz, T= 22°C.

In Figure 5.17 we compared two time-resolved fluorescence anisotropy experiments for P0-yEGFP in the presence or in the absence of sordarin. Anisotropy data was analyzed using the simplest model: a single population showing a single rotational correlation time, in both cases, in the presence and in the absence of sordarin.

Fluorescence intensity decay of P0-yEGFP was bi-exponential, with τ_1 = 2.7 ns (40 %) and τ_2 = 1.3 ns (60 %), and $<\tau>_1$ = 1.8 ns.

Comparing with L25-EGFP anisotropy decay (see Section 5.2.4 and Figure 5.16), the CTD domain of P0, in P0-yEGFP untreated cells, kept its flexible character in the cytoplasm of *S. cerevisiae* cells. Its rotational mobility was ~1.8 times slower than determined for the purified ribosome in buffer, as expected due to crowding effects of the cytoplasm, with an apparent micro-viscosity about 2 times larger than that of aqueous solution at room temperature (see Section 5.1.9). The rotational motions of yEGFP in P0-yEGFP are slowed down ~1.5 times with respect the mobility of the free protein yEGFP in the cytoplasm (see Table 5.5).

Sordarin treatment did not change the fluorescence lifetimes values of P0-yEGFP and their distribution. However, fluorescence anisotropy decays of P0-yEGFP cells treated with sordarin showed slower rotational behavior, comparing with P0-yEGFP untreated cells.

The anisotropy decay presented in Figure 5.17 (right) corresponds to one of the most affected cells treated with sordarin, showing near no motion of the CTD domain of P0 in P0-yEGFP: ϕ = 75 ns (65-100 ns).

The average rotational correlation times $<\phi>$ estimated from *n* independent experiments are summarized in Table 5.5. Treatment with sordarin increased $<\phi>$ from 47 ± 6 ns (*n*=68; untreated cells) to 52 ± 8 ns (*n*=51; treated cells).

These results suggest that sordarin could reduce P0 CTD mobility, and therefore, P0 stalk protein would be involved in the mechanism of action of sordarin. Comparing the mean rotational correlation time values from *n* independent determinations for sordarin treated and untreated cells, apparently the rotational change induced by sordarin was statistically significant, but these

results have to be taken with caution due to the large uncertainty in the TPE determination of these rotational correlation times. In Figure 5.17, the confidence interval for the rotational correlation time, estimated from rigorous error analysis, was smaller for P0-yEGFP (38-58 ns) in comparison to P0-yEGFP plus sordarin, that showed a broad and asymmetric error interval (65-100 ns). As rotational correlation times became longer, the larger the fitting error, due to the intrinsic limitation imposed by the EGFP lifetime (~2.6 ns). For this reason, this analysis showed the limitations of the time-resolved anisotropy technique for sordarin treated cells to distinguish between a single population of P0-yEGFP ribosomes whose mobility was reduced, or the existence of two populations, one keeping their flexibility, and the other immobile due to the sordarin effect. In the next section, we present the same study using OPE, a better approach to determine long rotational correlation times in our microscope setup.

It should be noted that the experimental time zero anisotropy values, r_0, for yEGFP ribosomal stalk constructions were smaller than determined for the ribosomal protein L25-EGFP in the cytoplasm of living cells (see Table 5.5). Since the experimental conditions are identical for both measurements, we cannot explain the observed decrease in r_0 for yEGFP as an effect of optical aberrations. yEGFP and EGFP are different variants of the green fluorescent proteins, showing different lifetimes, and different r_0 values. For TPE experimental conditions (λ_{exc}= 850 nm, and λ_{em}= 520nm), r_0 (P0-yEGFP) < r_0 (L25-EGFP).

OPE study of the rotational mobility of P0. Effect of sordarin.

The main limitation in the estimation of the very long rotational correlation times in P0 treated with sordarin was the estimation of the proper background contribution to the experimental TPE $I_{HH}(t)$ and $I_{HV}(t)$functions. Since the autofluorescence signal was very low in our TPE experimental conditions (see Section 5.2.2), we estimated and fixed the background contribution to the decays from the measured dark counts of the detectors.

OPE microscope setup allowed to a better estimation of the uncorrelated background in the time-resolved decays, and a better definition of the rotational

correlation times (see Section 5.1.9).

We have repeated the fluorescence anisotropy measurements on P0-yEGFP strain with and without sordarin using the OPE micro-spectrometer setup. Figure 5.18 shows fluorescence anisotropy decays for representative measurements of these samples, excited with a picosecond diode laser of 482 nm. As in the previous experiments, the anisotropy decays were fitted to a mono-exponential function without a residual anisotropy term, reflecting no hindered motion.

Table 5.6 resumes the fluorescence intensity and anisotropy parameters determined for free yEGFP (n=17), P0-yEGFP (n=21) and P0-yEGFO treated with sordarin (n=19) samples. The fluorescence lifetimes and their distribution didn't change when cells were treated with sordarin. Comparing with TPE, τ_2 decreased from ~2.6 ns to ~2.34 ns, along with an increase in its contribution from 40% to 63%, showing essentially the same average lifetime ($<\tau>_I$=1.8 ns).

The mean rotational correlation time determined from n independent determinations in single points chosen randomly, showed no differences between treated ($<\phi>$ = 41 ± 3 ns) and untreated ($<\phi>$ = 40 ± 3 ns) P0-yEGFP samples with sordarin. Also, in the representative experiment presented in Figure 5.18, the confidence intervals for the rotational correlation time, determined from rigorous error analysis, were equivalent and nearly symmetric for both, P0-yEGFP in the presence and absence of sordarin (38-48 ns).

Differences among the rotational correlation time values determined for P0-yEGFP with and without sordarin, using OPE and TPE, were mainly originated in the uncertainty of the background contribution in TPE.

As in the case of TPE measurements, time-zero anisotropy values, r_0, determined with OPE micro-spectrometer setup were smaller than in cuvette experiments for the same samples (P0-yEGFP: r_0=0.28 in OPE versus r_0=0.38 in OPE cuvette). As we showed before, this decrease can be caused by optical aberrations of the microscope setup, which can be corrected in part by (see Section 5.1.10).

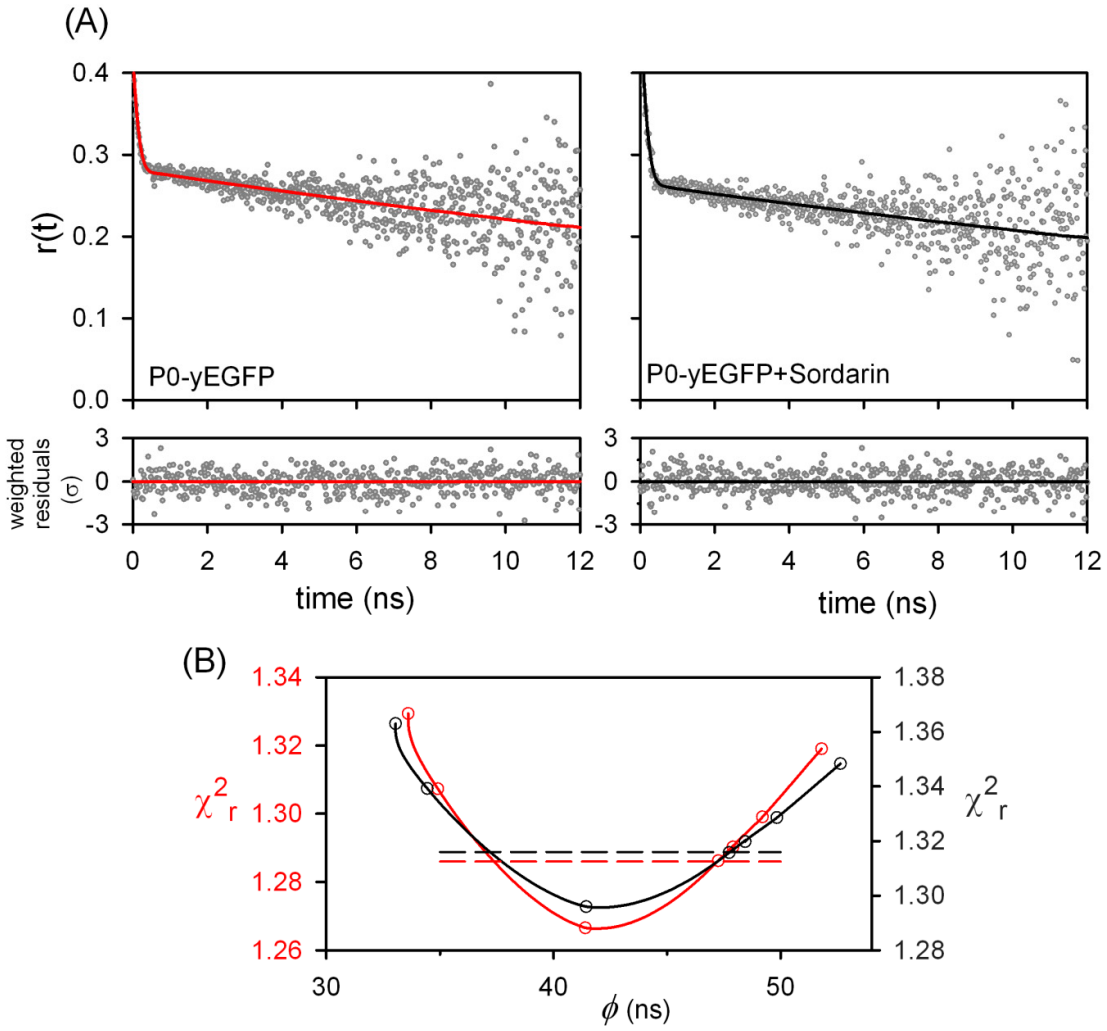

Figure 5.18. Representative experiments of single-point OPE fluorescence time-resolved anisotropy of cells expressing P0-yEGFP with (black) and without sordarin (red). (A) Fluorescence anisotropy decays built from the experimental and fitted polarized components, $I_{HH}(t)$ and $I_{HV}(t)$, corrected by the background, for untreated (left) and treated with sordarin (right) P0-yEGFP cells. The corresponding weighted residual distributions are shown below the anisotropy decays (χ^2 values lower than 1.5 for all the experiments).
Experimental *r(t)*: grey points. Fitted *r(t)*: red and black continuous line
P0-yEGFP: a_1=0.63, τ_1=2.34 ns, a_2=0.37, τ_2=1.12 ns, ϕ=41 ns
P0-yEGFP sordarin: a_1=0.61, τ_1=2.32 ns, a_2=0.39, τ_2=1.13 ns, ϕ=41 ns.
(B) Confidence intervals determined from the rigorous error analysis, for the rotational correlation times are shown as solid lines for P0-yEGFP (red) and P0-yEGFP sordarin (black). Dashed line represents the χ^2 value corresponding to the 67% confidence level ($\pm 1\sigma$) measurement.

λ_{exc} = 482 nm, λ_{emiss}= FF01-520/35 (Semrock), 5 MHz, T= 22°C.

Table 5.6. OPE fluorescence lifetimes and anisotropy decay parameters for free yEGFP and P0-yEGFP in the cytoplasm of living *S. cerevisiae* cells. Effect of Sordarin

Sample	a_1 (±0.02)	τ_1 (ns) (±0.05)	a_2 (±0.02)	τ_2 (ns) (±0.1)	$<\tau>_1$ (ns) (±0.1)	$<\tau>_2$ (ns) (±0.1)	r_0 (±0.01)	$<\phi>$ (ns) (±3)
yEGFP (n=17)	0.64	2.30	0.36	1.0	1.8	2.0	0.28	31
P0-yEGFP (n=21)	0.63	2.34	0.37	1.1	1.9	2.1	0.28	40
P0-yEGFP + Sordarin (n=19)	0.62	2.30	0.38	1.1	1.8	2.0	0.28	41

Samples: inmovilized yeast cells in freshly YNBD medium.
Sordarin treatment: cells in freshly YNBD medium were preincubated with 30 µg/ml sordarin for 30 min. at 30ºC without washing before measurements.
Fluorescence lifetimes and anisotropy decays were analysed using Globals program (LFD. Irvine, CA). Numbers in parentheses represent the sample to sample error (confidence limits at the 67% level, ±1σ). *n* represents the number of independent cell measurements

λ_{exc} = 482 nm, λ_{em}= FF01-520/35 (Semrock). 5 MHz. T= 22°C

TPE study of the rotational mobility of P1α. Effect of sordarin.

We characterized the mobility of other stalk proteins, P1α and P2β, and the effects of sordarin treatment.

P1α-yEGFP strain cells were incubated with or without 30 µg/ml of sordarin during 30 min. at 30ºC, before fluorescence intensity and fluorescence anisotropy measurements in the cell cytoplasm. Figure 5.19 shows a representative TPE anisotropy experiment for these samples.

Fluorescence intensity decay of P1α-yEGFP was bi-exponential, with τ_1 = 2.6 ns (41 %) and τ_2 = 1.2 ns (59 %), $<\tau>_1$ = 1.8 ns. TPE fluorescence anisotropy curves for P1α-yEGFP showed a single rotational correlation time, ϕ = 44 ± 5 ns, reflecting the flexibility of the CTD domain of the protein. The dynamics of yEGFP attached to the CTD of P1α were ~1.6 times slower in the cytoplasm comparing with buffer measurements (ϕ = 44 ± 5 ns and ϕ = 28 ± 1 ns,

respectively).

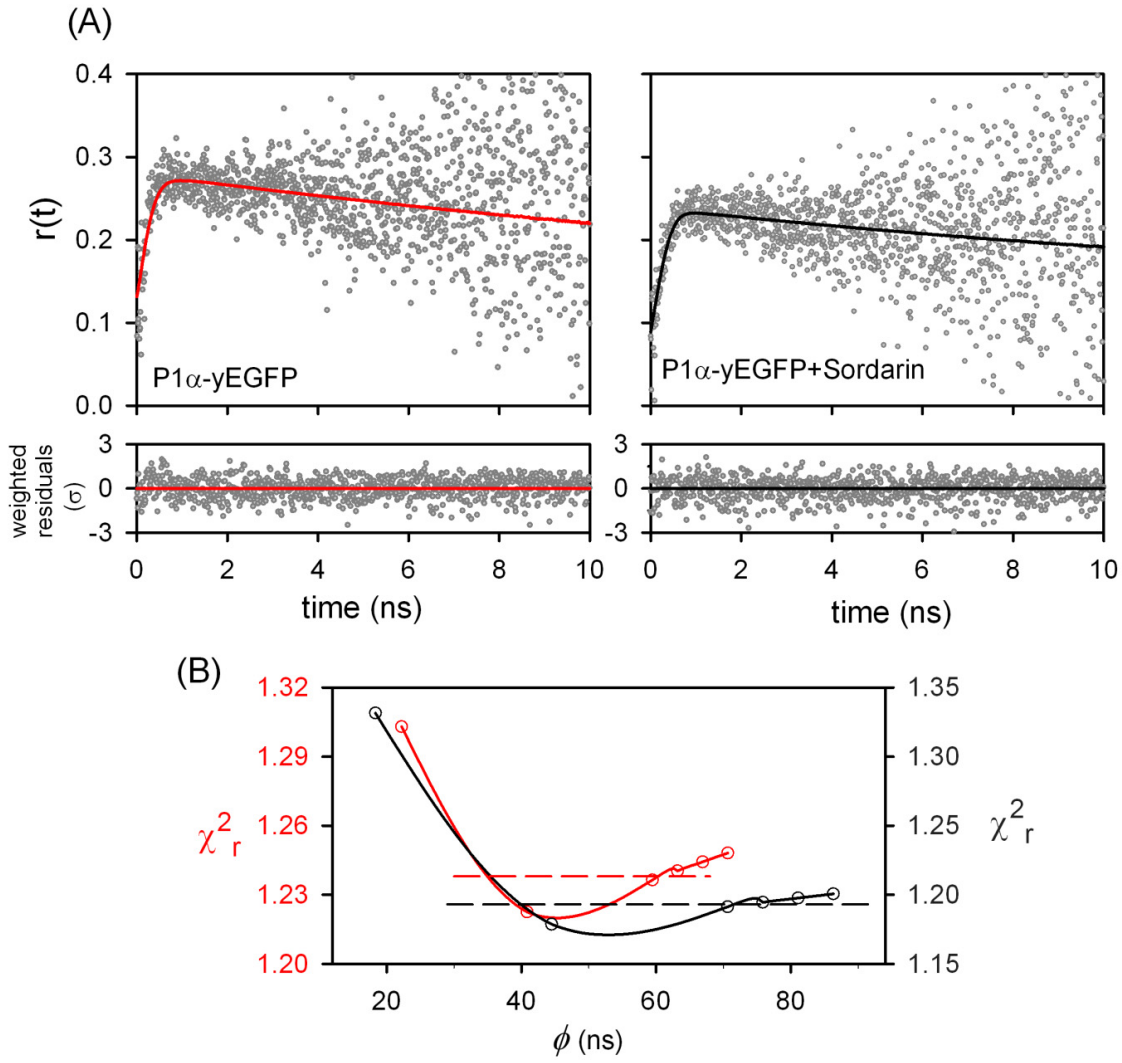

Figure 5.19. Representative experiments of single-point TPE fluorescence time-resolved anisotropy of cells expressing P1α-yEGFP with (black) and without sordarin (red). (A) Fluorescence anisotropy decays built from the experimental and fitted polarized components, $I_{HH}(t)$ and $I_{HV}(t)$, for untreated (left) and treated with sordarin (right) P1α-yEGFP cells. The corresponding weighted residual distributions are shown below the anisotropy decays (χ^2 values lower than 1.5 for all the experiments).
Experimental *r(t)*: grey points. Fitted *r(t)*: red and black continuous line
P1α-yEGFP: a_1=0.40, τ_1=2.61 ns, a_2=0.60, τ_2=1.22 ns, ϕ=41 ns
P1α-yEGFP sordarin: a_1=0.44, τ_1=2.56 ns, a_2=0.56, τ_2=1.23 ns, ϕ=44 ns.
(B) Confidence intervals determined from the rigorous error analysis, for the rotational correlation times are shown as solid lines for P1α-yEGFP (red) and P1α-yEGFP sordarin (black). Dashed line represents the χ^2 value corresponding to the 67% confidence level ($\pm 1\sigma$) measurement.

λ_{exc} = 850 nm, λ_{em}= FF01-520/35 (Semrock), 80.6 MHz, T= 22°C.

When we performed the same measurements in the presence of sordarin, we didn't observe appreciable changes in the fluorescence lifetimes and the rotational correlation time of P1α-yEGFP (ϕ = 45 ± 5 ns with sordarin *vs* ϕ = 44 ± 5 ns without sordarin). In contrast with P0–yEGFP, apparently sordarin binding to the ribosome didn't affect the mobility of the CTD domain of P1α–yEGFP.

The confidence interval of the rotational correlation time determined from rigorous error analysis (Figure 5.19 B) was asymmetric, with a similar shape in the presence or absence of sordarin (38-70 ns and 38-60 ns, respectively). The uncertainty increases at larger rotational correlation times because of the limitations imposed by the yEGFP ($<\tau>_I$ =1.8 ns).

TPE study of the rotational mobility of P2β. Effect of sordarin.

P2β-yEGFP strain cells were incubated with or without 30 μg/ml of sordarin during 30 min, at 30ºC, before fluorescence intensity and fluorescence anisotropy measurements in the cell cytoplasm.

Figure 5.20 shows a representative TPE anisotropy experiment for P2β-EGFP with and without sordarin.

Mean values of fluorescence intensity and anisotropy parameters are presented in Table 5.5. Fluorescence intensity decay of P2β-yEGFP was bi-exponential, with τ_1 = 2.6 ns (45 %) and τ_2 = 1.3 ns (55 %), $<\tau>_I$ = 1.9 ns. These data were very similar to those obtained for P0-yEGFP and P1α-yEGFP in the same experimental conditions (TPE). Also, rotational correlation time of P2β-yEGFP was similar to the other stalk proteins, ϕ = 41 ± 4 ns. As in the case of P1α-yEGFP, there was no variation with sordarin treatment: ϕ =42 ± 4 ns.

The confidence interval of the rotational correlation time obtained from rigorous error analysis (Figure 5.20 B) was similar in the presence or absence of sordarin (38-53 ns and 38-50 ns, respectively).

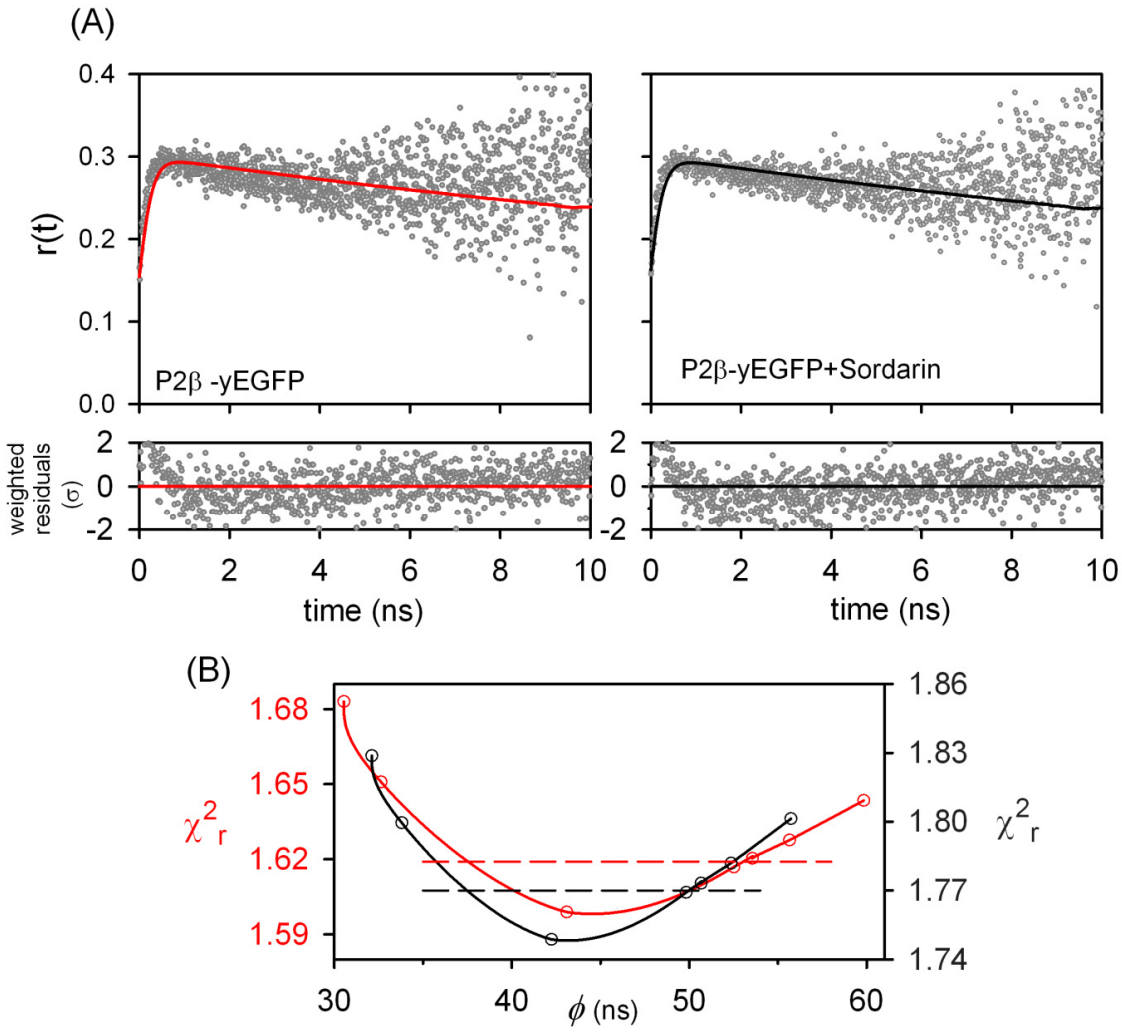

Figure 5.20. Representative experiments of single-point TPE fluorescence time-resolved anisotropy of cells expressing P2β--yEGFP with (black) and without sordarin (red). (A) Fluorescence anisotropy decays built from the experimental and fitted polarized components, $I_{HH}(t)$ and $I_{HV}(t)$, for untreated (left) and treated with sordarin (right) P2β-yEGFP cells. The corresponding weighted residual distributions are shown below the anisotropy decays (χ^2 values lower than 1.5 for all the experiments).
Experimental *r(t)*: grey points. Fitted *r(t)*: red and black continuous line
P2β-yEGFP: a_1=0.42, τ_1=2.64 ns, a_2=0.58, τ_2=1.29 ns, ϕ=43 ns
P2β-yEGFP plus sordarin: a_1=0.40, τ_1=2.58 ns, a_2=0.60, τ_2=1.25 ns, ϕ=42 ns.
(B) Confidence intervals determined from the rigorous error analysis, for the rotational correlation times are shown as solid lines for P2β-yEGFP (red) and P2β-yEGFP sordarin (black). Dashed line represents the χ^2 value corresponding to the 67% confidence level ($\pm 1\sigma$) measurement.

λ_{exc} = 850 nm, λ_{em}= FF01-520/35 (Semrock), 80.6 MHz, T= 22°C.

5.2.6 Global view of the effect of sordarin on the conformational dynamics of the ribosomal stalk proteins

Tables 5.5 and 5.6 summarize the mean values of the lifetimes and rotational correlation times from the *n* independent measurements performed in this study for each sample, with TPE and OPE, and the sample-to-sample error.

Surprisingly, the sample-to-sample error for each determined rotational correlation time is lower than the confidence interval from the rigorous error analysis (Globals program, Irvine CA). The sample-to-sample error was calculated from the fitting parameter values corresponding to the minimum χ^2. Rigorous error analysis χ^2 curves showed the limitations of the fitting procedure to provide absolute rotational correlation times values longer than 50-60 ns using yEGFP as fluorophore.

If we sum the *n* values for all the measured strains, it can be notice that the total number of independent measurements, performed on the cytoplasm of single cells, for the six different yeast strains used in this study was ~500. Each total intensity and anisotropy decays correspond to a single-point measurement in a random location of the cell cytoplasm, with no more than two points measured per cell. This implies that the analysed results were measured in ~250 cells, but really we have measured a larger number of samples during the setup of the instrument. Here we have presented only data determined in the optimal experimental conditions, and we excluded all the measurements associated to instrumental and preparation problems.

We were aware of the natural heterogeneity present in a living organism, and our first trial was to characterize the dynamics of the ribosome stalk components in the whole cytoplasm of each cell, taking the advantage of the optical spatial resolution of the TPE and OPE confocal microscope. We acquired steady-state XY anisotropy sections of single cells for the different strains (not shown), but steady-state measurements were a complex combination of lifetimes, time-zero anisotropy and rotational correlation time values of the yEGFP and the cell autofluorescence. For our instrumental conditions, steady-state anisotropy methods didn't provide any consistent information about the ribosome dynamics

in the cytoplasm of living yeast cells. For this reason, we moved to single-point time-resolved measurements, to get a detailed picture of the spectroscopic and hydrodynamical behaviour of yEGFP-tagged proteins.

Locations for the single-point time-resolved anisotropy measurements were chosen randomly in the cytoplasm, but the fact that we could not measure more than two points per cell to avoid damaging the cells, our results could hide possible changes in specific cellular locations not measured. In any case, we think that box and histogram plots may highlight better details that may be lost in the average values showed in Tables 5.5 and 5.6. Figure 5.21 is a global representation of OPE and TPE rotational correlation times of yEGFP and ribosome stalk proteins with and without sordarin: box whisker plots (A and B) and histograms (C).

The box plot or box chart, is a graphical representation of key values from summary statistics. The box is determined by the 25^{th} and 75^{th} percentiles, while whiskers indicate mean ± 1σ value. The middle line of the each box indicates 50% quartile and the inner square box indicates the mean value for the overall measurement. On the right side of each box, it is showed the normal distribution curve representing the experimental rotational correlation values (circles) from individual measurements.

In the P0-yEGFP samples treated with sordarin, the distribution curves and the circles representing each individual measurement in the boxes diagram (Figure 5.21 A) noticed the possible presence of two different populations, a flexible and a near immobile population. The histogram plot (Figure 5.21 C) discriminates better the presence of two populations in P0-yEGFP samples. An important group of cells seems to be not affected by the treatment of sordarin (black dashed line), while some of them may present a slowdown in their CTD rotational mobility (black dotted line), which could be explained by the effect of sordarin on these cells.

The rotational correlation times determined for P2β-yEGFP samples are slightly faster than determined for P0-yEGFP. This difference is less clear for P1α-yEGFP samples. The acidic proteins P1α and P2β are smaller (12 kDa) than

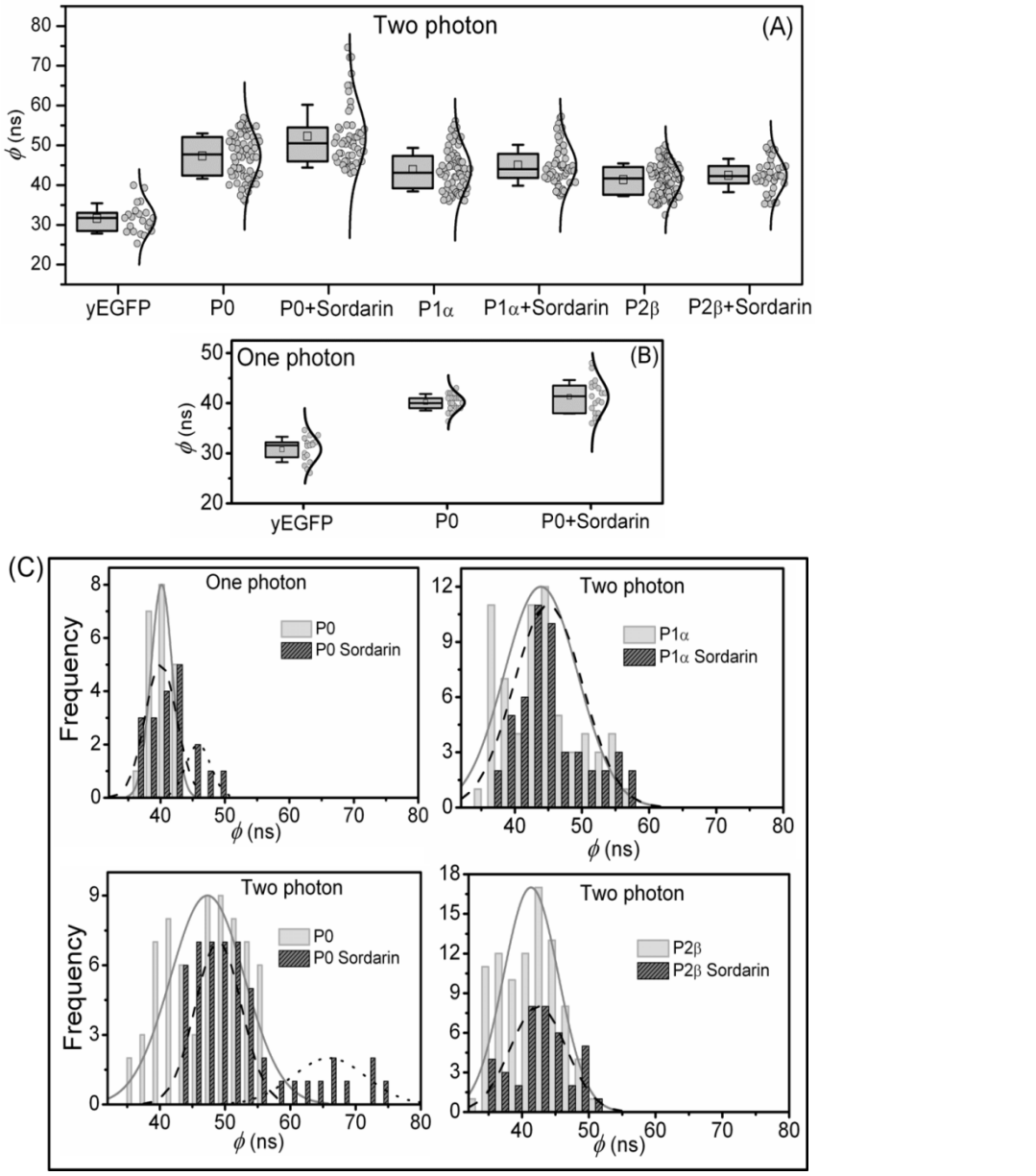

Figure 5.21. Statistical comparison of OPE and TPE rotational correlation times of ribosome stalk proteins. Effect of sordarin treatment. Box whisker plots show distributions of rotational correlation times from yEGFP (yEGFP free in cytoplasm), P0 (P0-yEGFP), P1α (P1α-yEGFP), P2β (P2β-yEGFP), with and without sordarin, determined using the TPE microscope setup **(A)** and the OPE microscope setup **(B)**. The box indicates the interquartile range from 25% to 75% and the whisker indicates the $\pm 1\sigma$ values. The middle line of the each box indicates 50% quartile; inner square box indicates the mean value for the overall measurement. Normal distribution of values plotted on the right side of the box, while circle indicates the correlation time values from individual measurements. **(C)** Histogram representation from data in (A) and (B) box whisker plots. Left: comparison between OPE (up) and TPE (down) of P0 (P0-yEGFP) rotational correlation times. Right: TPE data of P1α (P1α-yEGFP, up) and P2β (P2β-yEGFP, down). Sordarin treatment was represented with dark bars (sordarin) and light bars (no sordarin). The normal distribution curves were incorporated in each treatment: light grey continuous line for experiments without sordarin and black dashed and dotted lines for experiments with sordarin.

P0 (34 kDa). There are two possible explanation for this: *i)* the faster motions of yEGFP attached to the flexible CTD domain of these proteins reflect the size change from P0 to P2β or P1α, or *ii)* there are two populations of acidic proteins, free in the cytoplasm, and bound to the ribosome stalk.

It has been proposed that there is a cytoplasmic pool of free acidic stalk proteins (Tsurugi *et al.* 1985). The real proportion of free/bound proteins in the cytoplasm of living cells is not clear, but estimations from cell supernatant fractions (100000×g, S-100) showed that always the proportion of protein P2β free was around 1 to 2 fold higher than P2α, while P1β was from 10 to 30 times lower than the P2 proteins (Ballesta & Remacha 1996). These numbers were approximate due to the fact that the proportion of the different proteins may change with the cell growth conditions.

Looking in detail the histogram of the rotational correlation time for P2β-yEGFP, one can notice a population at shorter times possibly due to the contribution fast rotating P2β-yEGFP free in the cytoplasm.

For the stalk proteins, P1α and P2β, we didn't detect the presence of the immobile CTD population from the rotational correlation time histogram, when were treated with sordarin. Therefore, sordarin seems to have no effect on the flexibility of the CTD region of P1α and P2β stalk proteins.

However, small changes may occur in the microenvironment of yEGFP in P2β upon interaction with sordarin. The time-zero anisotropy of P2β-yEGFP was significantly lower than the other strains in absence of sordarin. This result was confirmed in *in vitro*, and in cells measurements, and may suggest some interactions between yEGFP attached to P2β and the CTD domain of P2β or the other stalk proteins. P2β-yEGFP cells treated with sordarin showed an increase in the time-zero anisotropy value, suggesting that sordarin interaction may affect the 3-D global organization of the CTD domains of the stalk proteins.

Then, despite of the limitations of the lifetime of the fluorophore (~2.6 ns) our TPE and OPE anisotropy approach was able to detect changes in the flexibility of proteins bound to a very big structure like the ribosome, in living cells.

5.3 Detection of the ribosomal protein P0 in nuclear pre ribosomal complexes

5.3.1 Motivation

The cellular localization of the incorporation of P0 protein to pre-ribosomal particles remains controversial. Recent biochemical report indicated that the protein P0 was present in nuclear pre-ribosomal complexes together with other assembly factors like Nop7 in purified cellular fractions (Rodriguez-Mateos *et al.* 2009b).

The encouraging results obtained using two-photon FCS, molecular brightness analysis (García-Marcos *et al*. 2008), FLIM and time-resolved anisotropy techniques (this thesis) to study the ribosomal stalk, prompted us to apply a combination of FLIM-FRET and scanning cross Number and Brightness (N&B) analysis to clarify the controversial biochemical data concerning the cellular location of the P0 protein (Francisco-Velilla *et al.* 2013a). This work was done in collaboration with Dr. Juan Pedro García Ballesta (CBM, CSIC-UAM, Madrid), and Dr. Catherine Royer (CBS, CNRS-INSERM, Montpellier. France).

Cross N&B analysis is a very powerful technique that allows quantitative spatial mapping of the existence and stoichiometry of homologous and heterologous protein complexes in live cells (Digman *et al*. 2008b, 2009). This technique extends Fluorescence Correlation Spectroscopy to spatial mapping in 2D cellular images by a variance and covariance analysis per pixel of fluorescence fluctuations in multiple, rapid two channel raster scans. This technique is not available in our microscope set because it requires the acquisition of a sequence of intensity images with pixel dwell times ~50 μs and 4s frame time. The minimum dwell time in our instrument is 0.2 ms/pixel, thus this part of the study was done by Dr. Royer Group, using their microscope setup (Francisco-Velilla *et al.* 2013b. Submitted).

N&B results suggested the presence of FRET between P0-mCherry and Nop7-EGFP, from the negative covariance of the fluctuations determined in complexes of pre-ribosomal particles, located in the nuclear periphery of *S. cerevisiae* yeast cells.

Here we have studied the same samples by FLIM-FRET techniques to determine if the N&B observations were due to the proximity of P0 and Nop7 proteins within the pre-ribosomal complexes.

5.3.2 Intracellular mobility of the nucleus in live yeast cells

S. cerevisiae strains used for this study were described in Table 4.2. All of them were derived from the proteinase deficient strain BJ5458 (Martinez et al., 1999), which had a reduced autofluorescence. Cells were grown up to exponential phase and immobilized for fluorescence intensity and TPE-FLIM images as described in Materials and Methods.

Although the cells were immobilized in the cover slip sandwich, one limitation during the acquisition of FLIM images of the nuclear region was the natural motion of the nucleus in living cells. Typical total acquisition times for FLIM images in this work were ~1 min. During this time, many images we acquired showed a blurry nucleus, resulting in a loss of spatial resolution. A further problem was the size of the detection volume element in Z direction, greater than the size of the nucleus (see Section 3.3.1; Figure 3.9), causing contamination of the nucleus fluorescence signal by cytoplasm fluorescence.

Figure 5.22 shows three consecutive fluorescence intensity images of a cell expressing Nop7-EGFP in the nucleus. The intensity scale was saturated to highlight the nuclear periphery regions where Nop7-EGFP expression was much lower. We can notice the random mobility of the nucleus in this small time interval.

In the experimental conditions, the signal from Nop7-EGFP expressed near the nuclear membrane was very low, but we couldn't increase the acquisition time per pixel of the images to increase the signal to noise ratio because of the internal motion of the nucleus. Hence, to overcome this problem, we acquired four consecutive images for each cell with a time interval of 0.8-1 min between images, to determine the optimal Z position for the nucleus, and we discarded the very blurred or low counts images.

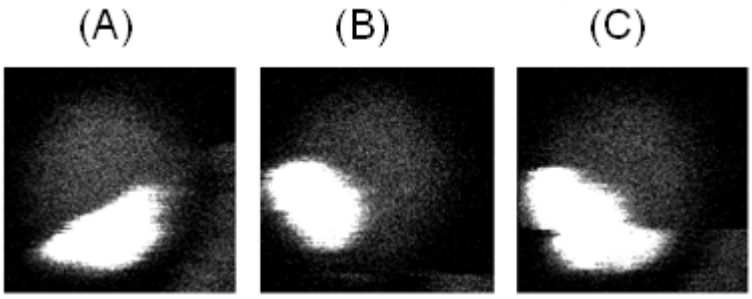

Figure 5.22. Three consecutive TPE fluorescence intensity images of a cell from Nop7-EGFP strain. Cells were grown up to exponential phase and immobilized for fluorescence intensity image in a "sandwich" coverslip. Three consecutive images (A, B and C) were collected at λ_{exc} = 850 nm, λ_{em} (donor channel) = FF01-520/35 (Semrock), 80.6 MHz and 22°C, with ~1 minute time interval between them. The intense region shows Nop7-EGFP protein expressed in the nucleus. The intensity scale was saturated to highlight all the nuclear regions.

5.3.3 Autofluorescence of WT strain cells in fixed and live conditions

We have tried to work with fixed cells to avoid the problem of nucleus motion. We started testing autofluorescence on fixed WT cells.

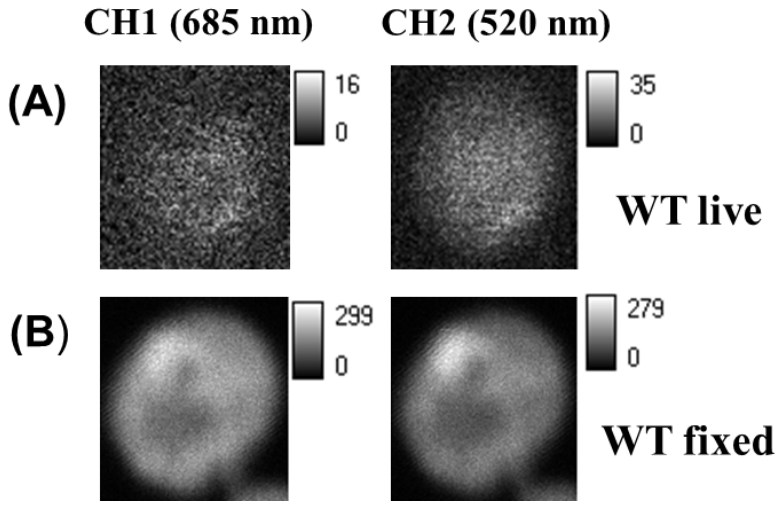

Figure 5.23. TPE autofluorescence intensity images from WT strain. WT cells were grown up to exponential phase. **(A)** Live cells were immobilized in a "sandwich" coverslip for live cell fluorescence image acquisition. **(B)** Fixed cells preparation using a standard fixing protocol for yeast cells (4% paraformaldehyde-2M sorbitol). Code set in the range 0 to the maximum counts per pixel in the image.
Left (CH1-acceptor): λ_{em}=FF01-685/40; Right (CH2-donor): λ_{em}=FF01-520/35 (Semrock).
λ_{exc} = 850 nm, 80.6 MHz. T= 22°C. 1.2 ms/pixel

Figure 5.23 shows representative fluorescence intensity images of live and fixed WT strain cells using a standard fixation protocol for yeast cells (4%

paraformaldehyde, 2 M sorbitol). Autofluorescence of WT live cells was very low as we showed before in the experimental conditions used in this work. However fixed cells presented an intense autofluorescence signal in both, donor and acceptor channels, in the whole cell, but especially in the nucleus, our region of interest in this study.

Autofluorescence lifetime parameters for live and fixed cells are summarized in Table 5.7. Fluorescence intensity decays of donor channel were built from the photons from ROIs of the 2P-FLIM image corresponding to the whole cell (live or fixed cells from WT strain). Time-resolved lifetime decay analysis showed a bi-exponential lifetime distribution with a longer lifetime component, τ_1= 2 ns, present in the two samples. Fixed cells showed higher contribution of the short lifetime component in comparison to live cells.

Table 5.7. Fluorescence lifetimes parameters of live and fixed WT cells

Sample	a_1 (±0.02)	τ_1 (ns) (± 0.1)	a_2 (±0.02)	τ_2 (ns) (± 0.1)	$<\tau>_1$ (ns) (± 0.1)
Live cells (*n*=10)	0.29	2.0	0.71	0.4	0.86
Fixed cells (*n*=7)	0.12	2.0	0.88	0.3	0.5

Fluorescence intensity decays were built from the photons from ROIs of the 2P-FLIM image in donor channel (λ_{em}=FF01-520/35, Semrock), corresponding to the whole cell (live or fixed cells from WT strain). Decays were analysed using Globals software (LFD, Irvine. CA).
(*n*) Indicates numbers of measured cells. Numbers in parentheses represent the sample to sample error (confidence limits at the 67% level).

The high autofluorescence level in fixed cells precludes its use in FRET-FLIM studies in the spectroscopic conditions of this work.

5.3.4 Rotational mobility of Nop7-EGFP and Mrt4-yEGFP proteins in the nucleus of live cells

Given the importance of the orientation factor in the interpretation of FRET experiments, we explored the rotational mobility of EGFP in P0-yEGFP, Mrt4-

yEGFP and Nop7-EGFP constructions using time-resolved fluorescence anisotropy techniques. We were not able to determine EGFP mobility in P0-yEGFP expressed in the nucleus, because of the low signal. As we showed in Section 5.2, EGFP showed unrestricted slow motions when attached to P0-ribosomes with an average rotational correlation time of 47 ± 6 ns under TPE. Note that this value corresponds to P0-yEGFP in the cytoplasm, where it is mainly expressed.

Figure 5.24 shows representative anisotropy decays for Mrt4-yEGFP and Nop7-EGFP proteins expressed in the nucleus. Mrt4-yEGFP and Nop7-EGFP show flat fluorescence anisotropy decays, ($r_0 = r_\infty = 0.44$) indicating no motion of EGFP in the nanosecond time range.

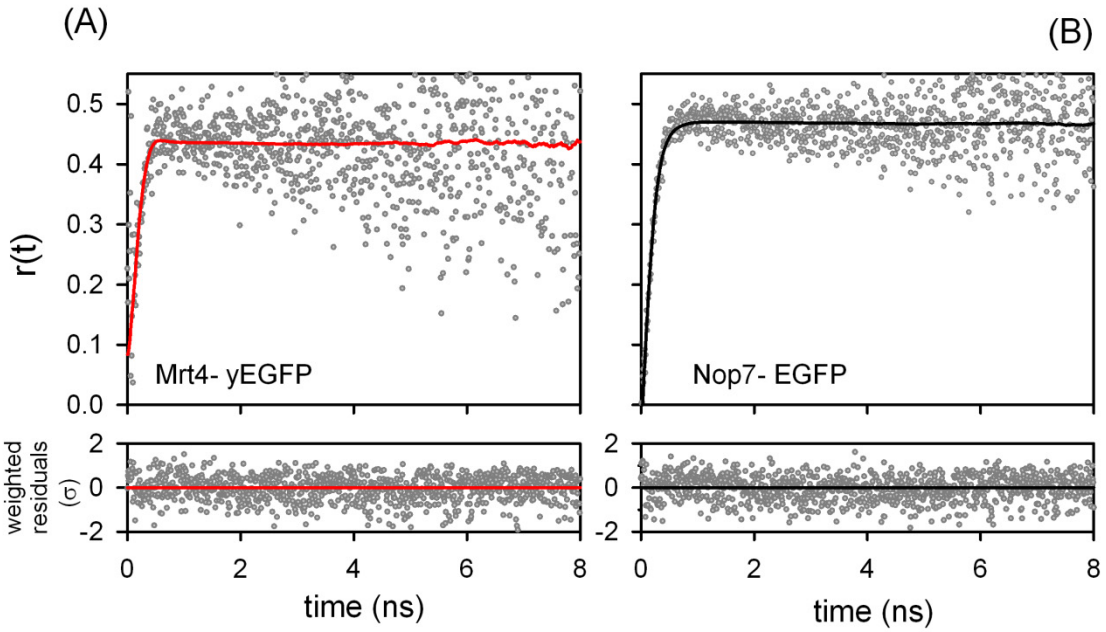

Figure 5.24. Representative TPE time-resolved anisotropy decays of cells expressing Mrt4-yEGFP (A, red) and Nop7-EGFP (B, black) proteins in the nucleus. Fluorescence anisotropy decays were built from the whole nucleus of single cells, and show flat fluorescence anisotropy decays, ($r_0 = r_\infty = 0.44$), indicating no motion of yEGFP or EGFP in the nanosecond time range.
Randomly distributed weighted residuals are presented (χ^2 values lower than 1.5 for all the experiments). Solid lines correspond to fitted data.

5.3.5 Interaction profile of P0-yEGFP with Nop7-mCherry and Mrt4-mCherry proteins in live yeast cells

We investigated the potential formation of complexes of pre-ribosomal particles in the nucleus of living cells containing P0 or Mrt4 proteins near Nop7

molecules (for intermolecular distances, $R < 10$ nm) by TPE fluorescence resonance energy-transfer/ fluorescence lifetime imaging (2P-FLIM FRET; EGFP: donor; mCherry: acceptor).

We have started this study using P0-yEGFP as a donor, expressed together with the acceptor FRET pairs: Mrt4-mCherry or Nop7-mCherry in *S. cerevisiae* yeast cells.

Two-color (GFP and mCherry) FLIM images were acquired simultaneously through a dichroic beam splitter FF560-Di01 and bandpass filters FF01-520/35 (EGFP; donor channel), and FF01-685/40 (mCherry; acceptor channel) (Semrock, Germany), with TPE at 850 nm. Limitation of the acquisition time per pixel imposed by nucleus motion led us to determine the FRET efficiency using the FRET-ROI approach, in which total fluorescence intensity decays of fusion proteins were built from the photons of regions of interest (ROIs) corresponding to the whole nucleus of single cells, and analyzed to a multi-exponential function, as described in 4.7.3 Section. Decays with less than 30,000 total counts were not included in the FRET-ROI analysis. With this strategy, we obtained an optimal number of counts for better fitting, but in other hand, we lost spatial resolution.

We quantified fluorescence lifetimes of P0-yEGFP, expressed alone or together with the mCherry-tagged proteins, from the whole nucleus of single cells. P0-yEGFP+Mrt4-mCherry sample was used as a negative control for FRET, since P0 and Mrt4 have the same binding site on the ribosome, and therefore, they can't be bound to the same pre-ribosomal particle.

Fluorescence intensity images presented in Figure 5.25 show the expression profile of cells from the strains: P0-yEGFP+Mrt4-mCherry (A) and P0-yEGFP+Nop7-mCherry (B). Left: acceptor emission channel; center, donor emission channel; and right, channels merge view, with artificial green color for donor image and red color for acceptor image. Figure 5.25 C presents the donor channel image for P0-yEGFP strain (donor only sample).

The proteins Mrt4-mCherry and Nop7-mCherry were homogenously distributed in the nucleus, while P0-yEGFP was distributed all over the

cytoplasm. Expression of Nop7 was higher in the nucleus than Mrt4. This homogeneous distribution suggested that tagged proteins complemented the absence of the native proteins in the transformed strains with little or no effect on cell growth. The expression of the protein P0 in the nucleus was very low, comparing with the cytoplasm and we were not able to detect it from the intensity images.

We can notice the reduced level of fluorescence signal in the acceptor channel: 20 or 60 counts per pixel in Mrt4-mCherry and Nop7-mCherry, respectively, *vs.* ~200-400 counts per pixel in the donor channel for P0-yEGFP, due to the low excitation efficiency for mCherry at 850 nm. The low fluorescence signal detected in the acceptor channel corresponded to the direct acceptor excitation plus the sensitized acceptor emission *via* FRET. Regardless, the low mCherry signal level, it helped us to localize the nucleus in the donor channel image (Figure 5.25; merged images).

Figure 5.25 D presents the box whisker plots of the amplitude weighted average lifetime determined at the donor channel emission, and Table 5.8 shows the corresponding fluorescence lifetime parameters.

P0-yEGFP in donor only samples showed two lifetimes of 2.3 ns and 1 ns, with an amplitude-weighted average lifetime $<\tau_D>_1$ = 1.8 ± 0.2 ns. For P0-yEGFP+Mrt4-mCherry donor-acceptor samples we didn't detect any significant decrease in the donor average lifetime $<\tau_{DA}>_1$ = 1.7 ± 0.2 ns. However, for P0-yEGFP+Nop7-mCherry donor-acceptor samples we observed a significant decrease in the donor average lifetime $<\tau_{DA}>_1$ = 1.6 ± 0.2 ns (*, significant). These results suggested the possible presence of FRET in P0-yEGFP+Nop7-mCherry pair, with an average efficiency of 11 %.

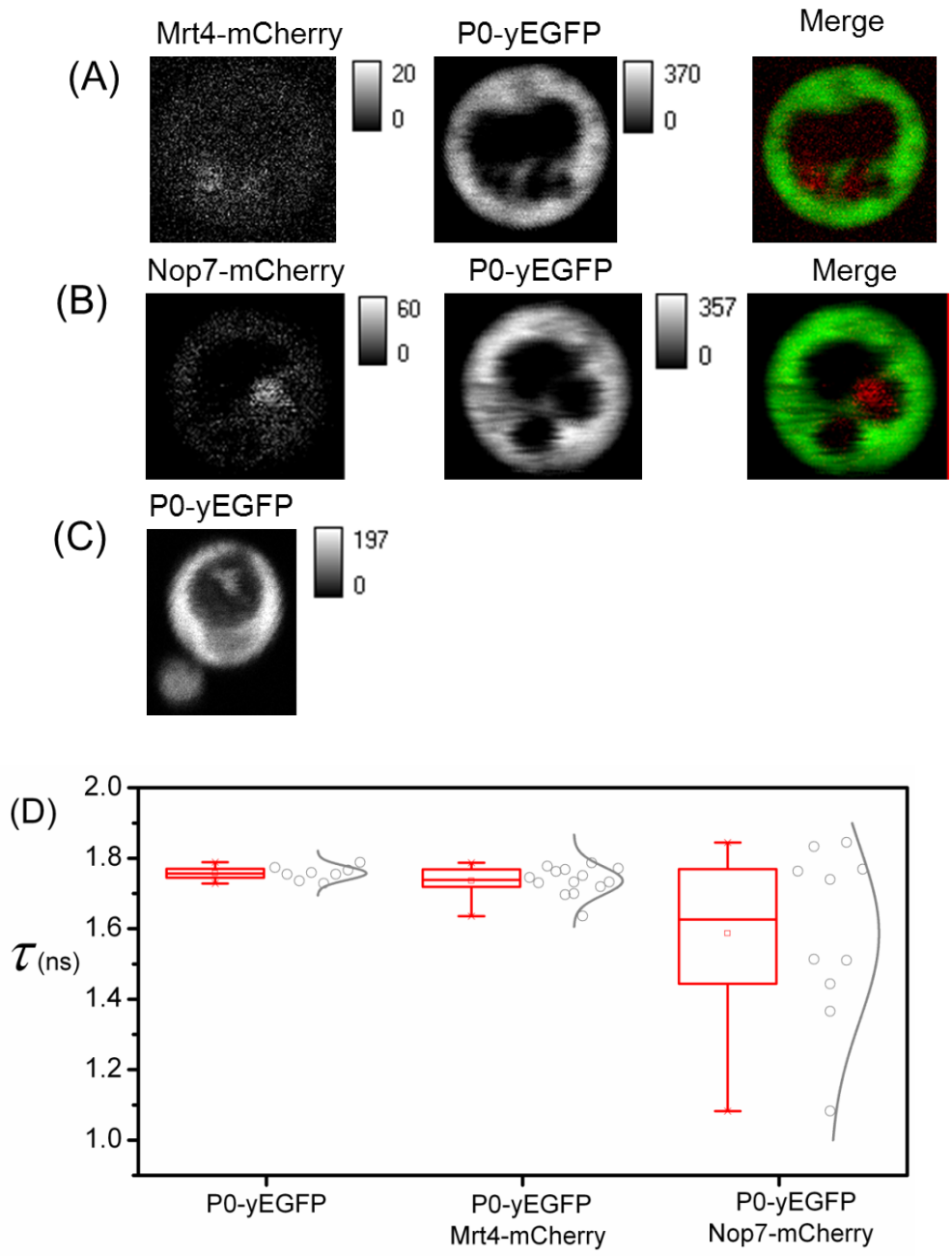

Figure 5.25. Expression profile and FRET-ROI analyses of P0-yEGFP strain (donor only), P0-yEGFP+Mrt4-mCherry (donor-acceptor) and P0-yEGFP+Nop7-mCherry (donor-acceptor) strains. (A-B) Fluorescence intensity images with the code set in the range 0 to the maximum counts per pixel in the image, determined for P0-yEGFP+Mrt4-mCherry (A) and P0-yEGFP+Nop7-mCherry (B) strains. Left: acceptor channel (FF01-685/40, Semrock); center: donor channel (FF01-520/35, Semrock); and right: donor and acceptor channels merge view, obtained with free Image J software (artificial green color for donor and red color for acceptor channels). **(C)** Donor channel image of P0-yEGFP strain (donor only). **(D)** Box whisker plots show distributions of the amplitude average lifetime of donor channel. The box indicates the interquartile range from 25% to 75%, whisker (the ±1σ values), middle line (50% quartile); inner square box (mean value for overall measurements). Normal distribution of values plotted on the right side of the box (circle indicates the values from individual measurements).

The same result can be obtained from the box whisker plots presented in Figure 5.25 D, *i.e.* no significant differences between $<\tau_D>_1$ and $<\tau_{DA}>_1$, in the case of P0-yEGFP+Mrt4-mCherry donor-acceptor samples (negative control for FRET), while there could be slightly differences for P0-yEGFP+Nop7-mCherry donor-acceptor samples.

Table 5.8. FRET-ROI analyses: Fluorescence lifetime parameters determined for P0-yEGFP (donor only), P0-yEGFP +Mrt4-mCherry (donor-acceptor), and P0-yEGFP+Nop7-mCherry (donor-acceptor)

Sample	a_1 (±0.05)	τ_1 (ns) (±0.2)	a_2 (±0.05)	τ_2 (ns) (±0.2)	$<\tau>_1$ (ns) (±0.2)	p value
P0-yEGFP (n = 8)	0.57	2.3	0.43	1	1.8	
P0-yEGFP + Mrt4-mCherry (n = 14)	0.58	2.3	0.42	1	1.7	p>0.05 (NS)
P0-yEGFP + Nop7-mCherry (n = 10)	0.5	2.4	0.50	0.8	1.6	p<0.05 (*) S

Fluorescence intensity decays were built from the photons from nuclear ROIs corresponding to the 2P-FLIM image in donor channel (FF01-520/35, Semrock), and were analysed using Globals software (LFD, Irvine. CA).
Numbers in parentheses represent the sample to sample error (confidence limits at the 67% level). The number of independent experiments (n) and statistical significance assessed by independent two-sample t-test are indicated (NS: no significant, (*) S: significant).

P0-yEGFP+Nop7-mCherry donor-acceptor samples presented notable variations in the average lifetime values from cell-to-cell measurements within different cells, showing a broad distribution, which may suggest two populations with low and high FRET in the nucleus. Anyway, it is important to note that there is a big uncertainty in the localization of the ROI corresponding to the nucleus region in the donor channel image of these samples, especially in the definition of the nucleus limits. Any contamination of pixels in the ROI from P0

expressed in the cytoplasm will contribute as donor only (no FRET) samples, since the protein Nop7 is a nuclear protein.

5.3.6 Interaction profile of Nop7-EGFP with P0-mCherry and Mrt4-mCherry proteins in live yeast cells

In the last section we have analysed the existence of FRET between P0 or Mrt4 and Nop7 using P0-yEGFP as donor, with the problem that donor protein is mainly expressed in cytoplasm, which increases the difficulty to select nuclear ROIs. To avoid this issue, we have changed donor protein to Nop7-EGFP, and donor-acceptor pairs to Nop7-EGFP+Mrt4-mCherry and Nop7-EGFP+P0-mCherry.

Figure 5.26 follows the same pattern as Figure 5.25, showing the expression profile of cells from the strains: Nop7-EGFP+P0-mCherry (A) and Nop7-EGFP+ Mrt4-mCherry (B) donor-acceptor pairs. Left: acceptor emission channel; center, donor emission channel; and right, channels merge view, with artificial green color for donor image and red color for acceptor image. Figure 5.26 C presents the donor channel image for Nop7-EGFP strain (donor only sample). Fluorescence intensity images revealed a heterogeneous distribution of the expression of Nop7-EGFP in the nucleus, with lower concentration in regions near the nuclear membrane. The higher expression level of this protein facilitated the proper selection of the ROIs for the FRET analysis in the nucleus.

Figure 5.26 D presents the box whisker plots of the amplitude-weighted average lifetime determined at the donor channel emission, and Table 5.9 shows the corresponding fluorescence lifetime parameters. Nop7-EGFP fluorescence decay was mono-exponential in all the nuclear regions, with a mean lifetime, τ_D = 2.5 ± 0.1 ns (n = 34 cells). Donor-acceptor pairs showed very similar fluorescence lifetime values for Nop7-EGFP+Mrt4-mCherry samples, τ_{DA} = 2.5 ± 0.1 ns (n = 26 cells; $p>0.05$; not significant), and lower lifetimes values for Nop7-EGFP+P0-mCherry donor-acceptor samples, τ_{DA} = 2.3 ± 0.1 ns (n = 32; $p<0.001$; ***markedly significant).

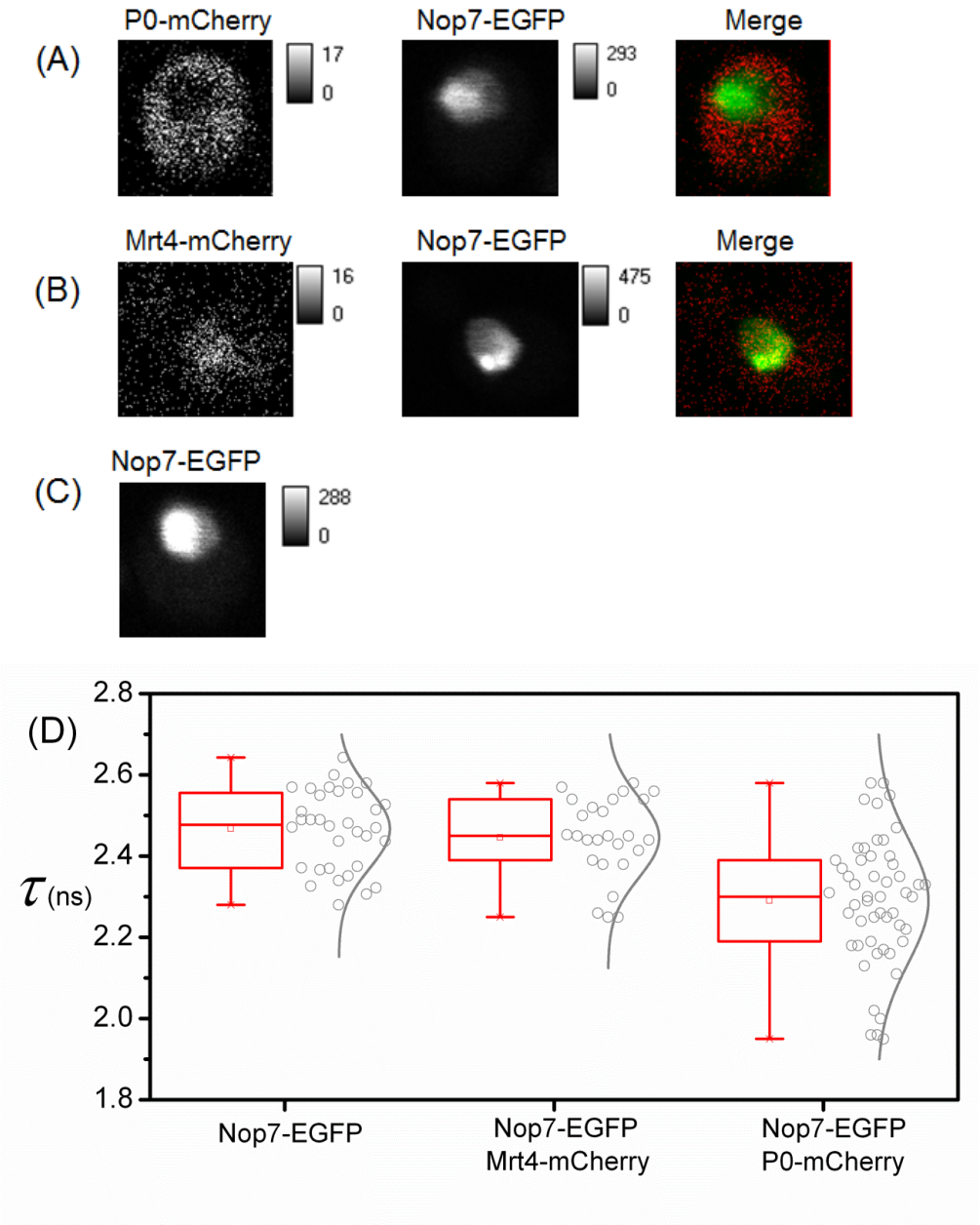

Figure 5.26. Expression profile and FRET-ROI analyses of Nop7-EGFP strain (donor only), Nop7-EGFP+Mrt4-mCherry and Nop7-EGFP+P0-mCherry strains (donor-acceptor). (A-B) Fluorescence intensity images with the code set in the range 0 to the maximum counts per pixel in the image, determined for Nop7-EGFP+P0-mCherry (A) and Nop7-EGFP+Mrt4-mCherry (B) strains. Left: acceptor channel (FF01-685/40, Semrock); center: donor channel (FF01-520/35, Semrock); and right: donor and acceptor channels merge view, obtained with free Image J software (artificial green color for donor and red color for acceptor channels). **(C)** Donor channel image for Nop7-EGFP strain (donor only). **(D)** Box whisker plots showing distributions of the donor lifetime from these samples. The box indicates the interquartile range from 25% to 75% and the whisker indicates the ±1σ values. The middle line of the each box indicates 50% quartile; inner square box indicates the mean value for the overall measurement. Normal distribution of values plotted on the right side of the box (circle indicates the values from individual measurements).

Table 5.9. FRET-ROI analyses: Fluorescence lifetime parameters determined for Nop7-EGFP (donor only), Nop7-EGFP+Mrt4-mCherry (donor-acceptor) and Nop7-EGFP+P0-mCherry (donor-acceptor)

Sample	τ (ns) (±0.1)	p value
Nop7-EGFP (n=34)	2.5	
Nop7-EGFP+Mrt4-mCherry (n=26)	2.5	p>0.05 (NS)
Nop7-EGFP+P0-mCherry (n=32)	2.3	p<0.001 (***) MS

Fluorescence intensity decays were built from the photons from nuclear ROIs corresponding to the 2P-FLIM image in donor channel (FF01-520/35, Semrock), and were analysed using Globals software (LFD, Irvine. CA).
Numbers in parentheses represent the sample to sample error (confidence limits at the 67% level). The number of independent experiments (*n*) and statistical significance assessed by independent two-sample t-test are indicated (NS: no significant, (***) MS: markedly significant).

We have run rigorous error analysis on individual Nop7-EGFP and Nop7-EGFP+P0-mCherry fitting decays, corresponding to single cells showing low and high FRET efficiencies. Results were summarized in Figure 5.27. The χ^2 surface plots showed the variations in the mean lifetime confidence interval from individual cell measurements of Nop7-EGFP+P0-mCherry: two samples with high τ_{DA} (low FRET efficiency, panel A, Figure 5.27, red) and three samples with low τ_{DA} (high FRET efficiency, panel B, Figure 5.27, red).

In Figure 5.27 we have presented three representative Nop7-EGFP donor only samples for comparison. We can see that rigorous error analysis curves from Nop7-EGFP+P0-mCherry samples showing low FRET efficiency overlap with donor alone curves, while we can observe a complete separation in the case of donor-acceptor samples with high FRET. This results evidence again the presence of two populations in Nop7 and P0 interaction, only one of them presents FRET.

Box whisker plot from Nop7-EGFP+P0-mCherry showed a broad distribution of values from individual measurements, which also suggested the coexistence of two populations with low and high FRET in the nucleus.

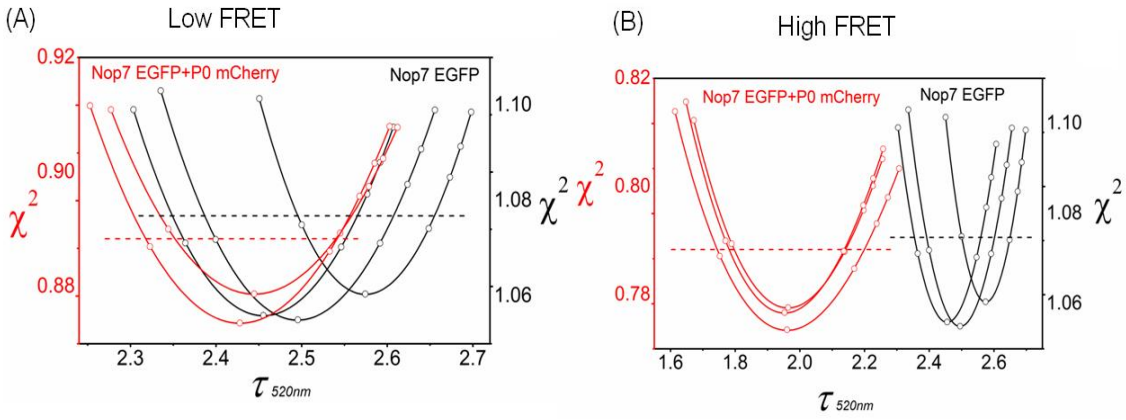

Figure 5.27. Rigorous error analysis of lifetime from low and high FRET samples. Confidence interval of lifetime from three representative measurements of Nop7-EGFP (donor only, black) and five Nop7-EGFP+P0-mCherry samples (donor-acceptor, red): two samples showing low average FRET efficiency (A, high τ_{DA} values) and three samples showing high average FRET efficiency (B, low τ_{DA} values). Dashed lines represent the χ^2 value for the 67% confidence level ($\pm 1\sigma$).

All these results together were compatible with P0-yEGFP+Nop7-mCherry strain, ratifying the presence of FRET between Nop7 and P0 proteins (average efficiency lower than 10%) in the pre-ribosomal particles, but not in the case of Nop7 and Mrt4 nuclear proteins.

The FRET efficiencies determined using the ROI-FRET approach are average values, and they are much lower than the real FRET efficiencies. We built the total intensity decays from the photons accumulated in all the pixels of the nucleus which would include, besides the pixels with FRET, the nuclear regions where Nop7-EGFP does not have a P0-mCherry molecule at distances lower than 10 nm. N&B results suggested the presence of FRET between P0-mCherry and Nop7-EGFP just in the pre-ribosomal particles located in the nuclear periphery of *S. cerevisiae* yeast cells. Therefore it would be essential to use a FLIM-FRET approach that maintains the spatial resolution of the fluorescence micro-spectrometer, and the FRET-phasor approach meets this need.

5.3.7 FRET-phasor measurements support the existence of P0-Nop7 interactions pre-ribosomal complexes located in the nuclear periphery

Fluorescence intensity images of representative yeast cells expressing Nop7-EGFP alone (A), and in the presence of P0-mCherry (D), and Mrt4-mCherry (G) (Figure 5.28, first row) revealed a heterogeneous distribution of Nop7-EGFP in the nucleus with lower concentration regions near the nuclear membrane.

The FLIM-phasor quantification of FRET efficiencies in different nuclear locations, in which the fluorescence decay in each pixel of the image gives a point in the phasor plot (Figure 5.28 J), revealed that only cells expressing Nop7-EGFP and P0-mCherry presented clusters of phasors located in regions of phasor space indicative of FRET (pink cursor), and these pixels are spatially located near the nuclear membrane.

The green line in the phasor representation marks the 0% FRET (donor-only phasors at different contributions of cell auto-fluorescence), whereas the yellow line marks the calculated 50% FRET efficiency position at different background contributions (0-100%), assuming that all the donors are quenched by FRET (0% contribution of donor unquenched). It is important to note that background contribution in this region can be up to 30%, and that the contribution of unquenched donor may very large due to the high stoichiometry of Nop7-EGFP in the pre-ribosomal complexes determined in N&B analysis.

The experimental position of the black cursor along the FRET trajectory (Figure 5.29) determines the amount of quenching and, therefore, the FRET efficiency, which from this trajectory was estimated to be 30%. The estimated FRET efficiency value from the phasor approach represents the lower limit for this value. The high percentage of Nop7 molecules located far from P0 molecules in the pre-ribosomal complexes was still an important limitation of the quantitative FRET analysis for these samples.

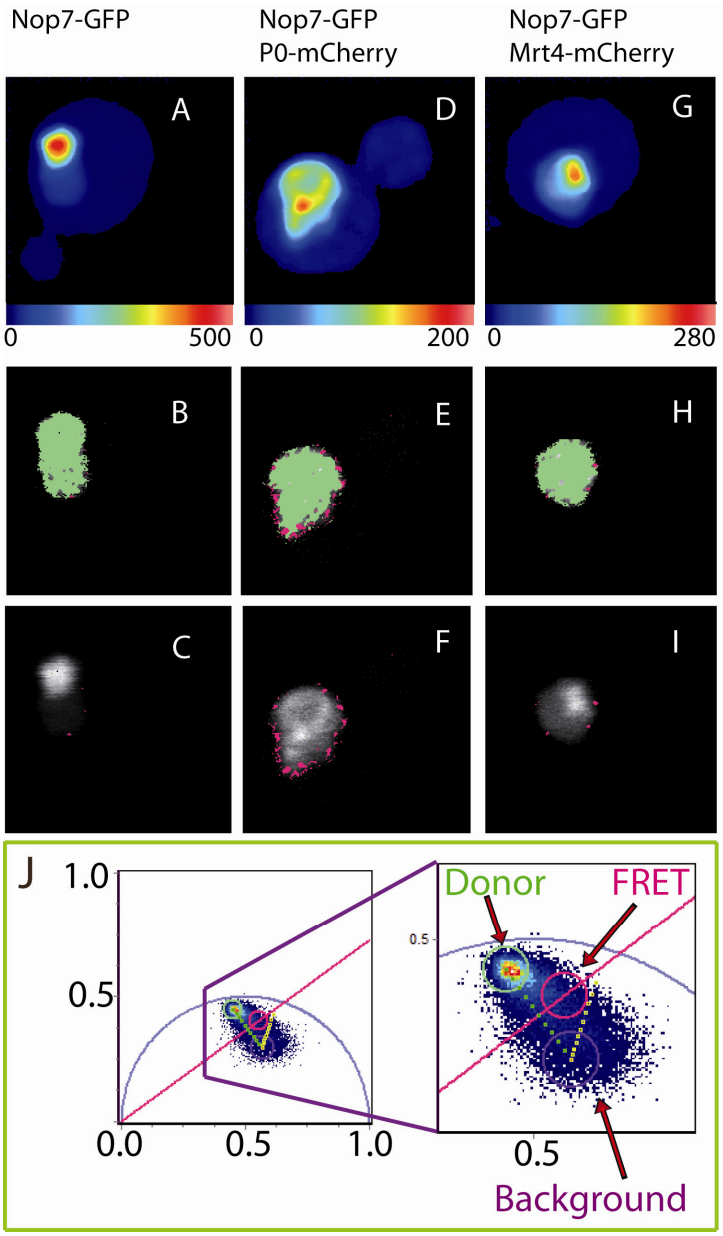

Figure 5.28. Representative FRET-FLIM analysis using the phasor plot approach for the different pairs. Intensity images of yeast cells expressing Nop7-EGFP alone **(A)**, Nop7-EGFP/ P0-mCherry **(D)**, and Nop7-EGFP/Mrt4-mCherry. **(G)** FLIM-phasor representations of donor-only phasor (green, 0% FRET), and FRET phasor (pink). Donor-only (green) and FRET (pink) phasor subsets are shown in the phasor plot **(J)**, and the correspondent pixels are localized in the FLIM images of Nop7-EGFP alone **(B-C),** and in the presence of P0-mCherry **(E-F)**, and Mrt4-mCherry **(H-I)**. The green line in the phasor representation (J), joins the cluster of phasors corresponding to the donor-only samples (cells expressing Nop7-EGFP alone; green cursor), and the background (autofluorescence from wild type cells; purple cursor). The yellow line marks the calculated 50% FRET efficiency position at different background contributions (0-100%), assuming that all the donors are quenched by FRET (0% contribution of donor unquenched) (*adapted from Francisco-Velilla et al. 2013b*).

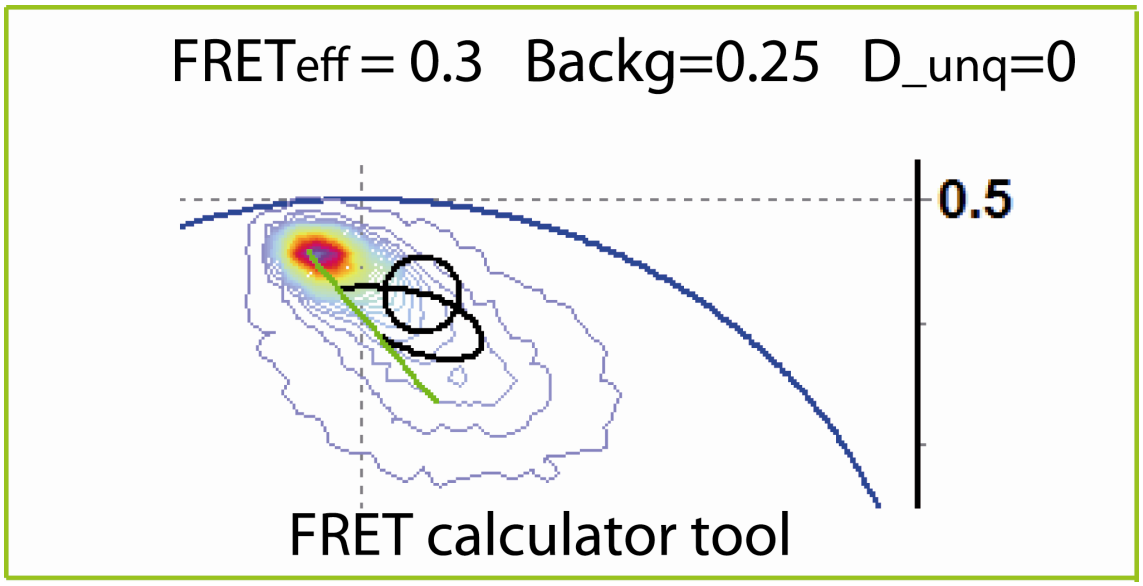

Figure 5.29. FRET calculator tool for the phasor approach. Example of the estimation of the FRET efficiency using the program SimFCS (LFD, Irvine. CA). Black curve line represents the calculated FRET trajectory starting in the donor only phasor (0% FRET efficiency), assuming a cell autofluorescence of 25% and contribution of donor unquenched of 30%. The experimental position of the black cursor along the trajectory (pink cursor) corresponds to an average FRET efficiency of 30%.

Scanning two photon cross N&B experiments in live yeast cells, supported by the FRET-FLIM results presented in this work (Francisco-Velilla *et al.* 2013b. Submitted), revealed that P0-mCherry and Nop7-EGFP proteins associate in the nucleus, probably implicating multiple pre-ribosome particles. The tagged proteins exhibit near the nuclear membrane negative cross-brightness and FRET.

An evident conclusion from these results is that in living cells the P0 protein is present in nuclear pre-ribosomal particles that also contain Nop7. This evidence confirms that the detection of this protein in Nop7 pre-ribosome complexes from cell extracts previously reported (Rodríguez-Mateos *et al.* 2009b, Francisco-Velilla *et al*. 2013a) was not due to a contamination during purification. Moreover, the results demonstrate that in some particles the two fluorescent tags are close enough (R < 10 nm) to undergo FRET. Considering that the binding site for P0 and Mrt4 in the stalk base seems to be far from Nop7 in the pre-ribosome structure (Granneman *et al.* 2011, Talkish *et al.* 2012), the contrasted FRET levels for P0-Nop7 and P0-Mrt4 protein pairs could be explained by the differences in mobility of the fluorescent proteins, confirmed

here by time-resolved fluorescence anisotropy. The mCherry attached to the highly flexible P0 CTD (Cowgill *et al.* 1984), exhibited high mobility which would favor FRET, while the observed restricted mobility of the mCherry attached to Mrt4 would disfavor FRET if the relative orientation of the two fluorescent proteins were non-favorable.

The function of P0 in the nucleus is not well-understood. The presence of the stalk protein in nuclear particles may be compatible with the existence of an alternative Mrt4-independent P0 assembly pathway, as previously suggested (Rodríguez-Mateos *et al.* 2009b). However, alternative interpretations are possible.

6 CONCLUSIONS

1. We have completed the instrumental micro-spectrometer setup, optimized to measure single-point time-resolved polarized fluorescence decays in specific subcellular locations, with high spatial (sub-μm) and temporal (ps-ns) resolution, with one-photon (OPE) or two-photon (TPE) excitation.

2. We have developed an IRF iterative re-convolution approach that allows to resolve minor lifetime differences and provided a quantitative comparison for the different fluorescent protein (FPs) variants, located in different subcellular regions.

3. The single point TPE polarization microscope setup allows to determine high accuracy rotational correlation times in ~1fL detection volumes, in the range 1-30 ns, of fluorophores, FPs and FP-tagged proteins, in buffer and in the cytoplasm of living yeast cells.

4. The single point confocal OPE polarization microscope setup allows to extend the rotational correlation time determination range with acceptable accuracy in ~1fL detection volumes, to ~40-50 ns. OPE set up would be more appropriate for the determination of long rotational correlation times in complex systems with significant background contribution.

5. We have measured the rotational mobility of EGFP, expressed free in the cytoplasm of *S. cerevisiae*. EGFP slows its rotational mobility by comparison with EGFP in buffer solution, revealing a cytoplasmic apparent microviscosity about two times larger than aqueous solutions viscosity (~2 cP). These results agree with previously published data about the crowded environment of the cytoplasm.

6. We have characterized the flexibility of the carboxy-terminal domains (CTD) of the stalk proteins P0, P1α, and P2β. CTDs keep its flexible character in the cytoplasm of *S. cerevisiae* cells. Comparing with purified ribosome determinations in buffer, their apparent mobility from the rotational correlation times of the EGFP attached to their CTDs, was slowed down in the cytoplasm: ~1.8 times for P0, ~1.6 times for P1α, and ~1.3 times for P2,

reflecting the macromolecular crowding effect and/or the 3-D organization of the ribosome stalk components in the cytoplasm.

7. The histogram plot of rotational correlation times determined for P0-yEGFP samples treated with sordarin, allows to discriminate between two cellular populations in terms of yEGFP mobility. An important group of cells seems not to be affected by the treatment with sordarin, while some of them may present a slowdown in their CTD rotational mobility. These results may suggest that sordarin could reduce P0 CTD mobility, and therefore, P0 stalk protein would be involved in the mechanism of action of sordarin.

8. The histogram plot of rotational correlation times allows to differentiate between P0 and P1α and P2β mobility changes upon sordarin treatment. Sordarin seems to have no effect on the flexibility of the CTD region of P1α and P2β stalk proteins.

9. Despite of the limitations of the lifetime of the fluorescent proteins used in this work (~2-2.6 ns) our TPE and OPE anisotropy approach was able to detect changes in the flexibility of proteins bound to a nanometric size structure, like the ribosome, in living cells.

10. The FLIM-phasor improves the FLIM-ROI approach to characterize protein interactions in the nucleus of *S. cerevisiae* yeast cells, expressing Nop7-EGFP, Mrt4-mCherry and P0-mCherry in different nuclear locations.

11. FLIM-FRET phasor approach demonstrates that in the nuclear periphery of *S.cerevisiae* yeast cells there are pre-ribosomal particles containing P0-mCherry and Nop7-EGFP close enough (R < 10nm) to undergo FRET, confirming previous reported *in vitro* data from cell extracts. These results also support cross N&B data determined for the same samples in a complementary study in Dr. Royer laboratory.

1. Hemos completado la puesta a punto de un micro-espectrómetro láser de fluorescencia, optimizado para medir decaimientos de fluorescencia polarizada en localizaciones subcelulares específicas, con una alta resolución espacial (sub-μm) y temporal (ps- ns), excitando con un fotón (OPE) o dos fotones (TPE).

2. Hemos desarrollado un protocolo de análisis de vidas medias de fluorescencia en el micro-espectrómetro, basado en métodos de re-convolución iterativa con la función instrumental IRF, que permite resolver pequeñas diferencias en los tiempos de vida del estado excitado, fundamentales para la caracterización y cuantificación de diferentes proteínas fluorescentes, en diferentes microentornos y/o regiones subcelulares.

3. El micro-espectrómetro láser de fluorescencia con excitación de dos fotones permite determinar con precisión tiempos de correlación rotacional, en volúmenes de ~1fL, en el intervalo de 1-30 ns, de fluoróforos, proteínas fluorescentes y proteínas marcadas fluorescentemente, en tampón y en el citoplasma de células de levadura vivas.

4. La configuración confocal del micro-espectrómetro láser de fluorescencia con excitación de un fotón permite ampliar el intervalo de tiempos de correlación rotacional determinados en volúmenes de ~1fL con una precisión aceptable hasta valores ~ 40-50 ns. Esta configuración, en principio es la más adecuada para la determinación de tiempos de correlación rotacional largos en sistemas complejos, con contribuciones de fondo no despreciables.

5. Hemos caracterizado la movilidad rotacional de la proteína fluorescente EGFP libre en el citoplasma. Presenta un tiempo de correlación rotacional ~2 veces más lento que el medido para EGFP en disolución acuosa. Esta diferencia refleja las características de aglomeración macromolecular del citoplasma de *S. cerevisiae*, con una microviscosidad aparente de ~ 2 cP.

6. Hemos caracterizado la flexibilidad de los dominios carboxi-terminal (CTD) de las proteínas del tallo ribosómico P0, P1α y P2β, en el citoplasma de

células de *S. cerevisiae*. Comparando con las determinaciones realizadas en ribosomas purificados en tampón, los dominios CTD de estas proteínas mantienen su carácter flexible, aunque con una movilidad disminuida por la aglomeración macromolecular y/o la organización 3-D del tallo ribosómico en el citoplasma. Los tiempos de correlación rotacional determinados son ~1,8 veces más lentos en P0, ~1,6 veces en P1α y ~1,3 veces en P2β.

7. El histograma de tiempos de correlación rotacional determinados para las muestras de P0-yEGFP tratadas con sordarina, nos ha permitido discriminar dos poblaciones celulares en términos de la movilidad de yEGFP. Un grupo importante de células no parecen estar afectadas, mientras que en una pequeña población, posiblemente afectada por el tratamiento con sordarina, los dominios CTD de P0 podrían perder su flexibilidad. Estos resultados podrían confirmar que la proteína P0 estaría involucrada en el mecanismo de acción de sordarina sobre la función del ribosoma.

8. El histograma de tiempos de correlación rotacional permite caracterizar el comportamiento diferencial en los cambios de movilidad de P0 y de las proteínas ácidas P1α y P2β, en células tratadas con sordarina. El inhibidor sordarina no parece tener ningún efecto sobre la flexibilidad de la región CTD de las proteínas P1α y P2 unidas al tallo ribosómico.

9. A pesar de las limitaciones experimentales impuestas por la corta vida media de las proteínas fluorescentes utilizadas en este trabajo (~ 2-2.6 ns), El micro-espectrómetro láser de fluorescencia, con excitación de uno y dos fotones, permite detectar cambios en la flexibilidad de proteínas unidas a una estructura de tamaño nanométrico, como el ribosoma, en células vivas.

10. La aproximación de imágenes de vidas medias, a través de fasores (FLIM-fasores) ha permitido la caracterización de interacciones proteína-proteína en células de levadura *S. cerevisiae* que expresan Nop7-EGFP, Mrt4-mCherry y P0-mCherry en diferentes regiones del núcleo.

11. Utilizando la aproximación FLIM-FRET-fasores hemos podido demostrar la existencia de partículas pre-ribosómicas en la periferia del núcleo de células de levaduras *S.cerevisiae* vivas. Estas partículas pre-ribosómicas contienen las proteínas Nop7-EGFP y P0-mCherry, suficientemente cerca (R <10 nm) como para que se produzca un proceso FRET. Este resultado confirma las conclusiones obtenidas a partir de estudios *in vitro* de extractos celulares y apoya los datos de correlación cruzada N&B determinados en un estudio complementario realizado en el laboratorio de la Dra. Royer con las mismas preparaciones.

REFERENCES

Acuña A, González-Rodríguez J, Lillo MP and Naqvi KR (1987) "Protein structure probed by polarization spectroscopy. II. A time-resolved fluorescence study of human fibrinogen" *Biophys Chem* 26: 63–70

Adams CC, Jakovljevic J, Roman J, Harnpicharnchai P and Woolford JL Jr (2002) "*Saccharomyces cerevisiae* nucleolar protein Nop7p is necessary for biogenesis of60S ribosomal subunits" *RNA* 8: 150–65

Andersen GR, Nissen P and Nyborg J (2003) "Elongation factors in protein biosynthesis" *Trends Biochem Sci* 28: 434-41

Axelrod D (1979) "Carbocyanine dye orientation in red cell membrane studied by microscopic fluorescence polarization" Biophys J 26: 557–574

Axelrod D (1989) "Fluorescence polarization microscopy" *Methods Cell Biol* 30: 333–352

Bader AN, Hofman EG, van Bergen en Henegouwen PM and Gerritsen HC (2007) "Imaging of protein cluster sizes by means of confocal time-gated fluorescence anisotropy microscopy," *Opt Express* 15: 6934–45

Bader AN, Hofman EG, Voortman J, en Henegouwen PM and Gerritsen HC (2009) "Homo-FRETimaging enables quantification of protein cluster sizes with subcellular resolution," *Biophys J* 97: 2613–22

Baird GS, Zacharias DA and Tsien RY (2000) "Biochemistry, mutagenesis, and oligomerization of DsRed, a red fluorescent protein from coral" *Proc Natl Acad Sci USA* 97: 11984–11989

Ballesta JPG and Remacha M (1996) "The large ribosomal subunit stalks as a regulatory element of the eukaryotic translational machinery" *Prog Nucleic Acid Res Mol Biol* 55: 157–193

Ban N, Nissen P, Hansen J, Mooer PB and Steitz TA (2000) "The complete atomic structure of the large ribosomal subunit at 2.4 Å resolution" *Science* 289: 905–920

Bastiaens PIH and Squire A (1999) "Fluorescence lifetime imaging microscopy: spatial resolution of biochemical processes in the cell" *Trends Cell Biol* 9: 48–52

Becker W, Bergmann A, Hink MA, König K, Benndorf K and Biskup C (2004) "Fluorescence lifetime imaging by time-correlated single photon counting" *Microsc Res Tech* 63: 58–66

Becker W (2012) "Fluorescence lifetime imaging – techniques and applications" *J Microsc* 247: 119–136

Beechem JM (1992) "Global analysis of biochemical and biophysical data" *Methods Enzymol* 210: 37–54

Beechem JM, Gratton E, Ameloot M., Knutson JR and Brand L (1991) in *Topics in Fluorescence Spectroscopy: Principles II* (Lakowicz JR, Ed) pp 241–305. Plenum Press. New York

Ben-Shem A, Garreau de Loubresse N, Melnikov S, Jenner L, Yusupova G and Yusupov M (2011) "The structure of the eukaryotic ribosome at 3.0 Å resolution" *Science* 334: 1524–1529

Berezin MY and Achilefu S (2010) "Fluorescence lifetime measurement and biological imaging" *Chem Rev* 110: 2641–2684

Blackman SM, Cobb CE, Beth AH and Piston DW (1996) "The orientation of eosin-5-maleimide on human erythrocyte band 3 measured by fluorescence polarization microscopy" *Biophys J* 71:194–208

Bocharov EV, Sobol AG, Pavlov KV, Korzhnev DM, Jaravine VA, Gudkov AT and Arseniev AS (2004) "From structure and dynamics of protein L7/L12 to molecular switching in ribosome" *J Biol Chem* 279: 17697–706

Borst JW and Visser AJWG (2010) "Fluorescence lifetime imaging microscopy in life sciences" *Meas Sci Technol* 21**:** 102002

Caiolfa VR, Zamai M, Malengo G, Andolfo A, Madsen CD, Sutin J, Digman M, Gratton E, Blasi F and Sidenius N (2007) "Monomer dimer dynamics and distribution of GPI-anchored uPAR are determined by cell surface protein assemblies" *J Cell Biol* 179: 1067–1082

Calleja V, Ameer-Beg S, Vojnovic B, Woscholski R, Downwards J and Larijani B (2003) "Monitoring conformational changes of proteins in cells by fluorescence lifetime imaging microscopy" *Biochem J* 372: 33–40

Cantor CR and Schimmel PR (1980) "Size and shape of macromolecules" in *Biophysical Chemistry—Part II: Techniques for the Study of Biological Structure and Function.* pp 539–590. WH Freeman. San Francisco, CA

Cao ZH, Huang CC and Tan WH (2006) "Nuclease resistance of telomere like oligonucleotides monitored in live cells by fluorescence anisotropy imaging" *Anal Chem* 78: 1478–1484

Chalfie M, Tu Y, Euskirchen G, Ward WW, Prasher DC (1994) "Green fluorescent protein as a marker for gene expression" *Science* 263: 802–805

Chattoraj M, King BA, Bublitz GU and Boxer SG (1996) "Ultra-fast excited state dynamics in green fluorescent protein: multiple states and proton transfer" *Proc Natl Acad Sci USA* 93: 8362–8367

Cheng L, Fu J, Tsukamoto A and Hawley RG (1996) "Use of green fluorescent protein variants to monitor gene transfer and expression in mammalian cells" *Nat Biotechnol* 14: 606–609

Clayton AH, Hanley QS, Arndt-Jovin DJ, Subramaniam V and Jovin TM (2002) "Dynamic fuorescence anisotropy imaging microscopy in the frequency domain (rFLIM)" *Biophys J* 83: 1631–1649

Clayton AHA, Hanley QS and Verveer PJ (2004) "Graphical representation and multicomponent analysis of single-frequency fluorescence lifetime imaging microscopy data" *J Microsc* 213: 1–5

Clegg RM (1996) "Fluorescence resonance energy transfer" in *Fluorescence imaging spectroscopy and microscopy* (Wang XF, Herman B, Ed) pp 179-252. John Wiley & Sons

Clementi N and Polacek N (2010) "Ribosome-associated GTPases: the role of RNA for GTPase activation" *RNA Biol* 7: 521–527

Cormack BP, Bertram G, Egerton M, Gow NAR, Falkow S and Brown AJP (1997) "Yeast-enhanced green fluorescent protein (yEGFP): a reporter of gene expression in *Candida albicans*" *Microbiology* 143: 303–311

Cowgill CA, Nichols BG, Kenny JW, Butler P, Bradbury EM, Traut RR (1984) "Mobile domains in ribosomes revealed by proton nuclear magnetic resonance" *J Biol Chem.* 259: 15257-63

Day RN, Davidson MW (2009) "The fluorescent protein palette: tools for cellular imaging" *Chem Soc Rev* 38: 2887–2921

Delagrave S, Hawtin RE, Silva CM, Yang MM and Youvan DC (1995) "Red-shifted excitation mutants of the green fluorescent protein" *Biotechnology* 13: 151–154

Devauges V, Marquer C, Lécart S, Cossec JC, Potier MC, Fort E, Suhling K and Lévêque-Fort S (2012) "Homodimerization of amyloid precursor protein at the plasmamembrane: a homoFRET study by time-resolved fluorescence anisotropy imaging" *PLoSOne* 7: e44434

Dez C and Tollervey D (2004) "Ribosome synthesis meets the cell cycle" *Curr Opin Microbiol* 7: 631-637

Diaconu M, Kothe U, Schlünzen F, Fischer N, Harms JM, Tonevitsky AG, Stark H, Rodnina MV and Wahl MC (2005) "Structural basis for the function of the ribosomal L7/12 stalk in factor binding and GTPase activation" *Cell* 121: 991–1004

Diaspro A, Chirico G, Federici F, Cannone F, Beretta S and Robello M (2001) "Two-photon microscopy and spectroscopy based on a compact confocal scanning head" *J Biomed Opt* 6: 300–310

Diaspro A and Sheppard CJR (2007) "Two photon excitation fluorescence microscopy" in *Confocal and Two-Photon Microscopy* (Diaspro A, Ed) Chap.3 pp 39–73. Wiley-Liss. New York

Diederix REM, Davila C, Giraldo R and Lillo MP (2008) "Fluorescence studies of the replication initiator protein RepA in complex with operator and iteron sequences and free in solution" *FEBS J* 275: 5393–5407

Digman M, Caiolfa VR, Zamai M and Gratton E (2008a) "The Phasor approach to fluorescence lifetime imaging analysis" *Biophys J* 94: L14–L16

Digman MA, Dalal R, Horwitz AF and Gratton E (2008b) "Mapping the number of molecules and brightness in the laser scanning microscope" *Biophys J* 94: 2320-2332.

Digman MA, Wiseman PW, Choi C, Horwitz AR and Gratton E (2009) "Stoichiometry of molecular complexes at adhesions in living cells" *Proc Natl Acad Sci U S A* 106: 2170-2175.

Digman M and Gratton E (2012) "Fluorescence lifetime microscopy: The Phasor approach" in *Comprehensive Biophysics* Vol. 2 (Egelman EH, Ed) pp 24-38. Elsevier

Dix JA and Verkman AS (1990) "Mapping of fluorescence anisotropy in living cells by ratio imaging. Application to cytoplasmic viscosity" *Biophys J* 57: 231–40.

Domínguez JM, Kelly VA, Kinsman OS, Marriott MS, Gómez de las Heras F and Martín JJ (1998) "Sordarins: A new class of antifungals with selective inhibition of the protein synthesis elongation cycle in yeasts" *Antimicrob Agents Chemother* 42: 2274–8

Drobizhev M, Makarov NS, Tillo SE, Hughes TE and Rebane A (2011) "Two-photon absorption properties of fluorescent proteins" *Nat Methods* 8: 393–399

Elliot AD, Gao L, Ustione A, Bedard N, Kester R, Piston DW and Tkaczyk TS (2012) "Real time hiperspectral fluorescence imaging of pancreatic β-cells dynamics with the image maping spectrometer" *J Cell Sci* 125: 4833–4840

Entwistle A and Noble M (1992a) "The use of polarization analysis in the quantification of fluorescent emission: general principles," *J Microsc* 165: 331–346

Entwistle A and Noble M (1992b) "The quantification of fluorescent emission from biological samples using analysis of polarization" *J Microsc* 165: 347–365

Förster T (1965) "Delocalized excitation and excitation transfer" in *Modern Quantum Chemistry* (Sinanoglu O, Ed) pp 93–137. Academic Press

Francisco-Velilla R, Remacha M and Ballesta JPG (2013a) "Carboxy terminal modifications of the P0 protein reveal alternative mechanisms of nuclear ribosomal stalk assembly T" *Nucleic Acid Res* in press

Francisco-Velilla R, Clerté C, Raja S, García C, Remacha M, Lillo MP, Ballesta JPG and Royer C (2013b) "Pre-ribosomal factories in live yeast revealed by two-photon cross number and brightness". Submitted

Frank J, Zhu J, Li Y, Srivastava S, Verschoor A, Radermacher M, Grassucci R, Lata RK and Agrawall RK (1995) "A model of protein synthesis based on cryo-electron microscopy of the E. coli ribosome" *Nature* 376: 441–444

Frank J and Agrawall RK (2000) "A ratchet-like inter-subunit reorganization of the ribosome during translocation" *Nature* 406: 318–322

Fung JJ, Deupi X, Pardo L, Yao XJ, Velez-Ruiz GA, Devree BT, Sunahara RK and Kobilka BK (2009) "Ligand-regulated oligomerization of beta(2)-adrenoceptors in a model lipid bilayer" *EMBO J* 28: 3315–3328

Fushimi K, Dix JA and Verkman AS (1990) "Cell membrane fluidity in the intact kidney proximal tubule measured by orientation-independent fluorescence anisotropy imaging" *Biophys J* 57, 241–254

García-Marcos A, Sánchez SA, Parada P, Eid J, Jameson DM, Remacha M, Gratton E and Ballesta JP (2008) "Yeast ribosomal stalk heterogeneity in vivo shown by two-photon FCS and molecular brightness analysis" *Biophys J* 94: 2884–2890

Gautier I, Tramier M, Durieux C, Coppey J, Pansu RB, Nicolas JC, Kemnitz K and Coppey-Moisan M (2001) "Homo-FRET microscopy in living cells to measure monomer-dimer transition of GFP-tagged proteins" *Biophys J* 80:3000–3008

Ghosh S, Saha S, Goswami D, Bilgrami S, Mayor S (2012) "Dynamic imaging of homo-FRET in live cells by fluorescence anisotropy microscopy" *Methods Enzymol.* 505: 291-327

Goedhart J, Vermeer JEM, Adjobo-Hermans MJW, van Weeren L and Gadella TWJ Jr. (2007) "Sensitive Detection of p65 Homodimers Using Red-Shifted and Fluorescent Protein-Based FRET Couples" *PLoS ONE* 10: e1011

Gómez-Lorenzo MG and García-Bustos JF (1998) "Ribosomal P-protein stalks function is targeted by sordarin antifungals" *J Biol Chem* 273: 25041–25044

Gonzalo P and Reboud JP (2003) "The puzzling lateral flexible stalks of the ribosome" *Biol Cell* 95: 179–93

Goodsell DS (1993) in *The machinery of Life*. Springer-Verlag, New York

Goswami D, Gowrishankar K, Bilgrami S, Ghosh S, Raghupathy R, Chadda R, Vishwakarma R, Rao M and Mayor S (2008) "Nanoclusters of GPI-anchored proteins are formed by cortical actin-driven activity" *Cell* 135: 1085–1097

Granneman S, Petfalski E and Tollervey D (2011) "A cluster of ribosome synthesis factors regulate pre-rRNA folding and 5.8S rRNA maturation by the Rat1 exonuclease" *EMBO J* 30: 4006–19

Gratton E, Jameson DM and Hall RD (1984) "Multifrequency phase and modulation fluorometry" *Annu Rev Biophys Bioeng* 13:105–124

Grela P, Gajda MJ, Armache JP, Beckmann R, Krokowski D, Svergun DI, Grankowski N and Tchórzewski M (2012) "Solution structure of the natively assembled yeast ribosomalstalk determined by small-angle X-ray scattering" *Biochem J* 444: 205–9

Guarinos E, Remacha M and Ballesta JPG (2001) "Asymmetric interactions between the acidic P1 and P2 proteins in the *S. cerevisiae* ribosomal stalk" *J Biol Chem* 276: 32474–32479

Gudkov AT, Tumanova LG, Gongadze GM and Bushuev VN (1980) "Role of different regions of ribosomal proteins L7 and L10 in their complex formation and in the interaction with the ribosomal 50 S subunit" *FEBS Lett* 109: 34–38

Guizy M, David M, Arias C, Zhang L, Cofán M, Ruiz-Gutiérrez V, Ros E, Lillo MP, Martens JR and Valenzuela C (2008) "Modulation of the atrial specific Kv1.5 channel by the n-3 polyunsaturated fatty acid, α-linolenic acid" *J Mol Cell Cardiol* 44: 323–335

Hameed FM, Rao M and Shivashankar GV (2012) "Dynamics of passive and active

particles in the cell nucleus" *PLoS One* 7: e45843

Hanley QS and Clayton AH (2005) "AB-plot assisted determination of fluorophore mixtures in a fluorescence lifetime microscope using spectra or quenchers" *J Microsc* 218: 62–67

Haupts U, Maiti S, Schwille P and Webb WW (1998) "Dynamics of fluorescence fluctuations in green fluorescent protein observed by fluorescence correlation spectroscopy" *Proc Natl Acad Sci USA* 95: 13573–13578

Heim R, Prasher DC and Tsien RY (1994) "Wavelength mutations and posttranslational autoxidation of green fluorescent protein" *Proc Natl Acad Sci USA* 91: 12501–12504

Heim R, Cubitt AB and Tsien RY (1995) "Improved green fluorescence" *Nature* 373: 663–664

Herz J, Siffrin V, Hauser AE, Brandt AU, Leuenberger T, Radbruch H, Zipp F, Niesner RA (2010) "Expanding two-photon intravital microscopy to the infrared by means of optical parametric oscillator" *Biophys J* 98: 715-723

Hess ST, Sheets ED, Wagenknecht-Wiesner A and Heikal AA (2003) "Quantitative analysis of the fluorescence properties of intrinsically fluorescent proteins in living cells" *Biophys J* 85: 2566–80

Hink MA, Griep RA, Borst JW, van Hoek A, Eppink MHM, Schots A and Visser AJWG (2000) "Structural dynamics of green fluorescent protein alone and fused with a single chain Fv protein" *J.Biol.Chem*. 275: 17556–17560

Huang C, Mandava CS and Sanyal S (2010) "The ribosomal stalk plays a key role in IF2-mediated association of the ribosomal subunits" *J Mol Biol* 399: 145–53

Hurt E, Hannus S, Schmelzl B, Lau D, Tollervey D and Simos G (1999) "A novel in vivo assay reveals inhibition of ribosomal nuclear export in ran-cycle and nucleoporin mutants" *J Cell Biol* 144: 389–401

Jameson DM, Gratton E and Hall RD (1984) "The measurement and analysis of heterogeneous emissions by multifrequency phase and modulation fluorometry" *Appl Spectrosc Rev* 20: 55–106

Jares-Erijman EA and Jovin TM (2006) "Imaging molecular interactions in living cells by FRET microscopy" *Currt Opin Chem Biol* 10: 409–416

Kampmann M, Atkinson CE, Mattheyses AL and Simon SM (2011) "Mapping the orientation of nuclear pore proteins in living cells with polarized fluorescence microscopy" *Nat Struct Mol Biol* 18: 643–649

Kemmler S, Occhipinti L, Veisu M and Panse VG (2009) "Yvh1 is required for a late maturation step in the 60S biogenesis pathway" *J Cell Biol* 186: 863–880

Kenworthy AK and Edidin M (1998) "Distribution of a glycosyl phosphatidyl inositol anchored protein at the apical surface of MDCK cells examined at are solution of <100 Å using imaging fluorescence resonance energy transfer" *J Cell Biol* 142: 69–84

Kramer G, Boehringer D, Ban N and Bukau B (2009) "The ribosome as a platform for co-translational processing, folding and targeting of newly synthesized proteins" *Nat Struct Mol Biol* 16: 589–597

Kremers GJ, Gilbert SG, Cranfill PJ, Davidson MW and Piston DW (2011) "Fluorescence proteins at a glance" *J Cell Sci* 124: 157–160. Erratum: *J Cell Sci* 124: 2676

Kressler D, Hurt E and Babetaler J (2010) "Driving ribosome assembly" *Biochim Biophys Acta- Molecular Cell Research* 1803: 673–683

Krokowski D, Tchórzewski M, Boguszewska A and Grankowski N (2005) "Acquisition of a stable structure by yeast ribosomal P0 protein requires binding of P1α-P2βcomplex in vitro formation of the stalk structure" *Biochim Biophys Acta* 1724: 59–70

Krokowski D, Boguszewska A, Abramczyk D, Liljas A, Tchorzewski M and Grankowski N (2006) "Yeast ribosomal P0 protein has two separate binding sites for P1/P2 proteins" *Mol Microbiol* 60: 386–400

Kudryavtsev V, Felekyan S, Wozniak AK, Koning M, Sandhagen C, Kuhnemuth R, Seidel CA and Oesterhelt F (2007) "Monitoring dynamic systems with multiparameter fluorescence imaging" *Anal Bioanal Chem* 387: 71–82

Kuimova MK, Botchway SW, Parker AW, Balaz M, Collins HA, Anderson HL, Suhling K and Ogilby PR (2009) "Imaging intracellular viscosity of a single cell during photoinduced cell death" *Nat Chem* 1: 69–73

Kummer AD, Kompa C, Lossau H, Pöllinger-Dammer F., Michel-Beyerle ME, Silva CM, Bylina EJ, Coleman WJ, Yang MM and Youvan DC (1998) "Dramatic reduction in fluorescence quantum yield in mutants of Green Fluorescent Protein due to fast internal conversion" *Chem Phys* 237: 183–193

Lakowicz JR (2006) in *Principles of fluorescence spectroscopy.* 3rd Ed. Springer

Lalioti VS, Perez-Fernandez J, Remacha M and Ballesta JP (2002) "Characterization of interaction sites in the *S. cerevisiae* ribosomal stalk components" *Mol Microbiol* 46: 719–729

Lancaster L, Lambert NJ, Maklan EJ, Horan LH and Noller HF (2008) "The sarcin-ricin loop of 23S rRNA is essential for assembly of the functional core of the 50S ribosomal subunit" *RNA* 14: 1999–2012

Larson AM (2011) "Multiphoton microscopy" (Application note) *Nat. Photonics.* 5: 65

Lee KM, Yu C W-H, Chiu T Y-H, Sze K-H, Shaw P-C and Wong K-B (2012) "Solution structure of the dimerization domain of the eukaryotic stalk P1/P2 complex reveals the structural organization of eukaryotic stalk complex" *Nucleic Acids Res* 40: 3172–3182

Levitt JA, Matthews DR, Ameer-Beg SM and Suhling K (2009) "Fluorescence lifetime and polarization-resolved imaging in cell biology" *Curr Opin Biotechnol* 20: 28–36

Levitt JA, Chung PH, Kuimova MK, Yahioglu G, Wang Y, Qu J and Suhling K (2011a) "Fluorescence anisotropy of molecular rotors" *Chemphyschem* 12: 662–72

Levitt JA, Chung PH, Alibhai DR and Suhling K (2011b) "Simultaneous measurements of fluorescence lifetimes, anisotropy and FRAP recovery curves" SPIE Proc 7902: 1–9

Li W, Wang Y, Shao HR, He YH and Ma H (2007) "Probing rotation dynamics of biomolecules using polarization based fluorescence microscopy" *Microsc Res Tech* 70: 390–395

Lillo MP, Beechem JM, Szpikowska BK, Sherman MA and Mas MT (1997) "Design and Characterization of a Multisite Fluorescence Energy-Transfer System for Protein Folding Studies: A Steady-State and Time-Resolved Study of Yeast Phosphoglycerate Kinase" *Biochemistry* 36: 11261–11272

Lillo MP, Cañadas O, Dale RE and Acuña AU (2002) "Location and properties of the taxol binding center in microtubules: a picosecond laser study with fluorescent taxoids" *Biochemistry* 41: 12436–12449

Lo KY, Li Z, Wang F, Marcotte EM and Johnson AW (2009) "Ribosome stalk assembly requires the dual-specificity phosphatase C for the exchange of Mrt4 with P0" *J Cell Biol* 186: 849–862

Lo KY, Li Z, Bussiere C, Bresson S, Marcotte EM and Johnson AW (2010) "Defining the Pathway of Cytoplasmic Maturation of the 60S Ribosomal Subunit" *Mol Cell* 39: 196-208

López-Gallego F, Acebrón I, Mancheño JM, Raja S, Lillo MP and Guisán Seijas JM (2012) "Directed, strong, and reversible immobilization of proteins tagged with aβ-trefoil lectin domain: a simple method to immobilize bio molecules on plain agarose matrixes" *Bioconjugate Chem* 23: 565–73

Lossau H, Kummer A., Heinecke R., Pöllinger-Dammer F, Kompa C, Bieser G, Jonsson T, Silva CM, Yang MM, Youvan DC and Michel-Beyerle ME (1996) "Time-resolved spectroscopy of wild-type and mutant Green Fluorescent Proteins reveals excited state deprotonation consistent with fluorophore-protein interactions" *Chem Phys* 213: 1–16.

Luby-Phelps K (2000) "Cytoarchitecture and physical properties of cytoplasm: volume, viscosity, diffusion, intracellular surface area" *Int Rev Cytol* 192: 189–221

Martinez E, Seguí-Real B, Silles E, Mazón MJ and Sandoval IV (1999) "The prepropeptide of vacuolar amino peptidase I is necessary and sufficient to target the fluorescent reporter protein GFP to the vacuole of yeast by the Ccvt pathway" *Mol Microbiol* 33: 52–62

Mattheyses AL, Kampmann M, Atkinson CE and Simon SM (2010) "Fluorescence anisotropy reveals order and disorder of protein domains in the nuclear pore complex" *Biophys J* 99: 1706–1717

Melnikov S, Ben-Shem A, Garreau de Loubresse N, Jenner L, Yusupova G and Yusupov M (2012) "One core, two shells: bacterial and eukaryotic ribosomes"

Nat Struct Mol Biol 19: 560–567

Mercier JF, Salahpour A, Angers S, Breit A and Bouvier M (2002) "Quantitative assessment of β1- and β2-adrenergic receptor homo and hetero dimerization by bioluminescence resonance energy transfer" *J Biol Chem* 277: 44925–44931

Meyer BH, Segura JM, Martinez KL, Hovius R, George N, Johnsson K and Vogel H (2006) "FRET imaging reveals that functional neurokinin-1 receptors are monomeric and reside in membrane micro domains of live cells" *Proc Natl Acad Sci USA* 103: 2138–2143

Michalec B, Krokowski D, Grela P, Wawiórka L, Sawa-Makarska J, Grankowski N and Tchórzewski M (2010) "Sub cellular localization of ribosomal P0-like protein MRT4 is determined by its N-terminal domain" *Int J Biochem Cell Biol* 42: 736–748

Miles TD, Jakovljevic J, Horsey EW, Harnpicharnchai P, Tang L and Woolford JL Jr. (2005) "Nop7, and Erb1 form a complex necessary for maturation of yeast 66S preribosomes" *Mol Cell Biol* 25: 10419–10432

Molina-Guijarro JM, Macías A, García C, Muñoz E, García-Fernández LF, David M, Núñez L, Martínez-Leal JF, Moneo V, Cuevas C, Lillo MP, Villalobos-Jorge C, Valenzuela C and Galmarini CM (2011) "Irvalec Inserts into the Plasma Membrane Causing Rapid Loss of Integrity and Necrotic Cell Death in Tumor Cells" *PLoS ONE* 6(4): e19042

Morise H, Shimomura O, Johnson FH and Winant J (1974) "Intermolecular energy transfer in the bioluminescent system of Aequorea" *Biochemistry* 13: 2656–2662

Nageswara Rao BD, Kemple MD and Prendergast FG (1980) "Proton nuclear magnetic resonance and fluorescence spectroscopic studies of segmental mobility in aequorin and a green fluorescent protein from *Aequoria victoria*" *Biophys J* 32: 630–632

Naora H (1951) "Micro-spectrophotometry and cytochemical analysis of nucleic acids" *Science* 114: 279–280

Nature Milestones: Light Microscopy. October 2009

Nguyen TA, Sarkar P, Veetil JV, Koushik SV and Vogel SS (2012) "Fluorescence polarization and fluctuation analysis monitors subunit proximity, stoichiometry, and protein complex hydrodynamics" *PLoS One* 7(5): e38209

O'Connor DVO and Phillips D (1984) in *Time-correlated Single Photon Counting* Academic Press, London

Oeffinger M, Leung A, Lamond A and Tollervey D (2002) "Yeast Pescadillo is required for multiple activities during 60S ribosomal subunit synthesis" *RNA* 8: 626–636

Oleinikov AV, Perroud B, Wang B and Traut RR (1993) "Structural and functional domains of Escherichia coli ribosomal protein L7/L12. The hinge region is

required for activity" *J Biol Chem* 268: 917–922

Olivini F, Beretta S and Chirico G (2001) "Two-Photon Fluorescence Polarization Anisotropy Decay on Highly Diluted Solutions by Phase Fluorometry" *Appl Spectroscopy* 55: 311–317

Ormö M, Cubitt AB, Kallio K, Gross LA, Tsien RY and Remington SJ (1996) "Crystal structure of the *Aequorea victoria* green fluorescent protein" *Science* 273: 1392–1395

Padilla-Parra S, Audugé N, Coppey-Moisan M and Tramier M (2008) "Quantitative FRET analysis by fast acquisition time domain FLIM at high spatial resolution in living cells" *Biophys J* 95: 2976–2988

Padilla-Parra S, Audugé N, Lalucque H, Mevel JC, Coppey-Moisan M and Tramier M (2009) "Quantitative Comparison of Different Fluorescent Protein Couples for Fast FRET-FLIM Acquisition" *Biophys J* 97: 2368–2376

Paila YD, Kombrabail M, Krishnamoorthy G and Chattopadhyay A (2011) "Oligomerization of the serotonin (1A) receptor in live cells: a time-resolved fluorescence anisotropy approach" *J Phys Chem B* 115: 11439-47

Patterson GH, Knobel SM, Sharif WD, Kain SR and Piston DW (1997) "Use of the green fluorescent protein and its mutants in quantitative fluorescence microscopy" *Biophys J* 73: 2782–2790

Pawley J (Ed) (2006) *Handbook of Biological Confocal Microscopy*. 3ed Edition Springer. New York

Perozzo MA, Ward KB, Thompson RB and Ward WW (1988) "X-ray diffraction and time-resolved fluorescence analyses of Aequoria green fluorescent protein crystals" *J Biol Chem* 263: 7713–7716

Peter M and Ameer-Beg SM (2004) "Imaging molecular interactions by multiphoton flim" *Biol Cell* 96: 231–236

Piston DW (2005) "When Two Is Better Than One: Elements of Intravital Microscopy" *PLoS Biol* 3(6): e207

Piston DW and Rizzo MA (2008) "FRET by fluorescence polarization microscopy" *Methods Cell Biol* 85: 415– 430

Prasher DC, Eckenrode VK, Ward WW, Prendergast FG and Cormier MJ (1992) "Primary structure of the *Aequorea victoria* green-fluorescent protein" *Gene* 111: 229–233

Quercioli F (2011) *in* "Optical Fluorescence Microscopy: from the Spectral to the Nano Dimension" Chap. 1. (Diaspro A, Ed) pp 1–36. Springer. Berlin Heidelberg

Rao J, Bliattacharya D, Banerjee B, Sarin A and Shivashankar GV (2007) "Trichostatin A induces differential changes in histone protein dynamics and expression in HeLa cells" *Biochem Biophys Res Commun* 363: 263–268

Redford GI and Clegg RM (2005) "Polar plot representation for frequency-domain

analysis of fluorescence lifetimes" *J Fluoresc* 15: 805–815

Remacha M, Santos C, Bermejo B, Naranda T and Ballesta JPG (1992) "Stable binding of the eukaryotic acidic phosphoproteins to the ribosome is not an absolute requirement for in vivo protein synthesis" *J Biol Chem* 267: 12061–12067.

Remacha M, Jimenez-Diaz A, Bermejo B, Rodríguez-Gabriel MA, Guarinos E and Ballesta JP (1995a) "Ribosomal acidic phosphoproteins P1 and P2 are not required for cell viability but regulate the pattern of protein expression in *Saccharomyces cerevisiae*" *Mol Cell Biol* 15: 4754–4762

Remacha M, Jimenez-Diaz A, Santos C, Zambrano R, Briones E, Rodriguez Gabriel MA, Guarinos E and Ballesta JP (1995b) "The proteins P1, P2, and P0, components of the eukaryotic ribosome stalk. New structural and functional aspects" *Biochem Cell Biol* 73: 959–968

Rigler R, Mets Ü, Widengren J and Kask P (1993) "Fluorescence Correlation Spectroscopy with high count rate and low background: analysis of translational diffusion" *Eur Biophys J* 22: 169–175

Rizzo MA, Davidson MW and Piston DW (2009) "Fluorescent Protein Tracking and Detection: Fluorescent Protein Structure and Colour Variants" *Cold Spring Harb Protoc* 4: 1–21

Roberti MJ, Jovin TM and Jares-Erijman E (2011) "Confocal fluorescence anisotropy and FRAP imaging of α-Synuclein amyloid aggregates in living cells" *PLoS ONE* 6(8): e23338

Roberts MS, Dancik Y, Prow TW, Thorling CA, Lin LL, Grice JE, Robertson TA, Konig K and Becker W (2011) "Non-invasive imaging of skin physiology and percutaneous penetration using 5D (space, time and anisotropy) fluorescence spectral and lifetime imaging with multiphoton and confocal microscopy" *Eur J Pharm Biopharm* 77: 469–488

Rodríguez-Gabriel MA, Remacha M and Ballesta JP (1998) "Phosphorylation of ribosomal protein P0 is not essential for ribosome function but can affect translation" *Biochemistry* 37: 16620–16626

Rodríguez-Mateos M, Abia D, García-Gómez JJ, Morreale A, de la Cruz J, Santos C, Remacha M and Ballesta JPG (2009a) "The amino terminal domain from Mrt4 protein can functionally replace the RNA binding domain of the ribosomal P0 protein. *Nucleic Acids Res* 37: 3514–3521

Rodríguez-Mateos M, García-Gómez JJ, Francisco-Velilla R, Remacha M, de laCruz J and Ballesta JP (2009b) "Role and dynamics of the ribosomal protein P0 and its related trans-acting factor Mrt4 during ribosome assembly in *Saccharomyces cerevisiae. Nucleic Acids Res* 37: 7519–7532

Saenz-Robles MT, Remacha M, Vilella MD, Zinker S and Ballesta JP (1990) "The acidic ribosomal proteins as regulators of the eukaryotic ribosomal activity" *Biochim Biophys Acta* 1050: 51–55

Santos C and Ballesta JP (1994) "Ribosomal protein P0, contrary to phosphoproteins P1

and P2, is required for ribosome activity and Saccharomyces cerevisiae viability" *J Biol Chem* 269: 15689–15696

Santos C and Ballesta JP (1995) "The highly conserved protein P0 carboxyl end is essential for ribosome activity only in the absence of proteins P1 and P2" *J Biol Chem* 270: 20608–20614

Santos C and Ballesta JPG (2002) "Role of the ribosomal stalk components in the resistance of Aspergillus fumigatus to the sordarin antifungals" *Mol Microbiol* 43: 227–237

Santos C, Rodríguez-Gabriel MA, Remacha M and Ballesta JP (2004) "Ribosomal P0 protein domain involved in selectivity of antifungal sordarin derivatives" *Antimicrob Agents Chemother* 48: 2930–2936

Scharf K-D and Nover L (1987) "Control of ribosome biosynthesis in plant cell cultures under heat shock conditions. II.Ribosomal proteins" *Biochim Biophys Acta* 909: 44–57

Schön P, Muñoz, Gasecka A, Brustlein S and Brasselet S (2008) "Polarization distortion effects in polarimetric two-photon microscopy" *Opt Express* 16: 20891–20901

Shaner NC, Campbell RE, Steinbach PA, Giepmans BN, Palmer AE and Tsien RY (2004) "Improved monomeric red, orange and yellow fluorescent proteins derived from *Discosoma sp*. red fluorescent protein" *Nature Biotechnol.* 22: 1567–1572

Sharma P, Varma R, Sarasij RC, Ira, Gousset K, Krishnamoorthy G, Rao M and Mayor S (2004) "Nanoscale organization of multiple GPI-anchored proteins in living cell membranes," *Cell* 116: 577–589

Sherman F (2002) "Getting stated with Yeast" *Methods Enzymology* 350: 3–41

Siegel J, Suhling K, Lévêque-Fort S, Webb SED, Davis DM, Phillips D, Sabharwal Y and French PMW (2003) "Wide-field time-resolved fluorescence anisotropy imaging (TR-FAIM):Imaging the rotational mobility of a fluorophore" *Rev Sci Instrum* 74: 182–192

Soto M, Requena JM and Alonso C (1993) "Isolation, characterization and analysis of the expression of the Leishmania ribosomal P0 protein genes" *Mol Biochem Parasitol* 61: 265–274

Spahn CM, Beckmann R, Eswar N, Penczek PA, Sali A, Blobel G and Frank J (2001) "Structure of the 80S ribosome from *Saccharomices cerevisiae*-tRNA-ribosome and subunit-subunit interactions" *Cell* 107: 373–386

Spahn CM, Gómez-Lorenzo MG, Grassucci RA, Jørgensen R, Andersen GR, BeckmannR, Penczek PA, Ballesta JP and Frank J (2004) "Domain movements of elongation factor eEF2and the eukaryotic 80S ribosome facilitate tRNA translocation" *EMBO J* 23: 1008–1019

Stryer L (1978) "Fluorescence energy transfer as a spectroscopic ruler" *Annu Rev Biochem.* 47: 819–846

Striker G, Subramaniam V, Seidel CAM and Volkmer A (1999) "Photochromicity and fluorescence lifetimes of Green Fluorescent Protein" *J Phys Chem B* 103: 8612–8617

Suhling K, Siegel J, Lanigan PM, Lévêque-Fort S, Webb SE, Phillips D, Davis DM and French PM (2004) "Time-resolved fluorescence anisotropy imaging applied to live cells" *Opt Lett* 29: 584–586

Swaminathan R, Hoang CP and Verkman AS (1997) "Photobleaching recovery and anisotropy decay of green fluorescent protein GFP-S65T in solution and cells: cytoplasmic viscosity probed by green fluorescent protein translational and rotational diffusion" *Biophys J* 72: 1900–1907

Szabelski M, Ilijev D, Sarkar P, Luchowski R, Gryczynski Z, Kapusta P, Erdmann R, Gryczynski I (2009) "Collisional quenching of erythrosine B as a potential reference dye for impulse response function evaluation" *Appl Spectrosc.* 63: 363–368.

Talkish J, Zhang J, Jakovljevic J, Horsey EW and Woolford JL, Jr. (2012) "Hierarchical recruitment into nascent ribosomes of assembly factors required for 27SB pre-rRNA processing in Saccharomyces cerevisiae" *Nucl Acids Res* 40: 8646–8661

Tang L, Sahasranaman A, Jakovljevic J, Schleifman E and Woolford JL Jr (2008) "Interactions among Ytm1, Erb1, and Nop7 required for assembly of theNop7-subcomplex in yeast preribosomes" *Mol Biol Cell* 19: 2844–56

Taylor DJ, Devkota B, Huang AD, Topf M, Narayanan E, Sali A, Harvey SC and Frank J (2009) "Comprehensive molecular structure of the eukaryotic ribosome" *Structure* 17: 1591–604

Tchorzewski M, Boguszewska A, Dukowski P and Grankowski N (2000) "Oligomerization properties of the acidic ribosomal P-proteins from Saccharomyces cerevisiae: effect of P1A protein phosphorylation on the formation of the P1A-P2B hetero-complex" *Biochim Biophys Acta* 1499: 63–73

Tchorzewski M. (2002) "The acidic ribosomal P proteins" *Int J Biochem Cell Biol* 34: 911–915

Thaler C, Koushik SV, Puhl HL 3rd, Blank PS and Vogel SS (2009) "Structural rearrangement of CaMKIIalpha catalytic domains encodes activation" *Proc Natl Acad Sci USA* 106: 6369–74

Trabuco LG, Schreiner E, Eargle J, Cornish P, Ha T, Luthey-Schulten Z and Schulten K (2010) "The role of L1 stalk-tRNA interaction in the ribosome elongation cycle" *J Mol Biol* 402: 741–760

Tramier M, Kemnitz K, Durieux C. Coppey J., Denjean P, Pansu R and Coppey-Moisan M (2000) "Restrained torsional dynamics of nuclear DNA in living proliferative mammalian cells" *Biophys J* 78: 2614–2627.

Tramier M, Gautier I, Piolot T, Ravalet S, Kemnitz K, Coppey J, Durieux C, Mignotte

V and Coppey-Moisan M (2002) “Picosecond-Hetero-FRET Microscopy to Probe Protein-Protein Interactions in Live Cells” *Biophys J* 83: 3570–3577

Tramier M, Zahid M, Mevel JC, Masse MJ and Coppey-Moisan M (2006) “Sensitivity of CFP/YFP and GFP/ mCherry pairs to donor photobleaching on FRET determination by fluorescence lifetime imaging microscopy in living cells” *Microsc Res Tech* 69: 933–939

Tsien R (1998) "The green fluorescent protein” *Annu Rev Biochem* 67: 509–44

Tsurugi K and Ogata K (1985) “Evidence for the exchangeability of acidic ribosomal proteins on cytoplasmic ribosomes in regenerating rat liver” *J Biochem* 98: 1427–1431

Uskova MA, Borst JW, Hink MA, van Hoek A, Schots A, Klyachko NL and Visser AJWG (2000) “Fluorescence dynamics of green fluorescent protein in AOT reversed micelles” *Biophys Chem* 87: 73–84

Valeur B (2002) in *Molecular Fluorescence.* Wiley-VCH. Weinhein.

van Wijk SJL, Fiskin E, Putyrski M, Pampaloni F, Hou J, Wild P, Kensche T, Grecco HE, Bastiaens P and Dikic I (2012) “Fluorescence-Based Sensors to Monitor Localization and Functions of Linear and K63-Linked Ubiquitin Chains in Cells” *Mol Cell* 47: 797–809.

Varma R and Mayor S (1998) “GPI-anchored proteins are organized in submicron domains at the cell surface” *Nature* 394: 798–801

Vishwasrao HD, Trifilieff P and Kandel ER (2012) “In vivo imaging of the actinpolymerization state with two-photon fluorescence anisotropy” *Biophys J* 102: 1204–14

Volkmer A, Subramaniam V, Birch DJS and Jovin TM (2000) “One and two-photon excited fluorescence lifetimes and anisotropy decays of green fluorescent proteins” *Biophys J* 78: 1589–1598

Von Arnim CAF, Kinoshita A, Peltan ID, Tangredi MM, Herl L, Lee BM, Spoelgen R, Hshieh TT, Ranganathan S, Battey FD, Liu CX, Bacskai BJ, Sever S, Irizarry MC, Strickland DK and Hyman BT (2005) “The low density lipoprotein receptor-related protein (LRP) is a novel beta-secretase (BACE1) substrate” *J Biol Chem* 280: 17777–17785

Wahl M (2009) “The correlated single photon counting” *Technical note TCSPC v2.1* PicoQuant GmbH. Germany

Warner JR (1999) “The economics of ribosome biosynthesis in yeast*” Trends Biochem Sci* 24: 437–440

Wouters FS, Verveer PJ and Bastiaens PI (2001) “Imaging biochemistry inside cells” *Trends Cell Biol* 11: 203–211

Wu Y, Sun F, Tong D and Taylor B (1996) “Changes in membrane properties during energy depletion-induced cell injury studied with fluorescence microscopy” *Biophys J* 71, 91–100

Yamaguchi M, Namiki Y, Okada H, Mori Y, Furukawa H, Wang J, Ohkusu M and Kawamoto S (2011) "Structome of Saccharomyces cerevisiae determined by freeze-substitution and serial ultrathin-sectioning electron microscopy" *J Electron Microscopy* 60: 337–351

Yasuda R, Harvey CD, Zhong H, Sobczyk A, van Aelst L and Svoboda K (2006) "Supersensitive Ras activation in dendrites and spine revealed bu two-photon fluorescence imaging" *Nat Neurosci* 9: 283–291

Yeow EKL and Clayton AHA (2007) "Enumeration of oligomerization states of membrane proteins in living cells by homo-FRET spectroscopy and microscopy: Theory and application" *Biophys J* 92: 3098–3104

Yuan L, Lin W, Zheng K and Zhu S (2013) "FRET-Based Small-Molecule Fluorescent Probes: Rational Design and Bioimaging Applications" *Acc Chem Res* 46: 1462–1473

Zinker S and Warner JR (1976) "The ribosomal proteins of *Saccharomyces cerevisiae*. Phosphorylated and exchangeable proteins" *J Biol Chem* 251: 1799–1807

Ziomkiewicz I, Loman A, Klement R, Fritsch C, Klymchemko AS, Bunt G, Jovin TM and Arndt-Jovin DJ (2013) "Dynamic conformational transitions of the EGF receptor in living mammalian cells determined by FRET and fluorescence lifetime imaging microscopy" *Cytometry* doi: 10.1002/cyto.a.22311

Zipfel WR, Williams RM and Webb WW (2003) "Nonlinear magic: Multi-photon microscopy in the biosciences" *Nat. Biotechnol.* 21:1368–1376

Zorrilla S, Rivas G and Lillo MP (2004a) "Structure and dynamics of proteins in crowded media: A time-resolved fluorescence polarization study" in *Methods in proteome and protein analysis* Chap.3 (Kamp RM, Calvete JJ, Choli-papadopoulou T, Eds) Springer-Verlag Berlin Heidelberg

Zorrilla, Rivas G and Lillo MP (2004b) "Fluorescence anisotropy as a probe to study tracer proteins in crowded solutions" *J Mol Recognit* 17: 408–416

Zorrilla S, Hink MA, Visser AJWG and Lillo MP (2007) "Translational and rotational motions of proteins in a protein crowded environment" *Biophys Chem* 125: 298–305